



# **Unraveling the origin of high-energy neutrino sources: follow-up searches of IceCube alert events**

Martina Stefanie Karl

Vollständiger Abdruck der von der Fakultät für Physik der Technischen Universität München zur Erlangung einer

Doktorin der Naturwissenschaften (Dr. rer. nat.)

genehmigten Dissertation.

Vorsitzender: Prof. Dr. Andreas Weiler

Prüferinnen der Dissertation:

1. Prof. Dr. Elisa Resconi
2. Prof. Dr. Susanne Mertens

Die Dissertation wurde am 11.04.2022 bei der Technischen Universität München eingereicht und durch die Fakultät für Physik am 16.05.2022 angenommen.

## Abstract

I investigate possible high-energy neutrino production sites — based on IceCube alert events — for additional neutrino emission. For this, I look at 11 years of muon data from the IceCube Neutrino Observatory. In total, this analysis covers the origin region of 122 alerts that were detected between 2009 and the end of 2021.

The signal I aim to find are neutrinos originating from a specific source with an energy distribution following  $E^{-\gamma}$ , whereas the background is a diffuse neutrino flux. This work investigates two main source classifications: sources with continuous neutrino emission and sources with transient neutrino emission. For the continuous case, the single strongest source out of 122 defined regions has a global p-value of 0.98 and is compatible with the background hypothesis. The upper flux limit for that source (with 90% confidence level) is  $\Phi_{90\%,100\text{TeV}} = 6.9 \times 10^{-17} (\text{TeV cm}^2 \text{ s})^{-1}$ .  $\Phi_{90\%,100\text{TeV}}$  is for a spectral index of  $\gamma = 2$  and normalized at 100 TeV. When looking at the combined lower-energy emission IceCube measures from all 122 alert origins (excluding the alert events from analyzed data), I find a p-value of 8%, which is also compatible with the background hypothesis. In total, the 90% confidence level upper flux limit is  $\Phi_{90\%,100\text{TeV}} = 4.2 \times 10^{-16} (\text{TeV cm}^2 \text{ s})^{-1}$  for an energy spectral index of  $\gamma = 2$  for the lower-energy component of all positions combined. This corresponds to 1.6% of IceCube's astrophysical diffuse flux. When investigating the maximal contribution from all positions including the alert events, the maximal overall flux is  $\Phi_{90\%,100\text{TeV}} = 1.2 \times 10^{-15} (\text{TeV cm}^2 \text{ s})^{-1}$  ( $\gamma = 2$ ) coming from all regions combined. This flux is 4.6% of IceCube's astrophysical diffuse flux.

Next, I search for transient neutrino emission and present new methods for identifying them. I find the transient neutrino emission associated with the blazar TXS 0506+056 as the most significant neutrino flare. The local p-value is  $p_{local} = 0.14\% = 2.99\sigma$ . The flare parameters of this work agree with previous works. I find a Gaussian flaring time window centered at  $\mu_T = 57001_{-44}^{+52}$  MJD with a width of  $\sigma_T = 64_{-15}^{+58}$  days. The likelihood maximization finds  $12_{-6}^{+9}$  neutrinos from the source following a source spectral index of  $\gamma = 2.3 \pm 0.4$ . The corresponding time-integrated flux — the fluence —  $J_{100\text{TeV}} = \int_{t_{start}}^{t_{end}} \Phi_{100\text{TeV}} dt$ , normalized at 100 TeV, is  $J_{100\text{TeV}} = 1.2_{-0.8}^{+1.1} \times 10^{-8} (\text{TeV cm}^2)^{-1}$ . The average flux during the  $2\sigma_T$  time window is  $\Phi_{100\text{TeV}} = 1.1_{-0.7}^{+1.0} \times 10^{-15} (\text{TeV cm}^2 \text{ s})^{-1}$ . When correcting for testing 122 positions, the global p-value is  $p_{global} = 0.156$  and is compatible with background.

In general, the lack of a softer neutrino component agrees with expectations from sources with hard neutrino emission. Finding the transient neutrino emission associated with TXS 0506+056 with IceCube data as the only flare with a local p-value at the level of  $\sim 3\sigma$  strengthens the hypothesis of TXS 0506+056 as a neutrino source.

## Zusammenfassung

In dieser Arbeit untersuche ich die Entstehungsorte der höchstenergetischsten Neutrinos (basierend auf IceCube Alerts) nach zusätzlicher Neutrinoemission. Für diese Suche verwende ich 11 Jahre überarbeiteter und verbesserter Muon Daten des IceCube Neutrino Observatoriums. Insgesamt werden die Entstehungsorte von 122 Alerts, gemessen zwischen 2009 und 2021, analysiert.

Diese Analyse besteht aus zwei Teilen: Der Suche nach Quellen, die Neutrinos gleichmäßig über Zeit (zeitunabhängig) emittieren und Quellen, die Neutrinos nur manchmal (zeitabhängig) produzieren. Die zeitunabhängige Analyse der 122 Regionen resultiert in einem globalen Signifikanzwert von 98% und ist damit kompatibel mit der Nullhypothese – Neutrinos, die nicht von einer bestimmten Quelle produziert werden sondern Teil eines diffusen Hintergrundes sind. Der maximal erwartete Fluss der signifikantesten Position ist  $\Phi_{90\%,100\text{TeV}} = 6,9 \times 10^{-17} (\text{TeV cm}^2 \text{ s})^{-1}$  mit 90% Konfidenz. Der Fluss  $\Phi_{90\%,100\text{TeV}}$  folgt einem Energiespektrum mit Index  $\gamma = 2$  und ist bei 100 TeV normiert. Die gesamte erwartete Neutrinoemission von allen 122 Regionen summiert, ergibt einen Signifikanzwert von 8% und ist somit auch kompatibel mit der Nullhypothese. Der maximal erwartete Gesamtfluss für niedrigere Neutrinoenergien von allen Regionen kombiniert ist  $\Phi_{90\%,100\text{TeV}} = 4,2 \times 10^{-16} (\text{TeV cm}^2 \text{ s})^{-1}$ , was 1,6% des diffusen astrophysikalischen Neutrinoflusses ausmacht. Der Fluss, den man allgemein maximal von allen 122 Entstehungsregionen erwarten kann, inklusive der Hochenergiekomponente in Form der Alert Events, ist  $\Phi_{90\%,100\text{TeV}} = 1,2 \times 10^{-15} (\text{TeV cm}^2 \text{ s})^{-1}$  mit  $\gamma = 2$ . Dies entspricht 4,6% des diffusen astrophysikalischen Neutrinoflusses.

Als Nächstes suche ich nach zeitabhängiger Neutrinoemission (Neutrinoflares) und präsentiere ein neues Verfahren, um diese temporären Neutrinoemissionen zu finden. Die signifikanteste zeitabhängige Neutrinoemission ist der Neutrinoflare, der mit dem Blazar TXS 0506+056 assoziiert wird. Der lokale Signifikanzwert ist  $p_{local} = 0,14\% = 2,988\sigma$ . Korrigiert man für die Tatsache, dass 122 Positionen untersucht wurden, ergibt sich ein globaler Signifikanzwert von  $p_{global} = 0,156$ , der kompatibel mit der Nullhypothese ist. Die Parameter der zeitabhängigen Neutrinoemission meiner Analyse stimmen mit früheren Ergebnissen überein. Das Emissionszeitfenster in Form einer Gaußkurve ist um  $\mu_T = 57001_{-44}^{+52}$  MJD zentriert und hat eine Breite von  $\sigma_T = 64_{-15}^{+58}$  Tagen. Aus der Likelihood ergibt  $n_S = 12_{-6}^{+9}$  Neutrinos, die von der Quelle emittiert werden und einem Energiespektrum mit Index  $\gamma = 2,3 \pm 0,4$  folgen. Integriert man den entsprechenden durchschnittlichen Fluss  $\Phi_{100\text{TeV}} = 1,1_{-0,7}^{+1,0} \times$

$10^{-15} \text{ (TeV cm}^2 \text{ s)}^{-1}$  über die Emissionszeit von  $2\sigma_T$ , ergibt sich eine Fluenz von  $J_{100\text{TeV}} = \int_{t_{\text{start}}}^{t_{\text{end}}} \Phi_{100\text{TeV}} dt = 1,2_{-0,8}^{+1,1} \times 10^{-8} \text{ (TeV cm}^2\text{)}^{-1}$ , jeweils bei 100 TeV normiert.

Allgemein kann das Fehlen von Neutrinos mit niedrigeren Energien auf ein sehr hartes Emissionsspektrum der möglichen Quellen deuten. Die Tatsache, dass die signifikanteste zeitabhängige Neutrinoemission der Neutrinoflare assoziiert mit TXS 0506+056 ist, unterstützt die Hypothese, dass TXS 0506+056 eine Neutrinoquelle ist.

# Acknowledgements

This work would not have been possible without the support and encouragement of the people around me. First, I want to thank my advisor and professor, Elisa Resconi, for introducing me to neutrino astronomy and always believing in my work. Especially all the fruitful discussions with the people in the IceCube collaboration and the TUM made the Ph.D. an enjoyable and fascinating experience. Here, especially Martin Wolf and Hans Niederhausen helped me during the beginning of my Ph.D. For the later part, this work could not have been finished without the dedicated help of Philipp Eller.

I want to thank my office mates Chiara, Stephan, and Martin, who accompanied me during various stages of my academic life and with whom I could spend many hours drinking tea and eating cake (and working, of course). I enjoyed coming to the office to a great part because of your company.

Great thanks go out to everyone who proofread this thesis, especially a huge thank you to Stephan and Philipp, who read every single page of this work. I owe you at least five cakes, several whiskey bottles, and probably some homemade Indian food.

I also want to thank my family and friends for their unconditional love and support. Especially to Linus for being there and always picking me up when I'm down.

Last but not least, I want to thank the Max Planck Institute for Physics and the IMPRS graduate school for enabling my work, travels, and participation in interesting workshops and all the friends I gained there.



# Contents

1	Introduction	1
2	High-energy cosmic rays and neutrinos	5
2.1	Cosmic rays	5
2.2	Source candidates	9
2.2.1	White dwarfs, neutron stars, and supernova remnants	9
2.2.2	Starburst galaxies	9
2.2.3	Gamma-ray bursts	10
2.2.4	Active galactic nuclei and blazars	10
2.3	Neutrinos from hadronic cosmic ray interactions at astrophysical sources	13
2.4	Atmospheric air showers and neutrinos	16
2.4.1	Hadrons in the atmosphere	16
2.4.2	Mesons in the atmosphere	18
2.4.3	Muons and neutrinos in the atmosphere	19
2.5	Neutrino oscillation	22
2.6	Neutrino interactions	25
2.6.1	Neutrino deep inelastic scattering	25
2.6.2	Neutrino interactions in the Earth	27
3	The IceCube Neutrino Observatory	31
3.1	Detection principle	31
3.2	Event selection	37
3.3	IceCube realtime alert events	41
3.4	Muon track reconstruction	43
3.4.1	MuEX Angular	46
3.4.2	SplineMPE	46
3.4.3	Uncertainty estimation	46

3.4.4	Energy reconstruction - Truncated mean . . . . .	48
3.4.5	Millipede reconstruction . . . . .	50
4	Search for neutrino sources – Motivation and Method . . . . .	53
4.1	Unbinned likelihood ratio test . . . . .	55
4.2	Signal and background PDF for steady neutrino emission . . . . .	57
4.3	Identifying the best point-source position . . . . .	59
4.4	Stacking of source candidates . . . . .	61
4.5	Test of the time-integrated analysis . . . . .	62
4.6	Signal and background PDF for transient neutrino emission . . . . .	64
4.7	Identifying neutrino flares . . . . .	65
4.7.1	Neutrino flare searches in previous IceCube analyses . . . . .	67
4.7.2	Development of optimized methods for neutrino flare searches . . . . .	69
4.7.3	Test of the time-dependent analysis . . . . .	75
4.7.4	Fitting lower-energetic neutrino flares . . . . .	75
4.7.5	Effect of the spectral index scan on parameter recovery . . . . .	77
4.8	Significance calculation . . . . .	79
4.9	Trial correction . . . . .	79
4.10	Sensitivity and discovery potential . . . . .	79
4.11	Flux limit calculation . . . . .	84
4.12	Confidence regions of fitted parameter . . . . .	84
5	Search for neutrino sources – results and discussion . . . . .	85
5.1	Search for continuous neutrino sources . . . . .	86
5.1.1	Single steady sources . . . . .	86
5.1.2	Multiple steady sources – stacking . . . . .	91
5.2	Search for transient neutrino sources . . . . .	93
6	Conclusion . . . . .	105
A	IceCube realtime alert events . . . . .	109
B	Parameter recovery for time-dependent analysis . . . . .	115
B.1	Flare: $\sigma_T = 55.18$ days, no spectral index scan . . . . .	115
B.2	Flare: $\sigma_T = 55.18$ days, with spectral index scan . . . . .	118
B.3	Flare: $\sigma_T = 10$ days, $\gamma = 2$ . . . . .	121
B.4	Flare: $\sigma_T = 100$ days, $\gamma = 2.0$ . . . . .	122
C	Time-integrated results . . . . .	125

D	Time-dependent results	131
D.1	P-value distribution and parameter distribution . . . . .	135
D.2	Event views of top 9 contributing events to TXS 0506+056 neutrino flare . . . . .	136



# List of Figures

2.1	Cosmic ray spectrum . . . . .	6
2.2	Cosmic ray model components . . . . .	7
2.3	Hillas plot . . . . .	8
2.4	AGN classes . . . . .	11
2.5	Spectral energy distribution for different AGN . . . . .	12
2.6	Astrophysical neutrino flux . . . . .	15
2.7	Simplified sketch of a cosmic ray air shower. Adapted from [33] and [70]. . . . .	16
2.8	Atmospheric lepton flux . . . . .	22
2.9	Flavor ratio $\nu_x/\nu_e$ for neutrinos traveling astronomical distances. . . . .	25
2.10	Neutrino deep inelastic scattering . . . . .	26
2.11	Neutrino cross sections of interactions with nucleons . . . . .	27
2.12	Energy transferred to the nucleon by the neutrino charged-current interactions. . . . .	27
2.13	Earth density and neutrino transmission probability . . . . .	29
3.1	Cherenkov effect . . . . .	32
3.2	Scattering (left) and absorption (right) in the Antarctic ice. . . . .	33
3.3	Track and Cascade Events . . . . .	34
3.4	The IceCube detector . . . . .	36
3.5	Event rates at trigger level . . . . .	38
3.6	Energy distribution and effective area of IC86 . . . . .	41
3.7	Realtime alert system . . . . .	42
3.8	Propagation of a Cherenkov photon originating from a muon track and track segmentation . . . . .	45
3.9	Photon delay times and median angular resolution . . . . .	47
3.10	Pull correction . . . . .	49
3.11	Muon energy losses in ice . . . . .	50

4.1	IceCube-170922A and the blazar TXS 0506+056 . . . . .	54
4.2	Example test statistic distributions for time-integrated neutrino emission. . . . .	59
4.3	Position fit illustration . . . . .	60
4.4	Effect of position fit on test statistic distribution . . . . .	61
4.5	$TS_{stacked}$ for all considered positions. . . . .	62
4.6	Recovery of source position for steady neutrino emission . . . . .	63
4.7	Recovery of $n_S$ and $\gamma$ for steady neutrino emission . . . . .	64
4.8	Time distribution of IceCube events . . . . .	66
4.9	$S/B$ of IceCube events . . . . .	67
4.10	Events that surpass a certain threshold of $S/B$ are considered as possible start and end points of neutrino flares. . . . .	67
4.11	TS values for different flare intensities . . . . .	70
4.12	Fit of TS values for different TS intensities with fixed flare strength. . . . .	71
4.13	Example flare fit with EM . . . . .	74
4.14	EM for multiple neutrino flares . . . . .	75
4.15	Recovery of $\mu_T$ for neutrino flares with $\gamma = 2.0, 3.0$ . . . . .	76
4.16	Recovery of $\sigma_T$ for neutrino flares with $\gamma = 2.0, 3.0$ . . . . .	76
4.17	Recovery of $\mu_T$ for neutrino flares with $\gamma = 3.0$ . . . . .	78
4.18	Recovery of $\sigma_T$ for neutrino flares with $\gamma = 3.0$ . . . . .	78
4.19	Concept of sensitivity and discovery potential . . . . .	80
4.20	Time integrated sensitivity and discovery potential . . . . .	81
4.21	Sensitivity and discovery potential for time-integrated individual search . . . . .	81
4.22	Expectation maximization vs. brute force . . . . .	82
4.23	Sensitivity and discovery potential for the time dependent case . . . . .	83
4.24	Effect of spectral index scan on sensitivity and discovery potential . . . . .	84
5.1	Map of all high-energy alerts . . . . .	86
5.2	Map of all high-energy alerts with time-integrated hot spot . . . . .	87
5.3	P-value map of time-integrated hot spot and blazars in the vicinity . . . . .	87
5.4	Uncertainty of time-integrated fitted parameter . . . . .	88
5.5	Blazars in the vicinity of best time-integrated position and squared angular distance between the best-fit position and reconstructed event origin direction . . . . .	89
5.6	Local p-value distribution and p-value vs. $n_S$ . . . . .	90
5.7	Time-integrated p-value vs. $\gamma$ and $n_S$ vs. $\gamma$ . . . . .	90
5.8	$\Phi_{90\%,100\text{TeV}}$ for the time integrated search . . . . .	91

5.9	90% confidence limit upper flux limit for stacked source candidates . . . . .	92
5.10	Map of all high-energy alerts with time-dependent hot spot . . . . .	94
5.11	$S/B$ distribution of events from TXS 0506+056 . . . . .	94
5.12	Uncertainty of $\mu_T$ and $\sigma_T$ . . . . .	95
5.13	Uncertainty of time-dependent fitted parameter . . . . .	95
5.14	Squared angular distance between TXS 0506+056 and reconstructed events and single event contribution to significance . . . . .	96
5.15	Position of contributing events to TXS 0506+056 neutrino flare . . . . .	98
5.16	P-value map of time-dependent hot spot and blazars in the vicinity . . . . .	99
5.17	Fermi test statistic map of source candidates for different photon energies during the neutrino flare . . . . .	100
5.18	Gamma-ray light curve of TXS 0506+056 . . . . .	101
5.19	Zoom into gamma-ray light curve of TXS 0506+056 . . . . .	101
5.20	Spectral energy distribution of TXS 0506+056 in photons and neutrinos	102
B.1	Recovery of $n_S$ for neutrino flares with $\gamma = 2.0, 3.0$ . . . . .	115
B.2	Recovery of $\gamma$ for neutrino flares with $\gamma = 2.0, 3.0$ . . . . .	116
B.3	Recovery of $\mu_T$ for neutrino flares with $\gamma = 2.0, 3.0$ . . . . .	116
B.4	Recovery of $\sigma_T$ for neutrino flares with $\gamma = 2.0, 3.0$ . . . . .	117
B.5	Recovery of the simulated source position for neutrino flares with $\gamma = 2.0, 3.0$ . . . . .	117
B.6	Recovery of $n_S$ for neutrino flares with $\gamma = 2.0, 3.0$ . . . . .	118
B.7	Recovery of $\gamma$ for neutrino flares with $\gamma = 2.0, 3.0$ . . . . .	118
B.8	Recovery of $\mu_T$ for neutrino flares with $\gamma = 2.0, 3.0$ . . . . .	119
B.9	Recovery of $\sigma_T$ for neutrino flares with $\gamma = 2.0, 3.0$ . . . . .	119
B.10	Recovery of the simulated source position for neutrino flares with $\gamma = 2.0, 3.0$ . . . . .	120
B.11	Recovery of $n_S$ and $\gamma$ for a neutrino flare with $\gamma = 2.0$ and $\sigma_T = 10$ d . . . . .	121
B.12	Recovery of $\mu_T$ and $\sigma_T$ for a neutrino flare with $\gamma = 2.0$ and $\sigma_T = 10$ d . . . . .	121
B.13	Recovery of the source position for neutrino flares with $\gamma = 2.0$ and $\sigma_T = 10$ d . . . . .	122
B.14	Recovery of $n_S$ and $\gamma$ for a neutrino flare with $\gamma = 2.0$ and $\sigma_T = 100$ d . . . . .	122
B.15	Recovery of $\mu_T$ and $\sigma_T$ for a neutrino flare with $\gamma = 2.0$ and $\sigma_T = 100$ d . . . . .	123
B.16	Recovery of the source position for neutrino flares with $\gamma = 2.0$ and $\sigma_T = 100$ d . . . . .	123
D.1	Time-dependent p-value distribution and p-value vs. ns . . . . .	135

D.2	Time-dependent p-value vs. $\gamma$ and $n_S$ . . . . .	136
D.3	Time-integrated p-value vs. $\mu_T$ and $\sigma_T$ . . . . .	136
D.4	Event view of the two most contributing events to TXS 0506+056 . .	137
D.5	Event view of the 3rd and 4th most contributing events to TXS 0506+056	137
D.6	Event view of the 5th and 6th most contributing events to TXS 0506+056	137
D.7	Event view of the 7th and 8th most contributing events to TXS 0506+056	138
D.8	Event view of the 9th most contributing events to TXS 0506+056 . . .	138

## List of Tables

3.1	Data samples . . . . .	40
3.2	Expected and observed alert rate. . . . .	43
5.1	Events contributing to the TXS 0506+056 neutrino flare . . . . .	97
A.1	Table of all IceCube alert events analyzed in this work . . . . .	113
C.1	Results individual time-integrated search . . . . .	129
D.1	Results individual time-dependent search . . . . .	135



# Chapter 1

## Introduction

The most energetic particles ever observed are cosmic rays, with energies exceeding  $10^{20}$  eV [1]. They were first observed in balloon experiments by Victor Hess in 1912 [2]. However, more than 100 years later, the origin of cosmic rays and how they are accelerated to these extreme energies remain outstanding questions. A major difficulty in answering these questions is the fact that cosmic rays do not point back to their origin. Instead, they are deflected by galactic and extragalactic fields due to their charge (see, for example, [3]). Thus the search for cosmic ray production sites requires additional messengers.

Cosmic ray acceleration and interactions produce photons and neutrinos in hadronic and electroweak processes. Both photons and neutrinos can serve as messengers. However, photons are also produced by many other leptonic processes. This constitutes additional experimental background. Furthermore, gamma rays can interact with ambient photons, and very-high-energy gamma rays interact with extragalactic background light [4] and the cosmic microwave background. Thus, the universe becomes opaque for very-high-energy gamma rays that do not originate in our vicinity (see [5–7]). With these challenges, gamma rays alone have not yet sufficed to identify the production sites of cosmic rays.

Neutrinos, on the other hand, traverse the universe nearly unhindered. They provide an additional observation channel even for the most distant and most hidden corners of our cosmos. The production of high-energy neutrinos is linked to cosmic ray interactions and is a smoking gun indication of hadronic interaction [8]. The first cosmic neutrinos were discovered in 2013 by the IceCube Neutrino Observatory [9]. However, no accumulation of these high-energy cosmic neutrinos around specific

origin directions was observed, and no indication of their source was found. Four years later, on the 22nd of September 2017, the IceCube Neutrino Observatory [10] detected a high-energy neutrino (IceCube-170922A), which had a high probability of being of astrophysical origin. Since neutrinos and gamma rays are closely linked, this detection triggered gamma-ray follow-up observations. At the arrival direction of IceCube-170922A, telescopes observed one of the most extreme objects in the universe in a flaring state – the blazar [11] TXS 0506+056 [12–15] (see Section 2.2 for a description of blazars). Further analysis of archival IceCube data presented evidence for additional neutrino emission originating from TXS 0506+056: a neutrino flare between September 2014 and March 2015 [16].

The  $3.5\sigma$  evidence of TXS 0506+056 as a neutrino source leads to the question of whether high-energy neutrinos point back to production sites of general neutrino emission. This would indicate production sites of cosmic rays, similar to IceCube-170922A. In this thesis, I aim to answer this question. I search for neutrino emission from arrival directions of 122 high-energy neutrinos in 11 years of archival IceCube data.

First, I present the theoretical basis of neutrino astronomy in Chapter 2. This chapter briefly introduces cosmic rays and their link to neutrinos, possible astrophysical production sites, and background from the atmosphere. It also covers neutrino oscillation, interactions, and neutrino attenuation in the earth, such that the expected neutrino flux is understood.

Chapter 3 describes the IceCube Neutrino Observatory, a cubic kilometer-scale neutrino detector in the Antarctic ice. In this chapter, I go through the data-taking process and introduce selection criteria of events and reconstruction algorithms to determine the neutrinos' origin direction and energy.

Chapter 4 contains the technical details and the statistical methods for the follow-up search for cosmic neutrino sources. This chapter describes the unbinned likelihood approach and details the signal and background assumptions that enter my analysis. This analysis integrates two classes of neutrino sources: sources that emit neutrinos continuously over time and sources that emit neutrinos in a flare. An additional test probes the total neutrino emission emitted by all potential sources. In this chapter, I also present my approach to deal with the uncertainties of the origin direction of high-energy neutrinos. Furthermore, I discuss the challenges of previous analyses and the development of new methods concerning the search for transient neutrino

emission. The last part of this chapter shows tests of the analysis performance on simulated data.

Finally, I present and discuss the results in Chapter 5 and conclude in Chapter 6. The appendix lists supplementary material.

In the scope of my work, I perform two analyses applying novel methods on newly processed IceCube data. The main result is the re-discovery of the neutrino flare associated with TXS 0506+056 and the alert event IceCube-170922A as the primary neutrino emission. The other alerts show no indication of lower-energy neutrinos, emphasizing the uniqueness of TXS 0506+056 as a neutrino source candidate. This suggests that the other alerts are mainly connected to higher energetic neutrinos and cannot yet be associated with lower-energy emission. More information could be gained by improving and refining the source candidate selection combined with more multi-messenger observations. In general, more data, e.g. by the addition of new and larger neutrino telescopes, is required to shed light on the mystery of high-energy neutrino origins.



## Chapter 2

# High-energy cosmic rays and neutrinos

Neutrinos are evidence of hadronic interactions of cosmic rays. This chapter discusses the link between cosmic rays and neutrinos and presents sources that can accelerate particles to extreme energies. Subsequent sections consider the atmospheric background for astrophysical neutrinos and describe neutrino oscillation and attenuation.

### 2.1 Cosmic rays

Cosmic rays are fully-ionized nuclei that hit the Earth's atmosphere with a flux of roughly 1000 particles per square meter per second [17]. They consist of 90% protons, followed by helium and heavier nuclei, spanning a wide energy range up to  $10^{20}$  eV. The flux is almost isotropic due to deflection in extragalactic and galactic magnetic fields. The energy spectrum is shown in Figure 2.1. The shape of the spectrum has only a few features and can be described by a power law  $\phi \propto E^{-2.7}$ . The softening at  $\sim 3$  PeV, called the knee, leads to a spectrum  $\propto E^{-3}$ . The spectrum then hardens again to  $E^{-2.7}$  [17]. Another suppression happens at the second knee, followed by a re-hardening of the spectrum at  $\sim$ EeV energies (the ankle).

Different cosmic ray composition models [19] and source models can explain the knee in the cosmic ray spectrum. Propagation and acceleration depend on magnetic fields and magnetic rigidity. For a nucleus with total energy  $E$  and charge  $Ze$ , the magnetic rigidity is

$$R = \frac{E}{Ze(\text{GeV})}. \quad (2.1)$$

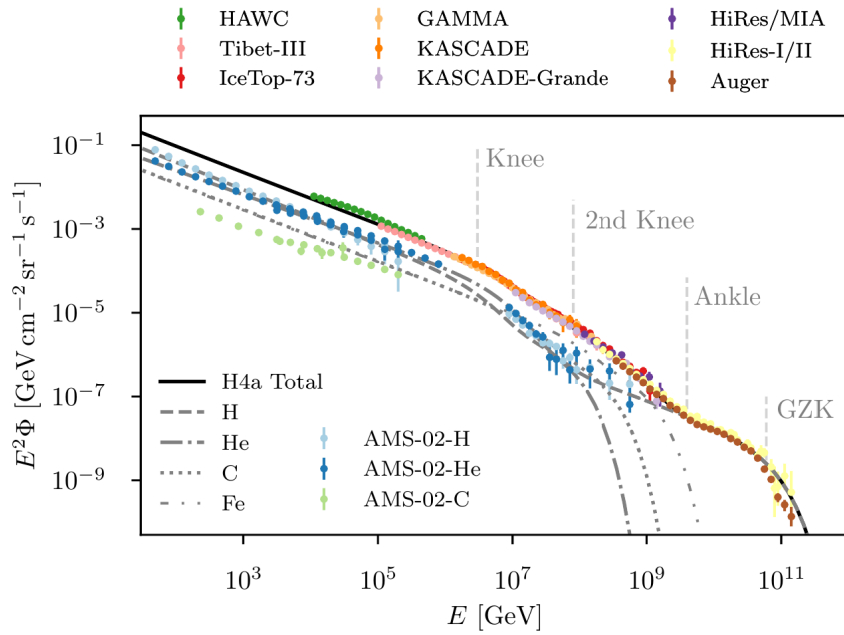


Figure 2.1: The energy flux density of cosmic rays. Different colors represent different experimental data. Features of the spectrum are pointed out in the plot as discussed in the text. The H4a cosmic ray model shows the contribution of different nuclei. Data from <http://lpsc.in2p3.fr/crd/> and [17]. Figure reprinted with permission from T. Glauch [18].

Thus, if acceleration processes reach a limit at a characteristic rigidity  $R_C$ , light particles will experience this effect first, following a successive cutoff for different heavier nuclei. The maximum energy is  $E_C = Ze \cdot R_C$ ; thus protons will steepen at  $E = R_C$ , He at  $E = 2R_C$ , and so on. Apart from cosmic ray composition, it is possible to model cosmic rays using different populations (see Figure 2.2). For example, cosmic rays up to the first knee are associated with galactic supernova remnants [20]. A higher energetic galactic component could dominate the spectrum between the first and second knee, whereas cosmic rays in the highest energies are from extragalactic sources [20].

The highest energetic cosmic rays cut off at approximately  $10^{20}$  eV. This cutoff could be due to limited acceleration power [17, 34]. It could also be the result of interaction with photons of the cosmic microwave background (CMB) and the production of delta resonance  $\Delta^+$ , as proposed by Greisen [35], Zatsepin, and Kuzmin [36], the GZK

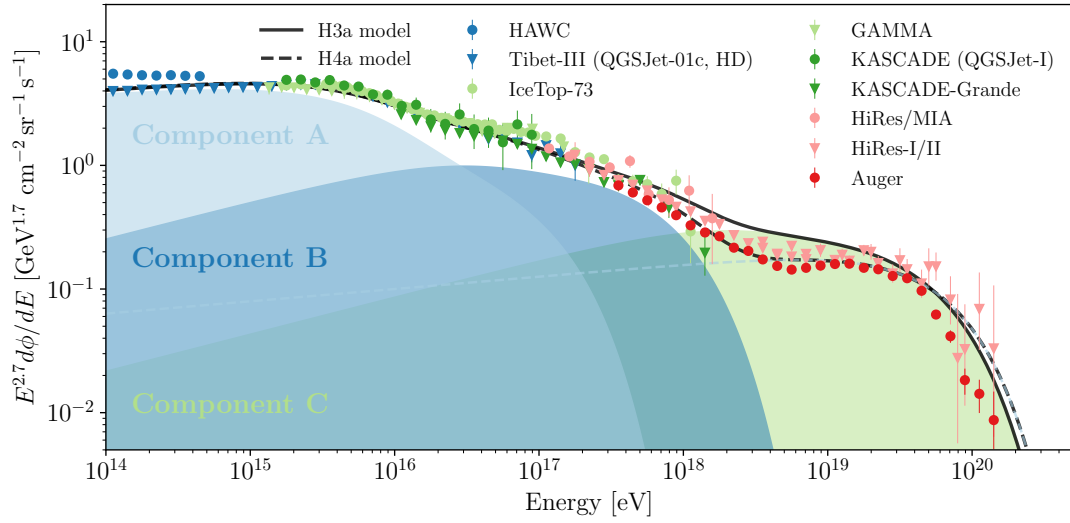


Figure 2.2: Cosmic ray model comprising three source populations [20]. The H3a model includes lighter and heavier nuclei in component C, whereas H4a includes an additional energetic proton component [21]. Data taken from [22–32]. Figure adapted from [33].

cutoff:

$$\begin{aligned}
 \gamma_{CMB} + p &\rightarrow \Delta^+ \rightarrow p + \pi^0, \\
 \gamma_{CMB} + p &\rightarrow \Delta^+ \rightarrow n + \pi^+, \\
 \gamma_{CMB} + p &\rightarrow p + e^+ + e^-.
 \end{aligned} \tag{2.2}$$

If a proton collides with a CMB photon of  $\sim 10^{-3}$  eV, it needs  $\sim 50$  EeV to produce the delta resonance. Thus, the energy threshold for electron pair production is lower ( $E \sim 6 \times 10^{17}$ ). However, energy losses by pair production are significantly smaller than in pion and delta production [17, 37].

In general, power-law energy dependency is not consistent with thermal black body radiation. Thus, there must be non-thermal mechanisms that accelerate cosmic rays. Shock acceleration, as described by Fermi [38], produces a spectral shape close to the observed cosmic ray spectrum. In the model of Fermi acceleration, particles scatter at astrophysical plasma clouds or shock fronts and gain a fraction of energy in each encounter [39, 40]. This naturally produces a spectrum  $\phi \propto E^{-2}$  [17] at the production site. Considering the propagation and escape of particles in magnetic fields; a source spectrum  $\propto E^{-2}$  would be observed as  $\propto E^{-2.6}$ , which agrees well with the observed cosmic ray spectrum of  $\propto E^{-2.7}$  [17]. The observed spectrum reflects

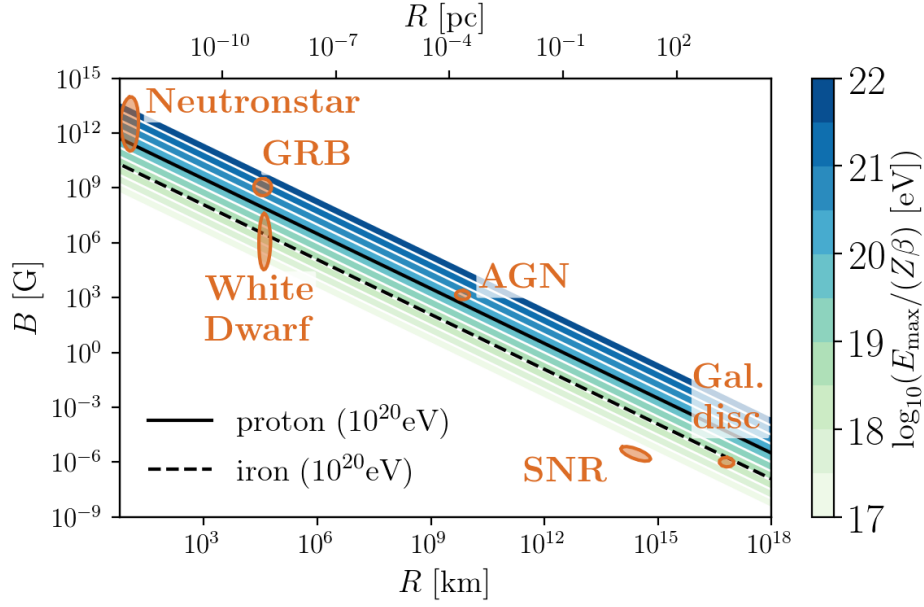


Figure 2.3: Hillas plot of possible cosmic ray accelerators. The diagonal lines show the threshold where the Hillas condition is satisfied. Objects on or above this line can accelerate particles up to  $10^{20}$  eV. The solid black line shows the threshold for protons, the dashed line for iron. The abbreviations stand for: GRB – gamma-ray burst, AGN – active galactic nuclei, Gal. disc – galactic disc, SNR – supernova remnant. Figure reprinted with permission from M. Huber [33], adapted from [17, 34].

the source spectrum if energy losses are primarily due to particle interactions instead of escaping the production site.

The acceleration stops as soon as the particle is no longer contained in the acceleration site. Thus, the Larmor radius of a relativistic particle constrains the size  $R_a$  of the acceleration region. This condition is also known as the Hillas criterion [34]. The particle energy  $E$  depends on the particle charge  $Z$ , the particle velocity as fraction of speed of light  $\beta = \frac{v}{c}$ , and the magnetic field  $B$  of the acceleration site in the following way:

$$E < ZR_a B \beta. \quad (2.3)$$

Figure 2.3 shows which objects are able to accelerate particles to extreme energies of  $10^{20}$  eV or higher with the Hillas condition. Neutron stars, gamma-ray bursts (GRBs), white dwarfs, and active galactic nuclei (AGN) are all suitable possible cosmic ray acceleration sites.

## 2.2 Source candidates

This section briefly presents possible source candidates of high-energy cosmic rays and hence also potential high-energy neutrino sources. Possible sources were constrained in the previous section and highlighted in Figure 2.3.

### 2.2.1 White dwarfs, neutron stars, and supernova remnants

When a star runs out of material to fuel its fusion process, the radiation pressure outwards stops. With no opposing pressure to gravity, the material falls inwards, and the star collapses [41]. The in-falling material has a velocity of  $0.25c$ . Depending on the initial stellar mass, its core becomes a white dwarf, a neutron star, or a black hole. For white dwarfs, gravitation is balanced by the pressure from electron degeneracy. Thus, a white dwarf is stable until its mass exceeds the Chandrasekhar mass limit  $M_{Ch} = 1.4 M_{\odot}$ .

Massive stars ( $M \geq 8 M_{\odot}$ ) produce a stellar remnant too heavy to be stabilized by electron degeneracy pressure. With the reaction  $e^{-} + p \rightarrow n + \nu_e$  neutrons are formed, and the star cools by emitting neutrinos. The neutron degeneracy pressure stabilizes the star until a core mass of  $M_{NS} < 3 M_{\odot}$ . For a core with a higher mass, the collapse cannot be avoided, and a stellar black hole is created. The sudden stabilization due to neutron degeneracy pressure stops the collapse very suddenly, and the in-falling material bounces against the core [42]. This creates an outward traveling shock wave, the supernova. The remnants of this supernova can be classified into different types. The shell-type supernova remnants remain for thousands of years and are called supernova remnants (SNR). Its shell and the shock waves are a suitable environment for the acceleration of particles.

Neutron stars are another possible acceleration site. Rotating neutron stars – pulsars – emit electromagnetic radiation. Pulsars could potentially accelerate particles directly by the strong electrostatic drop induced at their surface and their strong magnetic fields [37, 43].

### 2.2.2 Starburst galaxies

Starburst galaxies are luminous star-forming galaxies. They have an enhanced star-formation activity (i.e.,  $10\text{--}100 M_{\odot} / \text{year}$ ), compared to normal galaxies ( $1\text{--}5 M_{\odot} / \text{year}$ ), often due to galaxy mergers or high-density gas regions at the center of the galaxy [44, 45]. Starburst galaxies have the highest density at a redshift of  $\approx 2$  [46,

47]. The time scale over which gas is concentrated is comparable to the lifetime of massive stars. Thus, core-collapse supernova could enrich the gas and produce cosmic rays. The produced cosmic rays are further accelerated in collisionless shocks by supernovae [48]. Moreover, possible outflow from a central supermassive black hole may produce further relativistic particles [45, 49].

### 2.2.3 Gamma-ray bursts

Gamma-ray bursts are the most energetic transient eruptions observed [17, 43]. GRBs can be divided into two categories: long bursts ( $t > 2$  s) and short bursts ( $t < 2$  s). Long GRBs could be connected to massive stars collapsing into a stellar black hole [50], and short GRBs could be caused by merging compact object binaries [51, 52]. A possible mechanism that produces the bursts themselves is a relativistic expanding fireball and the dissipation of its kinetic energy [17, 43]. A longer afterglow follows both bursts. The afterglow can be caused by relativistic flow expanding into the surrounding medium.

### 2.2.4 Active galactic nuclei and blazars

Active galactic nuclei are extremely luminous central regions of galaxies. The central region outshines the rest of the galaxy, and stars do not cause its emission. They are the most luminous non-explosive objects in the universe with bolometric luminosities up to  $L_{bol} \approx 10^{48}$  erg/s  $\approx 3 \times 10^{13} L_{\odot}$  [53]. A schematic view is shown in Figure 2.4. A spinning supermassive black hole (SMBH) with masses exceeding  $10^6 M_{\odot}$  and an extension of  $10^{-7}$  to  $10^{-3}$  pc [53] is at the center of these objects. Around the SMBH, there is believed to be an accretion disk. The primary energy source of AGN is the release of gravitational energy in the accretion process. The accretion disk can extend up to 1 pc [53]. The gas clouds close to the center show broad emission lines — also called broad-line region (BLR) — and indicate high velocities and temperatures  $\approx 10^4$  K. The narrow-line region (NLR) is more distant from the center, and thus, the velocities and densities are lower. A dust torus obscures the accretion disk from some directions, and the hot dust produces infrared emission. Roughly 10 – 15% of AGN show an extended radio emission and produce a jet. If this jet points directly at the observer, the object is classified as a blazar. If the optical spectrum of a blazar shows strong emission lines, it is classified as a Flat-Spectrum Radio Quasar (FSRQ). Blazars with a nearly featureless spectrum are classified as BL Lacs. For a detailed overview of AGN, see [53, 54].

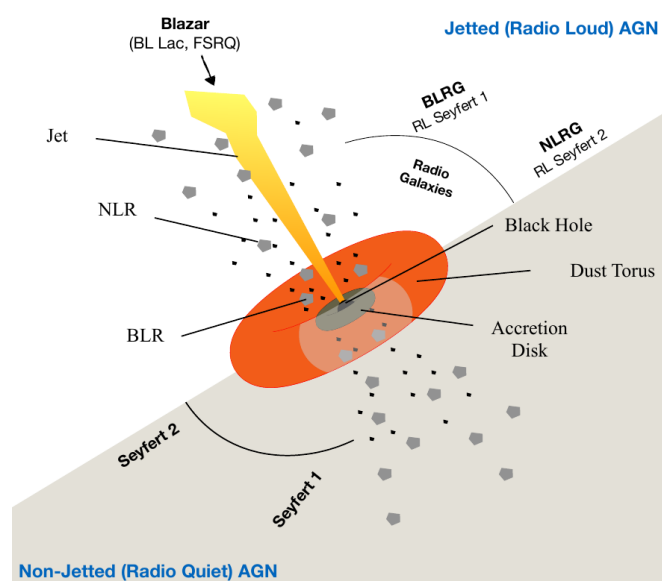


Figure 2.4: A simplified view of different AGN classes. The grey highlighted part shows objects without a radio jet. Depending on the viewing angle, they are divided into Seyfert type 1 or Seyfert type 2 galaxies. The opposite non-grey part shows the schematics of objects with a radio jet. Blazars are objects with their jet directly pointing at the observer. The abbreviations stand for: NLR – narrow-line region, BLR – broad-line region, BLRG – broad-line region galaxy, NLRG – narrow-line region galaxy. Figure reprinted with permission from T. Glauch [18], adapted from [54].

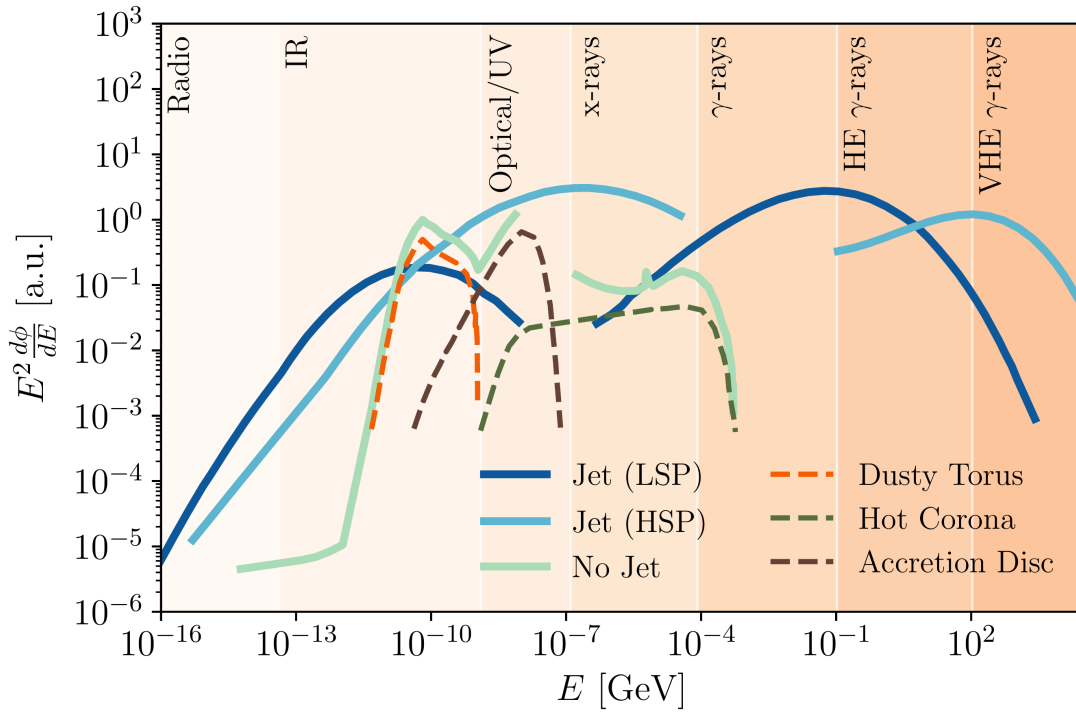


Figure 2.5: Example spectral energy distribution for different AGN classes. The light and dark blue lines show the double bump spectrum of blazars (here for HSP and LSP). The green line shows the SED of a non-jetted AGN, where different contributions are highlighted. Figure reprinted with permission from M. Huber [33], adapted from [53].

Figure 2.5 shows schematic spectral energy distributions (SEDs) of AGN. For blazars (jetted AGN), the position of the peak of the first bump  $\nu_{peak}$  is used to further classify blazars. Low synchrotron peaked (LSP) objects are blazars where  $\nu_{peak} < 10^{14}$  Hz ( $E_{peak} \lesssim 0.4$  eV), whereas high synchrotron peaked objects have their peak at energies  $\nu_{peak} > 10^{15}$  Hz ( $E_{peak} \gtrsim 4.1$  eV). If the peak is between those two thresholds, the object is intermediate synchrotron peaked (ISP) [53]. For a non-jetted AGN, individual components (the accretion disk, the dust torus, and photons from the accretions disk interacting with the surrounding atmosphere (corona)) contribute to emissions in different wavelengths (see Figure 2.5) [53].

AGN are promising candidates for cosmic ray and neutrino emission. The first association of neutrinos with a blazar was the discovery of the high-energy neutrino IceCube-170922A originating from the direction of the blazar TXS 0506+056 that was at that time in a high-emission state [12]. Further searches in IceCube archival data revealed a  $3.5\sigma$  evidence for additional neutrino emission coming from the same direction [16]. Another analysis from IceCube searched for signal in ten years of data and found the Seyfert type 2 galaxy NGC 1068 with  $2.9\sigma$  significance [55]. An

additional population study on a catalog of sources found a  $3.3\sigma$  evidence for neutrino emission from the direction of four AGN: NGC 1068, TXS 0506+056, PKS 1424+240, and GB6 J1542+6129 [55]. A search for time-dependent neutrino emission found the AGN M87 as the most significant source amongst a catalog of sources [56], and when looking for a cumulative neutrino-excess, they found a  $3\sigma$  evidence for neutrino emission from four AGN: M87, TXS 0506+056, GB6 J1542+6129, and NGC 1068 [56]. Furthermore, when looking at the origin directions of IceCube's most energetic events, the authors of [57] report a  $3.23\sigma$  excess of HSPs and ISPs in the origin regions.

## 2.3 Neutrinos from hadronic cosmic ray interactions at astrophysical sources

The main channel for neutrino production by high-energy cosmic rays is via pion decay. High-energy cosmic rays produce pions — and hence neutrinos — in hadronuclear interactions, usually dominated by inelastic  $pp$  scatterings:

$$p + p \rightarrow N(\pi^+, \pi^-, \pi^0) + X. \quad (2.4)$$

Another production channel of pions and hadronic gamma rays is photomeson production, also through  $\Delta^+$  resonance:

$$\begin{aligned} p + \gamma &\rightarrow N(\pi^+, \pi^-, \pi_0) + X, \\ p + \gamma &\rightarrow \Delta^+ \rightarrow \pi^+ n. \end{aligned} \quad (2.5)$$

The resulting pions have a lifetime of  $2.6 \cdot 10^{-8}$  s ( $\pi^\pm$ ) and  $8.4 \cdot 10^{-17}$  s ( $\pi^0$ )[58]. The previous processes are followed by these decays:

$$\pi^0 \rightarrow \gamma + \gamma, \quad (2.6)$$

$$\pi^+ \rightarrow \mu^+ + \nu_\mu \rightarrow \nu_\mu + \bar{\nu}_\mu + \nu_e + e^+, \quad (2.7)$$

$$\pi^- \rightarrow \mu^- + \bar{\nu}_\mu \rightarrow \bar{\nu}_\mu + \nu_\mu + \bar{\nu}_e + e^-. \quad (2.8)$$

Thus, in an idealized model, the resulting flavor ratio is  $(\nu_\mu : \nu_e : \nu_\tau) = (2 : 1 : 0)$ . Neutrinos can, in principle, also be a product of neutron decay or beyond standard model physics (for example [59]). Nevertheless, this section focuses on the neutrino production by mesons as a baseline scenario.

In both  $pp$  and  $p\gamma$  interactions, neutrinos are the product of meson and muon decay. The cross section of  $pp$  is approximately two orders of magnitudes higher than for  $p\gamma$ . However, depending on the astrophysical environment, the photon density is much larger than the proton density [17, 60].

The resulting spectrum of neutrinos for  $pp$  and  $p\gamma$  interactions can differ. The particle generation and propagation can be treated similarly to cosmic ray propagation in the atmosphere and will be described in detail in Section 2.4. The interaction length depends inversely on the density of the target particles (photons or protons). It is assumed that protons interact with ambient matter (such that pions are produced) but that pions escape the acceleration site with negligible interaction. Thus, the decay of pions is dominant compared to pion interactions. The respective equations are derived later in Section 2.4, specifically Equation (2.20) for pion decay and interaction, and Equation (2.24) for an approximation of the resulting neutrino spectrum.

In the case of  $pp$  collision, the proton threshold energy  $E_{thr,p}$  to produce a pion is

$$E_{thr,p} = m_p + \frac{m_\pi(m_\pi + 4m_p)}{2m_p} \sim 1.2 \text{ (GeV)}. \quad (2.9)$$

The interaction probability depends only on the particle mass and does not change with proton energy, and the density of target particles remains equally independent. With Equation (2.20) and Equation (2.24) the resulting neutrino spectrum shows the same power law behavior as the source cosmic ray spectrum, meaning  $\propto E^{-2}$  (see Section 2.1).

In the case of photomeson production, the proton energy threshold is inversely proportional to the photon energy  $E_\gamma$

$$E_{thr,\gamma} \sim \frac{2M_p m_\pi + m_\pi^2}{4E_\gamma}. \quad (2.10)$$

Assuming an initial photon spectrum following  $E^\alpha$ , the number density of target particles scales as  $\int_{E_{thr,\gamma}}^{\infty} E^{-\alpha} dE \propto E_{thr,\gamma}^{\alpha-1}$ . In this case, the resulting neutrino spectrum is harder ( $\alpha - 1$ ) than the source photon (and consequently cosmic ray) spectrum ( $\alpha$ ).

In these interactions,  $\pi^0$  produces gamma rays that are linked to hadronic interactions of cosmic rays. However, gamma rays are also produced in purely leptonic processes (for example, inverse Compton scattering); hence they are not necessarily an indication for cosmic ray interactions. Apart from an ambiguous production mechanism, gamma rays interact with radiation fields, such as the cosmic microwave background

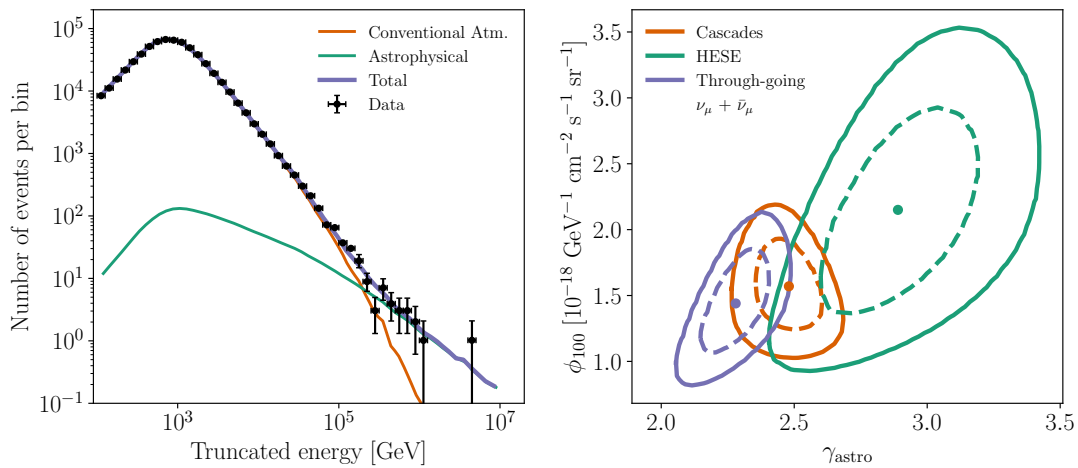


Figure 2.6: **Left:** Data and fits for the neutrino induced through-going muon analysis of astrophysical and atmospheric neutrinos [64]. **Right:** The best fit likelihood contours for three analyses of the astrophysical neutrino flux with respect to the source spectral index  $\gamma_{astro}$ . The lines indicate the 68% (dashed) and 95% (solid) confidence limit contours. Data taken from [64–66].

and extragalactic background light, and are attenuated. A thick target can also absorb them. For example, a TeV gamma-ray source with a redshift of  $z = 1$  would have a typical cutoff at approximately 0.1 TeV because of gamma-ray interactions with extragalactic background light [61]. However, high-energy neutrinos face no such caveats and are a smoking gun indication for hadronic cosmic ray interactions.

The first high-energy astrophysical neutrinos were discovered in 2013 [62]. Figure 2.6 shows the measured neutrino flux that can be described by the combination of astrophysical and atmospheric neutrinos. The flux is assumed to follow an unbroken power-law:

$$\frac{d\phi}{dE} = \phi_{100} \left( \frac{E}{100 \text{ TeV}} \right)^{-\gamma_{astro}}, \quad (2.11)$$

with the current best fit of  $\gamma_{astro} = 2.53$  [63]. For energies above  $\approx 100$  TeV, the astrophysical neutrinos dominate. The different observed neutrino spectra by IceCube when looking at specific positions in the sky have varying spectral indices, such as a relatively hard emission of  $\gamma = 2.1 \pm 0.2$  [16], but also indications of softer emission with  $\gamma = 3.4$  [55]. The sources generating the diffuse astrophysical neutrino flux remain unidentified. The main challenges that have to be overcome are uncertainties in the reconstruction of the origin direction, the low interaction rate, and a sizable atmospheric background caused by cosmic ray interaction in the atmosphere.

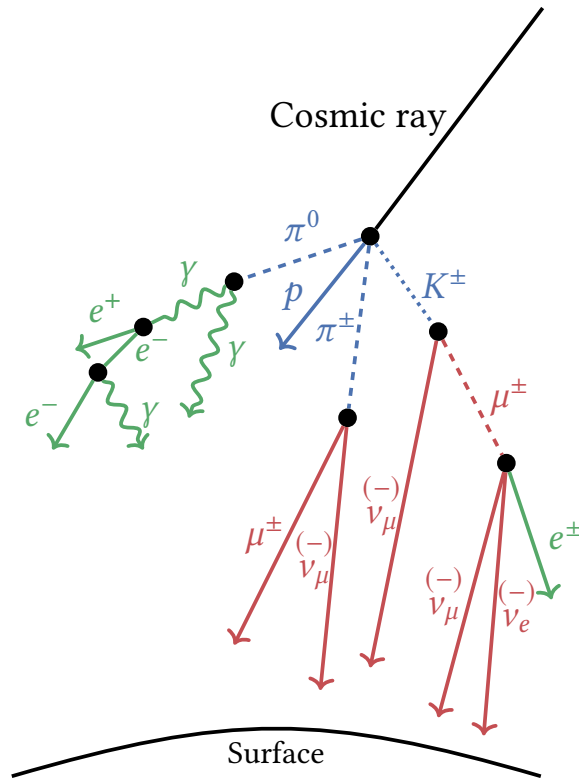


Figure 2.7: Simplified sketch of a cosmic ray air shower. Adapted from [33] and [70].

## 2.4 Atmospheric air showers and neutrinos

Cosmic rays interact in the Earth or Sun atmosphere and produce cascades of secondary particles (e.g., [17, 67–69]). Among these secondary particles are atmospheric muons and atmospheric neutrinos. A simplified air shower is shown in Figure 2.7.

Atmospheric muons and neutrinos leave similar or even identical signatures in a detector as astrophysical neutrinos. Thus, atmospheric muons and neutrinos are a background source for astrophysical neutrinos. They are created by the interaction of cosmic rays with the atmosphere and the following decay of produced mesons. To understand this background, it is vital to consider the development of air showers, and decay and interaction processes.

### 2.4.1 Hadrons in the atmosphere

Cosmic rays hitting the atmosphere prompt a cascade of particles. These particles travel a distance  $l_{Obs}$  and can interact or decay. The surrounding matter is relevant for the propagation of particles. The trajectory  $l$  through a material with density

$\rho_{atm}(l)$  is expressed with the slant depth [17]:

$$X(l_{Obs}) = \int_0^{l_{Obs}} \rho_{atm}(l) dl. \quad (2.12)$$

The slant depth begins at the top of the atmosphere and is measured downward along the particle trajectory. The differential particle flux  $\phi_i(E, X)dE = \frac{dN}{dAd\Omega dt}$  of particles of type  $i$  with energies in the interval  $E$  to  $E + dE$  at slant depth  $X$  in the atmosphere is described by cascade equations [17]

$$\begin{aligned} \frac{d\phi_i(E, X)}{dX} = & -\frac{\phi_i(E, X)}{\lambda_i(E)} - \frac{\phi_i(E, X)}{d_i(E)} \\ & + \sum_{j=1}^J \int_E^\infty \frac{dN_{j(E_j) \rightarrow i(E)}^{int}}{dE} \frac{\phi_j(E_j, X)}{\lambda_j(E_j)} dE_j \\ & + \sum_{j=1}^J \int_E^\infty \frac{dN_{j(E_j) \rightarrow i(E)}^{dec}}{dE} \frac{\phi_j(E_j, X)}{d_j(E_j)} dE_j \\ & - \frac{\partial}{\partial E} (\mu(E)\phi_i(E, X)). \end{aligned} \quad (2.13)$$

The flux decreases due to particles interacting (with interaction length  $\lambda_i$ ) and decaying (with decay length  $d_i$ ), as described in the first two terms (loss terms). However, it increases as other particles of type  $j$  with quantity  $\phi_j$ , energy  $E_j$ , and interaction length  $\lambda_j$  or decay length  $d_j$  produce  $N$  particles  $i$  at energy  $E$ . This is described by the third and fourth gain terms. The lower bound on the integral contains the condition that the parent particles need energies  $E_j > E$  to generate particles with energy  $E$ . The last term describes ionization losses or radiative losses with  $\mu(E)$  as the stopping power. Ionization losses vary slowly with energy, radiative losses (such as bremsstrahlung, pair production or hadroproduction) increase proportional to particle energy [17]. The ionization (a) and radiative (b) losses can be approximated by [58, 71]

$$-\frac{dE}{dX} = a(E) + b(E)E. \quad (2.14)$$

In general, bremsstrahlung losses involve transverse acceleration of a particle with mass  $M$  and are proportional to  $(m_e/M)^2$  [17]. The critical energy is the energy where the ionization losses are of equal strength as the radiation losses  $E_C = a/b$ . For electrons, this critical energy is  $E_C = 87$  MeV [17]. For muons, the factor  $(m_e/m_\mu)^2$  suppresses bremsstrahlung and their critical energy is much higher  $E_C \sim 500$  GeV [17].

Hence, electrons quickly cause showers and lose energy. Contrary, muons cover long distances before losing energy significantly.

For high-energy hadrons in the atmosphere, assumptions are that losses are entirely due to interaction and that gains are only due to hadronic interactions in the atmosphere. Equation (2.13) simplifies to

$$\frac{d\phi_N(E, X)}{dX} = -\frac{\phi_N(E, X)}{\lambda_N(E)} + \int_E^\infty \frac{dN_{N(E_N) \rightarrow N(E)}^{int}}{dE} \frac{\phi_N(E', X)}{\lambda_N(E')} dE'. \quad (2.15)$$

For large energies, further assumptions are possible, such as  $\lambda_N(E) \rightarrow \lambda_N = \text{constant}$  and that the interaction yield depends on the ratio of energies  $\frac{E_i}{E_j}$  [72]. The interaction yields are

$$\frac{dN_{j(E_j) \rightarrow i(E_i)}^{int}}{dE_i} \rightarrow \frac{dN_{j \rightarrow i}^{int} \frac{E_i}{E_j}}{d\frac{E_i}{E_j}} \cdot \frac{E_i/E_j}{dE_i}. \quad (2.16)$$

With an initial flux  $\phi_N(E, X) = \phi_0(X) \cdot E^{-\gamma}$ , a solution for the nucleon flux in Equation (2.15) is then:

$$\phi(E, X) = \phi_0(X=0) \exp\left(-\frac{X}{\Lambda}\right) \cdot E^{-\gamma}, \quad (2.17)$$

with the attenuation length  $\Lambda = \lambda_N/(1 - Z_{NN})$  and  $Z_{NN}$  as the spectrum-weighted moment for the nucleon to produce a nucleon. The flux of nucleons in the atmosphere follows the spectral shape of the initial primary cosmic ray spectrum.

## 2.4.2 Mesons in the atmosphere

Interacting cosmic rays produce secondary particles via scattering processes. In these processes, the majority of atmospheric muons and neutrinos are the product of charged meson decay. The flux of secondary mesons can be expressed similarly to the flux of nucleons. The main differences are that mesons can also be produced in the interaction of higher energetic mesons and both, interactions and decays, cause the loss. Analogous to Equation (2.13), the meson flux  $\phi_M(E, X)$  is expressed as [17]

$$\begin{aligned} \frac{d\phi_M(E, X)}{dX} &= -\frac{\phi_M(E, X)}{\lambda_M} - \frac{\phi_M(E, X)}{d_M(E)} + \frac{\phi_N(E, X)}{\lambda_N} Z_{NM} + \frac{\phi_M(E, X)}{\lambda_M} Z_{MM} \\ &= -\phi_M(E, X) \left( \frac{1}{\lambda_M} + \frac{\epsilon_M}{EX \cos \theta} \right) + \frac{\phi_N(E, X)}{\lambda_N} Z_{NM}, \end{aligned} \quad (2.18)$$

with the decay length as  $\frac{1}{d_M} = \frac{\epsilon_M}{E X \cos \theta}$  depending on the zenith angle  $\theta$  of the incoming cosmic ray. The characteristic energy of particle  $i$  is  $\epsilon_i = \frac{h_0 m_i c}{\tau_i}$ , with  $h_0$  as

the atmospheric height, the mass  $m_i$ , and the particle lifetime  $\tau_i$ . For energies above the characteristic energy  $E \gg \epsilon_M$  the interactions dominate and the decays of mesons become irrelevant. The meson flux  $\phi_M$  can be expressed as

$$\phi_M(E, X)|_{E \gg \epsilon_M} = \phi_0(X=0) \frac{Z_{NM}}{1 - Z_{NN}} \frac{\Lambda_M}{\lambda_N - \Lambda_M} \left[ \exp\left(-\frac{X}{\lambda_M}\right) - \exp\left(-\frac{X}{\lambda_N}\right) \right] \times E^{-\gamma}. \quad (2.19)$$

Thus, atmospheric mesons in this high-energy limit follow the same spectral shape as atmospheric nucleons and cosmic rays.

For the low-energy case  $E \ll \epsilon_M$  the decay terms dominate and the interactions become negligible. The result for the meson flux is

$$\phi_M(E, X)|_{E \ll \epsilon_M} = \left[ \frac{Z_{NM}}{\lambda_N} \exp\left(-\frac{X}{\Lambda_N}\right) X \right] \frac{\phi_0(X=0) \cos \theta}{\epsilon_M} \times E^{-\gamma+1}. \quad (2.20)$$

In this low-energy approximation, the spectral index of the resulting meson flux is one power harder than the original nucleons and cosmic ray spectrum. Most neutrinos and muons are produced in the decay of mesons. Hence meson energies below the characteristic energy dominate neutrino production.

### 2.4.3 Muons and neutrinos in the atmosphere

After cosmic rays interact with the atmosphere via scattering processes, charged and neutral pions and kaons are produced, among other particles. These pions and kaons decay further into muons and neutrinos and produce the conventional neutrino flux.

Repeating the approach of the previous sections, the muon flux caused by the decay of pions according to Equation (2.13) is

$$\frac{d\phi_\mu(E, X)}{dX} = -\frac{\phi_\mu(E, X)}{\lambda_\mu(E)} - \frac{\phi_\mu(E, X)}{d_\mu(E)} + \int_E^\infty \frac{dN_{\pi(E_\pi) \rightarrow \mu(E)}^{int}}{dE} \frac{\phi_\pi(E_\pi, X)}{d_\pi(E_\pi)}. \quad (2.21)$$

Neglecting the first term simplifies the expression, since interactions only contribute small corrections. Furthermore, it is possible to neglect the decay term as a first estimation since the muon decay length becomes larger than its production height. Considering that charged pions decay into a muon and muon neutrino with a branching ratio of 99.99% [58], the muon receives a fraction  $a_\mu$  of the pion energy. With

these assumptions, the flux becomes

$$\frac{d\phi_\mu(E, X)}{dX} \approx \frac{\phi_\pi(E/a_\mu, X)}{d_\pi(E/a_\mu)} = \frac{\epsilon_\pi}{X \cos \theta E/a_\mu} \phi_\pi(E/a_\mu, X). \quad (2.22)$$

Thus, the shape of the muon flux caused by pion decay is one power softer than the original pion flux. Accounting for muon decay with the decay rate

$$\frac{d\phi_\mu}{dX} = -\frac{\epsilon_\mu}{EX \cos \theta} \phi_\mu, \quad (2.23)$$

and approximating the rate of energy loss by  $dE/dX = -a \approx 2 \text{ MeV/g/cm}^2$  [17] the muon spectrum remains one power softer with respect to the original pion flux.

The flux of atmospheric neutrinos only includes the production terms and can be approximated similarly to the muon flux. As a first approximation, there is a similar energy dependency of the spectrum as for muons. The spectral index of the neutrino flux is shifted by one power with respect to the pion spectrum. For the pion spectrum a low energy case (see Equation (2.20)) and a high energy case (see Equation (2.19)) were evaluated. In the low energy regime where decays dominate, the spectral shape of the atmospheric muons and neutrinos is expected to follow the original cosmic ray spectrum

$$\phi_{\nu/\mu}(E, X)|_{E \ll \epsilon_\pi} \propto E^{-\gamma}. \quad (2.24)$$

However, for the case where interactions dominate over meson decay, the spectrum of atmospheric muons and neutrinos is expected to be softer

$$\phi_{\nu/\mu}(E, X)|_{E \gg \epsilon_\pi} \propto E^{-(\gamma+1)}. \quad (2.25)$$

Additional to the production chains of pions (Equation (2.7) and 2.8), kaons contribute mainly with [58]

$$K^\pm \rightarrow \mu^\pm + \nu_\mu(\bar{\nu}_\mu) \quad (\sim 63.6\%), \quad (2.26)$$

$$K^\pm \rightarrow \pi^0 + e^\pm + \nu_e(\bar{\nu}_e) \quad (\sim 3.3\%), \quad (2.27)$$

$$K^\pm \rightarrow \pi^\pm + \pi^0 \quad (\sim 20.7\%), \quad (2.28)$$

$$K_L^0 \rightarrow \pi^\pm e^\mp \bar{\nu}_e(\nu_e) \quad (\sim 40.55\%), \quad (2.29)$$

$$K_L^0 \rightarrow \pi^\pm \mu^\mp \bar{\nu}_\nu(\nu_\nu) \quad (\sim 27.04\%), \quad (2.30)$$

$$K_L^0 \rightarrow \pi^+ \pi^- \pi^0 \quad (\sim 12.5\%), \quad (2.31)$$

where the charged pions decay further into neutrinos (Equation (2.7) and (2.8)). The muon flux from kaons or heavier mesons can be expressed similarly to Equation (2.21). With increasing energies, kaons dominate the neutrino production with respect to pions. The top panels of Figure 2.8 show the different contributions producing atmospheric muons and muon neutrinos. Pion decay dominates muon production (top left panel), whereas kaons become the leading contributor to muon neutrino production for energies  $\gtrsim 10^2$  GeV (top right panel). With the kaon contribution the atmospheric neutrino flux can be estimated as [17, 37]:

$$\frac{dN_\nu}{dE_\nu} \approx 0.0096 \frac{1}{\text{cm}^2 \text{ s sr GeV}} \left( \frac{E_\nu}{\text{GeV}} \right)^{-\gamma} \times \left( \frac{1}{1 + \frac{3.7E_\nu \cos \theta}{115 \text{ GeV}}} + \frac{0.38}{1 + \frac{1.7E_\nu \cos \theta}{850 \text{ GeV}}} \right). \quad (2.32)$$

Thus, for energies below the characteristic pion energy ( $\epsilon_\pi = 115$  GeV) the neutrino flux spectrum follows the primary cosmic ray spectrum ( $-\gamma \approx -2.7$ ). Then kaons start dominating the neutrino flux and for neutrino energies larger than the characteristic kaon energy ( $\epsilon_K = 850$  GeV) the spectrum follows the softer distribution of  $-(\gamma + 1) \approx -3.7$ .

Apart from pions and kaons, neutrinos are also produced by decaying muons. The energy spectral index of neutrinos produced by muon decay shifts by another power  $E_\nu^{-(\gamma+2)}$ . This is caused by the muon Lorentz factor. The decay probability of muons decreases, whereas scattering becomes more likely [73].

Another component in the atmospheric neutrino flux is neutrinos produced by the decay of charmed or heavier mesons (e.g.,  $D$ ). They have a short lifetime (e.g.,  $\tau_{D^\pm} = (1040 \pm 7) \times 10^{-15}$  s [58]) and decay predominantly without interaction. Muons and neutrinos produced by these or other short-lived mesons are called the prompt neutrino flux. The energy spectrum of the prompt flux resembles the primary cosmic ray spectrum until  $E_\mu \approx \epsilon_{charm} \approx 4 \times 10^7$  GeV [17], the characteristic energy of charmed mesons. The flux is isotropic and does not depend on the zenith angle, contrary to the conventional flux. The decay path is longer at the horizon for conventional neutrinos, which causes an enhanced flux for zenith angles towards the horizon. The factor  $1/(E_\nu \cos \theta)$  in Equation (2.32) represents the competition between decay and interaction.

The flatter spectrum of prompt neutrinos dominates the atmospheric neutrino flux at higher energies. In the calculation from [74], the prompt  $\nu_\mu$  flux exceeds the conventional  $\nu_\mu$  contribution for energies beyond a few hundred TeV (see Figure 2.8). Another important factor is flavor oscillation. Additionally, interactions in the Earth

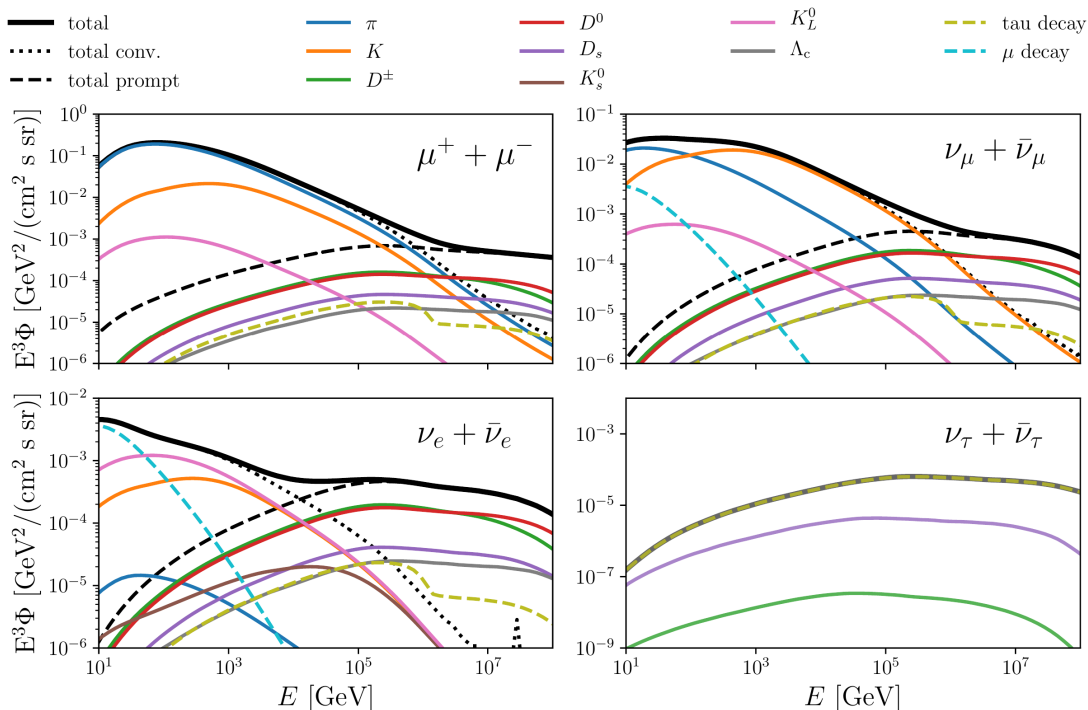


Figure 2.8: The atmospheric lepton flux and its composition. The top left panel shows the muon flux, and the remaining panels the fluxes for different neutrino flavors. The pion and kaon contributions are shown in dark blue and orange. The conventional and prompt components are displayed as black dotted and dashed lines. Figure reprinted with permission from M. Huber [33], adapted from [74].

become relevant for energies exceeding few TeV (see Section 2.6.2). Thus the flux through the Earth decreases for high-energy neutrinos.

## 2.5 Neutrino oscillation

Neutrino mass eigenstates  $|v_i\rangle$  are different from neutrino flavor eigenstates  $|v_\alpha\rangle$  (with  $\alpha = e, \mu, \tau$ ). They relate with [17, p. 153]:

$$\begin{pmatrix} v_1 \\ v_2 \\ v_3 \end{pmatrix} = U^* \begin{pmatrix} v_e \\ v_\mu \\ v_\tau \end{pmatrix}, \quad \begin{pmatrix} v_e \\ v_\mu \\ v_\tau \end{pmatrix} = U \begin{pmatrix} v_1 \\ v_2 \\ v_3 \end{pmatrix}. \quad (2.33)$$

The unitary mixing matrix  $U$  connects flavor and mass eigenstates.  $U$  is also called the Pontecorvo-Maki-Nakagawa-Sakata (PMNS) mixing matrix [75, 76]. It is often parametrized as

$$U = \begin{pmatrix} c_{12}c_{13} & s_{12}c_{13} & s_{13}e^{-i\delta} \\ -s_{12}c_{23} - c_{12}s_{23}s_{13}e^{i\delta} & c_{12}c_{23} - s_{12}s_{23}s_{13}e^{i\delta} & s_{23}c_{13} \\ s_{12}s_{23} - c_{12}c_{23}s_{13}e^{i\delta} & -c_{12}s_{23} - s_{12}c_{23}s_{13}e^{i\delta} & c_{23}c_{13} \end{pmatrix}, \quad (2.34)$$

with  $c_{ij} = \cos \theta_{ij}$ ,  $s_{ij} = \sin \theta_{ij}$ , and  $\theta_{ij}$  as the mixing angles.  $\delta$  is a CP-violating phase. Recent values of the mixing angles are [77]

$$\theta_{12}, \theta_{13}, \theta_{23}, \delta = 33.82_{-0.76}^{+0.78} \text{ deg}, 8.61_{-0.13}^{+0.12} \text{ deg}, 49.7_{-1.1}^{+0.9} \text{ deg}, 217_{-28}^{+40} \text{ deg}. \quad (2.35)$$

The probability for a neutrino in original state  $\alpha$  to oscillate to state  $\beta$  after traveling distance  $L$  is described by

$$P_{\alpha\beta} = |\langle v_\alpha | v_\beta(L) \rangle|^2. \quad (2.36)$$

The stationary state solution of the time-dependent Schrödinger equation propagates the neutrino mass state:

$$|v_j(t)\rangle = e^{-\frac{iEt}{\hbar}} |v_j(0)\rangle, \quad (2.37)$$

with  $E$  as the relativistic neutrino energy:

$$E = \sqrt{p^2c^2 + m_j^2c^4} \approx pc + \frac{m_j^2c^4}{2E}, \quad (2.38)$$

assuming that the neutrino mass is small and using the linear approximation  $\sqrt{1+x} \approx 1 + \frac{1}{2}x$ . Combining Equation (2.38), Equation (2.37), and  $L = t \cdot c$ , the transition amplitude is

$$\langle v_\alpha | v_\beta(L) \rangle = e^{-\frac{i p L}{\hbar}} \sum_j U_{\beta j}^* U_{\alpha j} e^{-\frac{i m_j^2 c^3 L}{2E \hbar}}. \quad (2.39)$$

The transition probability can then be expressed as

$$\begin{aligned}
P_{\alpha\beta} = & \delta_{\alpha\beta} \\
& - 4 \sum_{i>j} \text{Re}(U_{\beta j}^* U_{\alpha j} U_{\beta i} U_{\alpha i}) \sin^2 \Delta m_{ij}^2 \frac{L}{4E} \\
& + 2 \sum_{i>j} \text{Im}(U_{\beta j}^* U_{\alpha j} U_{\beta i} U_{\alpha i}) \sin \Delta m_{ij}^2 \frac{L}{2E},
\end{aligned} \tag{2.40}$$

with  $\Delta m_{ij}^2 = m_i^2 - m_j^2$ . The square of the mass differences is  $\Delta m_{21}^2 = 7.55_{-0.16}^{+0.20} \times 10^{-5} \text{eV}^2$  and  $|\Delta m_{31}^2| = 2.50 \pm 0.03 \times 10^{-3} \text{eV}^2$  [78]. The mixing matrix determines the amplitude of the oscillation, whereas  $L/E$  affects the oscillation frequency. Cosmic neutrinos travel large distances, thus it is useful to express  $L/E$  in parsec (with  $L = \hbar c/E$ ) and PeV:

$$\frac{L}{E} \rightarrow 1.563 \times 10^8 \frac{L \text{ PeV}}{\text{pc} E}. \tag{2.41}$$

An estimation of the oscillation length for a neutrino with an energy of 1 PeV and a mean  $\Delta m^2 = 10^{-4} \text{eV}^2$  is thus:

$$L_{osc} = \frac{2\pi}{(1.563 \times 10^8 \times 10^{-4})/4} \text{pc} = 1.6 \times 10^{-3} \text{pc}. \tag{2.42}$$

The oscillation length is in the range of a few milliparsecs and plays a significant role for neutrinos traveling astrophysical distances. Figure 2.9 shows the flavor oscillation for different distances  $L$ . The oscillation parameters are taken from [78]. For an initial flavor ratio of  $(\nu_e : \nu_\mu : \nu_\tau) = (1 : 2 : 0)$  (see Section 2.3), the average distribution of flavors becomes uniform for astronomical distances of more than  $10^{-2} \text{pc}$ . As an example, Milky Way's neighbor galaxy M31 is at a distance of  $772 \pm 44 \text{kpc}$  [79]. Thus, the average expected flavor ratio is uniform (1:1:1) for extragalactic neutrinos from pion decay. This assumption is valid for a diffuse neutrino flux, and more specifically, for all neutrino sources with an emission region of a similar or larger scale as the oscillation length.

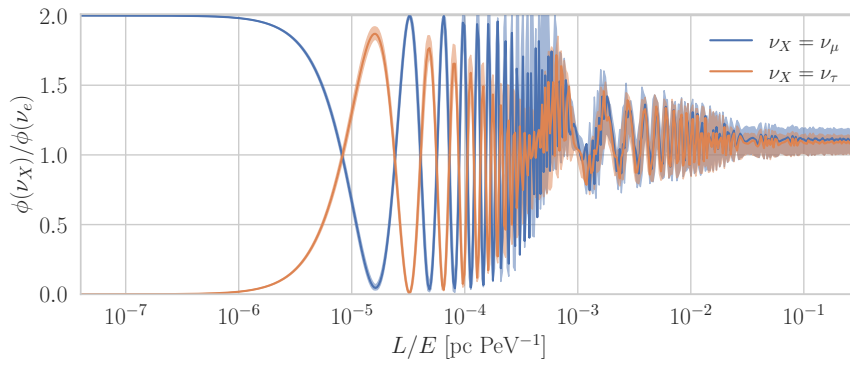


Figure 2.9: Flavor ratio  $\nu_x/\nu_e$  for neutrinos traveling astronomical distances. The initial flavor ratio is  $(\nu_e : \nu_\mu : \nu_\tau) = (1 : 2 : 0)$  (see Section 2.3). For a neutrino with an energy of 1 PeV, the average flavor ratio becomes  $(1:1:1)$  for distances  $> 10^{-2}$  pc. The shaded bands indicate the  $\pm 1\sigma$  uncertainties on the oscillation parameter [78].

## 2.6 Neutrino interactions

A neutrino detector does not directly measure neutrinos but the products of neutrino interaction. Neutrino interactions depend on neutrino energies. For neutrino energies of less than few GeV, coherent elastic scattering ( $\nu_x + p \rightarrow \nu_x + p$ ) and quasi-elastic scattering (e.g.  $\bar{\nu}_e + p \rightarrow e^+ + n$ ) dominate the interaction cross section. For energies between 1 – 10 GeV processes involving resonances dominate the cross section, e.g.  $\nu_e + p \rightarrow e^- + \Delta^{++}$ . However, high-energy neutrinos interact mainly through deep inelastic scattering with a nucleon  $N$  (e.g.  $\nu_\mu + N \rightarrow \mu^- + X$ , with  $X$  as a particle shower).

### 2.6.1 Neutrino deep inelastic scattering

In this work, neutrino-induced muons are used for the search of astrophysical neutrino sources. These muons result from charged-current (CC) deep inelastic scattering of a neutrino with a nucleon (see left of Figure 2.10). In charged-current processes, neutrinos interact with a quark in the nucleon  $N$  by exchanging a charged  $W$  boson

$$\nu_l + N \rightarrow l + X. \quad (2.43)$$

A charged lepton  $l$  with the same flavor as the neutrino is produced. Another possible interaction is the neutral-current (NC) interaction, where a neutral  $Z^0$  boson is exchanged (see right of Figure 2.10)

$$\nu_l + N \rightarrow \nu_l + X. \quad (2.44)$$

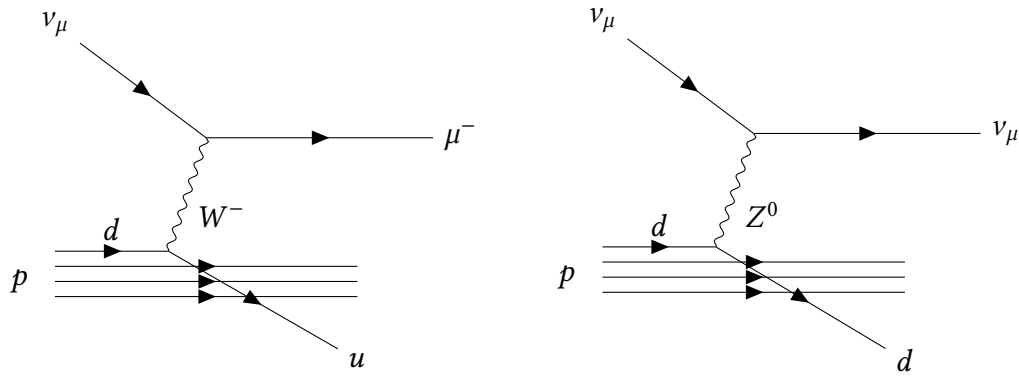


Figure 2.10: **Left:** Charged-current deep inelastic interaction of a muon neutrino with a proton. **Right:** Neutral-current interaction of a muon neutrino with a proton.

Here, the neutrino scatters and afterward carries a fraction of the primary neutrino energy. In CC and NC interactions, the nucleon  $N$  disintegrates into a hadronic shower  $X$ .

In most cases, the scattering of neutrinos with electrons at rest can be neglected at high energies. In the rest frame of the electron, the cross sections scale with  $E_\nu \cdot m_e$  and the smallness of the electron mass suppresses the interaction [80]. However, the resonant production of a  $W$  boson in electron antineutrino interaction is an exception

$$\bar{\nu}_e + e^- \rightarrow W^- . \quad (2.45)$$

The peak of the cross section for resonant scattering with electrons is at the Glashow resonance energy [81]

$$E_{\nu,GR} = \frac{m_W^2 - m_\nu^2 - m_e^2}{2m_e} \sim 6.3 \text{ PeV} . \quad (2.46)$$

The  $W^-$  boson then decays into hadrons or an antineutrino lepton pair  $\bar{\nu}_l + l$ . The first particle shower at Glashow resonance energies was detected recently [82].

Figure 2.11 shows the cross sections for charged and neutral-current neutrino and antineutrino interactions with nucleons, as well as the cross section for resonant scattering. The cross section for neutrinos and antineutrinos below 1 PeV is different because of weak interaction's parity violation [17]. Above 100 TeV, scattering off sea quarks dominates the cross sections, and neutrino and antineutrino cross sections are nearly identical. The Glashow resonance is sub-leading except for energies around 6.3 PeV, where it becomes the prevailing process for  $\bar{\nu}_e$ .

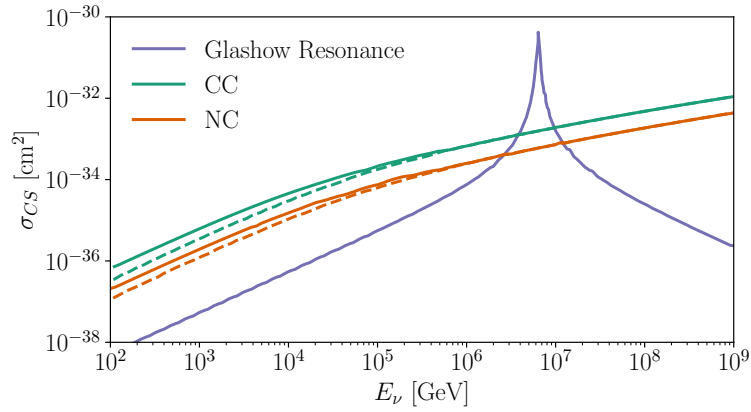


Figure 2.11: Neutrino cross sections of charged and neutral-current neutrino and antineutrino (dashed line) interactions with nucleons, according to ZEUS global probability distribution function fits [83] and [84]. The Glashow resonance (peak in purple line) shows the cross section for resonant interaction of  $\bar{\nu}_e$  with electrons.

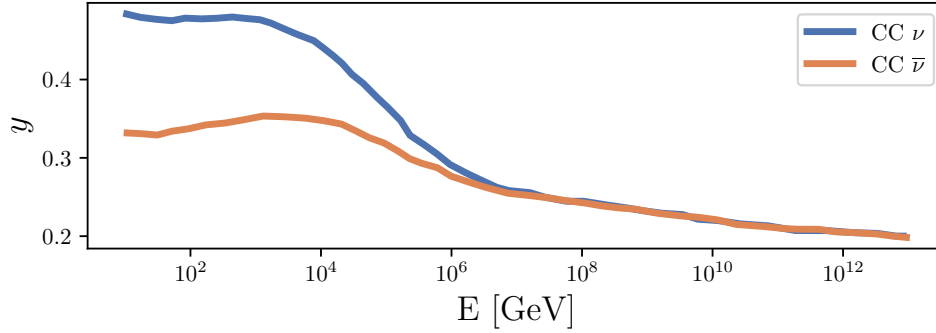


Figure 2.12: Energy transferred to the nucleon by the neutrino charged-current interactions [84]. The secondary lepton energy is  $E_l = (1 - y)E_\nu$ .

For neutrino astronomy, it is also important to know how much energy of the neutrino is transferred to the nucleon and the lepton. Figure 2.12 shows the distribution of  $y = (E_{\nu_l} - E_l)/E_{\nu_l}$  for charged-current interactions. The energy of the secondary lepton is then  $E_l = (1 - y)E_\nu$ .

### 2.6.2 Neutrino interactions in the Earth

Neutrinos pass a distance  $l$  through the Earth until they reach the detector:

$$l(\theta_N, d) = (R_E - d) \cos(\theta_N) + \sqrt{R_E^2 - (R_E - d)^2 \cdot (\sin \theta_N)^2}, \quad (2.47)$$

with  $\theta_N$  as the nadir angle,  $R_E$  the Earth radius, and  $d$  the detector depth. The absorption cross section  $\sigma_{abs}$  of neutrinos increases with neutrino energy  $E_\nu$ . This is

mainly caused by charged-current interactions with nucleons ( $\sigma_{abs} \approx \sigma_{CC}$ ) [85], see for example Figure 2.11.

The opacity factor  $\tau$  for neutrino absorption as in  $e^{-\tau}$  depends on the column density  $z(\theta_N)$  and is defined as [85]

$$\tau = \sigma_{abs}(E_\nu) \cdot z(\theta_N). \quad (2.48)$$

The column density describes the number of nucleons per  $\text{cm}^2$  that the neutrinos cross coming from nadir angle  $\theta_N$ . It can be estimated as [85]

$$z(\theta_N) = 2N_A \int_0^{R_E \cos \theta_N} \rho \left( \sqrt{x^2 + (R_E \sin \theta_N)^2} \right) dx, \quad (2.49)$$

with  $N_A$  as the Avogadro constant,  $\rho$  as the Earth's density, and  $x$  as the coordinate along the neutrino trajectory through the Earth. The inverse of the column density is the critical cross section [85]

$$\sigma_*(\theta_N) = \frac{1}{z(\theta_N)}. \quad (2.50)$$

For the case  $\sigma_{abs}(E_\nu) = \sigma_*(\theta_N)$ , the opacity factor is  $\tau = 1$  and the absorption becomes  $1/e \approx 0.37$ . Figure 2.13 shows the Earth's density depending on the distance to the core on the left and neutrino transmission probabilities depending on energy and zenith angle on the right [86] with the critical cross section. These transmission probabilities are based on standard model neutrino-matter cross sections [86]. The absorption of high-energy neutrinos in the Earth limits the region where neutrino telescopes are sensitive to very high-energy neutrinos to the local horizon. For angles away from the horizon, absorption dominates, and the transmission probability goes towards 0.

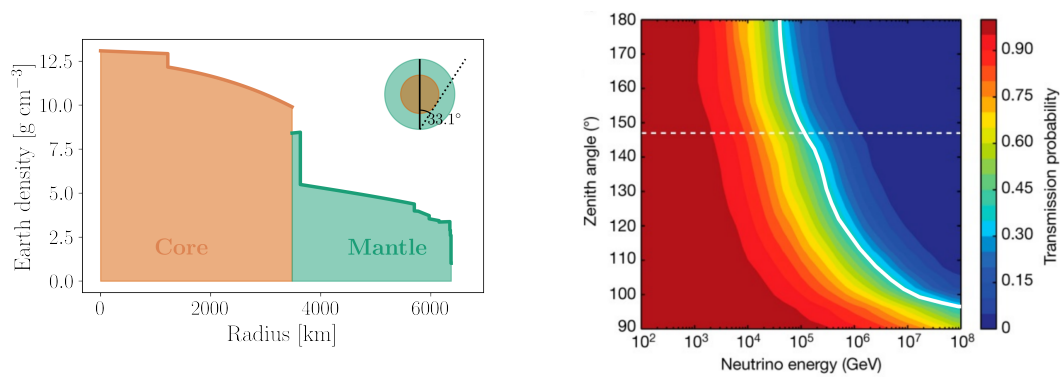


Figure 2.13: **Left:** Earth's density with the PREM model [87]. Green shows the mantle, orange shows the core. The nadir angle to pass through the core is  $\theta_N \leq 33.1^\circ$ . Figure adapted from [85]. **Right:** Transmission probability for neutrinos traversing the Earth, depending on zenith angle and neutrino energy. The horizontal dashed white line indicates the location of the core-mantle boundary. High-energy neutrinos reach the detector only near the horizon (zenith angle  $\approx 90^\circ$ ). The solid white line shows the critical value of the cross section  $\sigma_*$  with transmission probability of  $1/e \approx 0.37$ . Figure adapted from [86].



## Chapter 3

# The IceCube Neutrino Observatory

The IceCube Neutrino Observatory is located at the geographic South Pole. It is currently the largest operating neutrino telescope worldwide, focusing on the detection of high-energy neutrinos up to PeV-scale energies. IceCube does not detect neutrinos directly; it searches for the signatures of secondary charged particles from high-energy neutrinos interacting via deep inelastic scattering (see Section 2.6.1). The resulting charged leptons and hadrons have a higher velocity than the phase velocity of light in ice and produce Cherenkov radiation. Neutrino-induced leptons and hadrons traveling through the Antarctic ice leave a trace of Cherenkov photons. This chapter presents the detection principle and design of IceCube in the first half. The latter part describes the data processing and the IceCube realtime alert system.

### 3.1 Detection principle

Charged particles passing through a medium cause a brief polarization of ambient atom electron hulls. This polarization induces changing dipole moments, which emit electromagnetic waves. For velocities exceeding the phase velocity of light, the superposition is constructive in phase and produces a light cone — called Cherenkov radiation (see Figure 3.1). The opening angle  $\vartheta_C$  is [88]

$$\cos \vartheta_C = \frac{1}{\beta n}, \quad (3.1)$$

for a charged particle with velocity  $v/c = \beta$  in a medium with refractive index  $n$  ( $n_{ice} \simeq 1.32$ ). The number of photons  $N$  the charged particle generates while traveling

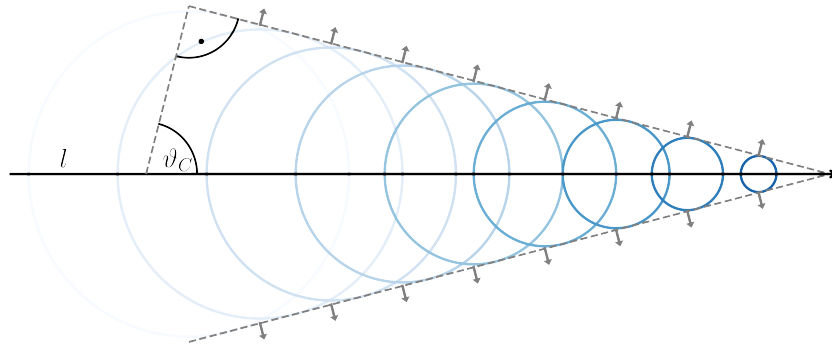


Figure 3.1: Example Cherenkov cone for a relativistic particle  $l$ . The circles show how the radiation propagates through the medium. For ice the cone opening angle is  $\vartheta_C \approx 41^\circ$ . Figure adapted from [33].

a distance  $dx$  is described by the Frank-Tamm formula [89]

$$\frac{d^2 N}{dx d\lambda} \sim \frac{2\pi\alpha}{\lambda^2} \left( 1 - \frac{1}{\beta^2 n(\lambda)^2} \right), \quad (3.2)$$

with  $\lambda$  as the radiation wavelength and  $\alpha$  as the fine structure constant. The number of photons increases with shorter wavelengths. Water and ice absorb photons with  $\lambda < 300$  nm and strongly suppress Cherenkov radiation with smaller wavelengths. Typical detectors are most efficient between 300 nm and 600 nm [43], where ice and water are transparent to light.

The optical properties of the detector material (the Antarctic ice) are important for a precise measurement. The main quantities are effective scattering and absorption length ( $\Lambda_{sct}$  and  $\Lambda_{abs}$ ). They each describe the distance  $x$  after which the intensity  $I$  of light with wavelength  $\lambda$  drops by  $1/e$

$$I(\Lambda, x) = I_0 \exp\left(-\frac{x}{\Lambda_{sct/abs}}\right), \quad (3.3)$$

due to either lowering the number of detectable photons (absorption) or changing the photon direction and arrival times (scattering). Figure 3.2 shows the optical parameter for Antarctic ice. The ice quality increases with depth, since snow has been gradually compressed into ice and the high pressure has removed air bubbles. A dust layer in the ice causes the peak between  $\sim 1800$  m – 2000 m depth.

In the case of ice, light is scattered significantly along the path of relativistic particles. However, the low absorption allows for a sparser distribution of detector modules.

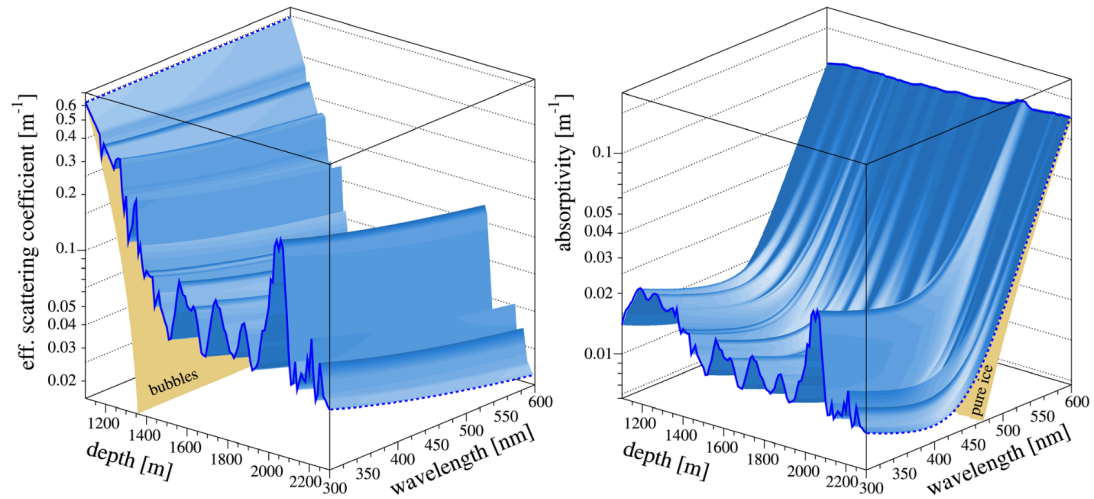


Figure 3.2: Scattering and absorption in the Antarctic ice for 300–600 nm at depths between 1100 and 2300 m. The contribution from air bubbles to scattering is highlighted and disappears at  $\sim 1300$  nm. It is independent of the wavelength. The absorption by pure ice is also highlighted in the right figure. Dust causes the peak between  $\sim 1800$  m – 2000 m depth. Figures taken from [90].

The particle signatures in the medium depend on the interaction and the particle type. They can be roughly divided into three categories.

*Cascades* — The hadronic fragments in neutral-current interactions cause a hadronic cascade, and the scattered neutrinos carry away the majority of the energy. In charged-current interactions of electron neutrinos, the electron and its interaction cause a forward electromagnetic cascade. In this case, the majority of the neutrino energy is deposited in the cascade. Additionally, the nuclear fragments produce a cascade with the residual energy (approximately 20%). The neutrino energy is thus fully deposited inside the medium. This allows a good resolution of the neutrino energy if the event is contained in the detector. The small traveled distance of secondary particles leads to a poor angular resolution of the neutrino origin direction with cascades ( $\sim 10^\circ - 15^\circ$  [91]). Figure 3.3 shows an example cascade on the left.

*Tracks* — Charged-current interactions of muon neutrinos produce muons, which pass through the medium while emitting light and cause track-like signatures in a detector. The neutrino vertex can lie inside the detector (starting track) or outside the detector (through-going track). The timing of the detected Cherenkov photons allows the directional reconstruction of the muon origin direction. This leads to a better angular resolution of the neutrino origin (typically  $\leq 1^\circ$  above TeV energies [55]). On the other hand, the energy resolution is poorer since the muon deposits energy in

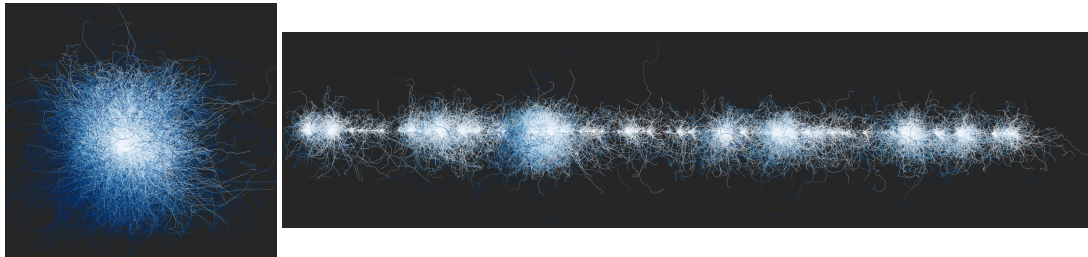


Figure 3.3: Photon trajectories for  $\sim 100$  TeV events. The color shows the time from early (white) to late (blue). Figures reprinted with permission from T. Glauch [18]. **Left:** A cascade event with a typical spherical emission. The photons are boosted into the original neutrino direction, which is why the photons on the bottom left appear later. **Right:** A muon track. Stochastic energy losses along the track create the light pattern. The long lever arm allows a more precise pointing to the origin direction.

the detector only while passing through it and continues to carry a part away. Thus, the neutrino energy can only be determined on a statistical basis. Figure 3.3 shows an example muon track on the right.

*Double bang* — The  $\tau$  neutrino interaction causes a hadronic cascade at the neutrino vertex. The majority of the neutrino energy is carried by the resulting  $\tau$ -lepton. The  $\tau$  decays after traveling distance  $l_\tau \approx 50 \text{ m} \times \left(\frac{E_\nu}{\text{PeV}}\right)$ . The  $\tau$  branching ratio for hadronic decay is  $\sim 64.79\%$ , for decay into  $\nu_\tau e \nu_e$  it is  $17.82\%$ , and for decay into  $\nu_\tau \mu \nu_\mu$  it is  $17.39\%$  [58]. Both, the hadronic decay and the leptonic decay into an electron cause a cascade-like signature. In the case of muon decay, the muon leaves a track-like signature. For tauons with PeV energies and above, the interaction vertex and decay vertex are recognizable as two distinct cascades. In between, the tauon leaves a track-like signature along its path [92]. High-energy  $\tau$  neutrinos have a high probability to be of astrophysical origin, since atmospheric  $\tau$  neutrinos are rare [93].

High-energy neutrinos are challenging to detect. They interact only weakly and have a small cross section. Neutrino telescopes need to instrument sufficient target material and volume to achieve good performance. The Waxman-Bahcall bound [94] derives a neutrino flux from the energy density of cosmic rays. If neutrinos and cosmic rays are produced in  $p\gamma$  or  $pp$  mechanisms and the sources are optically thin, then the cosmic ray energy flux provides an upper limit on the neutrino energy flux. The upper Waxman-Bahcall bound is [94]

$$E^2 \frac{d\phi_{\nu_\mu}}{dE} \sim 2 \times 10^{-8} \text{ GeV}^{-2} \text{ s}^{-1} \text{ sr}^{-1}. \quad (3.4)$$

Neutrinos with high energies (200 TeV or above) induce thus approximately 50 muons per square kilometer per year [95]. This number includes neutrino absorption in the Earth. Hence, neutrino telescopes need to be kilometer-scale detectors such that they detect astrophysical neutrinos at an acceptable rate.

The IceCube Neutrino Observatory [10] is at the geographic South Pole and instruments a cubic kilometer of Antarctic ice. Its primary goal is to detect astrophysical neutrinos with energies in the TeV to PeV range [10]. A total of 5160 digital optical modules (DOMs) are deployed on 86 cables (strings) at a depth of 1450 m to 2450 m. The distance between two strings is approximately 125 m. On each string, 60 DOMs are evenly spaced at 17 m distance [10]. The strings are deployed in a hexagonal shape, with eight closely-spaced strings at the center (DeepCore). These strings and denser spacing of detectors lower the energy threshold to approximately 10 GeV. At the ice surface, the ice Cherenkov detector IceTop [96] searches for cosmic ray air showers above 300 TeV. Figure 3.4 shows a sketch of IceCube on the left.

Each DOM contains a downward-facing 10 inch (25 cm) diameter photomultiplier tube inside a glass pressure housing. Onboard electronics allow a nearly autonomous operation, including, for example, data acquisition and digitization of detected photon waveforms, calibration LEDs, communication with other modules, and power conversion [10]. It detects photons from particles in distances up to 500 m and energy ranges from 10 GeV to 10 PeV [10]. Figure 3.4 shows a sketch of a DOM on the right.

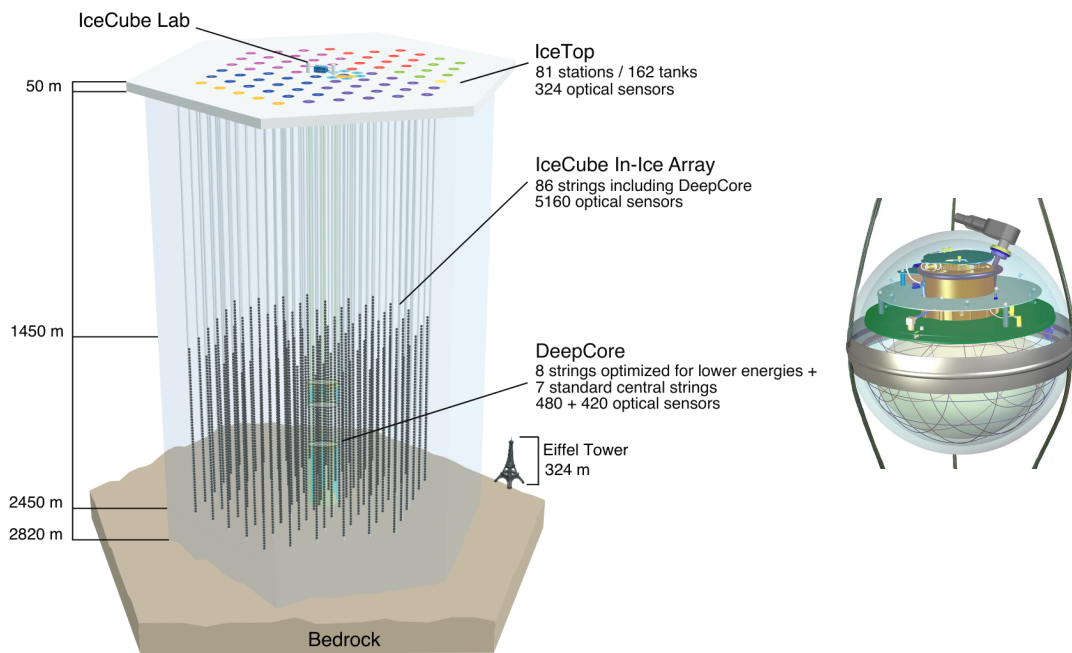


Figure 3.4: **Left:** The IceCube detector. The in-ice array is between 1450 m and 2450 m depth. IceTop vetoes atmospheric air showers from cosmic ray interactions. The denser central region DeepCore detects lower energy neutrinos down to 10 GeV. Figure taken from [10]. **Right:** Illustration of an IceCube digital optical module (DOM). The spherical glass pressure vessel contains, amongst others, a 10 inch photomultiplier tube, calibration LEDs, electronics for waveform digitization and communication [10]. Figure taken from [97].

## 3.2 Event selection

A careful event selection aims to reduce background as much as possible and to select high-energy events useful for identifying astrophysical neutrino sources. Neutrino-induced muon tracks provide the best pointing to their origin. Additionally, the interaction vertex of muon neutrinos can lie far outside the detector, which expands the target material beyond the instrumented volume. The main background is particle showers from cosmic ray interaction in the atmosphere (see Section 2.4). The muon tracks need reconstruction in direction and energy, an overview of the reconstructions used in the final sample is given in Section 3.4.

For events from the Northern Hemisphere, the Earth acts as a shield to atmospheric muons. Atmospheric neutrinos, however, pose a background for both down-going (from the Southern Hemisphere) and up-going (from the Northern Hemisphere) events. Some atmospheric muons can be erroneously reconstructed as originating from the Northern Sky. These events can be filtered by only allowing high-quality tracks [98]. The following provides a conceptual overview of different data acquisition and processing steps.

*Simple Multiplicity Trigger* — When a DOM detects light, IceCube uses a hard local coincidence (HLC) to reduce noise. This requires the next or next-to-next DOM to be hit within  $\pm 1 \mu\text{s}$  before the collected waveforms are sent for processing [10]. The main data acquisition trigger looks for spatial and temporal clusters of HLC hits. Here, the trigger condition is satisfied if  $N$  HLC hits are recorded within a certain time [10] — the Simple Multiplicity Trigger (SMT). One trigger condition is, for example, 8 recorded hits within  $5 \mu\text{s}$  (SMT8) [10]. In this case, the IceCube data acquisition system records all DOM signals between  $-4 \mu\text{s}$  and  $+6 \mu\text{s}$  as a single event. Data processing and filtering include calibration of DOM digitized waveforms, extraction of light arrival times and amplitudes from the DOM waveforms, and calibration of the relative timing [10, 99].

Muons produced by cosmic ray interaction in the atmosphere cause a trigger rate of  $\approx 2.7 \text{ kHz}$  [100]. Neutrinos are detected at a rate of a few mHz and are mainly atmospheric [100] (see Figure 3.5). Strict requirements on reconstruction quality and energy reduce the atmospheric background.

*Muon Filter* — All events that fulfill SMT are input to the “Muon Filter” [102]. In the Muon Filter, several reconstruction algorithms (see e.g. Section 3.4 and [103, 104])

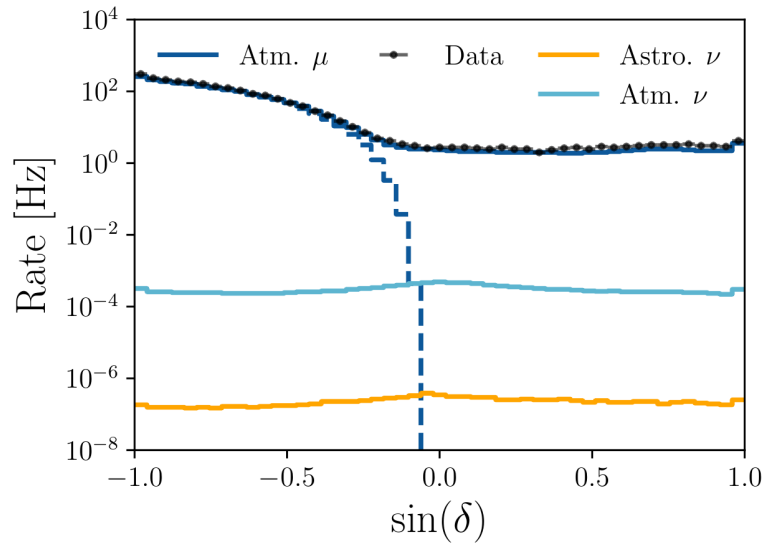


Figure 3.5: Event rates at SMT8 condition depending on declination. The solid lines show the reconstructed arrival direction whereas the dashed lines show the true direction. Atmospheric muons are often incorrectly reconstructed as up-going. Data from [101], figure reprinted with permission from M. Huber [33].

compare light arrival information of each event with expected signatures from track and cascade events to determine direction, position, and energy [104]. Additionally, the extremely-high-energy (EHE) filter selects events where the number of photoelectrons in the detector exceeds a certain threshold [105]. Approximately 1% of these reconstructed events are evaluated to be potentially neutrino induced [99]. The event rate after the Muon and EHE Filter is about 34 Hz [106].

*Online Level 2* — IceCube also acts as a trigger for other telescopes. Paramount priority is sending out realtime notifications about interesting, well-reconstructed events. The sample from the Muon Filter is still background dominated. The “Online Level 2” (OnlineL2) selection [99, 102] singles out well-reconstructed track-like events. More sophisticated and expensive reconstruction algorithms (see, e.g., Section 3.4.2) and additional cuts on track quality further reduce background. Relevant for the selection are, for example, the number of direct DOM hits (from photons with little scattering), the track length, and the error of the reconstruction (see Section 3.4.3) [102]. After OnlineL2, the event rate is approximately 2 Hz in the upgoing region [102]. Then, the selection is further refined depending on the alert criteria (see Section 3.3).

*Offline Level 2* — Up to now, all described steps happened in situ at the South Pole with limited resources available. For general data analysis, the pre-selected sample from the Muon and EHE Filter is sent north via satellite for more advanced reconstructions. The transfer bandwidth is limited; thus, most reconstructions are not transmitted. Data processing and reconstructions are redone in the north with fewer constraints on resources (“Offline Level 2”) [105].

*Muon Level 3 Filter* — The “Muon Level 3 Filter” [105] further improves the event selection. The neutrino signal in the Northern Sky is dominated by misreconstructed muon tracks. Stringent cuts on reconstruction quality thus reduce the contamination [105]. Furthermore, lower energy events are removed [105]. The background in the Southern Hemisphere requires additional constraints. Algorithms searching for causally connected hits can recognize atmospheric muon bundles [107]. Events caused by multiple muons are then split into sub-events and reconstructed. The final Muon Level 3 selection requires the likelihood of the directional reconstruction to exceed certain thresholds [105]. These cuts and constraints remove large fractions of atmospheric muons while retaining most neutrino events [105]. The event rate is now  $\sim 3$  Hz [105]. Even though most atmospheric muons have been removed, data are still dominated by this background component.

*Boosted Decision Trees* — Boosted Decision Trees [108] (BDTs) reduce the background (atmospheric muons and cascade events) even further. They use variables connected to event quality and clear track-like topology [109]. In the Northern Sky, a single BDT recognizes three signatures. Single muon tracks from atmospheric or astrophysical neutrino interactions are considered as signal, whereas atmospheric muons and cascade events are classified as background. With the Northern Sky BDT  $\sim 90\%$  of atmospheric neutrinos and  $\sim 0.1\%$  of atmospheric muons from the initial selection remain in the sample [55]. The BDT is trained for two source spectra,  $E^{-2.0}$  and  $E^{-2.7}$  [109], in order to be sensitive to hard spectra as well as to softer source spectra.

The Southern Sky (declination  $\delta < -5^\circ$ ) is dominated by atmospheric muon background. Additionally, cosmic ray showers produce muons in bundles that produce a bright signature in the detector. These muon bundles imitate the signature of a single high-energy muon. BDTs select the best reconstructed high-energy events based on event quality and track topology [109]. Additionally, the detector’s deposited energy and photons’ light-arrival time help filter muon bundles [109]. For high-energy muons, stochastic cascades dominate energy losses. Those cascades superimpose

Year	Livetime [days]	Number of events	Start	End
IC59	353.578	107011	2009 May 5	2010 May 31
IC79	316.045	93133	2010 June 1	2011 May 13
IC86 2011-2019	3184.163	1133364	2011 May 13	2020 May 29

Table 3.1: Overview of the used data samples. The columns list the configuration of the detector, uptime (livetime) of the detector in days, number of events in the sample, start, and end date.

the muon Cherenkov cone. On the other hand, muon bundles lose less energy via stochastic cascades, and the light yield along the track is smoother [109]. Additional superposition of several Cherenkov cones leads to earlier photon arrival times than a single Cherenkov cone. Contrary to the Northern Sky, the Southern Sky BDT is trained for a single signal spectrum of  $E^{-2.0}$ . Only high-energy events remain in the selection because of the large background in lower energies. This leads to a rising energy threshold of  $\sim 10\text{--}100$  TeV [98, 109]. IceTop vetoes coincident cosmic ray air showers for down-going events to further reduce background. This filters 90% of high-energy down-going events, with 0.1% being random coincidences [110]. The final selection aims to be most sensitive for sources following an  $E^{-2}$  spectrum.

This work intends to find neutrino sources; thus, I select events with the best angular resolution — track-like events. IceCube has still been under construction but functional during the first years of data taking. I use data that were taken with 59, 79, and finally, all 86 strings. In total, I analyze IceCube data from 2009–2020 (two years with incomplete detector configuration, nine years with the completed detector), as listed in Table 3.1. Analyzing those data sets together requires re-weighting each point with the effective area weight of the respective data-taking period (see Equation (3.5)). This also includes signal simulations. There, signal neutrinos need to be distributed according to the effective area ratios of the different detector configurations.

Figure 3.6 shows the distribution and effective areas of the final event selection. The effective area  $A_{eff}$  describes how many neutrinos  $N$  IceCube observes per solid angle  $\Delta\Omega$  and energy range  $\Delta E$  during time  $T$  for a certain neutrino flux  $\frac{d^3\phi_{\nu_\mu+\nu_{\bar{\mu}}}}{dt d\Omega dE}$ :

$$N_{\nu_\mu+\nu_{\bar{\mu}}} = \int_T dt \int_{\Delta\Omega} \int_{\Delta E} dEA_{eff}(E, \delta) \frac{d^3\phi_{\nu_\mu+\nu_{\bar{\mu}}}}{dt d\Omega dE}. \quad (3.5)$$

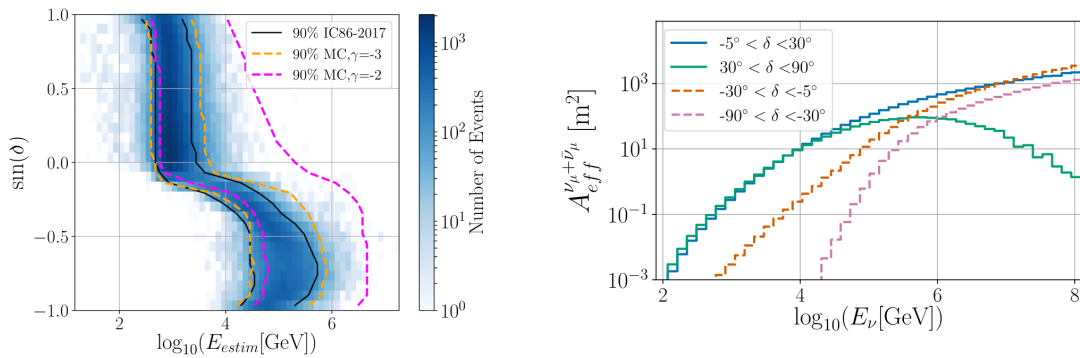


Figure 3.6: **Left:** The distribution of one year of events in energy and declination. The black line shows the 90% contour for data. Orange and purple dashed lines show the 90% contour for simulated data following a spectrum of  $E^{-2}$  and  $E^{-3}$ . **Right:** Effective area depending on energy for different declinations. Figures taken from [55].

The effective area already includes all detector effects and neutrino propagation and interactions. For energies above 100 TeV, neutrino absorption in the Earth for near-vertically up-going events becomes visible in Figure 3.6.

### 3.3 IceCube realtime alert events

IceCube has an average uptime of  $> 99\%$ , and its field of view covers the full sky, with its most sensitive region to high energy neutrinos being the horizon (see Section 2.6.2). This makes it ideally suitable to alert other observatories of rare events [99, 111]. Such rare events are, for example, neutrinos with extremely high energies and a good angular resolution that are highly likely of being of astrophysical origin. If IceCube detects such neutrinos, multi-messenger observations (e.g., from gamma-ray telescopes) should be triggered as fast as possible to detect transient astrophysical phenomena. This requires a fast reconstruction and evaluation of neutrino events directly at the South Pole (see Section 3.2). Events must also pass a filtering system considering event quality, energy, and topology criteria. Simultaneously, monitoring systems ensure that the detector has been running stable. Remaining interesting events are sent north to the IceCube Data Center (see Figure 3.7 for an overview) [99]. This process, from triggering the event, running reconstructions, filtering interesting events, transmitting and receiving them north, takes  $\sim 33$  s (median value) [99].

Further selection criteria in the IceCube Data Center determine if events are astrophysical neutrino candidates. Candidate events are then sorted into two categories “Gold” alerts and “Bronze” alerts [111]. The category depends on the signalness [111]

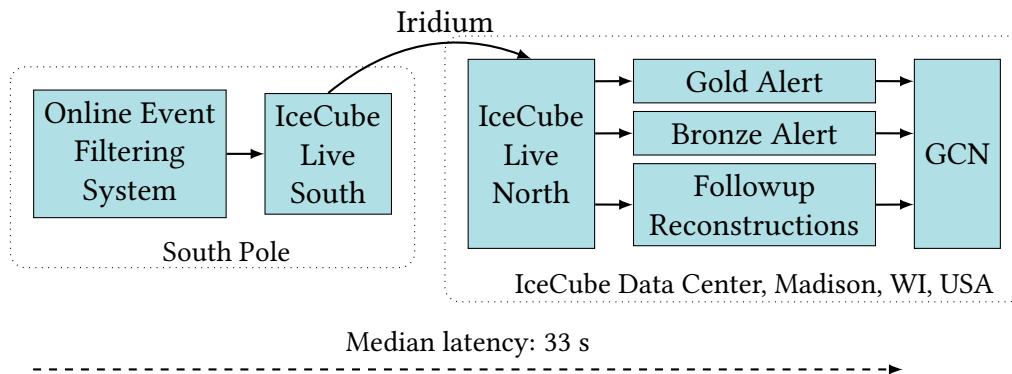


Figure 3.7: Overview of the realtime alert system. Events pass through the filters and are transmitted north via the Iridium satellite system. Further processing in the North selects events with a high probability to be of astrophysical origin. Adapted from [111].

$$\text{Signalness}(E, \delta) = \frac{N_{\text{signal}}(E, \delta)}{N_{\text{signal}}(E, \delta) + N_{\text{background}}(E, \delta)}, \quad (3.6)$$

with  $N_{\text{signal}}(E, \delta)$  and  $N_{\text{background}}(E, \delta)$  as the expected number of signal and background events at declination  $\delta$  above energy  $E$ .  $E$  can for example be the estimated reconstructed neutrino energy. Events with a signalness  $> 30\%$  fall into the Bronze category, whereas events with a signalness  $> 50\%$  qualify as Gold [111]. Both alerts are subsequently distributed as notices via the Gamma-ray Coordinates Network<sup>1</sup> (GCN).

More sophisticated algorithms (see Section 3.4.5) provide a more accurate position and uncertainty region after a few hours. This updated information is also circulated as an update to the initial GCN notice. The selection criteria for alerts are as follows.

*GFU track selection* — The Gamma-ray Follow-Up [112] (GFU) track selection focuses on through-going high-quality tracks from all directions [99, 111]. Only the highest energy events qualify as alerts. The energy is based on the reconstructed muon energy for events from the Northern Sky [111]. For Southern Sky events, the charge of photoelectrons in the detector provides an energy estimate [111]. The selection criteria for southern events depends additionally on their declination [111].

*EHE track selection* — The Extremely-High-Energy (EHE) track selection targets neutrinos with energies between 500 TeV and 1 EeV [99]. It requires at least  $\sim 4000$

<sup>1</sup><https://gcn.gsfc.nasa.gov/>

Gold alerts	Signal ( $E^{-2.19}$ )	Atmospheric Background	Observed
Total	6.6	6.9	9.9
GFU	5.1	4.7	7.8
EHE	2.1	1.9	4.3
HESE	0.5	0.4	1.1

Table 3.2: Expected and observed Gold alert rates per year. There is an overlap between the GFU and EHE selection, thus the total rate is different from the sum of all selections. Data from [111].

photoelectrons detected by DOMs and at least 300 DOMs recording a signal [99, 111]. The precise threshold of the number of photoelectrons depends on the event’s declination. Only well-reconstructed tracks qualify for this selection.

*HESE track selection* — High-Energy-Starting-Events (HESE) select only tracks where the neutrino interaction vertex lies inside the detector [99, 111]. Hence, the track does not pass through the entire detector, but it starts inside and leaves the detector. The track length needs to be at least 200 m, also to ensure good reconstruction quality [111]. Additionally, there is a threshold on the detected charge in the DOMs depending on the event declination [111].

If an event passes multiple of these criteria, the hierarchical order is first GFU, then EHE, followed by HESE [111]. This work focuses on the purest astrophysical neutrino source candidate selection. Hence, I consider only alerts from the Gold stream. Table 3.2 lists the expected alert rates.

### 3.4 Muon track reconstruction

The detection of neutrino sources requires an accurate reconstruction of the primary neutrino direction and energy. This work uses events caused by through-going muons since their large lever arm allows the best directional pointing back to their origin. The mean kinematic angle between original neutrino direction and secondary muon direction is  $0.7^\circ / (E_\nu/\text{TeV})^{0.7}$  [113]. It decreases with energy and becomes negligible for high-energy events.

IceCube events’ directional and energy reconstructions use the timing and charge of pulses from digitized waveforms. Several reconstruction algorithms are applied, each with increasing accuracy, complexity, and computing time. The faster algorithms can be applied to all events and can seed more advanced algorithms. All algorithms are

based on the same principle: The expected outcome of a track hypothesis is compared with the actually observed photon time and charge distributions in every DOM [114]. The track hypothesis is typically optimized by maximizing a likelihood function, which returns best-fit parameters for the desired muon track [114]. For an overview of maximum likelihood methods, see, for example, [115].

As a first general simplification the muon track is approximated by a track hypothesis  $H$ . The unit vector  $\mathbf{d}$  gives the direction from the initial position  $\mathbf{x}_0$  at time  $t_0$ . After time  $t$  the muon is at position  $\mathbf{x}(t)$  [114]

$$H : \mathbf{x}(t) = (t - t_0) \cdot c_{vac} \cdot \mathbf{d} + \mathbf{x}_0, \quad (3.7)$$

with  $c_{vac}$  as the vacuum speed of light. This track hypothesis neglects the muon stochastic energy losses. A photon from a muon described by  $H$  that travels directly (without scattering) to a DOM at position  $\mathbf{x}$  would hit the DOM after an expected arrival time  $t_{geo}$  [116] (see also Figure 3.8 on the left)

$$t_{geo}(\mathbf{x}|H) = t_0 + \frac{1}{c_{vac}} \cdot \left( \mathbf{d} \cdot (\mathbf{x}_0 - \mathbf{x}) + q \frac{n_{gr} n_{ph} - 1}{\sqrt{n_{ph}^2 - 1}} \right), \quad (3.8)$$

with  $n_{gr}$  and  $n_{ph}$  as the group and phase refractive indices in ice. Photons propagate with the group velocity and the phase velocity defines the Cherenkov angle. The distance of the track to the DOM at  $\mathbf{x}$  is

$$q = \frac{\|(\mathbf{x} - \mathbf{x}_0) \times \mathbf{d}\|}{\|\mathbf{d}\|}. \quad (3.9)$$

The time residual between the actual arrival time of a photon  $t_{photon}$  and the expected arrival time for unscattered photons  $t_{geo}$  is

$$t_{res}(\mathbf{x}|H) = t_{photon} - t_{geo}(\mathbf{x}|H). \quad (3.10)$$

Figure 3.9 (left) shows distributions of  $t_{res}$  for different distances from track to DOM. There are several ways to describe the probability distribution function (PDF) of the time residuals  $p(t_{res}|\mathbf{x}, H)$ . In MuEX Angular (Section 3.4.1), the time residual PDF is parametrized by a gamma distribution – the Pandel-function [116]. Another way is to base the distribution on Monte-Carlo photon propagation [104] and to use a smooth spline interpolation [117] of tabulated photon data (see for example Section 3.4.2).

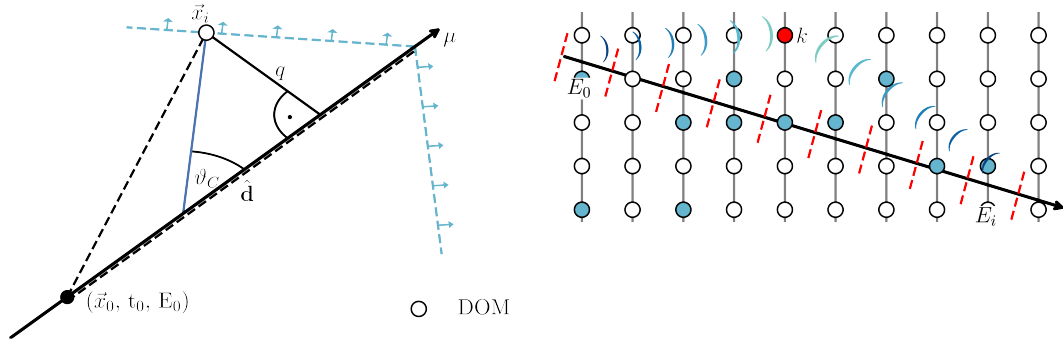


Figure 3.8: Adapted from [33]. **Left:** Propagation of a Cherenkov photon originating from a muon track. The Cherenkov light hits the DOM  $i$  at distance  $q$  from the track. **Right:** For unfolding, energy losses from all parts of the tracks contribute. The DOM detects  $k$  photons.

Optical ice properties are more precisely described by the spline interpolation [114]. Multiplying the time-residual PDFs of every measured pulse  $j$  at DOM  $i$  located at  $\mathbf{x}_i$  yields the “Single-Photo-Electron” (SPE) likelihood [114]

$$\mathcal{L}_{\text{SPEALL}} = \prod_i^{N_{\text{DOMs}}} \prod_j^{N_{\text{Pulses},i}} p(t_{\text{res}}^j | \mathbf{x}_i, H). \quad (3.11)$$

Here,  $N_{\text{Pulses},i}$  is the number of all detected pulses at DOM  $i$ , and  $N_{\text{DOMs}}$  is the number of DOMs with at least one recorded pulse. Including all pulses makes the likelihood sensitive to pulses related to PMT effects that are not part of the time residual PDF. These PMT effects are avoided when considering only the first photons arriving at a DOM. Furthermore, the first photons are usually least scattered in ice, compared to the average photon, and are less affected by mismodeled ice properties [114]. With the time residual PDFs,  $t_{\text{res}}^{1,i}$ , of the first detected photon pulse at every DOM  $i$ , the likelihood becomes [103]

$$\mathcal{L}_{\text{SPEFirst}} = \prod_i^{N_{\text{DOMs}}} p(t_{\text{res}}^{1,i} | \mathbf{x}_i, H). \quad (3.12)$$

Expanding this to the probability to observe the first photon at  $t_{\text{res},1}$  followed by  $N_{\text{Pulses}} - 1$  hits, the “Multi-Photo-Electron” (MPE) likelihood becomes [118]

$$\mathcal{L}_{\text{MPE}} = \prod_i^{N_{\text{DOMs}}} p(t_{\text{res}}^{1,i} | \mathbf{x}, H) \cdot N_{\text{Pulses},i} \cdot \left( \int_{t_{\text{res}}^1}^{\text{inf}} p(t | \mathbf{x}_i, H) dt \right)^{N_{\text{Pulses},i}-1} \quad (3.13)$$

### 3.4.1 MuEX Angular

MuEX Angular is a first guess algorithm that seeds more expensive reconstructions [114]. It approximates the time-residual PDF with a Pandel-function and is based on the SPEALL likelihood (Equation (3.11)) [114]. A Cauchy distribution considers noise pulses and additional pulses caused by stochastic energy losses [114]

$$\mathcal{L}_{MuEX}(\mathbf{x}|H) = \prod_i^{N_{DOMs}} \prod_j^{N_{Pulses}} \left( \alpha \cdot \text{Cauchy}(t_{res}^j, \sigma) + (1 - \alpha) \cdot p_i(t_{res}^j|\mathbf{x}, H) \right), \quad (3.14)$$

with  $\alpha = 1 \times 10^{-3}$  as a mixture parameter for the relative probability of noise pulses and  $\sigma = 2 \times 10^3$  ns as the typical muon propagation time through IceCube. MuEX Angular applies a bootstrap resampling algorithm of input pulses that improves convergences and estimates uncertainties [114].

### 3.4.2 SplineMPE

The result from MuEX Angular seeds SplineMPE. For SplineMPE, the time-residual PDFs are interpolated by smooth splines [117] from tabulated photon data based on Monte-Carlo photon propagation [104]. The reconstruction uses a mixture of bare muon splines and averaged stochastic muon splines combined with the MPE likelihood. Figure 3.9 compares the median angular resolution for different reconstruction algorithms [114]. SplineMPE allows the best resolution while still being efficient enough to be applied on a large event sample.

In general, the directional reconstruction is validated by measuring the Moon shadow. The Moon shields the Earth from cosmic rays, which produce atmospheric muons. IceCube then measures the lack of atmospheric muons as the Moon shadow. The observed moon shadow is within  $0.2^\circ$  of the expected position [119].

### 3.4.3 Uncertainty estimation

Estimating the uncertainties of the angular reconstruction is important for determining spatial coincidence with sources. A detailed scan of the likelihood region around the best-fit direction would be most accurate. However, due to computational constraints, some simplifications are necessary.

The PDF of a maximum likelihood estimate  $\hat{\Psi}$  for a position  $\Psi = (\text{azimuth } \theta, \text{zenith } \phi)$  becomes Gaussian in the large sample limit [120]. The Gaussian is centered around the true position  $\Lambda$  and has a standard deviation  $\sigma_{\hat{\Psi}}$ . In the large sample limit, the

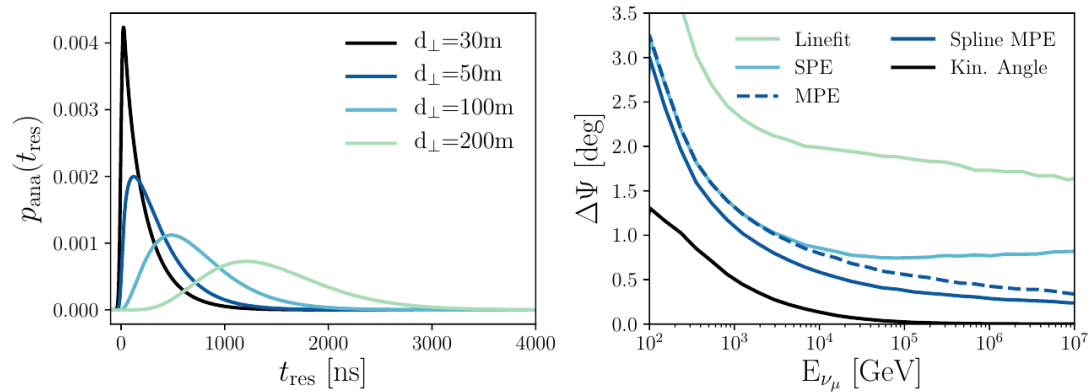


Figure 3.9: **Left:** The analytic distribution of photon delay times for different distances. **Right:** Median angular resolution for different reconstruction algorithms. The Single Photo Electron (SPE) likelihood only considers the very first arriving photon. Considering all arriving photons improves the reconstruction (blue dashed line), as does the spline tabulation (solid dark blue line). The black line is the kinematic angle between neutrino and muon. Line-fit is a robust first guess algorithm that estimates the muon track by connecting all triggered PMTs with a line [103]. Figures reprinted with permission from M. Huber [33].

Likelihood function  $\mathcal{L}(\Psi)$  also becomes a Gaussian centered around the estimate  $\hat{\Psi}$  [120]. From the Cramér-Rao Inequality [115, 120] follows that both, the PDF of  $\hat{\Psi}$  and  $\mathcal{L}(\Psi)$  have the same standard deviation  $\sigma_{\hat{\Psi}}$ . Hence,  $\mathcal{L}(\Psi)$  determines the variance of  $\hat{\Psi}$ . Thus,  $\sigma_{\hat{\Psi}}$  can be estimated using the following relation: Changing  $\Psi$  by  $N$  standard deviations leads to a decrease of the log-likelihood function by  $N^2/2$  from the maximum value [120]

$$\log \mathcal{L}(\hat{\Psi} \pm N\sigma_{\hat{\Psi}}) = \log \mathcal{L}_{\max} - \frac{N^2}{2}. \quad (3.15)$$

This means that the contour where the log-likelihood is  $\frac{1}{2}\mathcal{L}_{\max}$  defines the one sigma error region (the 68.3% confidence interval) of  $\hat{\Psi}$ .

In IceCube, a two-dimensional parabola approximates the likelihood [121, 122]. The directional likelihood is evaluated at distinct points on three rings around the best-fit direction [122]. The parabola is interpolated between these points, yielding variances of the likelihood estimator for both axes  $\sigma_{\hat{\theta}}$  and  $\sigma_{\hat{\phi}}$ . For simplification, these elliptical uncertainties are approximated by a circular angular uncertainty  $\sigma_p$  [122]

$$\sigma_p = \sqrt{\frac{\sigma_{\hat{\theta}}^2 + \sigma_{\hat{\phi}}^2}{2}}. \quad (3.16)$$

The angular distribution is hence assumed to follow a normal distribution around the true direction  $\Lambda$  with standard deviation  $\sigma_p$ .

IceCube uses the median angular resolution, meaning a 50% probability for both, azimuth and zenith, to lie within the uncertainty region. The probability of variables to be in the error circle with radius  $r$  is given by the integral over the error circle of the underlying distribution. This integral can be solved analytically into the expression  $1 - \exp\left(-\frac{r^2}{2\sigma_p^2}\right)$ . Hence the median angular resolution is computed with

$$0.5 \stackrel{!}{=} 1 - \exp\left(-\frac{r^2}{2\sigma_p^2}\right) \Rightarrow r = \sqrt{2 \ln 2} \cdot \sigma_p = 1.177 \cdot \sigma_p. \quad (3.17)$$

Thus, for the median angular resolution, the resulting paraboloid uncertainty  $\sigma_p$  needs to be extended by a factor of 1.177 to cover the 50% contour [121].

The paraboloid value is an estimator for the angular difference  $\Delta\Psi$  between the reconstructed neutrino direction and the true neutrino direction. This requires consideration of the kinematic angle between muon and neutrino. The angle is not observable in IceCube, however it can be corrected on a statistical basis. This so-called pull correction takes the relation between paraboloid uncertainty  $\sigma_p$  and true angular difference  $\Delta\Psi$  for different energy bins [121, 123]

$$\rho_{pull}(\log E_\nu) = \frac{\Delta\Psi}{\sigma_p}. \quad (3.18)$$

For an accurate uncertainty estimation, this correction factor evaluates to one. The uncertainty for each event  $i$  is corrected with the pull by

$$\sigma_i(\log E_\nu) = \rho_{pull}(\log E_\nu) \cdot \sigma_i(\log E_\nu). \quad (3.19)$$

The pull correction also compensates for discrepancies in the paraboloid description of the likelihood space on a statistical basis. However, the correction is not necessarily ideal on an event-by-event basis. Figure 3.10 shows the effect of the pull correction.

### 3.4.4 Energy reconstruction - Truncated mean

Energy losses  $dE$  of muons traveling through ice are described by Equation (2.14):  $-dE/dx = a + bE$  per length  $dx$ . Those losses are a combination of ionization losses and radiative losses (see Figure 3.11). Ionization losses dominate below  $\sim 1$  TeV. They pose a continuous component. For higher energies, radiative losses produce particle

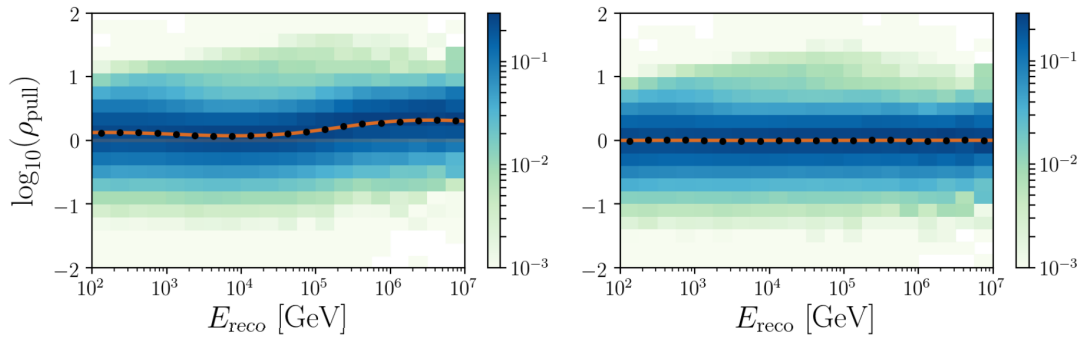


Figure 3.10: The effect of the pull correction. The color shows the PDF on each energy bin. The black dots show the median pull value with a spline fit through these points (orange). **Left:** the distribution before the correction. **Right:** the pull correction is applied and the distribution is shifted. Figures reprinted with permission from M. Huber [33].

cascades along the particle track (see right of Figure 3.3 for an example). These losses cannot be treated as a continuous process and depend on energy. They are thus referred to as stochastic. Hence, energy reconstruction becomes more challenging for energies in TeV range or higher since the particle may display varying loss patterns for the same initial muon energy.

Conventional calculations of  $dE/dx$  [104, 124] take the sum of all photoelectrons observed by all DOMs and compare them to the expected number of photoelectrons for a loss of 1 GeV/m with the same path. The number of photoelectrons is assumed to be proportional to the muon energy loss for muon energies above  $\sim 1$  TeV. Thus  $dE/dx$  is approximately the ratio of observed to the expected number of photoelectrons times 1 GeV/m. Simulations yield a distribution of  $dE/dx$  for different muon energies. A fit through the distribution allows estimating the muon energy based on  $dE/dx$ . However, the variability of stochastic cascades leads to some large energy depositions, which result in an overestimation of muon energies. For 5.4% of muons, the muon energy is overestimated by a factor of  $> 5$  [124]. This shifts the fit curve towards higher energies, and the estimation for the bulk of events is consequently too low.

Truncated mean  $dE/dx$  [104, 124] solves this issue by excluding large energy losses for the muon energy reconstruction.  $dE/dx$  is calculated for every DOM within 60 m of the track hypothesis [124]. The algorithm then omits the highest 50% of DOMs and averages the remaining  $dE/dx$  for the remaining DOMs [124]. This approach reduces the muons with reconstructed energies overestimated by a factor of  $> 5$  from 5.4% to  $\approx 1.3\%$  [124].

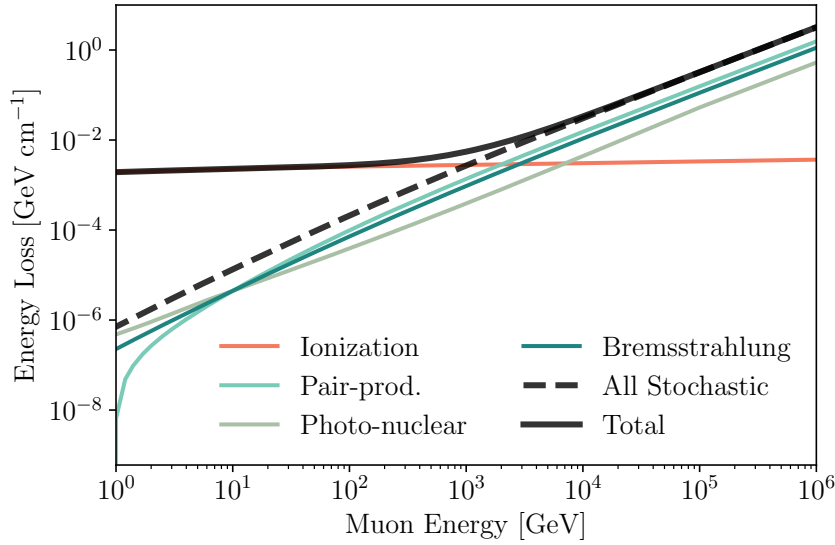


Figure 3.11: Energy losses of muons traveling through ice. The colors show different contributions. Above 2 TeV stochastic losses dominate. Data from [58], figure adapted from [33].

### 3.4.5 Millipede reconstruction

Another reconstruction algorithm is Millipede (or unfolding) [104]. Millipede considers the timing of all photons and does not rely on the infinite-track assumption. The track is divided into segments, and the energy loss is estimated for each segment. However, photons from bright stochastic losses can travel further than the size of one segment. Thus the PMT readout can comprise light from nearer segments of the muon track as well as photons from more distant bright stochastic cascades from everywhere along the track (see the right panel of Figure 3.8).

In general, the number of detected photons from a shower is described by a Poisson distribution with mean  $\lambda = E\Lambda$ . Thus, the likelihood  $\mathcal{L}$  to detect  $k$  photons from a shower with energy  $E$  that produces  $\Lambda$  photons per unit energy is [104]

$$\mathcal{L} = \frac{(\lambda)^k}{k!} \cdot e^{-\lambda}. \quad (3.20)$$

The expected number of photons  $\lambda$  is the summed contribution of all track segments  $i$  as well as detector noise  $\rho$  [104]

$$\lambda \rightarrow \sum_i E_i \Lambda_i + \rho. \quad (3.21)$$

Here, a particular source  $i$  deposits energy  $E_i$  in a time bin, leading to an expected light yield  $\Lambda_i$  in a photomultiplier. With the expression from Equation (3.20) the likelihood becomes

$$\ln \mathcal{L} = k \ln \left( \sum_i E_i \Lambda_i + \rho \right) - \sum_i E_i \Lambda_i - \rho - \ln(k!), \quad (3.22)$$

which needs to be summed over time bins  $j$  [104]

$$\sum_j \ln \mathcal{L} = \sum_j k_j \ln (\mathbf{E} \Lambda_j + \rho_j) - \sum_j (\mathbf{E} \Lambda_j - \rho_j) - \sum_j (\ln k_j!). \quad (3.23)$$

This can be solved in the first order with  $k_j = \mathbf{E} \Lambda_j + \rho_j$  or as a matrix multiplication  $\mathbf{k} - \boldsymbol{\rho} = \mathbf{\Lambda} \mathbf{E}$ , where  $\mathbf{\Lambda}$  is the matrix describing the predicted light yield at every point in the detector from any source position and a reference energy [104].

The best-fit energy maximizes the likelihood and can be determined analytically or by using a non-negative least-squares algorithm [104]. For different track directions and locations, the likelihood needs to be optimized numerically [104]. This scan is very time-consuming and computationally expensive and can only be done for a small selection of events, i.e., the highest-energy events.



## Chapter 4

# Search for neutrino sources — Motivation and Method

On the 22nd of September 2017, IceCube observed a high-energy neutrino (IceCube-170922A) that fulfilled the alert criteria (see Section 3.3). Within one minute after triggering, IceCube sent out notices of its detection and triggered follow-up observations [12]. Gamma-ray telescopes registered a cataloged source within  $0.1^\circ$  of the reconstructed origin direction of IceCube-170922A — the blazar TXS 0506+056 (see Figure 4.1 on the left). TXS 0506+056 was at that time in a flaring state and showed high gamma-ray emission [12]. The correlation of a high-energy neutrino event with a flaring blazar is significant at a level of  $3\sigma$  [12].

Complementary to the mentioned non-neutrino channels, IceCube searched for additional neutrino emission from the direction of the alert event IceCube-170922A — and hence the blazar TXS 0506+056. Analyzing 9.5 years of archival IceCube data, both steady and transient neutrino emissions were considered. The time-integrated search for continuous neutrino emission showed no statistically significant emission [16].

However, the hypothesis of TXS 0506+056 as a transient source yields a  $3.5\sigma$  evidence [16]. Between September 2014 and March 2015, there is an excess of neutrinos with a total emitted time-integrated flux (also called fluence) of  $J_{100\text{TeV}} = \int \Phi_{100\text{TeV}}(t)dt = (2.1_{-0.7}^{+0.9}) \times 10^{-4} \text{ TeV cm}^{-2}$  at 100 TeV. The assumed energy spectral shape is a power law best fitted by  $E^{-2.1 \pm 0.2}$  [16]. Figure 4.1 shows the neutrinos flare window on the right. This motivates the question I investigate in this work: Do high-energy

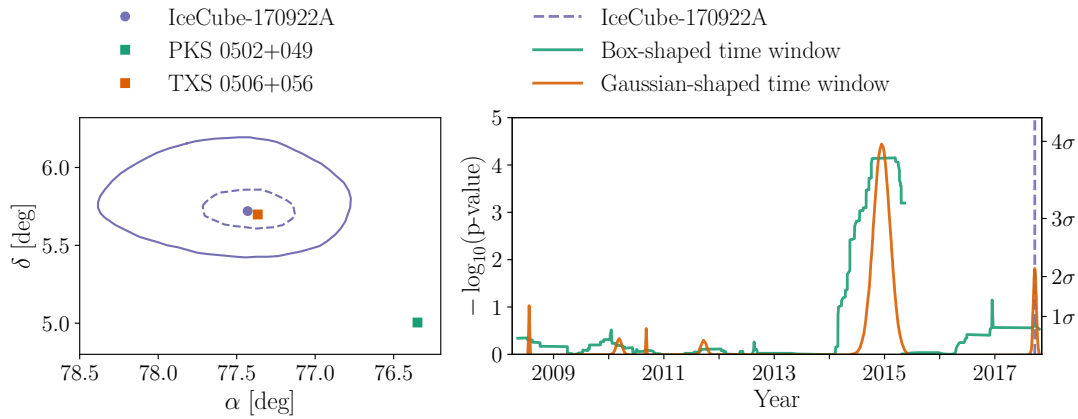


Figure 4.1: Figure adapted from [33]. **Left:** The blazar TXS 0506+056 is located within  $0.1^\circ$  of the best fit position of IceCube-170922A. **Right:** The best-fit time windows for the neutrino flare from the direction of TXS 0506+056.

neutrinos, in general, originate from potential neutrino sources that also emit a lower-energetic neutrino component?

In this analysis, I investigate the origin directions of all events that fulfill the alert criteria from 2009 until November 2021. For each alert, I search for a total emission over 11 years of data and for a time-dependent emission, similar to [16]. Additionally, I look at the combined time-integrated emission from all directions where alerts were detected. Since the alert events trigger the analysis and I aim to find additional neutrino emission, the alert events themselves are removed from the data prior to the analysis.

The search for neutrino emission requires thorough statistical tests since the data is background dominated. The background for a neutrino signal coming from a specific non-resolved object (a point source) consists of two parts: the atmospheric flux and the diffuse astrophysical neutrino flux. The search for neutrino emission tests if the data is better described by background compared to background plus signal from the source. This requires a detailed understanding of source properties and the expected background. This chapter presents an overview of an unbinned likelihood ratio test in the first part. Afterward follows a description of the background and signal probability distributions and how to find time-dependent neutrino emission (neutrino flares).

## 4.1 Unbinned likelihood ratio test

The following section is mainly based on [115, 120]. The likelihood,  $\mathcal{L}(\text{model}|\text{data})$ , is the probability of observing the data given a certain theory or model  $P(\text{data}|\text{model})$ . The goal is to find the theory or model that makes it most likely to observe the data. The model is defined by a set of parameters  $\boldsymbol{\theta}$ . Given a set of parameters  $\boldsymbol{\theta}$ , there is a certain probability for a data point to assume value  $x_i$ . This is described by the PDF  $f(x_i|\boldsymbol{\theta})$ . The likelihood is the product of this probability over all observed events  $i$

$$\mathcal{L}(\boldsymbol{\theta}|\mathbf{x}) = f(\mathbf{x}|\boldsymbol{\theta}) = \prod_i f(x_i|\boldsymbol{\theta}). \quad (4.1)$$

A likelihood ratio test compares two hypotheses –  $H_0 : \boldsymbol{\theta} = \boldsymbol{\theta}_0$  and  $H_1 : \boldsymbol{\theta} = \boldsymbol{\theta}_1$ . The two hypotheses are

- **Background Hypothesis**  $H_0 : \boldsymbol{\theta} = \boldsymbol{\theta}_0$  – The neutrino flux is caused by atmospheric muons and neutrinos, and diffuse astrophysical neutrinos.
- **Signal Hypothesis**  $H_1 : \boldsymbol{\theta} = \boldsymbol{\theta}_1$  – The neutrino flux is caused by an additional signal component on top of the atmospheric background, and the diffuse astrophysical neutrinos. The signal clusters around a point-like source at position  $\mathbf{x}_S = (\alpha_S, \delta_S)$ . The source emission spectrum follows an unbroken power law  $\frac{d\phi}{dE_\nu} \propto E_\nu^{-\gamma}$ . In the case of a transient source hypothesis, the neutrino emission occurs within a time window  $T$ .

The test compares the hypothesis using the likelihood ratio

$$\lambda(\mathbf{x}) = \frac{\sup_{\boldsymbol{\theta}_0} \mathcal{L}(\boldsymbol{\theta}|\mathbf{x})}{\sup_{\boldsymbol{\theta}_1} \mathcal{L}(\boldsymbol{\theta}|\mathbf{x})}. \quad (4.2)$$

The supremum is over all possible parameters  $\boldsymbol{\theta}$  for the signal and background hypothesis. The Neyman-Pearson lemma [125] states that the most powerful test at significance level  $\alpha$  requires the likelihood ratio  $\lambda$  to exceed a certain threshold value  $k$  in order to accept the null hypothesis.  $H_0$  is rejected for  $\lambda < k$ . For large sample sizes  $\rightarrow \infty$ , the asymptotic distribution of the log-likelihood ratio test statistic ( $TS$ ) approaches a  $\chi^2$ -distribution (Wilks' theorem) [126]:

$$TS = -2 \times \ln \lambda(\mathbf{x}) \rightarrow \chi^2\text{-distribution}. \quad (4.3)$$

The number of degrees of freedom of the  $\chi^2$ -distribution is the difference between the number of free parameters in  $H_0$  and  $H_1$ . Combining Equation (4.2) and Equation (4.3), the expression for the test statistic,  $TS$ , is

$$TS = -2 \ln \left[ \frac{\mathcal{L}(\boldsymbol{\theta}_0|\mathbf{x})}{\mathcal{L}(\boldsymbol{\theta}_1|\mathbf{x})} \right] = 2 \ln \left[ \frac{\mathcal{L}(\boldsymbol{\theta}_1|\mathbf{x})}{\mathcal{L}(\boldsymbol{\theta}_0|\mathbf{x})} \right]. \quad (4.4)$$

The hypotheses  $H_0$  and  $H_1$  define the likelihood that is evaluated over all events. The number of observed events is Poisson distributed. Thus, the probability to observe  $N$  events with expectation  $\lambda$  is  $e^{-\lambda} \lambda^N / N!$ . The likelihood is extended by this factor (also see extended likelihood in [127]). The ordering of events is not relevant thus  $N!$  does not need to be considered

$$\mathcal{L} = e^{-\lambda} \prod_i^N \lambda \times f(x_i|\boldsymbol{\theta}) = e^{-\lambda} \prod_i^N P(x_i|\boldsymbol{\theta}), \quad (4.5)$$

where  $P(x_i|\boldsymbol{\theta})$  is normalized to expectation  $\lambda$  instead of unity. The data are a combination of a certain number of signal events  $n_S$  and background events  $n_B$ , with the total number  $\lambda \rightarrow n_S + n_B$ . The probability  $P$  to observe each event is thus a composition of its probability to be signal,  $S$ , or its probability to be background,  $B$ ,

$$P = \frac{n_S}{n_S + n_B} S + \frac{n_B}{n_S + n_B} B. \quad (4.6)$$

The expected total number of events can be approximated by the observed number of neutrinos  $\lambda \rightarrow n_S + n_B = N$ . The expression for the likelihood is thus

$$\mathcal{L}(\boldsymbol{\theta}|\mathbf{x}) = e^{-N} \prod_i^N \left( \frac{n_S}{N} S(x_i|\boldsymbol{\theta}) + \left( 1 - \frac{n_S}{N} \right) B(x_i) \right). \quad (4.7)$$

The expression for the test statistic in Equation (4.4) becomes

$$\begin{aligned} TS &= -2 \ln \left[ \frac{\mathcal{L}(\boldsymbol{\theta}_0|\mathbf{x})}{\mathcal{L}(\boldsymbol{\theta}_1|\mathbf{x})} \right] = 2 \ln \left[ \frac{\mathcal{L}(n_S = \hat{n}_S)}{\mathcal{L}(n_S = 0)} \right] \\ &= 2 \sum_i \ln \left[ \frac{\hat{n}_S}{N} \left( \frac{S_i}{B_i} - 1 \right) + 1 \right], \end{aligned} \quad (4.8)$$

for a signal hypothesis of a source emitting  $\hat{n}_S$  neutrinos. The hat indicates the optimized value for  $n_S$ . This test statistic value is maximized varying the number of signal neutrinos  $n_S$  and the source spectral index  $\gamma$ . The optimization algorithm is L-BFGS-B [128–130] with bounds on  $n_S \in [0, 10^3]$  and  $\gamma \in [1, 4]$ . The following section derives expressions for the signal and background PDFs.

## 4.2 Signal and background PDF for steady neutrino emission

In this section, the signal hypothesis  $H_1$  describes a source with emitting neutrinos independent of time – a steady emission. The case for transient neutrino sources is an extension of the steady case.

The expected signature of an astrophysical source differs from an atmospheric and diffuse astrophysical background – neutrinos originating from an astrophysical object cluster in space around the object’s position. Additionally, as derived in Section 2.3, the assumed energy spectrum follows a harder distribution  $\propto E^{-\gamma}$  than the atmospheric background. The relevant parameters  $\theta$  are the source position  $\mathbf{x}_S = (\alpha_S, \delta_S)$  in right ascension and declination, and the source spectral index  $\gamma$ . The data comprises the reconstructed origin direction of a neutrino event  $\mathbf{x}_i$ , the uncertainty of the reconstruction  $\sigma_i$ , and the reconstructed energy  $E_i$ . The signal PDF combines both assumptions of the neutrino spatial and energy distribution [131]

$$S_i(\mathbf{x}_i, \sigma_i, E_i | \mathbf{x}_S, \gamma) = S_{spatial} \cdot S_{energy}, \quad (4.9)$$

$$\begin{aligned} S_i(\mathbf{x}_i, \sigma_i, E_i | \mathbf{x}_S, \gamma) &= S_{spatial}(\mathbf{x}_i, \sigma_i | \mathbf{x}_S) \cdot S_{energy}(E_i | \delta_i, \gamma) \\ &= \frac{1}{2\pi\sigma_i^2} \exp\left(-\frac{|\mathbf{x}_i - \mathbf{x}_S|^2}{2\sigma_i^2}\right) \cdot S_{energy}(E_i | \delta_i, \gamma). \end{aligned} \quad (4.10)$$

The spatial clustering is here modeled by a two-dimensional Gaussian distribution around the source position  $\mathbf{x}_S$  and with standard deviation  $\sigma_i$ . The energy PDF  $S_{energy}$  describes the probability for a signal neutrino of energy  $E_i$  given its declination  $\delta_i$  and the source spectral index  $\gamma$ . This energy PDF is calculated from Monte Carlo data [131] and is based on the detector effective area.

The background probability density functions  $B$  are defined similarly. The background from atmospheric and diffuse astrophysical neutrino flux is expected to be uniformly distributed in right ascension due to earth rotation [131]. The background hypothesis is fixed by choosing an atmospheric and astrophysical diffuse flux model and does not depend on any free parameter

$$B(\mathbf{x}_i, E_i) = B_{spatial} \cdot B_{energy}, \quad (4.11)$$

$$B(\mathbf{x}_i, E_i) = B_{spatial}(\mathbf{x}_i) \cdot B_{energy}(E_i|\delta_i) = \frac{1}{2\pi} \cdot P(\delta_i) \cdot B_{energy}(E_i|\delta_i). \quad (4.12)$$

The spatial term shows that in right ascension, the PDF assumes complete uniformity in the data. This is because IceCube is directly located at the Geographic South Pole. Earth rotation causes the same background everywhere in right ascension when integrated over more than a few days. The only spatial dependency is in declination  $\delta_i$  because IceCube is not spherically symmetric and neutrinos pass different materials depending on their arrival direction (see for example Section 2.6.2). Here again, the energy term  $B_{energy}$  describes the probability for a background event with energy  $E_i$  at declination  $\delta_i$ .  $B_{energy}$  is estimated directly from experimental data.

These PDFs can then be plugged into the expression of the test statistic (Equation (4.4)) and the optimal estimates for  $n_S$  and  $\gamma$  yielding the highest test statistic value are determined. Figure 4.2 shows example test statistic distributions for different source strengths and with a source position fit (see Section 4.3). Stronger sources shift the test statistic distribution towards higher values.

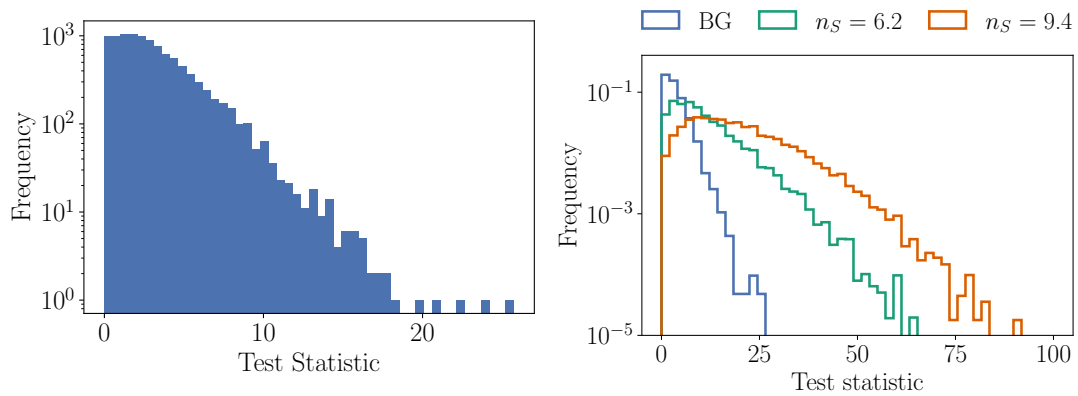


Figure 4.2: **Left:** Test statistic distribution for simulated background data. **Right:** Test statistic distributions for background data (blue) and data with simulated neutrino sources. The green histogram shows the distribution for a source with a mean neutrino emission of 6.2 neutrinos over the data taking period of 11 years. The orange histogram is the distribution for a source emitting a mean of 9.4 neutrinos in 11 years. The distribution shifts toward higher test statistic values for stronger signals.

### 4.3 Identifying the best point-source position

Each IceCube alert event is treated as a potential neutrino source, similar to sources in a catalog. However, contrary to an astrophysical source catalog, the uncertainty of the reconstructed direction yields an extended region in the sky and not a precise, point-like position for the sources. Nevertheless, high-energy neutrino sources are not, in general, spatially extended compared to IceCube’s resolution. As an example, the counterpart to IceCube-172209A, the blazar TXS 0506+056, has a diameter in the order of sub-arc minutes [132]. IceCube’s best resolution is sub-degree, whereas sub-arc minute resolution cannot be achieved. Hence, objects with arc minute extension or lower are seen as point-like sources.

The approach in this work is to fit the best position within the alert uncertainty region. Finding a stable minimization scheme proved to be difficult, and the most stable was to scan all different positions within the uncertainty region. For this, I maximize the test statistic on a grid within the uncertainty region with a spacing of  $0.2^\circ$ , which is the best directional reconstruction uncertainty in the data. In the end, the grid point with the maximal test statistic value is the best-estimated source position. Figure 4.3 shows an example where the position with the best test statistic value is indicated by a red cross. The left side shows the resulting best-fit position for only background events. On the right, a source emits ten signal neutrinos on top of background. The position scan recovers the simulated neutrino source position.

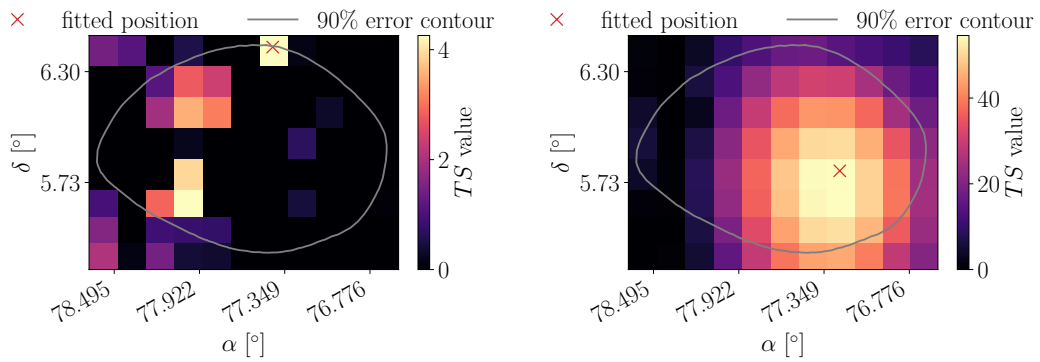


Figure 4.3: Map with test statistic values. The alert uncertainty region is divided into steps with  $0.2^\circ$  spacing. In each grid point, the highest test statistic value is determined by fitting the best mean number of signal events  $n_S$  and spectral index  $\gamma$ . The position with the best test statistic value is considered the point-source position. **Left:** Test statistic map for background data. The scan finds the position with the highest background fluctuation. **Right:** Data includes a simulated neutrino source with 10 signal neutrinos. The scan recovers the position where the source was simulated.

The position shifts the test statistic distribution towards higher values because there is a higher chance to find background fluctuations yielding higher test statistic values. This effect depends on the size of the uncertainty region (with radius  $r$ ). Larger regions contain more background fluctuations and the shift is larger than for smaller uncertainty regions (see Figure 4.4).

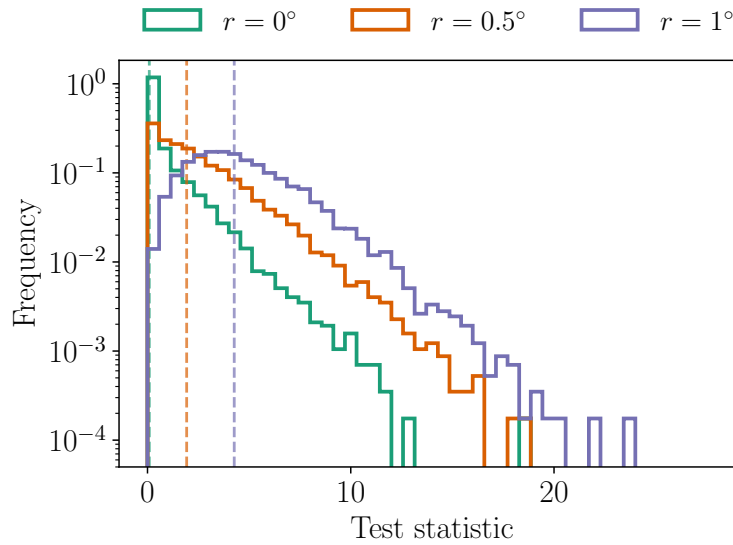


Figure 4.4: Test statistic distribution of the same alert for differently sized uncertainty regions with radius  $r$ . For an exact position ( $r = 0^\circ$ ), the distribution resembles a  $\chi^2$  distribution and the median of the distribution is at 0 (dashed line). Increasing the uncertainty region shifts the distribution and the median towards higher values.

## 4.4 Stacking of source candidates

I investigate two different scenarios of steady neutrino emission. The first consists of a few strong sources dominating the signal. In order to detect such sources, I investigate each source candidate position individually and report the most significant one as the result. The second scenario is a population of sources that individually emit a low flux. This case can be covered by combining the neutrino emission of all source candidates – called a stacking analysis. This stacking can be done in two ways. The simplest way is to calculate a stacked test statistic value  $TS_{stacked}$  by taking the sum of all the individual test statistic values of all alert positions  $k$ :

$$TS_{stacked} = \sum_k TS_k. \quad (4.13)$$

Figure 4.5 shows the resulting distribution of  $TS_{stacked}$  for background only and for a certain number of sources emitting flux  $\Phi_1 = 4.502 \times 10^{-14}$  ( $\text{TeV}^{-1}\text{cm}^{-2}\text{s}^{-1}$ ).  $\Phi_1$  is the flux corresponding to one neutrino from TXS 0506+056 in 11 years.

Another possibility is to not stack the test statistic values themselves, but the corresponding p-values  $p_k$  (see Section 4.8). The product of all  $p_k$  defines the p-score

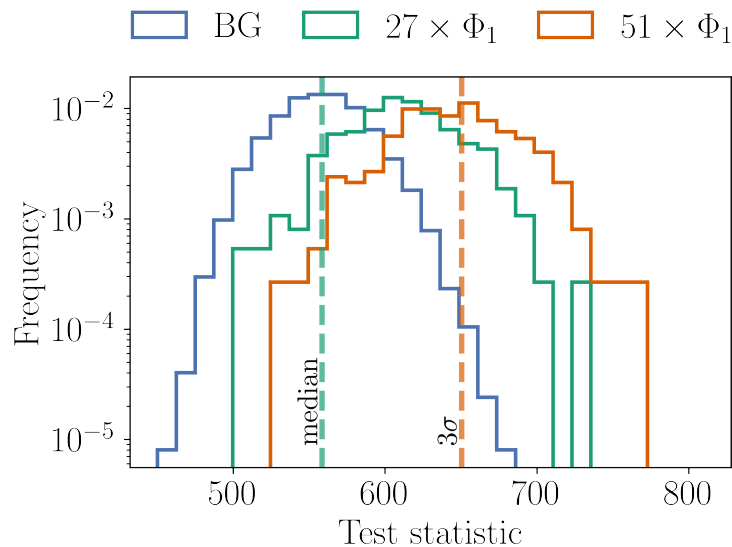


Figure 4.5:  $TS_{stacked}$  for all considered positions. The blue curve shows the distribution for simulated background data. The green and orange curve show the distribution if a certain number of sources (27 or 51) emit a flux  $\Phi_{1,100\text{TeV}} = 4.502 \times 10^{-18}$  ( $\text{TeV}^{-1}\text{cm}^{-2}\text{s}^{-1}$ ) corresponding to one neutrino in 11 years from TXS 0506+056 at an energy of 100 TeV with  $\gamma = 2$ . The dashed lines indicate the median and  $3\sigma$  quantiles of the background distribution.

value

$$TS_{stacked} = \sum_k \log_{10} p_k. \quad (4.14)$$

This has the advantage that the p-values are comparable quantities between sources. In comparison, test statistic values are not directly comparable for different source candidates since they depend on source properties such as the size of the uncertainty region (see Section 4.3) or the source declination.

## 4.5 Test of the time-integrated analysis

An accurate model and fit should recover the parameters of a simulated signal. I simulate neutrino emission of different strengths and compare how well the likelihood maximization recovers the true parameters. Angular distance from the simulated position tests the recovery of the source position. Additional quantities are the strength of neutrino emission  $n_S$  and the source spectral index  $\gamma$ . Figure 4.6 shows that the source position is recovered well for a strong signal. However, in Figure 4.7, the fit shows a bias towards more neutrinos with a softer spectrum. This implies that

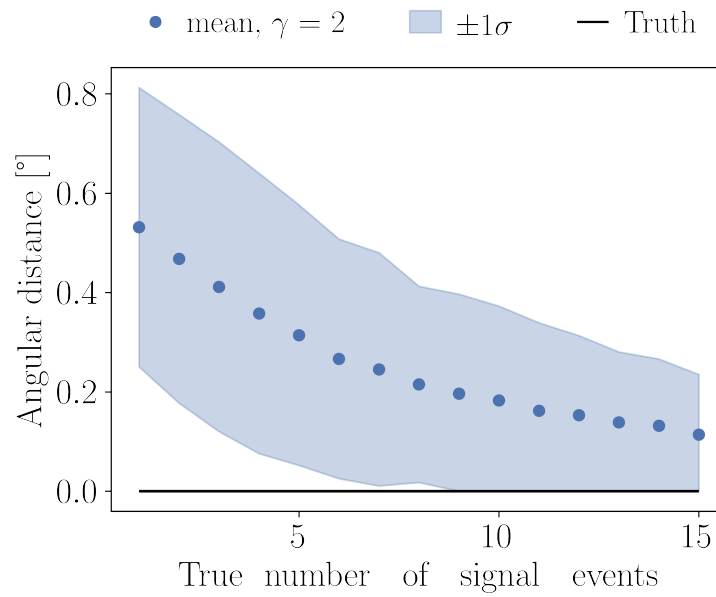


Figure 4.6: Recovery of the source position with increasing signal strength. The black line shows the truth. The blue dots depict the fitted mean value, and the shaded blue region is  $\pm 1\sigma$ . The fit does not recover the position well for a weak signal. For stronger emission, the signal events dominate the background fluctuations and the fit recovers the position down to the position step size of  $0.2^\circ$ .

an estimate of the source neutrino flux has to be calculated independent of the fit parameter  $n_S$ .

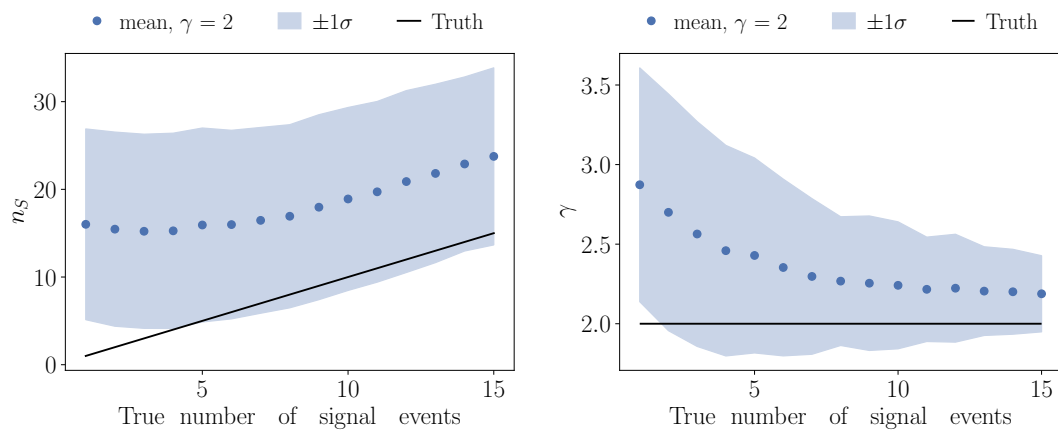


Figure 4.7: Recovery of signal parameter with increasing signal strength. The black line shows the truth. The blue dots depict the fitted mean value, and the shaded blue region is  $\pm 1\sigma$ . **Left:** The fitted number of signal events. The fit overestimates the number of signal neutrinos. **Right:** The fitted spectral index  $\gamma$ . The fit shows a tendency towards softer spectral indices.

## 4.6 Signal and background PDF for transient neutrino emission

The time-integrated analysis from Section 4.2 needs some adjustments for a transient neutrino source. This extends the signal and background PDFs from Equations 4.9 to 4.12 by a temporal part. Thus, the signal PDFs  $S$  are:

$$S(\mathbf{x}_i, \sigma_i, E_i, t_i | \mathbf{x}_S, \gamma, T) = S_{\text{spatial}} \cdot S_{\text{energy}} \cdot S_{\text{temporal}}, \quad (4.15)$$

where  $S_{\text{spatial}}$  and  $S_{\text{energy}}$  are the same as defined in Equation (4.10). The temporal PDF depends on the flare parameter,  $T$ , and can be modeled in various ways. The two approaches investigated in this work are either neutrino emission following a rectangular function or following a Gaussian distribution. The rectangular case (or box-shaped flare) includes a temporal signal PDF  $S_{\text{temporal}}$  for a flare starting at  $t_{\text{start}}$  and ending at  $t_{\text{end}}$  described by:

$$S_{\text{temporal}}(t_i) = \begin{cases} 0 & \text{if } t_i < t_{\text{start}} \\ \frac{1}{t_{\text{end}} - t_{\text{start}}} & \text{if } t_{\text{start}} \leq t_i \leq t_{\text{end}} \\ 0 & \text{if } t_{\text{end}} < t_i. \end{cases} \quad (4.16)$$

The emission before and after the flare is 0, whereas, during the flare, the source emits a constant flux of neutrinos. The Gaussian neutrino flare has signal neutrinos distributed around a mean time  $\mu_T$  with a standard deviation  $\sigma_T$

$$\mathcal{S}_{temporal}(t_i|\mu_T, \sigma_T) = \frac{1}{\sigma_T\sqrt{2\pi}} e^{-(t_i-\mu_T)^2/2\sigma_T^2}. \quad (4.17)$$

Similarly, the background probability density functions are extended by a temporal background PDF

$$B(\mathbf{x}_i, E_i) = B_{spatial} \cdot B_{energy} \cdot B_{temporal}, \quad (4.18)$$

$$B_{temporal} = \frac{1}{livetime}, \quad (4.19)$$

which is uniform in time. Hence, the temporal factor  $B_{temporal}$  is the normalization over the whole 11 years of considered data.

The time-dependent analysis introduces an additional optimization step for finding the flaring time best describing the data. The framework varies the flare parameter, fits the best  $n_S$  and  $\gamma$ , and picks the flare yielding the highest test statistic value. This method introduces a bias since there are more possible small intervals than larger ones. Introducing a penalty factor [133] corrects for this effect. For a box-shaped time PDF the penalty factor is  $\frac{t_{end}-t_{start}}{300 \text{ d}}$ . For a Gaussian time PDF the penalty factor is  $\frac{\sqrt{2\pi}\sigma_T}{300 \text{ d}}$ . The factor 300 days comes from the maximum of the considered flaring time of 300 days. Longer neutrino flares are also detectable when considering the total emission in the time-integrated search. The expression for the test statistic (see Equation (4.8)) is

$$\begin{aligned} TS &= -2 \left( \ln \left[ \frac{\mathcal{L}(n_S = 0)}{\mathcal{L}(n_S = \hat{n}_S)} \right] + \ln(\text{PenaltyFactor}) \right) \\ &= 2 \left( \sum_i \ln \left[ \frac{\hat{n}_S}{N_{obs}} \left( \frac{S_i}{B_i} - 1 \right) + 1 \right] + \ln(\text{PenaltyFactor}) \right). \end{aligned} \quad (4.20)$$

## 4.7 Identifying neutrino flares

Identifying neutrino flares is a challenge for time-dependent analyses since the data is background dominated. Figure 4.8 shows histograms of background data and

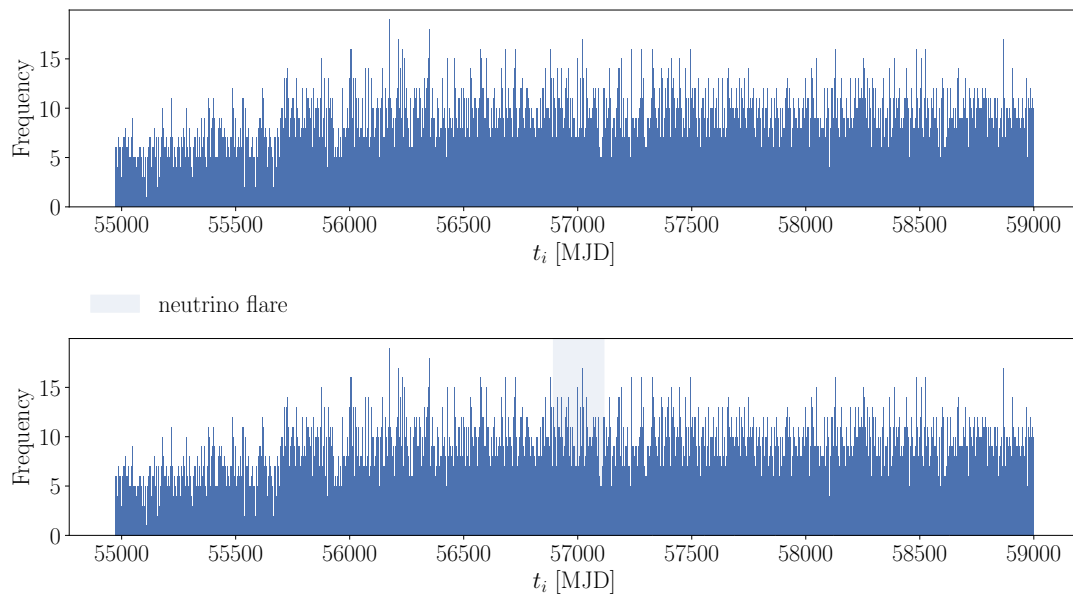


Figure 4.8: Histogram of event times of IceCube events. The first two years show a lower rate because the detector was not yet complete. **Top:** Histogram of event times of randomized background events. The times follow a uniform distribution. **Bottom:** Histogram of event times of randomized background events with a simulated neutrino flare. The flare is in the highlighted time with a total emission of 5 neutrinos. The signal is dominated by background, which makes both distributions indistinguishable by eye.

background data with a simulated neutrino flare. Both distributions cannot be distinguished by eye. More information about potentially important events can help make potential signal neutrinos distinguishable from background, such as including expectations from neutrino sources as weights to events. For this, I take the spatial and energy PDFs from Equation (4.10) and Equation (4.12) and calculate the signal over background ratio ( $S/B$ ) for each event. The signal over background ratio provides a measure of how well an event fits the source hypothesis (considering spatial clustering and energy with a fixed  $\gamma$ ) compared to the background expectation.

Figure 4.9 shows the  $S/B$  for all events (background and simulated signal). Now, few events are weighted stronger than the majority of events. However, even with additional spatial and energy information, it is not necessarily straightforward to determine the flaring time because the likelihood space has many local minima. Furthermore, the  $S/B$  depends on the assumed source spectral index  $\gamma$  (see Equation (4.10)). Thus, events are weighted incorrectly if the actual source spectral index is different from the assumed spectral index.

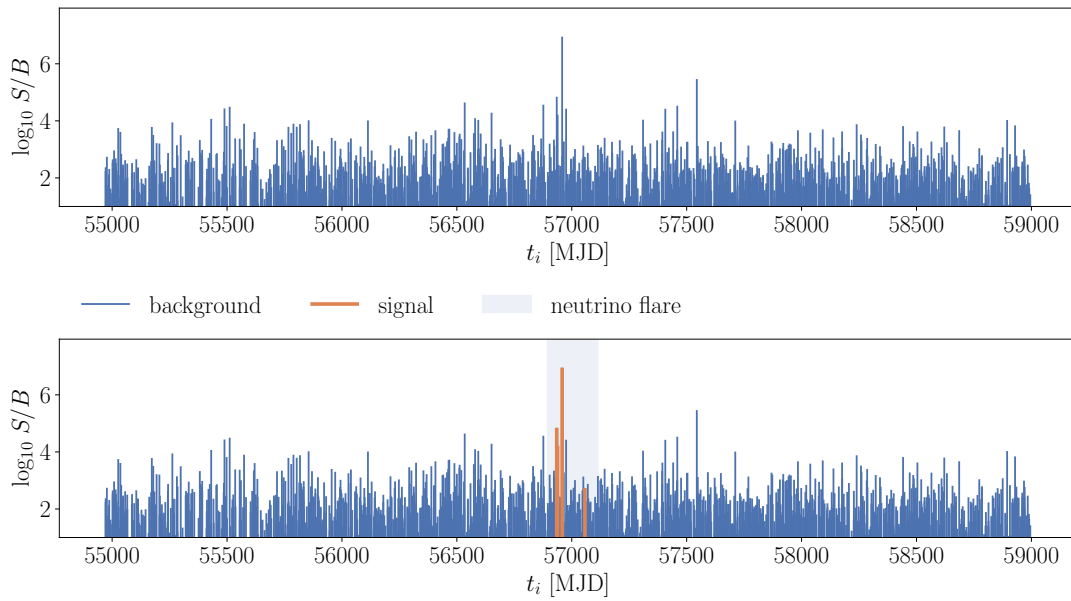


Figure 4.9: The signal over background ratio  $S/B$  for IceCube events (with fixed  $\gamma = 2$ ). The figure only includes events with  $S/B > 1$  for better readability. **Top:**  $S/B$  for background data and a simulated neutrino flare. Few events show significantly higher values than the majority of data. **Bottom:** The events from the neutrino flare are highlighted in orange. One signal neutrino has a  $S/B \sim 10^{-30}$  and is not visible.

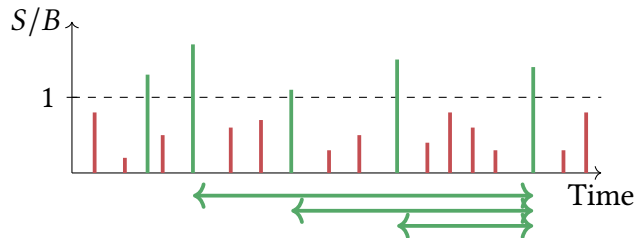


Figure 4.10: Events that surpass a certain threshold of  $S/B$  are considered as possible start and end points of neutrino flares.

#### 4.7.1 Neutrino flare searches in previous IceCube analyses

Previous time-dependent IceCube analyses [16, 56, 134, 135] all followed similar approaches. First, the  $S/B$  was calculated for all events. Then, all events that exceeded a threshold value were considered possible start and end points of flares that could be used for further optimization. For the analysis in [16], all events that fulfilled the condition  $S/B > 1$  were considered as a flare's possible starting ( $t_{start}$ ) and end points ( $t_{end}$ ), see Figure 4.10. All flares were evaluated with a likelihood ratio test, and the most significant flare was chosen as the result (brute-force approach).

At the beginning of this work, I tested if this approach could be used for the time-dependent alert follow-up. Flares in this test can have lengths between 10 and 300 days. Possible starting and end times are chosen with the following method:

1. calculate only the spatial and energy parts of the signal (Equation (4.10)) and background PDFs (Equation (4.12)),
2. calculate the ratio of the signal over background PDF ( $S/B$ ) from the previous step,
3. choose events with  $S/B > 1$ . This means that they are better described by the signal PDF compared to the background PDF and their contribution to the  $TS$  value (Equation (4.8)) is  $> 0$ ,
4. go through selected events, choose events as starting time and all events detected within 10 to 300 days as the end time for intervals.

The flare starting and end times are then plugged into the temporal PDF (Equation (4.17)). Then the test statistic value is determined with a likelihood ratio test as in Equation (4.20). In the end, the time parameters yielding the highest test statistic value is chosen as the best-fit time parameters. This brute-force approach can be sped-up by increasing the  $S/B$  threshold. However, events from lower-energy flares are then easily excluded. For reproducing the time-dependent results of the TXS 0506+056 analysis [16], I chose the same threshold of  $S/B > 1$ .

*Problems with previous approaches* — This method yields accurate results; however, the computing time is a limiting factor once this method is applied to my analysis: Scanning a single point of the grid covering one alert uncertainty region took between 7 to 8 hours on a single core on my local machine. Furthermore, there is also the position fit (Section 4.3), and the time scan is run at every point in the position grid. This scan in temporal and spatial dimensions makes the flare search computationally very expensive. Using the resources of the open science grid and  $> 1000$  cores, it took  $\sim 1$  week for an alert with a smaller uncertainty region ( $\sim 0.5^\circ$ ) until the analysis was completed 100 times on scrambled background data (background trials). With 100 background trials, the background distribution can be estimated, but there are many uncertainties left, especially since the tail of the distribution is not well sampled.

Typical are  $\sim 10^5$  background trials or more for an accurate background description. Additionally, the signal needs to be simulated and analyzed in order to calculate the analysis' sensitivity (see Section 4.10). Another important factor: In the case of detecting a significant signal, it is necessary to drastically increase the number of background trials to determine the accurate p-value. This is very expensive on resources and leads to the question whether different approaches need less computing power.

## 4.7.2 Development of optimized methods for neutrino flare searches

This section explores different possibilities to improve and speed up the search for transient neutrino sources. The first ideas followed an analytical description of how the test statistic distribution changes for different flare lengths and intensities. This could replace the computation of simulated signal. The final approach applies unsupervised learning as a flare finding algorithm and significantly speeds up the time fit. With this improved run time, simulating the signal becomes affordable, and the distribution can be sampled directly.

### 4.7.2.1 Analytical approximation of test statistic quantiles depending on flare properties

The signal simulation needs to sample the parameter space of neutrino flares with varying durations and intensities. This section investigates whether it is possible to describe the change of the test statistic median (and other test statistic quantiles) depending on the flare length  $t_{duration}$  and flare strength  $n_S$  (see also [136]). This will save computational resources if the  $TS$  median shifts were determined analytically for flares with a variety of strengths and durations while only having to simulate few flare durations and strengths. A map of the test statistic median for different flare properties is shown in Figure 4.11.

I select fixed flare strengths ( $n_S$ ) and fit the shift of the  $TS$  median with increasing flare length. From Equation (4.20) I choose the simplest approximation:

$$median(TS) \propto a + b \cdot \ln\left(\frac{n_S}{t_{duration}}\right). \quad (4.21)$$

In the left of Figure 4.12 the simple analytical description of Equation (4.21) can describe the  $TS$  median value for different time flaring lengths. The fitting parameters

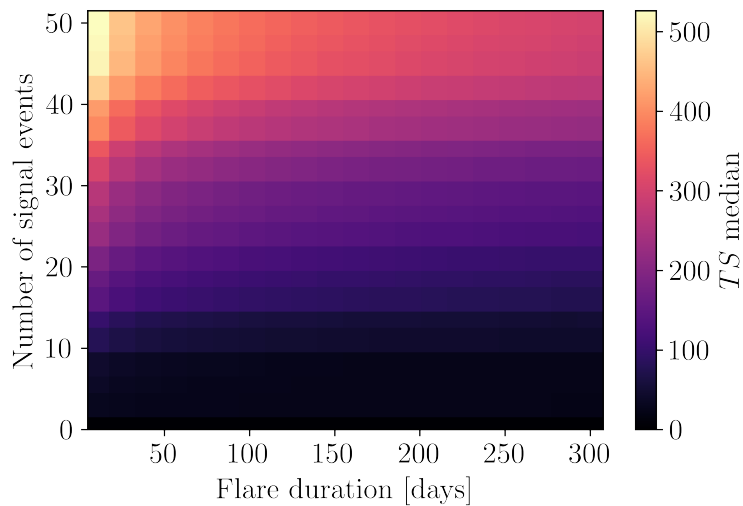


Figure 4.11: Heat map of the the test statistic median for different flare durations and flare intensities. Short, strong flares yield the highest test statistic values.

$a$  and  $b$  are described by a linear function for different flare strengths (see right of Figure 4.12).

Thus, it is sufficient to determine the parameter  $a$  and  $b$  with few flare simulations and extrapolate the TS quantile shift for the remaining parameter space. This is useful to estimate the sensitivity of analyses (see Section 4.10) without running extensive simulations. This approach was not used in this analysis, since I found another way of making trial generation more efficient (see Section 4.7.2.3).

#### 4.7.2.2 Finding new test statistic distributions

Another possible approach how to speed up the transient neutrino sources analysis is by carefully choosing which locations are worth investigating. This could, for example, be achieved by determining if events at a specific position are uniformly distributed (thus background like). In [137], different test statistic descriptions have been investigated for this purpose, and the “recursive product of spacings” has proven the most efficient. It would, for example, be possible to determine which positions have time clustering (meaning are not well described by a uniform distribution) and thus trigger further investigation.

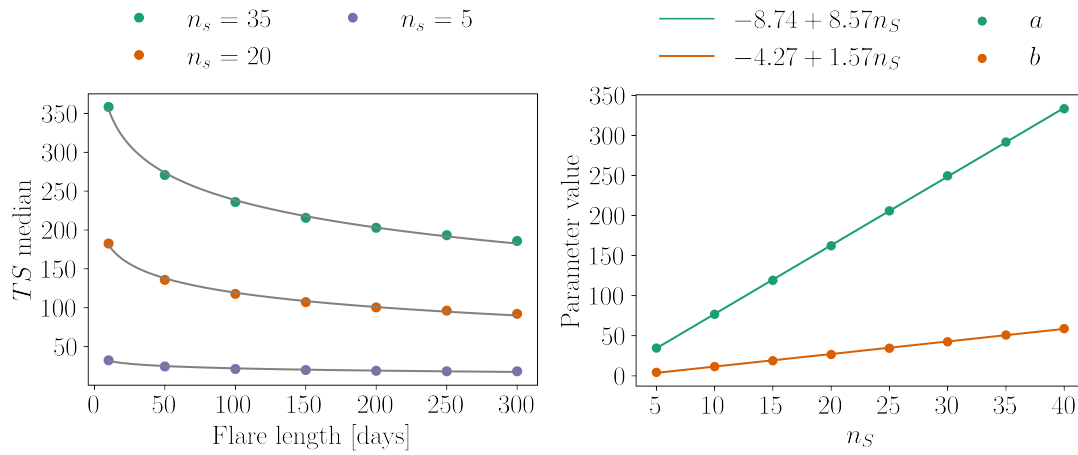


Figure 4.12: **Left:** A selection of vertical slices of Figure 4.11 show the TS median for fixed flare strengths varying over flare duration. The black line is the fit of a logarithmic function  $a + b \log\left(\frac{n_{\text{signal}}}{t_{\text{duration}}}\right)$  through the TS median values. **Right:** The fit parameter  $a$  and  $b$  follow a linear function for different flare intensities.

#### 4.7.2.3 Fitting neutrino flares with unsupervised learning – expectation maximization

The most promising approach is using unsupervised learning [138] to determine when a neutrino flare was emitted by a source. The algorithm used is expectation maximization (EM) [139]. This method provided a significant speed-up of flare finding and was thus chosen for this work. The previously mentioned methods are worth considering for future approaches, such as a time-dependent all-sky scan.

Expectation maximization is an unsupervised learning algorithm for data described by Gaussian mixture models. For  $N$  data points, there are a set of  $K$  Gaussian distributions that best describe the observed data points. The user fixes the number  $K$  in advance; however, each distribution's mean values and standard deviations are optimized. This can be done for  $M$ -dimensional data with multivariate Gaussian distributions.

The general description of the algorithm is [140]:

*Expectation step* — For each data point,  $i$ , the algorithm calculates the probability  $P(k|i)$  to belong to Gaussian distribution  $k$ . The parameters to be estimated are thus:

- $\mu_k$ : the  $K$  means
- $\Sigma_k$ : the  $K$  covariance matrices with dimension  $M \times M$

- $P(k|i)$ : the  $K$  probabilities for each data point  $i$  of  $N$ , also called the responsibility matrix (the responsibility of component  $k$  for data point  $i$ ).

For a mixing model, each Gaussian  $k$  contributes to the observed data. The probability that a random data point belongs to  $k$  is  $P(k)$ .  $P(k)$  can also be viewed as the fraction of all data points  $\mathbf{x}_i$  that originate from Gaussian  $k$ .

The likelihood  $\mathcal{L}$  is defined as the product of the probability of finding a data point at its observed position  $\mathbf{x}_i$

$$\mathcal{L} = \prod_n P(\mathbf{x}_i). \quad (4.22)$$

The Gaussian contributions of  $P(\mathbf{x}_i)$  are

$$P(\mathbf{x}_i) = \sum_k \mathcal{N}(\mathbf{x}_i|\mu_k, \Sigma_k)P(k), \quad (4.23)$$

with  $\mathcal{N}(\mathbf{x}_i|\mu_k, \Sigma_k)$  as the Gaussian distribution with mean  $\mu_k$  and standard deviation  $\Sigma_k$ .  $P(k)$  is the fraction of all data points in  $k$  and can also be interpreted as the number of neutrinos in a flare  $n_{flare}$ .

The individual probabilities for each data point  $i$  to belong to distribution  $k$  are expressed as

$$P(k|i) = \frac{\mathcal{N}(\mathbf{x}_i|\mu_k, \Sigma_k)P(k)}{P(\mathbf{x}_i)}. \quad (4.24)$$

With these equations, it is possible to calculate  $\mathcal{L}$  and the responsibility matrix  $P(k|i)$ , knowing  $\mu_k$ ,  $\sigma_k$ , and  $P(k) = n_{flare}$ . This is called the expectation step (E-step).

*Maximization step* — This step calculates  $\mu_k$ ,  $\sigma_k$ , and  $P(k)$ . It uses the definitions of the mean and the covariance, and includes the appropriate contributing fraction  $P(k|i)$  of each data point to Gaussian  $k$ . The estimation of these values is

$$\hat{\mu}_k = \frac{\sum_n P(k|i)\mathbf{x}_i}{\sum_i P(k|i)}, \quad (4.25)$$

$$\hat{\Sigma}_k = \frac{\sum_i P(k|i)(\mathbf{x}_i - \hat{\mu}_k) \otimes (\mathbf{x}_i - \hat{\mu}_k)}{\sum_i P(k|i)}, \quad (4.26)$$

and thus

$$\hat{P}(k) = \frac{1}{N} \sum_i P(k|i) = n_{flare}. \quad (4.27)$$

Equation (4.25), and Equation (4.27) are the maximization step (M-step).

*Procedure* — The EM algorithm is step by step:

1. Guess starting values for  $\mu_k$ ,  $\sigma_k$ , and  $n_{flare}$ .
2. Repeat the following:
  - E-step to calculate new  $P(k|i)$ , and new  $\mathcal{L}$
  - M-step to determine new  $\mu_k$ ,  $\sigma_k$ , and  $n_{flare}$ .
3. Stop when  $\mathcal{L}$  has converged.

The algorithm stops either after 500 iterations or when the likelihood has not changed in the past 20 iterations.

*Example* — For this analysis I consider only the time dimension and set  $M = 1$ . Future approaches could consider adding the spatial dimension to the time dimension. In this specific case, I look for a single flare; thus, I set the number of Gaussians to  $K = 1$ . By increasing  $K$ , future searches can easily extend this approach to multiple flares. Also, I expect the background to be uniformly distributed. Thus, in this case, the mixture is between a Gaussian (signal) and a uniform background distribution. Hence,  $\mu$  is the mean flaring time,  $\Sigma$  the flare width, and  $t_i$  the time event  $i$  was detected.

The explicit expressions are

$$P(t_i) = U(t_i) + \sum_1^K \mathcal{N}(t_i|\mu_k, \Sigma_k)P(k), \quad (4.28)$$

for the probability to observe a specific data point for a mixture model of a uniform distribution  $U(t_i)$  and Gaussians.

The expected signal with  $n_{flare}$  neutrinos is

$$p_S = \frac{n_{flare}}{N} S(\mathbf{x}_i, \gamma) \times S_{temp}, \quad (4.29)$$

with  $S(\mathbf{x}_i, \gamma)$  comprising the energy and spatial PDFs (see Equation (4.10)). The flare shape is Gaussian,  $S_{temp} = \mathcal{N}(t_i|\mu, \Sigma)$ .

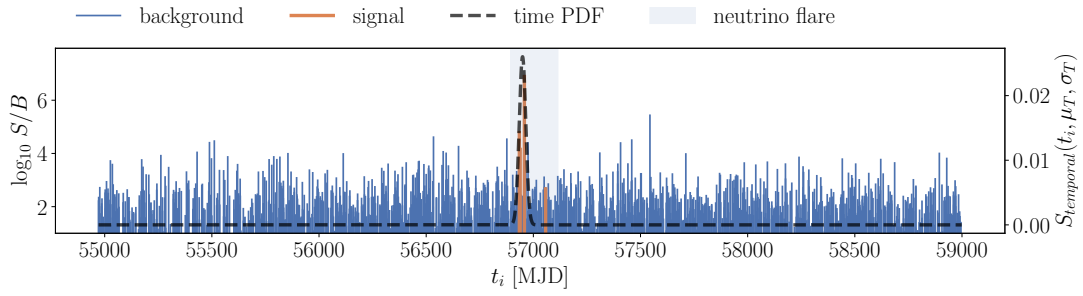


Figure 4.13: EM finds the neutrino flare after 0.38 seconds. The brute-force scan would have lasted several hours.

Similarly, the background is

$$p_B = \left(1 - \frac{n_{flare}}{N}\right) B(\mathbf{x}_i) \times B_{temp}. \quad (4.30)$$

Here,  $B(\mathbf{x}_i)$  comprises the spatial and energy background PDFs (see Equation (4.12)) and  $B_{temp} = \frac{1}{lifetime}$ .

With the mixture model of the signal and background components, the responsibility matrix becomes

$$\begin{aligned} P(k=1|i) &= \frac{p_S}{p_S + p_B} = \frac{\frac{n_{flare}}{N} S(\mathbf{x}_i, \gamma) \mathcal{N}(t_i|\mu, \Sigma)}{\frac{n_{flare}}{N} S(\mathbf{x}_i, \gamma) \mathcal{N}(t_i|\mu, \Sigma) + (1 - \frac{n_{flare}}{N}) B(\mathbf{x}_i) \frac{1}{lifetime}} \\ &= \frac{n_{flare} \frac{S(\mathbf{x}_i, \gamma)}{B(\mathbf{x}_i)} \mathcal{N}(t_i|\mu, \Sigma)}{n_{flare} \frac{S(\mathbf{x}_i, \gamma)}{B(\mathbf{x}_i)} \mathcal{N}(t_i|\mu, \Sigma) + \frac{N - n_{flare}}{lifetime}}. \end{aligned} \quad (4.31)$$

For the example at the beginning of this Section 4.7, EM yields an appropriate time window of the simulated neutrino flare (see Figure 4.13). The computing time was 0.38 seconds.

The resulting mean flare time and the standard deviation of the EM algorithm are then plugged into the likelihood ratio test (Equation (4.20)) for maximization. The framework maximizes the likelihood and gets the best-estimated mean number of signal events  $n_S$  and the energy spectral index  $\gamma$ . The quantity  $n_{flare}$  is only used during EM. The final source strength  $n_S$  is the result of the likelihood maximization. I repeat these steps at each point of the position fit (see Section 4.3).

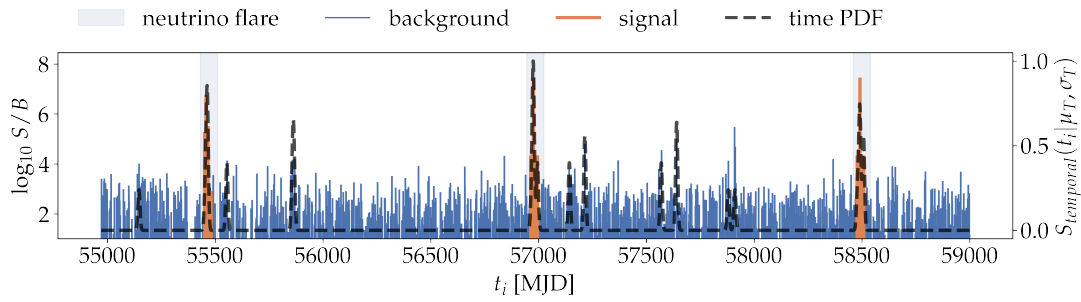


Figure 4.14: EM with multiple ( $K = 100$ ) Gaussian distributions. Many distributions are fit to 0. The three flares (marked with shaded blue) are recovered. Additionally, background fluctuations are found as less significant flares.

*Outlook: Extension to multiple flares* — The EM algorithm can also search for multiple flares. Instead of a single Gaussian time PDF, multiple time PDFs (e.g.,  $K = 100$  Gaussian curves) build the signal assumption. Many of those will become flat and background like, whereas others will describe multiple neutrino flares in the data (see Figure 4.14).

### 4.7.3 Test of the time-dependent analysis

This section presents how well the simulated flare parameters ( $\mu_T, \sigma_T, \mathbf{x}_S, n_S, \gamma$ ) are recovered. I simulate flares with different lengths  $\sigma_T = 10, 55, 100$  days and with different spectral indices  $\gamma = 2.0, 3.0$ . Figure 4.15 and Figure 4.16 show the effect of the fixed source spectral index in the  $S/B$  calculation on the recovery of the mean flare time  $\mu_T$  and the flare width  $\sigma$ . Generally, for a softer emission spectrum, the source needs to emit many more neutrinos to allow a correct recovery of mean flaring time and flare width than for a harder emission spectrum. All plots for parameter recovery are shown in Appendix B.

### 4.7.4 Fitting lower-energetic neutrino flares

The  $S/B$  depends on the source spectral index  $\gamma$  as in Equation (4.10). Assuming a certain value for  $\gamma$  hence disfavors neutrino flares with a different power-law index. This analysis aims to be sensitive to other spectral indices, i.e., softer ones, as well. To achieve this, the framework evaluates the event  $S/B$  for different source spectral indices and starts the flare fitting procedure for every spectral index. In the end, the highest test statistic value is the result. The scan over these spectral indices only affects the best fitted time parameter since  $\gamma$  is once more optimized in the final likelihood maximization fit.

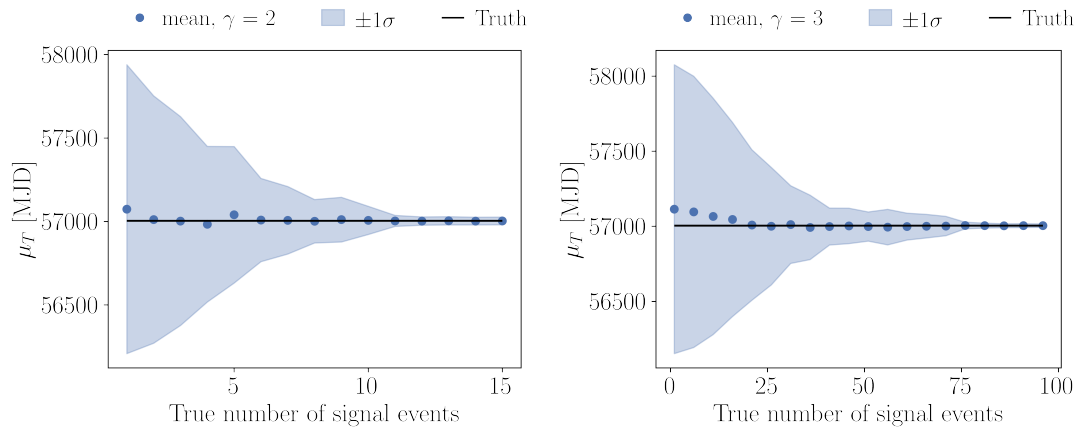


Figure 4.15: Recovery of mean flaring time  $\mu_T$  with increasing flare strength (x-axis). The simulated flare has a width of  $\sigma_T = 55.18$ . The black line shows the truth. The blue dots depict the fitted mean value and the shaded blue region is  $\pm 1\sigma$ . **Left:** Neutrino flare with  $\gamma = 2.0$ . The fit finds the mean flare time for a reasonably strong neutrino flare. For strong flares with  $n_S > 10$ , the mean flaring time is recovered in nearly all cases. **Right:** Neutrino flare with  $\gamma = 3.0$ . The required neutrino emission is much higher (around 50 neutrinos) for a reliable estimation of the mean flaring time.

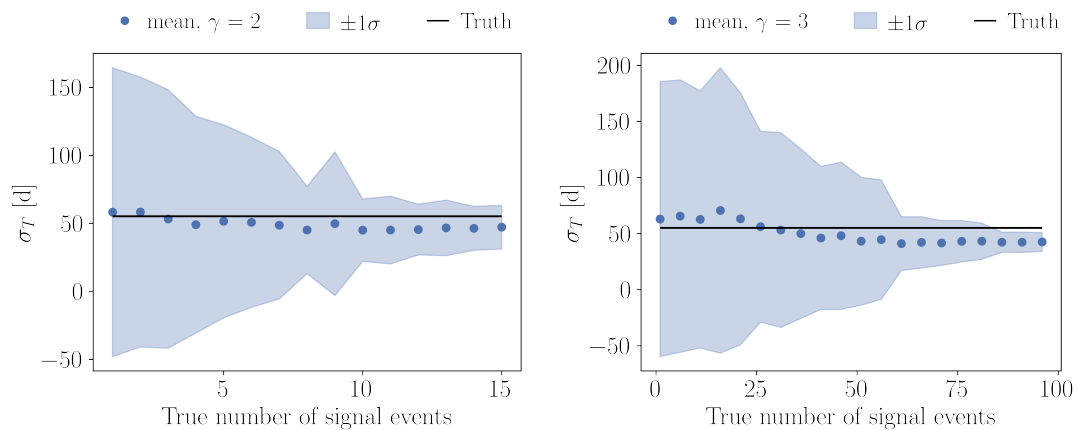


Figure 4.16: Recovery of flare width  $\sigma_T$  with increasing flare strength (x-axis). The simulated flare had  $\sigma_T = 55.18$ . The black line shows the truth. The blue dots depict the fitted mean value and the shaded blue region is  $\pm 1\sigma$ . **Left:** Neutrino flare with  $\gamma = 2.0$ . The fit finds the flare width for a reasonably strong neutrino flare (e.g. for  $n_S \geq 10$ ). There is a slight bias towards shorter flares. **Right:** Neutrino flare with  $\gamma = 3.0$ . The width is only recovered for very strong neutrino emission (around 60 neutrinos).

The steps to calculate a test statistic value for the time dependent analysis are

1. Divide the alert uncertainty region into steps of  $0.2^\circ$ .
2. Select one position.
3. Calculate  $S/B$  for a specific spectral index.
4. Run EM and determine best fit  $\mu_T$  and  $\sigma_T$ .
5. Use  $\mu_T$  and  $\sigma_T$  for the temporal signal PDF of the  $TS$  (Equation (4.20)). Optimize for  $n_S$  and  $\gamma$ .
6. Repeat steps 3. to 5. for different spectral indices in range  $[1.5, 4]$  with steps of  $0.2$ .
7. Repeat steps 2. to 6. for the remaining positions in the alert uncertainty region.
8. Choose the highest test statistic value from the above steps.

The outcome is precisely one  $TS$  value, independent of the in-between evaluations of the uncertainty region and the source spectral index. Hence, the look-elsewhere effect is intrinsically corrected by choosing the highest test statistic value resulting from the described procedure. This results in a shift of the test statistic distribution to higher values because of background fluctuations.

#### 4.7.5 Effect of the spectral index scan on parameter recovery

The scan of spectral indices improves how well the flare parameters are recovered for soft flares ( $\gamma = 3.0$ ). The mean flaring time is recovered more reliably for weaker neutrino emission ( $\approx 27$  neutrinos) compared to the case without a spectral index scan ( $\approx 40$  neutrinos) (see Figure 4.17). The flaring width scatters less and is also more reliably recovered for weaker neutrino emission ( $\approx 30$  neutrinos) compared to the case without the spectral index scan ( $\approx 60$  neutrinos) (Figure 4.18). This also lowers the required emission of a neutrino source such that it can be detected with this analysis (see Section 4.10). Thus, the spectral index scan improves parameter recovery and the sensitivity of the analysis.

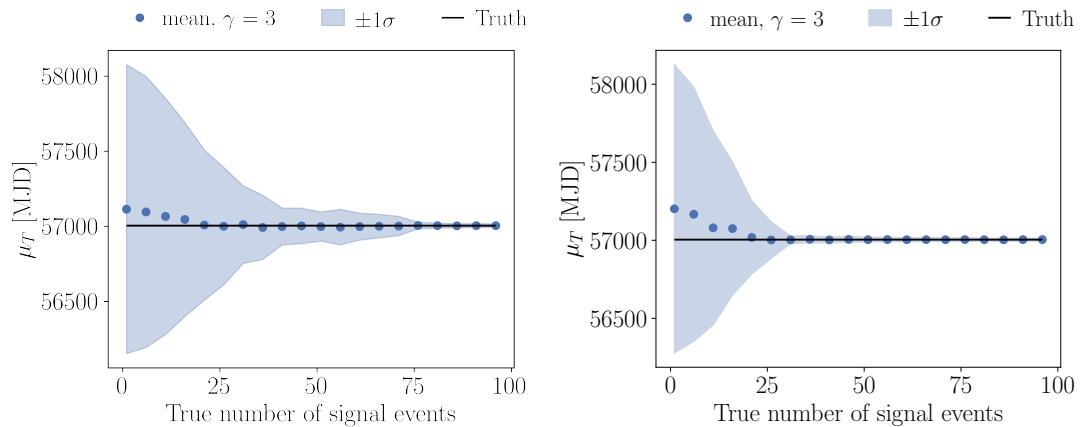


Figure 4.17: Recovery of mean flaring time  $\mu_T$  with increasing flare strength (x-axis). The simulated flare had  $\sigma_T = 55.18$  and  $\gamma = 3$ . The black line shows the truth. The blue dots depict the fitted mean value and the shaded blue region is  $\pm 1\sigma$ . **Left:** Recovery of mean flare time with no spectral index scan. A strong signal of  $\sim 40$  neutrinos is required for a reliable recovery. **Right:** Recovery with spectral index scan. The mean flare time is already accurately and reliably determined for  $\approx 27$  neutrinos.

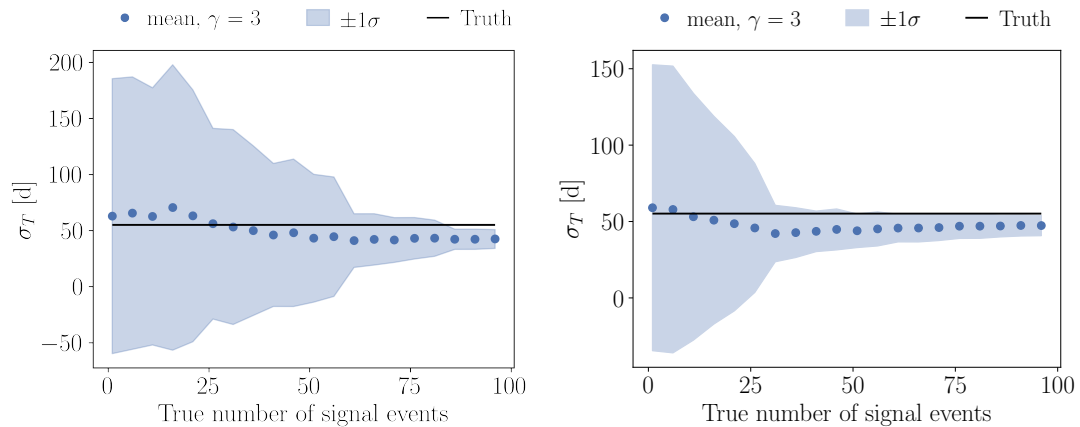


Figure 4.18: Recovery of flare width  $\sigma_T$  with increasing flare strength (x-axis). The simulated flare had  $\sigma_T = 55.18$  and  $\gamma = 3$ . The black line shows the truth. The blue dots depict the fitted mean value, and the shaded blue region is  $\pm 1\sigma$ . **Left:** Recovery of the flare width  $\sigma_T$  without the spectral index scan. The fit finds the flare width for an emission of  $\approx 60$  neutrinos. There is a slight bias towards shorter flares. **Right:** Recovery of the flare width  $\sigma_T$  with the spectral index scan. The fit recovers the parameter more reliably already when  $\approx 30$  neutrinos are emitted. There is a slight bias towards short flares.

## 4.8 Significance calculation

The p-value is the probability of observing the resulting test statistic value given the null hypothesis – fluctuations from the atmospheric and diffuse astrophysical background. It is calculated by comparing the observed test statistic value  $TS_{obs}$  with the background test statistic distribution. The fraction of values exceeding  $TS_{obs}$  with respect to the entire distribution defines the p-value  $p_0$

$$p_0(TS_{obs}) = \int_{TS_{obs}}^{\text{inf}} p(TS|H_0) dTS, \quad (4.32)$$

with  $p(TS|H_0)$  as the PDF of the test statistic with true null hypothesis  $H_0$ . These p-values are calculated by mimicking background data and running the analysis on background. Background is generated by randomizing the right ascension  $\alpha$  for all events. IceCube analyses reject  $H_0$  if the p-value is smaller than  $p_0 = 2.87 \times 10^{-7}$ . This corresponds to the one sided  $5\sigma$  threshold.

## 4.9 Trial correction

This analysis evaluates 122 positions in the sky and reports the most significant one. The significance of a source has to be corrected for the probability to find a respective p-value by chance due to background fluctuations – the look elsewhere effect. To correct this, I take the best local p-value out of  $N_{sources} = 122$  sources for  $N_{trials} = 10^4$  trials. These  $N_{trials}$  p-values build the background p-value distribution. The chance to get the true p-value  $p_{local}$  as a result of background (global p-value  $p_{global}$ ) is hence the significance of the true p-value with respect to the background local p-value distribution. Analytically, the expression for the global p-value is [115]

$$p_{global} = 1 - (1 - p_{local})^{N_{sources}}. \quad (4.33)$$

## 4.10 Sensitivity and discovery potential

The sensitivity of an analysis is the source flux for which the p-value is smaller than 0.5 in 90% of the cases. The  $3\sigma$  discovery potential is the source flux for which the p-value is less than  $3\sigma = 1.35 \times 10^{-3}$  in 50% of the cases. The  $5\sigma$  discovery potential is the same for a p-value smaller than  $< 5\sigma = 2.867 \times 10^{-7}$ .

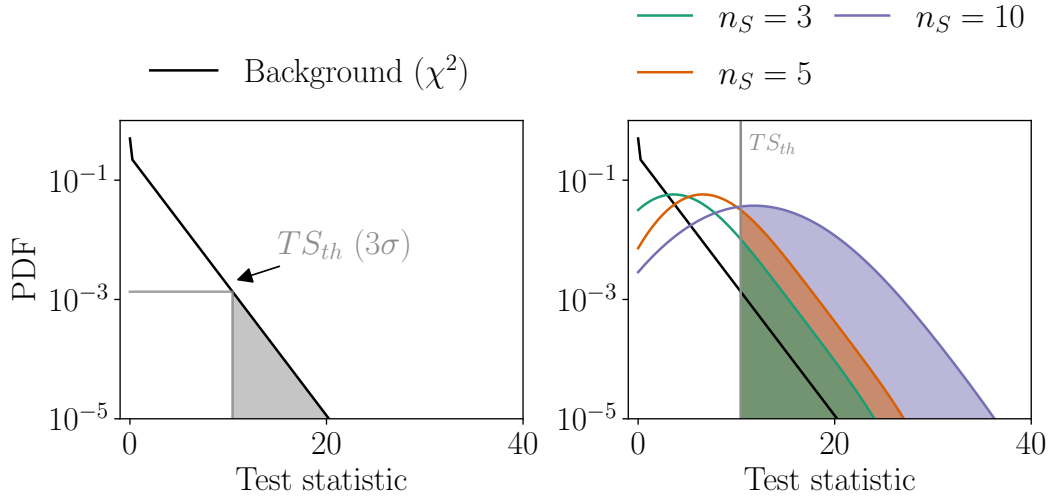


Figure 4.19: Concept of  $3\sigma$  discovery potential. **Left:** The threshold value  $TS_{th}$  is the 0.99865 ( $3\sigma$ ) quantile of the background test statistic distribution. **Right:** The  $3\sigma$  discovery potential is the source flux for which the median of the signal test statistic distribution corresponds to  $TS_{th}$ .

Figure 4.19 shows an example of the calculation of the  $3\sigma$  discovery potential. The threshold test statistic value  $TS_{th}$  is the test statistic value corresponding to a p-value of  $3\sigma$ , hence the 0.99865 quantile. Then it is relevant what percentage of different signal test statistic distributions lie above  $TS_{th}$ . The discovery potential is the signal flux where 50% of the signal test statistic distribution exceeds  $TS_{th}$ . The same concept applies to the calculation of the sensitivity. There,  $TS_{th}$  is the background test statistic median, and 90% of the signal test statistic distribution needs to have higher values.

Figure 4.20 shows the construction of sensitivity and discovery potential for the time-integrated alert follow-up. The number of signal neutrinos translates into a flux with Equation (3.5)

$$\phi_{100\text{TeV}} = \frac{n_S}{\int dt dE_\nu A_{eff}(E_\nu) \left(\frac{E_\nu}{100\text{TeV}}\right)^{-\gamma}}. \quad (4.34)$$

The mean number of signal neutrinos of 6.2 and 9.4 neutrinos correspond to a flux of  $2.79 \times 10^{-20} (\text{TeVcm}^2\text{s})^{-1}$  and  $4.23 \times 10^{-20} (\text{TeVcm}^2\text{s})^{-1}$  normalized at 100 TeV. The respective fluxes for all source candidates are depicted in Figure 4.21. The required flux depends on the source declination and the source uncertainty region. Larger uncertainties require a stronger flux.

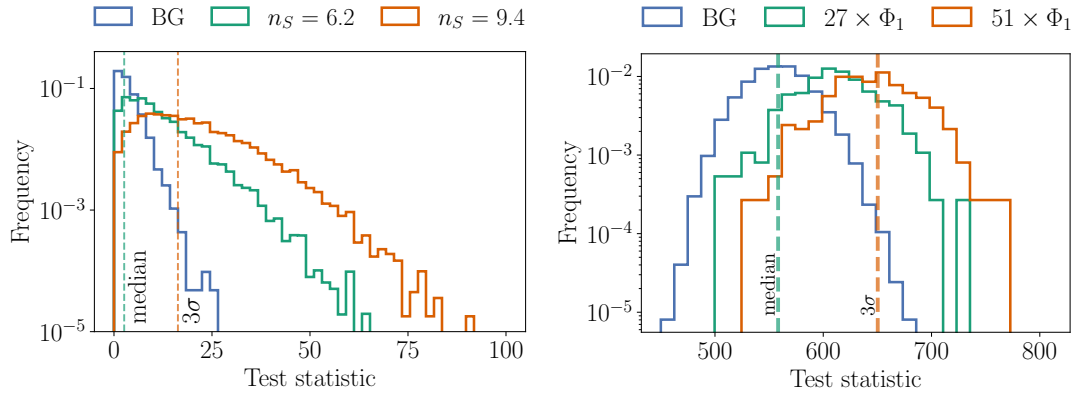


Figure 4.20: Test statistic distributions of background, sensitivity and discovery potential flux for the time integrated alert follow-up. **Left:** Test statistic distributions of background, sensitivity and discovery potential flux for the position of IceCube-170922A. **Right:** Test statistic distributions of background, sensitivity and discovery potential flux for the stacked analysis. The signal is a number of sources (27 and 51) with the flux  $\phi_{1,100\text{TeV}} = 4.502 \times 10^{-18}$  ( $\text{TeV}^{-1}\text{cm}^{-2}\text{s}^{-1}$ ).  $\phi_{1,100\text{TeV}}$  corresponds to the flux of one neutrino from TXS 0506+056 in 11 years at an energy of 100 TeV with  $\gamma = 2$ .

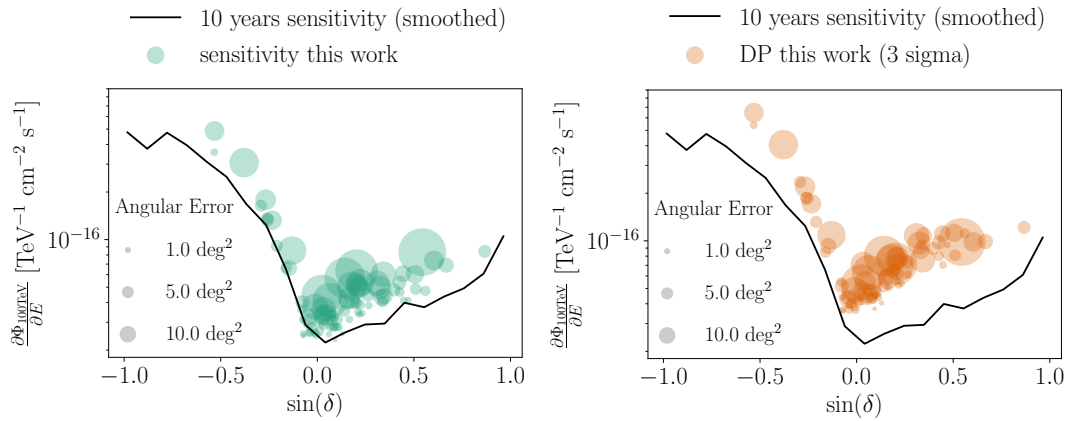


Figure 4.21: Sensitivity (**left**) and discovery potential (**right**) for time-integrated individual search vs. source declination. The respective fluxes depend on the source declination and the size of the angular uncertainty region. The source flux has to be stronger in the south due to the high background. IceCube is most sensitive at the horizon. Sources with a large uncertainty region require a stronger flux than sources with a small uncertainty region. The black line shows the sensitivity for a previous IceCube analysis on 10 years of data [55].

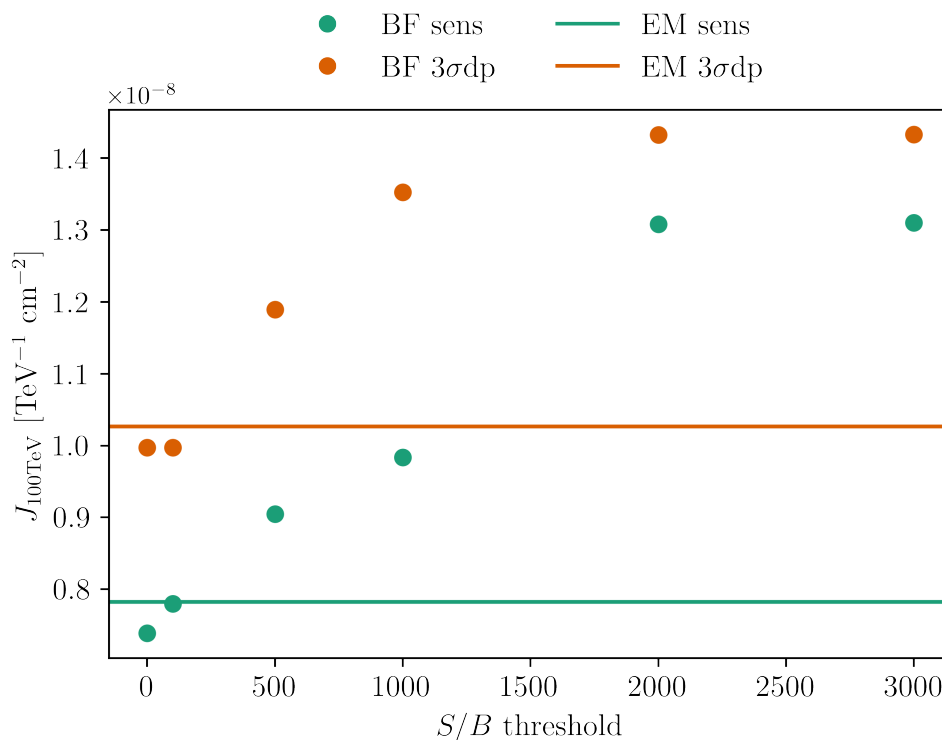


Figure 4.22: This plot compares how different thresholds for the brute-force flare search in Section 4.7.1 perform compared to expectation maximization. Expectation maximization has a similar sensitivity and discovery potential as a brute-force search with a  $S/B$  threshold of  $\sim 100$ .

For time-dependent sources, the total neutrino emission during a flare is relevant. A suitable expression for sensitivity and discovery potential is the flux integrated over flaring time — the fluence

$$J_{100\text{TeV}} = \int \phi_{100\text{TeV}}(t) dt, \quad (4.35)$$

where the emission is Gaussian distributed. The sensitivity and discovery potential vary depending on the neutrino flare properties. The example location is IceCube-170922A ( $\alpha = 77.36^\circ, \delta = 5.69^\circ$ ) unless mentioned otherwise. First, Figure 4.22 compares the performance of expectation maximization with the previous brute-force flare-fitting approach (see Section 4.7.1). This comparison was done on only a subsample of the data. Expectation maximization achieves low sensitivity and discovery potential fluences, similar to a brute-force scan with a  $S/B$  threshold of  $\sim 100$ .

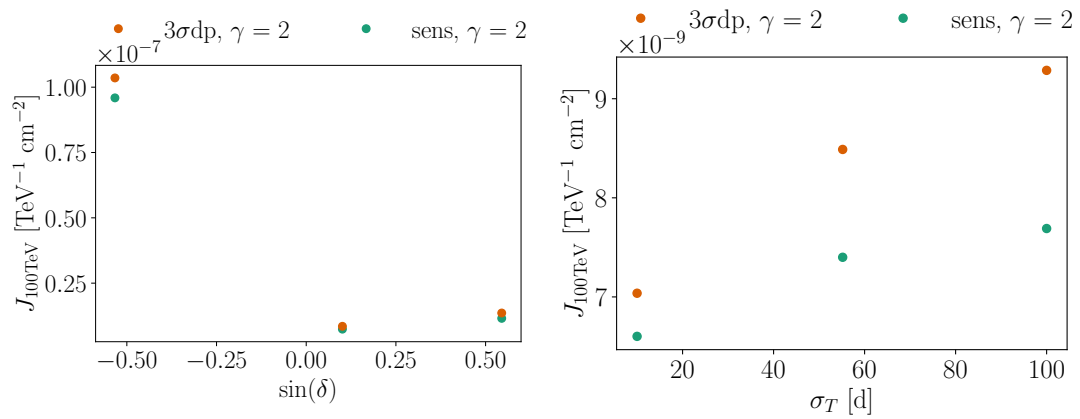
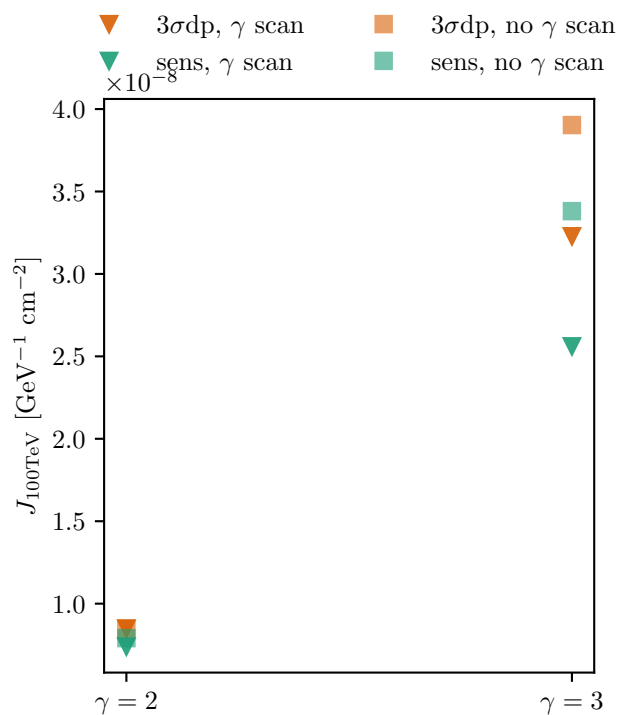


Figure 4.23: The sensitivity (green) and discovery potential (orange) for the time-dependent analysis. **Left:** Sensitivity and discovery potential fluences vs. the sine of source declination. The figure shows three sources at different declinations ( $\sim \pm 33^\circ, 5^\circ$ ). The declination dependency is the same as for the time integrated case in Figure 4.21. **Right:** Sensitivity and discovery potential of a single source at declination  $+5.69^\circ$  vs. the width of the time PDF  $\sigma_T$ . The required integrated flux is lower for shorter flares and rises with flare duration.

Figure 4.23 shows the time-dependent sensitivity and discovery potential for different declinations on the left. The declination dependency is similar to the time-integrated case in Figure 4.21. The right shows the dependency on the flare width  $\sigma_T$ . Longer flares require a stronger flux than shorter ones.

Another dependency is the spectral index of neutrino emission. I assume a power-law  $\propto E^{-\gamma}$ . Signal that follows a harder emission spectrum requires a lower fluence for detections, whereas softer emission is more similar to background and needs a higher emission. Figure 4.24 shows the dependency of the necessary fluences on the source spectral index. The spectral index scan (see Section 4.7.4) improves the sensitivity and discovery potential fluences for soft source spectra, whereas it does not significantly worsen the sensitivity and discovery potential fluences for hard emission spectra.

Figure 4.24: Sensitivity and discovery potential for a flare with  $\sigma_T = 55.18$  days. The x-axis shows the spectral index of the source emission spectrum  $\propto E^{-\gamma}$ . A source with a harder emission spectrum requires a weaker fluence for detections. A source with a softer emission spectrum is more similar to background and needs a higher fluence. The spectral index scan (see Section 4.7.4) improves the sensitivity and discovery potential fluences for soft spectra (squares vs. triangles), whereas it does not significantly worsen the fluences for hard signal emission.



## 4.11 Flux limit calculation

Upper flux limits can be calculated similarly to sensitivity and discovery potentials (Section 4.10). Here, the resulting test statistic value of the analysis is the test statistic threshold value  $TS_{th}$ . The flux limit with 90% confidence level,  $\Phi_{90\%}$ , is hence the flux of a source where 90% of its signal test statistic distribution exceeds  $TS_{th}$ .

## 4.12 Confidence regions of fitted parameter

Another likelihood ratio test evaluates the compatibility of the fitted parameters  $n_{S,fit}, \gamma_{fit}$  with experimental data

$$\Lambda_{param} = -2 \ln \left( \frac{\mathcal{L}(n_S = n_{S,fit}, \gamma = \gamma_{fit})}{\sup_{n_S \neq n_{S,fit}, \gamma \neq \gamma_{fit}} \mathcal{L}(n_S, \gamma)} \right). \quad (4.36)$$

Assuming Wilks' theorem, the p-values for the parameter are described by a  $\chi^2_2$  distribution with two degrees of freedom [126]. P-values smaller than  $X\%$  can be rejected. The resulting level curve is the fitted source parameter's  $X\%$  confidence level contour.

## Chapter 5

# Search for neutrino sources – results and discussion

In this work, I investigate neutrino emission from the direction of IceCube high-energy alerts (see Section 3.3). In total, 122 high-energy events and their reconstruction uncertainties define areas of interest. A list of all events is in Table A.1. Figure 5.1 shows their reconstructed origin directions and their 90% confidence region. The first part of this chapter describes the results of the search for steady neutrino emission. The results differ from the ones reported in [141] since the alert selection and data have been updated. The second part presents the outcome of the search for transient neutrino emission. In total, I search for neutrino emission in 11 years of IceCube neutrino-induced through-going muon data. If not explicitly stated, all flux and fluence values refer to the combined muon-neutrino and muon-antineutrino flux.

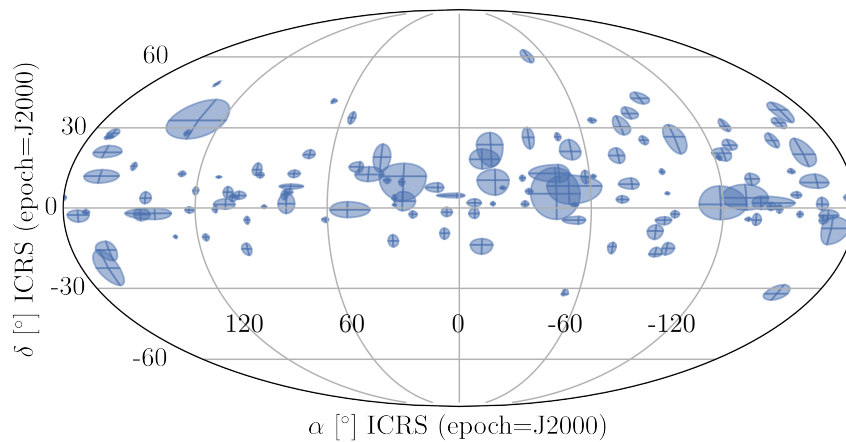


Figure 5.1: Sky map of all high-energy IceCube alerts. The shaded blue region indicates the 90% confidence region for the reconstructed origin direction. At each position, this work searches for additional steady and transient neutrino emission.

## 5.1 Search for continuous neutrino sources

First, I search for time-integrated neutrino emissions over the whole data-taking period of 11 years (see also Table 3.1). This analysis is sensitive to sources that continuously emit neutrinos or that emit neutrinos over an extended period of several years.

### 5.1.1 Single steady sources

As a first hypothesis, I test if there is steady low-energetic neutrino emission coming from the direction of IceCube alert events. A discovery of such an emission would show that high-energy neutrino sources also produce a lower-energy part. The case of non-discovery shows that these objects are mainly bright in high-energy neutrinos. A very hard power law of e.g.  $E^{-\leq 1}$ , as expected in some models (see for example [142, 143]), folded with the IceCube effective area (see Figure 3.6) would for example result in single high-energy events. In this analysis, I find the most significant local p-value  $p_{local} = 0.015$ , which corresponds to a global p-value of  $p_{global} = 0.98$ . Hence, this result is compatible with the background hypothesis of no steady low-energy emission. Table C.1 lists the results for all alert positions.

Figure 5.2 shows the location of the most significant spot. The corresponding alert event has a reconstructed uncertainty region in right ascension extending over  $\sim 10^\circ$  (see also Figure 5.3). The best-fit position is within one degree of the original reconstructed alert position.

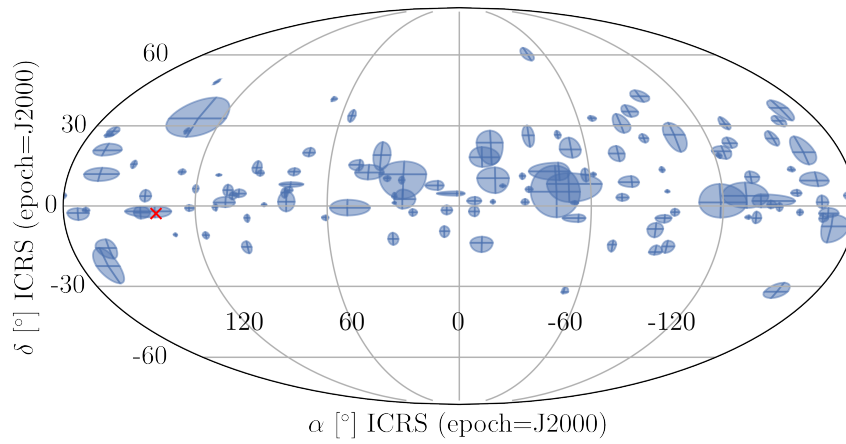


Figure 5.2: Sky map of all high-energy IceCube alerts. The shaded blue region indicates the 90% confidence region for the reconstructed origin direction. The red cross shows the position of the most significant neutrino emission for the time-integrated analysis.

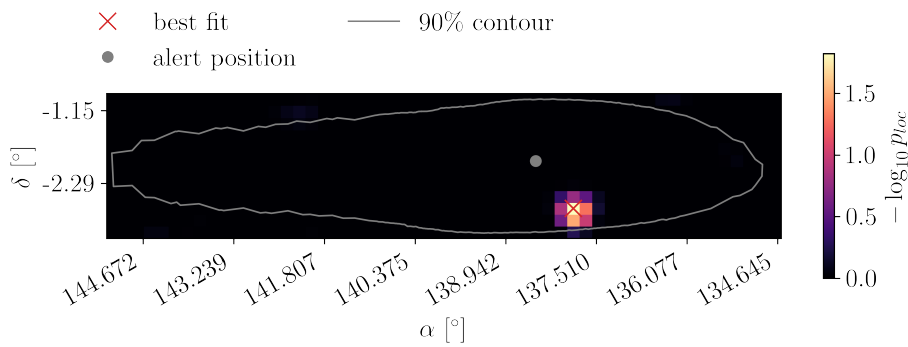


Figure 5.3: P-value map of the most significant spot for the time-dependent analysis. The grey dot shows the original reconstructed alert position, the red cross shows the best-fit position.

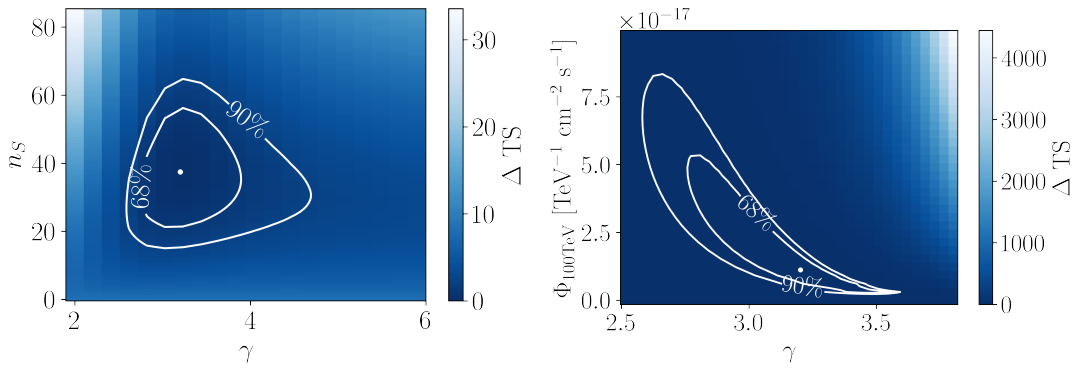


Figure 5.4: Conditional change of the test statistic value when varying parameter of the likelihood. **Left:** Variation of  $TS$  when changing values of  $n_S$  and  $\gamma$ . The errors of the 68% contour are  $n_S = 37_{-16}^{+19}$  and  $\gamma = 3.2 \pm 0.4$ . **Right:** Difference of  $TS$  when varying the signal flux  $\Phi_{100\text{TeV}}(n_S, \gamma)$ . The error of the 68% contour are  $\Phi_{100\text{TeV}} = 1.1_{-0.8}^{+4.2} \times 10^{-17} (\text{TeV cm}^2 \text{ s})^{-1}$ .

In the following, I shortly investigate the most significant spot of this analysis to check if all properties agree with a background-like scenario. For the most significant position, the best-fit values of the likelihood maximization are  $n_S = 37_{-16}^{+19}$  and  $\gamma = 3.2 \pm 0.4$  (see left of Figure 5.4 for the likelihood contours and Section 4.12 for the determination of the uncertainties). The corresponding flux normalized at 100 TeV is  $\Phi_{100\text{TeV}} = 1.1_{-0.8}^{+4.2} \times 10^{-17} (\text{TeV cm}^2 \text{ s})^{-1}$ . These parameters are biased compared to the true signal parameters, as was shown in Section 4.5. Hence derivations about the source flux from these fit parameters must be treated with caution. The upper flux limit on the muon flux (90% confidence level) is  $\Phi_{90\%,100\text{TeV}} = 6.9 \times 10^{-17} (\text{TeV cm}^2 \text{ s})^{-1}$  (see also Table C.1).

Next, I investigate the region around the hot spot for source candidates. The left of Figure 5.5 shows blazar candidates in the vicinity (radius of  $1^\circ$ ) of the best-fit position. Potential candidates for neutrino emission are objects 1 (PKS 0907-023), 2 (MQ J091113.84-020745.2), and 3 (3HSP J091408.3-015945). Object 4 (CRATES J091112-020740) misses information about radio and X-ray emission for further evaluation. However, when looking at the expected spatial clustering from background and signal events (based on the fitted signal flux), the measured data does not agree well with the fit and does not cluster around the source position (see right of Figure 5.5). This is also an indication that this hot spot is probably the result of background fluctuations.

As a further step, I investigate the p-values and fit parameters of all analyzed positions. When looking at the distribution of all local p-values (as listed in Table C.1), they resemble a uniform distribution, which is expected for background-like data (see

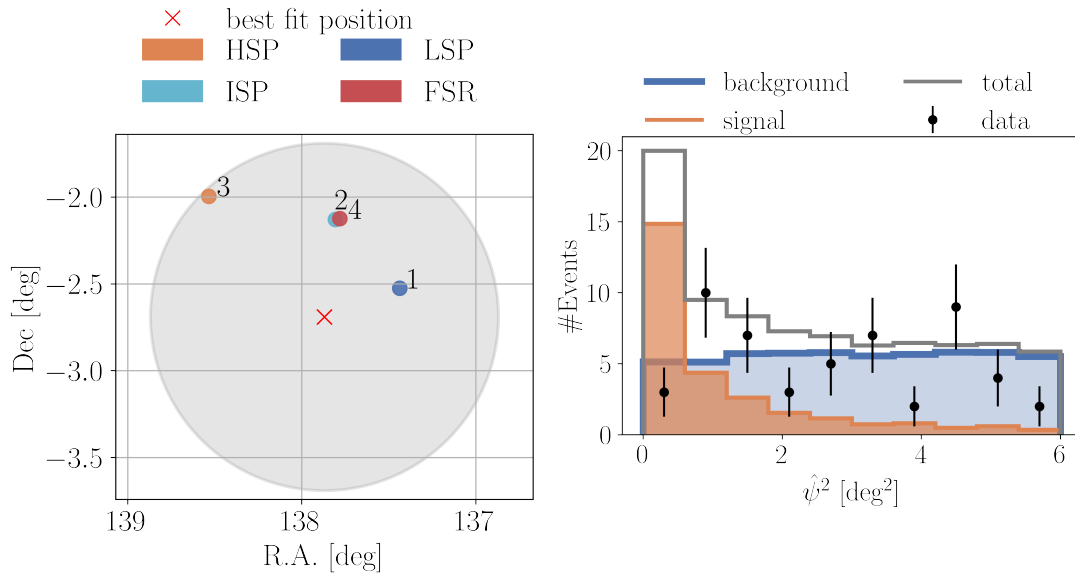


Figure 5.5: **Left:** Known and candidate blazars in the vicinity (radius of  $1^\circ$ , grey circle) of the best-fit position from VOU-Blazars [144]. Orange symbols show high synchrotron peaked blazar candidates, light blue shows intermediate synchrotron peaked blazar candidates, dark blue indicates low synchrotron peaked blazar candidates, and dark red marks a flat spectrum radio source without a match in radio/X-ray catalogs. Candidates for neutrino emission are objects 1 (PKS 0907-023), 2 (MQ J091113.84-020745.2), and 3 (3HSP J091408.3-015945). **Right:** Squared angular distance between the best-fit position and reconstructed event origin direction. The background (blue) is scrambled data in right ascension and the signal (orange) is from Monte Carlo simulations (for the fitted values of  $n_S = 37$  and  $\gamma = 3.2$ ). The grey line shows the expectation of background and signal combined. The data points (black) do not agree with the expectation of background + signal.

left of Figure 5.6). The right of Figure 5.6 shows the fitted  $n_S$  plotted against the local p-values. High  $n_S$  are more often found for more significant local p-values, which is also expected behavior from background fluctuations. Figure 5.7 displays the local p-values vs.  $\gamma$  on the left. There is no correlation of spectral indices  $\gamma$  with p-values. The right of Figure 5.7 plots  $n_S$  vs.  $\gamma$ . High numbers of signal neutrinos  $n_S$  are associated with a softer spectral index and stay background-like. Overall, all distributions agree with the hypothesis of no steady lower-energy neutrino emission. I constrain the maximally expected neutrino flux additional to the alert events from these directions and show the results in Figure 5.8 and in Table C.1.

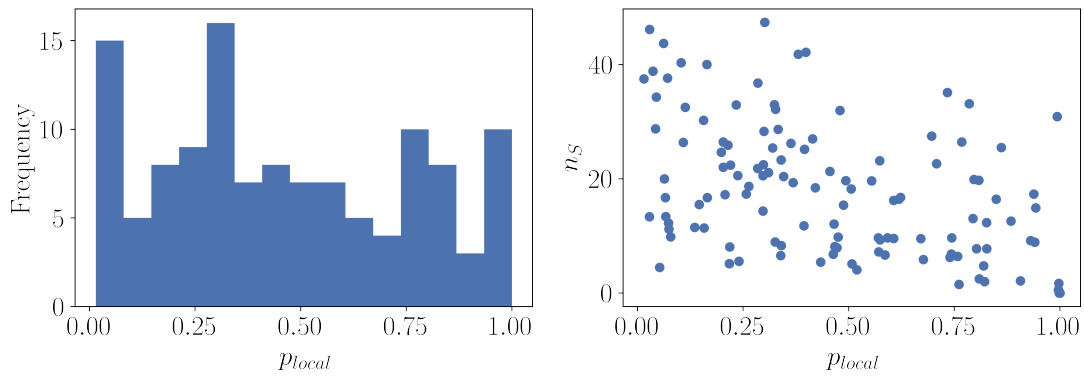


Figure 5.6: **Left:** The distribution of local p-values from the time-integrated search. The distribution agrees with a uniform distribution that would be expected from background data. **Right:** P-value distribution vs. the fitted  $n_S$  values. There is a slight tendency for strong  $n_S$  to be associated with lower p-values, which is also expected behavior from background fluctuations.

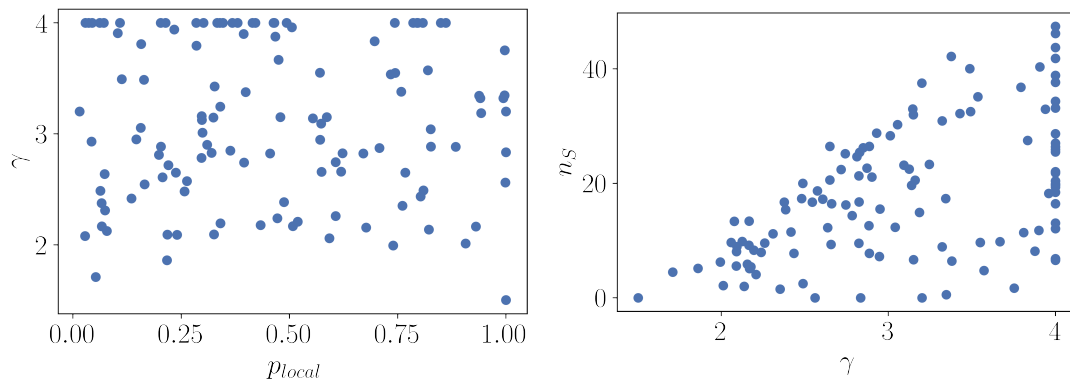


Figure 5.7: **Left:** P-value distribution vs. the fitted  $\gamma$  values. There is no correlation between p-values and the spectral indices. The highest allowed value for  $\gamma$  was 4. **Right:** The fitted spectral indices  $\gamma$  vs. the fitted  $n_S$ . Softer emissions with a higher spectral index can include more signal neutrinos while still agreeing with background.

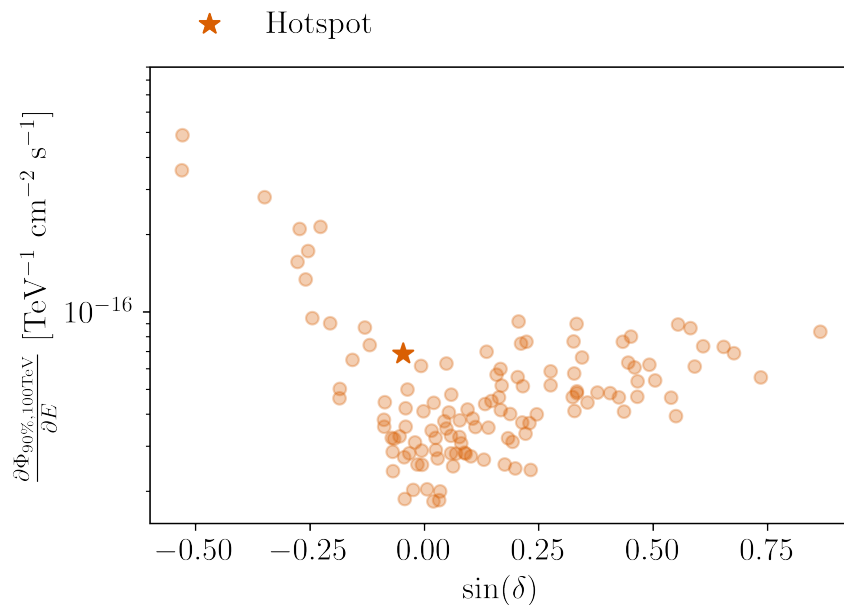


Figure 5.8: The 90% confidence level upper flux limit  $\Phi_{90\%,100\text{TeV}}$  for all alert positions as listed in Table C.1 plotted vs. the sine of their declination. The declination dependency is the same as in Section 4.10. The upper flux limit for the most significant position is marked by a star.

### 5.1.2 Multiple steady sources — stacking

Another possible source scenario is that a single source emits a signal too weak to be detected. However, if there are many sources emitting a weak signal, the combined signal from all sources could be significant compared to only background emission. For this, I stack all sources together and treat them as one (see Equation (4.13) in Section 4.4). The p-value for a combined emission of all source candidates is 8%. This is still compatible with the background hypothesis of no additional steady low-energy emission. However, I constrain the maximally combined flux from all source positions in the following.

The 90% confidence level upper flux limit,  $\Phi_{90\%,100\text{TeV}}$ , (see Section 4.11) is calculated by adding sources with a flux of  $\phi_1 = 4.502 \times 10^{-18} (\text{TeVcm}^2\text{s})^{-1}$ , corresponding to the flux of one neutrino from TXS 0506+056 in 11 years with a spectral index of  $\gamma = 2$ . The upper limit of the low-energy emission additional to the detected alert events is  $\Phi_{90\%,100\text{TeV}} = 4.2 \times 10^{-16} (\text{TeV cm}^2 \text{ s})^{-1}$ . The energy range in which this flux limit is valid is determined by the true energy of the Monte Carlo signal events. The central 90% of the Monte Carlo true energies range from 4.2 TeV to 3.6 PeV. The left of Figure 5.9 compares the upper flux limit with the diffuse flux, which is

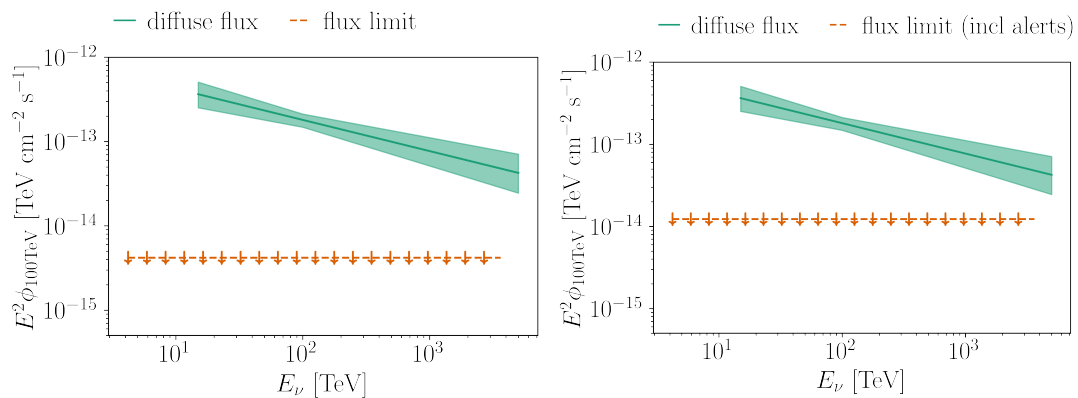


Figure 5.9: **Left:** 90% confidence level upper flux limit for stacked source candidates for the combined lower-energy emission of all source candidates (depicted in orange, energy ranges from 4.2 TeV to 3.6 PeV). The upper flux limit is 1.6% of the astrophysical diffuse flux [145] (green, energy ranges from 15 TeV to 5 PeV) in the overlapping energy range. **Right:** 90% confidence level upper flux limit for stacked source candidates for the total emission of all source candidates including the high-energy alert events (depicted in orange, energy ranges from 4.2 TeV to 3.6 PeV). The upper flux limit is 4.6% of the astrophysical diffuse flux [145] (green, energy ranges from 15 TeV to 5 PeV) in the overlapping energy range.

$\Phi_{diffuse} = 1.44 \times 10^{-15} \text{ (TeV cm}^2 \text{ s)}^{-1}$  (energy range from 15 TeV to 5 PeV) [145]. When integrating both fluxes over their overlapping energy range, I find that the upper flux limit accounts for 1.6% of the diffuse flux. This concerns the lower-energy flux, excluding the alert events.

However, this does not quantify the total expected flux from all positions where high-energy neutrino events have been observed. This can be calculated by including the alerts in the data and determining the respective  $TS$  value. The new stacked test statistic value as in Equation (4.13) including the alert events is then the new threshold for the upper flux limit calculation. The flux limit including the alert events is  $\Phi_{90\%,100\text{TeV}} = 1.2 \times 10^{-15} \text{ (TeV cm}^2 \text{ s)}^{-1}$  for a spectral index of  $\gamma = 2$  and energies between 4.2 TeV and 3.6 PeV. The right of Figure 5.9 shows the upper flux limit of the total contribution (including the alerts) from the origin direction of the alert events together with the astrophysical diffuse flux. When integrating over the overlapping energy range, I find a maximal contribution (with 90% confidence level) of 4.6%.

## 5.2 Search for transient neutrino sources

The final part of this analysis searches for time-dependent neutrino emission similar to what was found in [16], i.e. I assume a Gaussian-shaped neutrino emission with a minimal  $\sigma_T = 5$  days. However, I have developed a new method (see Section 4.7.2.3) and apply my analysis to updated data with respect to previous analyses. The most significant time-dependent neutrino emission in my transient analysis has a local p-value of  $p_{local} = 0.14\% = 2.988\sigma$ . The corresponding neutrino flare is a re-discovery of the neutrino flare reported in [16]. In [16], the analysis was triggered by the high-energy alert IceCube-170922A and it suggested TXS 0506+056 as a neutrino source. All other alert positions do not yet show similar low-energy emission, which indicates that potential sources are mainly associated to high-energy neutrinos. This further highlights the uniqueness of TXS 0506+056, since it is the primary neutrino emitter in my analysis and no other position shows similar behavior. Figure 5.10 shows the origin direction of the neutrino flare.

The flare properties of my analysis agree with the neutrino flare published in [16] (see also Figure 5.11). I find a mean flare time of  $\mu_T = 57001_{-44}^{+52}$  MJD, and  $\sigma_T = 64_{-15}^{+58}$  days (see Figure 5.12 for the time uncertainty estimation). Comparing this further with previous analyses, this work's local p-value is more significant than the local significance of the neutrino flare published in [98]. Since the publication in [16] and [98] the data sample has been updated with improved directional and energy reconstruction.

When correcting for the look-elsewhere effect (see Section 4.9), the global p-value is  $p_{global} = 0.156$ . Hence, the excess does not appear significant since this work adds penalization for investigating all alert positions. In [135], the authors search for time-dependent neutrino emission at all possible points in the whole sky and find the neutrino flare associated with TXS 0506+056 as the second most significant position in the northern sky. The results for all position are listed in Table D.1, and the time-dependent local p-value distribution of all alerts and plots of local p-values vs. fit parameters can be found in Appendix D.1.

The best-fit parameters of the likelihood maximization can yield insights about the measured emission. The best-fit values of the likelihood maximization are  $n_S = 12_{-6}^{+9}$  and  $\gamma = 2.3 \pm 0.4$  (see left of Figure 5.13). The corresponding fluence,  $J_{100\text{TeV}} = \int_{t_{start}}^{t_{end}} \Phi_{100\text{TeV}} dt$ , normalized at 100 TeV, is  $J_{100\text{TeV}} = 1.2_{-0.8}^{+1.1} \times 10^{-8} (\text{TeV cm}^2)^{-1}$ . The values differ slightly from [16], where  $J_{100\text{TeV}} = 2.1_{-0.7}^{+0.9} \times 10^{-8} (\text{TeV cm}^2)^{-1}$  and  $\gamma = 2.1 \pm 0.2$ . This agrees with the reduced significance and updated data between [16], [98],

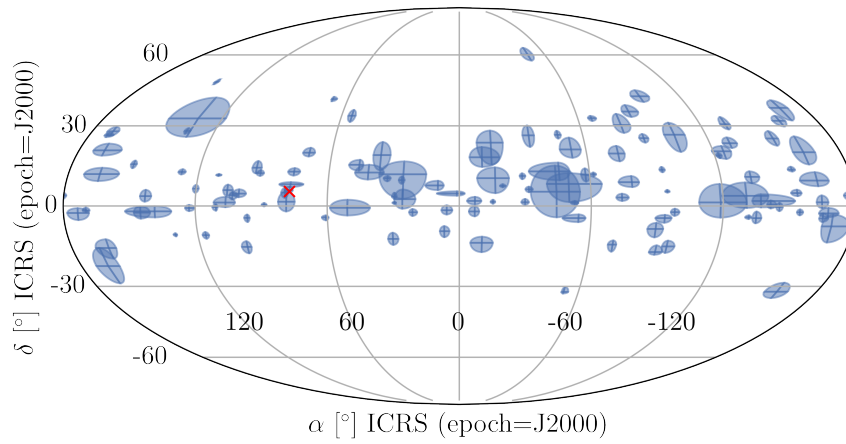


Figure 5.10: Sky map of all high-energy IceCube alerts. The shaded blue region indicates the 90% confidence region for the reconstructed origin direction. The red cross shows the position of the most significant neutrino emission for the time-dependent analysis (at the position of TXS 0506+056).

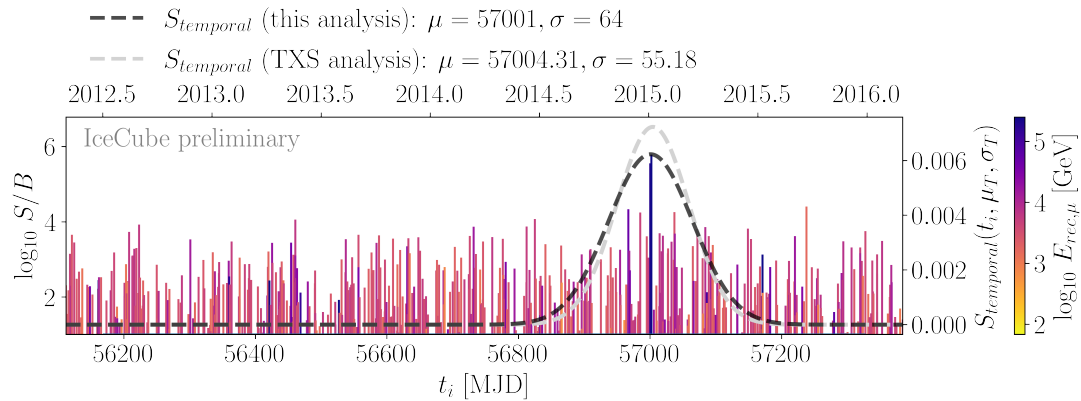


Figure 5.11: The  $\log_{10} S/B$  distribution of individual events,  $i$ , plotted vs. their detection time,  $t_i$ , between early 2012 and 2016. The color coding shows the reconstructed muon energy. The black-dashed line describes the fitted time PDF  $S_{temporal}$  of this work. It agrees well with the time PDF of [16] (labeled as “TXS analysis”) depicted as the grey-dashed line.

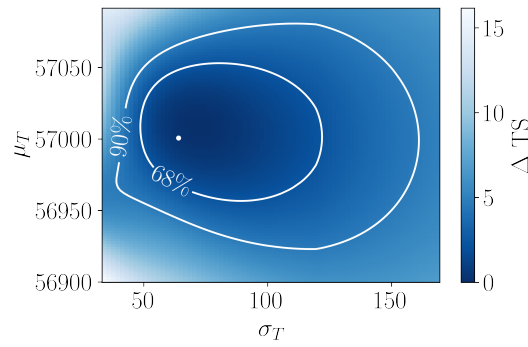


Figure 5.12: Profiled change of the test statistic for different  $\mu_T$  and  $\sigma_T$ . For each  $\mu_T$  and  $\sigma_T$ , the best  $n_S$  and  $\gamma$  are fitted. The 68% uncertainties are  $\mu_T = 57001^{+52}_{-44}$  MJD,  $\sigma_T = 64^{+58}_{-15}$  days.

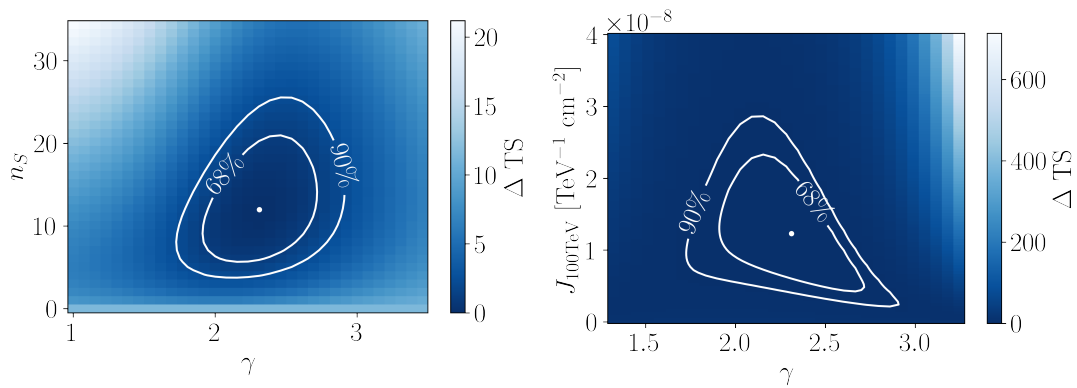


Figure 5.13: Change of the test statistic value when varying parameter of the likelihood. **Left:** Variation of  $TS$  when changing values of  $n_S$  and  $\gamma$ . The errors of the 68% contour are  $n_S = 12^{+9}_{-6}$  and  $\gamma = 2.3 \pm 0.4$ . **Right:** Variation of  $TS$  when varying the signal fluence  $J_{100\text{TeV}}(n_S, \gamma)$ . The error of the 68% contour are  $J_{100\text{TeV}} = 1.2^{+1.1}_{-0.8} \times 10^{-8} (\text{TeV cm}^2)^{-1}$ .

and this work. These parameters are biased compared to the true signal parameters, as was shown in Section 4.7.3. Hence derivations about the source flux or fluence from these fit parameters must be treated with caution.

Next, I investigate how the events are distributed with respect to the expected source position. The left of Figure 5.14 shows the squared angular distance and a clustering of expected signal events around the source position. The signal flux for this plot is simulated according to the best-fit result of the likelihood ratio test:  $n_S = 12$  and  $\gamma = 2.3$ . The background is created by scrambling the data in right ascension. The signal flux on top of background data explains well the observed data.

The signal of the flare is dominated by few strongly contributing events. The right side of Figure 5.14 shows how much the significance changes if single events are removed

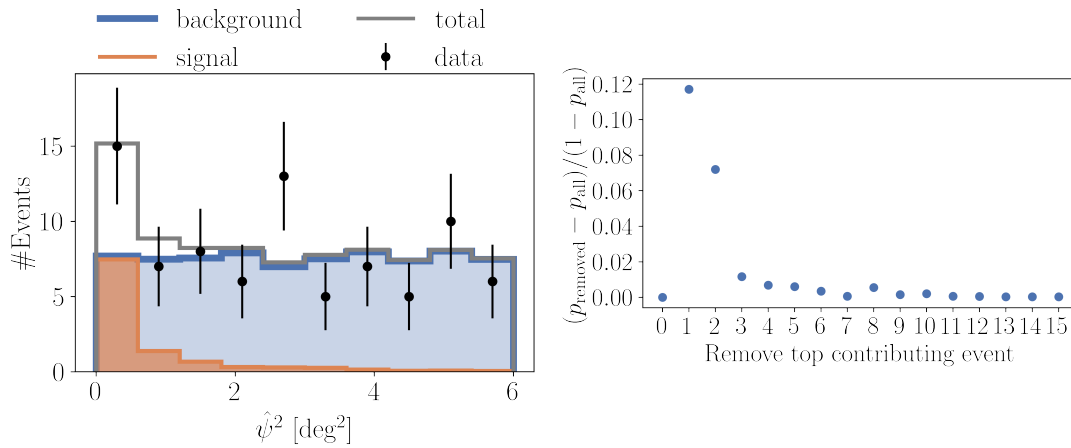


Figure 5.14: **Left:** Squared angular distance between the position of TXS 0506+056 and reconstructed event origin direction during the neutrino flare ( $57001 \text{ MJD} \pm 2 \times 64$  days). The background (blue) is scrambled data in right ascension and the signal (orange) is from Monte Carlo simulations (for the fitted values of  $n_S = 12$  and  $\gamma = 2.31$ ). The grey line shows the expectation of background and signal combined and matches the data points (black). **Right:** The difference of the p-value when removing individual events of the neutrino flare of TXS 0506+056. The p-value difference is normalized to the p-value when all events contribute  $p_{\text{all}}$ . The x-axis states which event was removed from the data. The first point ( $x = 0$ ) still includes all events. Two events contribute most to the significance of the flare.

from the data, sorted by their  $S/B$  value multiplied with  $S_{\text{temporal}}$ . The top two events make up for most of the significance. Table 5.1 lists the top 14 contributing events, also sorted by their  $S/B$  value multiplied with  $S_{\text{temporal}}$ . Furthermore, it contains the corresponding event from previous data samples (if the event was included), such that the differences in reconstructed direction, angular error, and energy can be compared.

MJD	This work				PSTracks v3 [98]				Ranking
	RA (deg)	Dec (deg)	$\sigma$ (deg)	$\log_{10}(E/\text{GeV})$	RA (deg)	Dec (deg)	$\sigma$ (deg)	$\log_{10}(E/\text{GeV})$	
56940.9084	77.36	5.42	0.20	3.81	77.35	5.42	0.20	3.97	1
57009.5301	77.36	5.53	0.34	3.85	77.32	5.50	0.34	3.91	2
56973.3971	77.03	5.01	0.39	3.61	77.05	5.05	0.40	3.71	12
57112.6530	77.39	5.32	0.20	3.23	77.43	5.34	1.09	3.46	7
57072.2088	77.13	5.04	0.42	3.50	76.35	5.22	0.36	3.43	9
56981.1313	76.20	6.13	0.63	4.03	76.16	6.19	0.43	4.13	5
57089.4395	77.67	5.91	0.20	3.62	77.71	5.90	0.20	3.69	3
56927.8601	77.43	4.93	0.39	3.46	77.39	4.93	0.33	3.53	13
56955.7917	77.61	5.58	0.51	2.99	77.60	5.56	0.48	3.09	6
57072.9895	76.05	6.80	1.97	4.09	76.35	5.22	0.36	4.17	4
56940.5215	77.82	5.79	0.44	2.80	–	–	–	–	–
57031.8224	77.64	4.61	0.76	2.96	–	–	–	–	–
56937.8189	77.77	6.29	0.63	2.98	77.75	6.23	0.63	2.91	11
56983.2476	77.47	6.80	0.92	3.09	–	–	–	–	–

Table 5.1: The left half of the table lists the top 14 events with the strongest contribution to the neutrino flare of TXS0506+056 from top to bottom. The right half lists the respective events in the data sample published in [98] and states the ranking of the contribution in the last row. The data set used in this work has improved directional and energy reconstruction. Some events have shifted in position and have slightly different energies.

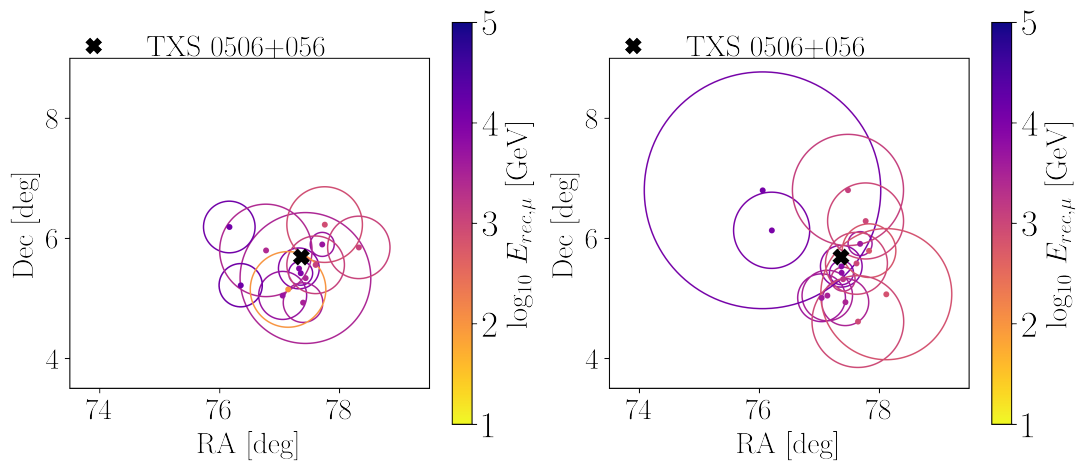


Figure 5.15: Position and energy (color) of the contributing events to the TXS 0506+056 neutrino flare. The circles show the  $\sigma$  uncertainty of the directional reconstruction. **Left:** The 14 most contributing events from the old data sample presented in [98]. **Right:** The 14 most contributing events from the data sample used in this work (see Table 5.1).

The improved directional and energy reconstruction has changed the contributing events with respect to previous analyses [16, 98]. The two most contributing events remain the same. However, their position is shifted, and their energy is changed. For the remaining events, the contributing order has changed or the events themselves differ. Figure 5.15 shows the position and energy of the 14 most contributing events to the neutrino flare from the previous data set (left) and the improved data used in this work (right). The event with the largest error region ( $\sigma = 1.9^\circ$ ) on the right panel is also included in the left panel. However, in the previous data sample, the uncertainty was underestimated ( $\sigma = 0.36^\circ$ ) and its position has shifted. The event views of the top 9 contributing events are displayed in Appendix D.2.

Next, I investigate potential source candidates of the neutrino flare. The left of Figure 5.16 shows the p-value map of the investigated alert uncertainty region. The neutrino excess is close to the blazar TXS 0506+056 (at a distance of  $0.32^\circ$ ). The right of Figure 5.16 depicts all known and candidate blazars within  $1^\circ$  of the best-fit position.

Looking at the source SEDs and the gamma-ray signatures, two of those objects make promising source candidates [14]. The blazar TXS 0506+056 (source 4 in Figure 5.16 (right)) and the blazar 3HSP J050833.4+053109 (source 2 in Figure 5.16 (right)). Figure 5.17 shows the test statistic value of the gamma-ray telescope Fermi-LAT [146] for the time period of the flare of the region. The  $TS$  is defined as

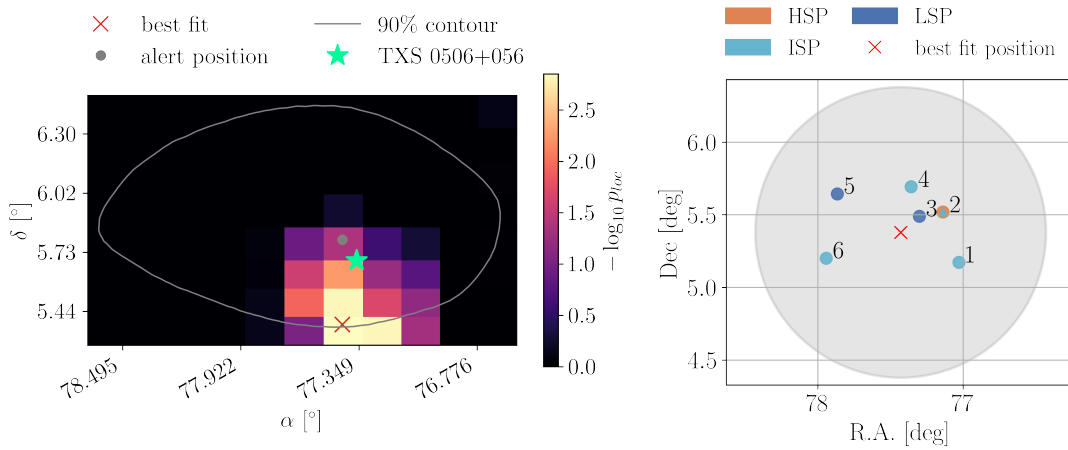


Figure 5.16: **Left:** P-value map of the most significant spot for the time-dependent analysis. The grey dot shows the original reconstructed alert position, and the red cross shows the best-fit position. TXS 0506+056 is depicted as the green star. **Right:** Known and candidate blazars in the vicinity (radius of  $1^\circ$ , grey circle) of the best-fit position from VOU-Blazars [144]. TXS 0506+056 is candidate source 4. Orange symbols show high synchrotron peaked blazar candidates, light blue shows intermediate synchrotron peaked blazar candidates, and dark blue indicates low synchrotron peaked blazar candidates. Objects 1, 3, and 5 are not at the position of cataloged sources, whereas object 2 corresponds to 3HSP J050833.4+053109 and object 6 to ZG 4472.

$TS = 2 \times [\ln \mathcal{L}(source) - \ln \mathcal{L}(background)]$  [147] for a specific source and background hypothesis. For lower energies another blazar (PKS 0506+049, with a distance of  $> 1^\circ$  from the best-fit position of the neutrino flare) is the stronger source, whereas TXS 0506+056 is the dominant source at higher energies.

Figure 5.18 shows the photon light curve for TXS 0506+056 from 2009 to  $\sim 2018$  and the respective photon indices. The blazar TXS 0506+056 has its hardest emission in the investigated period during the neutrino flare while showing faint emission in the Fermi-LAT band (10 MeV to  $> 300$  GeV [146]) [14]. The average photon index during the neutrino flare is 1.62 for  $E > 2$  GeV [146] (see Figure 5.19). The blazar behaves differently during the neutrino alert IceCube-170922A, where it flares the brightest but remains in a softer spectrum emission state [14]. In [14], the authors conclude that the behavior of TXS 0506+056 in photons and neutrinos is consistent with a hadronic flare during the neutrino flare period.

In order to gain a more complete picture of the emission of TXS 0506+056, Figure 5.20 shows the SED of TXS 0506+056 in photons with the all-flavor neutrino flux during  $57000.7031 \pm 64.0307$  MJD. The all-flavor flux is the muon neutrino flux  $\Phi_{100\text{TeV}}$

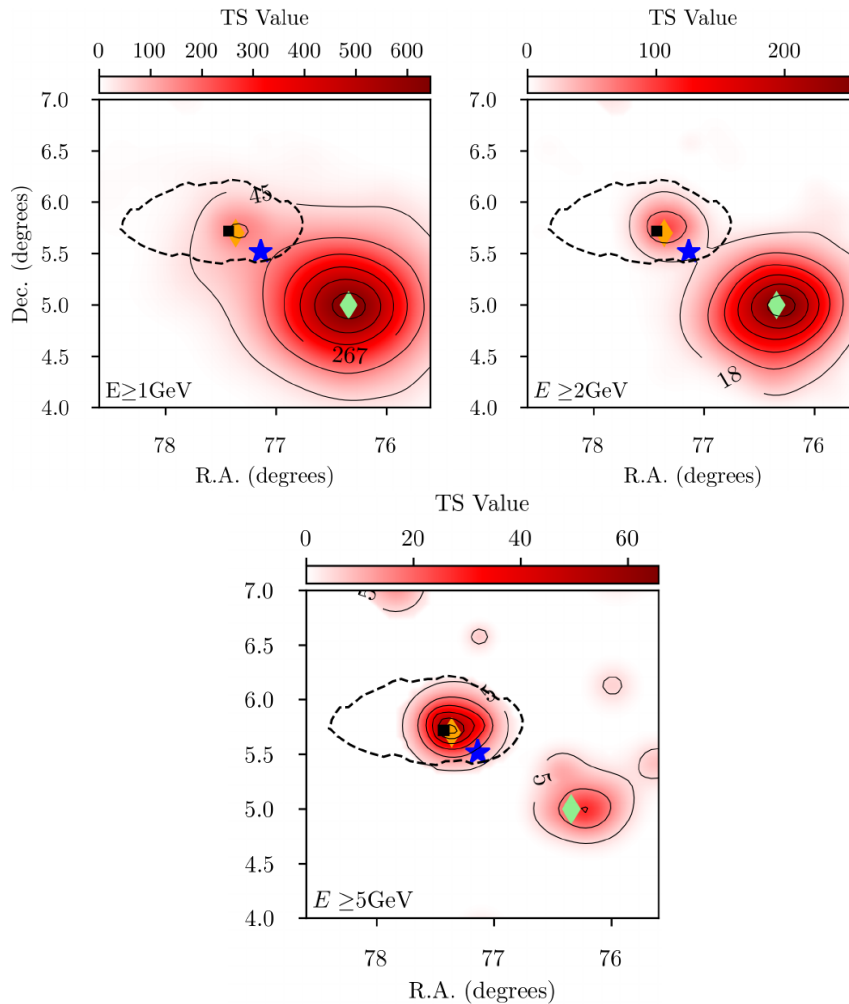


Figure 5.17: Fermi test statistic map of the region around the alert IceCube-170922A. The black square shows the reconstructed alert position and the dashed black line depicts the alert uncertainty region. TXS 0506+056 is marked as an orange diamond, 3HSP J050833.4+053109 as the blue star. The green diamond is the blazar PKS 0502+049 that dominates the gamma-ray emission in low energies ( $E \geq 1$  GeV, top left panel). For higher energies, TXS 0506+056 is the stronger source (see top right for  $E \geq 2$  GeV and bottom panel for  $E \geq 5$  GeV). Figures taken from [14].

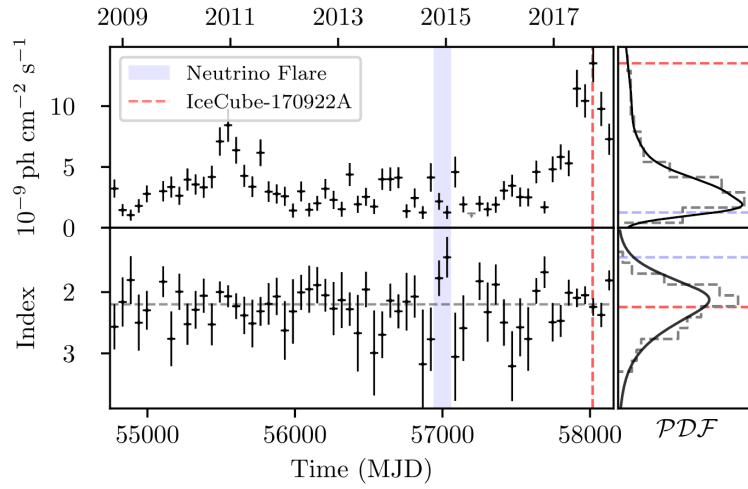


Figure 5.18: The gamma-ray light curve of TXS 0506+056 in 55-day bins with  $E > 2$  GeV and the respective photon index curve below. The light curve shows the data from 2009 until  $\sim 2018$  with  $E > 2$  GeV. The blue band highlights the time of the neutrino flare, the red-dashed line indicates the arrival time of IceCube-170922A. The right panel depicts the index and light curve PDF, with dashed lines highlighting the values for the flare (blue) and the alert event (red). Figure from [14].

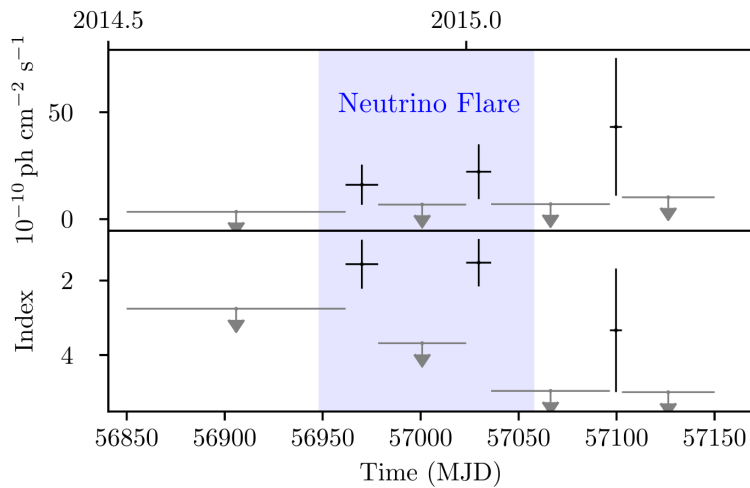


Figure 5.19: Zoom into the gamma-ray light curve of TXS 0506+056 in 55-day bins with  $E > 2$  GeV and the respective photon index curve below. Figures from [14]. The blue band highlights the time of the neutrino flare. During the neutrino flare, there is high-energy emission ( $E > 10$  GeV) in gamma-rays. The bottom panel shows the respective spectral index (average of 1.6). Figure from [14].

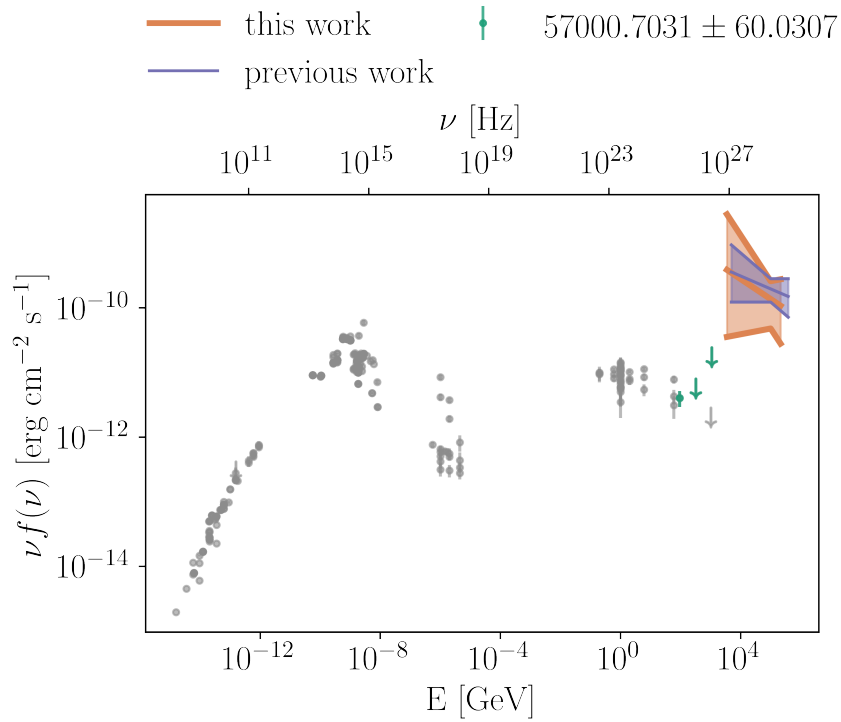


Figure 5.20: SED of TXS 0506+056 in photons (dots) and the neutrino flare. The green dots (arrows) show measured gamma-ray data (upper limits) during  $57000.7031 \pm 64.0307$  MJD. This work’s all-flavor flux during the neutrino flare (marked in orange,  $3 \cdot \Phi_{100\text{TeV}} = 3 \cdot 1.1^{+1.0}_{-0.7} \times 10^{-15} (\text{TeV cm}^2 \text{s})^{-1}$  for energies between 3.5 TeV and 213 TeV) agrees with the all-flavor flux from [16] (in dark purple,  $3 \cdot \Phi_{100\text{TeV}} = 3 \cdot 1.6^{+0.7}_{-0.6} \times 10^{-15} (\text{TeV cm}^2 \text{s})^{-1}$  for energies between 4.9 TeV and 384 TeV). Data for the photon SED from [152–173].

multiplied with 3 (for a neutrino flavor ratio of  $((\nu_e, \nu_\mu, \nu_\tau) = (1 : 1 : 1))$  from Section 2.5). The energy range for the neutrino flux is determined via Monte Carlo data. I chose Monte Carlo events that are similar in declination, reconstruction uncertainty, and reconstructed energy to the most contributing events of the flare (see Table 5.1). The central 90% of the Monte Carlo events’ true energies are 3.5 TeV and 213 TeV for this work and 4.9 TeV and 384 TeV for [16]. In [14], the authors found the neutrino flux and the photon flux at the same level, which agrees with lepto-hadronic models [148]. In [149–151] it is concluded that the gamma-ray and neutrino flux can be explained when considering different production and interaction zones. In [151], it is suggested that gamma-ray and neutrino production happen close to the supermassive black hole, and the gamma rays are then absorbed in a more distant region and generate emission in the MeV region. Future observations in the MeV region combined with future neutrino flares can constrain these models.

The lack of evidence for further transient neutrino emission from the origin direction of high-energy neutrino events (apart from the reported neutrino flare associated with TXS 0506+056) can be interpreted in different ways. The fact that probably only one neutrino flare from TXS 0506+056 has occurred in eleven years of data indicates that the neutrino-flaring states of TXS 0506+056 are not recurring within this time [56]. Hence, similar sources might flare rarely. I investigated 122 source candidates within eleven years. One of those sources shows indications of neutrino emission additional to the alert event. Thus, under the assumption that all source candidates are similar objects, I expect one flare from 122 sources within eleven years if a flare occurs every 1342 years. This value changes if not all source candidates are expected to produce neutrino flares. Another possible interpretation could be that only a few source candidates flare in lower-energetic neutrinos.

In general, the lack of a softer neutrino component agrees with predictions for a very hard neutrino spectrum. The lower-energy component of a hard neutrino emission with a spectral index of  $\gamma \leq 1$  (see for example [142, 143]) would be dominated by atmospheric background. With IceCube's effective area (see Figure 3.6), a hard neutrino emission would eventually result in single high-energy events, which agrees well with this work's result.



## Chapter 6

### Conclusion

The detection of a high-energy neutrino event in 2017 (IceCube-170922A) triggered multi-messenger follow-up observations. It was found that the event came from the direction of the blazar TXS 0506+056, which was at that time in a flaring state [12]. The evidence of one high-energy neutrino from a blazar triggered a follow-up study [16] in archival IceCube data to search for additional emission from that source. In the time period between September 2014 and March 2015, the study found a  $3.5\sigma$  evidence for additional transient neutrino emission from the very same origin direction [16]. This then triggers the question if any of the other high-energy alerts IceCube has detected originate from a source that emits neutrinos at different or lower energies.

In this thesis, I aim to answer this question. I searched for additional neutrino emission from possible neutrino production sites of extremely high-energy neutrinos — the IceCube alerts. A discovery of neutrinos in lower energies would mean the identification of a source producing high- and low-energy neutrinos. For this, I looked at 11 years of revised muon data of the IceCube Neutrino Observatory. I investigated the reconstructed origin directions of IceCube alert events within their 90% uncertainty contours, considering all neutrinos except the alert events themselves. In total, this analysis covered the origin region of 122 alerts that were detected between 2009 and end of 2021.

The analysis used an unbinned likelihood ratio test. In my signal hypothesis, neutrinos originating from a neutrino source cluster in their origin direction around the source position and have higher energies compared to neutrinos expected from atmospheric background. I assumed that the source emits a power law spectrum with

$E^{-\gamma}$ . The background hypothesis comprises spatially uniformly distributed origin directions and a softer energy distribution following a power law of  $E^{-3.7}$ .

I focused on two main source categories: continuous neutrino emission and transient neutrino emission. In the steady case, when looking for a single strong source among the 122 defined regions, the most significant source has a global p-value of 0.98 and is compatible with background. The upper flux limit for that source (with 90% confidence level) is  $\Phi_{90\%,100\text{TeV}} = 6.9 \times 10^{-17} \text{ (TeV cm}^2 \text{ s)}^{-1}$ . When looking at the combined lower-energy emission IceCube measures from all 122 alert origins, I find a p-value of 8%, which is also compatible with background. In total, the 90% confidence level upper flux limit is  $\Phi_{90\%,100\text{TeV}} = 4.2 \times 10^{-16} \text{ (TeV cm}^2 \text{ s)}^{-1}$  for an energy spectral index of  $\gamma = 2$  for the lower-energy component. This corresponds to 1.6% of IceCube's astrophysical diffuse flux. When investigating what maximal contribution I expect from all positions including the alert events, I find a maximal overall flux of  $\Phi_{90\%,100\text{TeV}} = 1.2 \times 10^{-15} \text{ (TeV cm}^2 \text{ s)}^{-1}$  ( $\gamma = 2$ ) coming from all regions combined. The latter value is 4.6% of IceCube's astrophysical diffuse flux.

Next, I have searched for transient neutrino emission. I have revised the original approach because it was computationally too expensive. I tried different approaches and eventually used unsupervised machine learning (expectation maximization) for the neutrino flare search. With this new and improved method, I could reduce the computation time for determining the neutrino flare time at one position from  $\approx 10$  h to below one second while still ensuring a reasonable performance. This improvement makes time-dependent catalog searches that investigate many sources or even time-dependent all-sky sources computationally feasible, even with an increasing data set and reasonable statistics at each pixel. Expectation maximization can also be easily extended to multiple flare searches.

I find the neutrino flare associated with the blazar TXS 0506+056 as the most significant transient neutrino emission. The local p-value is  $p_{local} = 0.14\% = 2.988\sigma$ . When correcting for the fact that I searched 122 positions, the global p-value is  $p_{global} = 0.156$  and is compatible with background. The flare parameters of this work agree with the parameters determined in [16] within the error bars. I find a Gaussian flaring time window at mean  $\mu_T = 57001_{-44}^{+52}$  MJD with width  $\sigma_T = 64_{-15}^{+58}$  days. The likelihood maximization finds a number of  $n_S = 12_{-6}^{+9}$  neutrinos from the source following a source spectral index of  $\gamma = 2.3 \pm 0.4$ . The corresponding time-integrated flux — the fluence —  $J_{100\text{TeV}} = \int_{t_{start}}^{t_{end}} \Phi_{100\text{TeV}} dt$ , normalized at 100 TeV, is  $J_{100\text{TeV}} = 1.2_{-0.8}^{+1.1} \times 10^{-8} \text{ (TeV cm}^2 \text{)}^{-1}$ . The average flux during the time window of  $2\sigma$  is  $\Phi_{100\text{TeV}} = 1.1_{-0.7}^{+1.0} \times 10^{-15} \text{ (TeV cm}^2 \text{)}^{-1}$ .

$s)^{-1}$ . However, the fit parameters  $n_S$  and  $\gamma$  have a bias compared to the true value. Hence, the derived fluxes and fluences must be considered with caution. An accurate Monte-Carlo based description of the spatial PDFs combined with improved energy reconstructions will remove this bias and allow accurate flux determinations in the future [18]. Finding the transient neutrino emission associated with TXS 0506+056 with revised IceCube data as the only flare with a local p-value of  $\sim 3\sigma$  strengthens the hypothesis of TXS 0506+056 as a neutrino source.

In general, the lack of a softer neutrino component agrees with expectations from sources with hard neutrino emission. The lower energy component of a hard neutrino emission with a spectral index of  $\gamma \leq 1$  would be dominated by atmospheric background. Whereas the higher-energy emission would result in single high-energy events due to IceCube's effective area, which agrees well with this work's result.

Future searches aiming to understand the origin of high-energy neutrinos could profit from a refined source candidate selection, e.g., by including information from multi-messenger observations. Apart from improving the source selection and the analysis method, a major factor will be the available data from neutrino telescopes. The detection of high-energy neutrino sources requires more data, either by longer data-taking periods or by building and completing more neutrino telescopes, ideally complementary to IceCube's field of view.



# Appendix A

## IceCube realtime alert events

Index	Time [MJD]	RA [deg]	RA err [deg]	Dec [deg]	Dec err [deg]
1	55056.6983	29.51	+0.40, -0.38	1.23	0.18, -0.22
2	55141.1275	298.21	+0.53, -0.57	11.74	0.32, -0.38
3	55355.4872	344.93	+3.39, -2.90	23.58	2.31, -4.13
4	55370.7355	141.25	+0.46, -0.45	47.80	0.56, -0.48
5	55387.5362	306.96	+2.70, -2.28	21.00	2.25, -1.56
6	55464.8959	266.29	+0.58, -0.62	13.40	0.52, -0.45
7	55478.3806	331.09	+0.56, -0.72	11.10	0.48, -0.58
8	55497.3033	88.68	+0.54, -0.55	0.46	0.33, -0.27
9	55512.5516	110.56	+0.80, -0.37	-0.37	0.48, -0.65
10	55513.5995	285.95	+1.29, -1.50	3.15	0.70, -0.63
11	55589.5628	307.53	+0.82, -0.81	1.19	0.35, -0.32
12	55624.9548	116.37	+0.73, -0.73	-10.72	0.57, -0.65
13	55695.0642	138.47	+6.68, -3.78	-1.94	0.97, -1.12
14	55702.7666	235.13	+2.70, -1.76	20.30	1.00, -1.43
15	55722.4261	272.55	+1.67, -2.42	35.64	1.30, -1.05
16	55756.1130	68.20	+0.31, -1.10	40.67	0.44, -0.44
17	55764.2196	315.66	+5.91, -5.35	5.29	4.85, -4.72
18	55806.0922	9.76	+2.85, -1.32	7.59	0.87, -0.86
19	55811.7946	196.08	+3.92, -2.68	9.40	1.56, -1.05
20	55834.4451	266.48	+2.09, -1.55	-4.41	0.59, -0.86
21	55896.8575	222.87	+1.95, -7.73	1.87	1.25, -1.18
22	55911.2769	36.74	+1.80, -2.24	18.88	2.46, -2.82

Continued on next page

Table A.1 – continued from previous page

Index	Time [MJD]	RA [deg]	RA err [deg]	Dec [deg]	Dec err [deg]
23	55987.8069	237.96	+0.53, -0.61	18.76	0.47, -0.51
24	56062.9590	198.94	+1.71, -1.41	32.00	0.97, -1.09
25	56070.5743	171.08	+0.66, -1.41	26.44	0.46, -0.37
26	56146.2071	330.07	+0.84, -0.83	1.42	0.59, -0.45
27	56186.3053	182.24	+1.36, -1.71	3.88	0.68, -0.82
28	56192.5493	70.62	+1.49, -1.27	19.79	0.91, -0.71
29	56211.7709	205.14	+0.66, -0.71	-2.28	0.53, -0.56
30	56226.5995	169.80	+1.32, -1.40	27.91	0.85, -0.88
31	56319.2800	352.97	+1.32, -1.01	-1.98	0.97, -0.89
32	56390.1888	167.83	+2.63, -3.96	20.66	1.28, -0.99
33	56470.1104	93.74	+1.01, -1.15	14.17	1.23, -1.04
34	56521.8320	224.89	+0.87, -1.19	-4.44	1.21, -0.94
35	56542.7931	130.17	+0.48, -0.31	-10.54	0.26, -0.30
36	56579.9092	32.92	+0.87, -0.71	10.28	0.41, -0.57
37	56588.5585	301.90	+1.02, -1.05	11.61	1.14, -1.30
38	56620.1451	285.16	+2.20, -1.54	19.47	1.43, -1.46
39	56630.4701	288.98	+1.10, -0.83	-14.21	0.77, -1.31
40	56658.4039	192.26	+2.07, -2.37	-2.69	1.01, -0.71
41	56665.3079	344.66	+0.53, -0.48	1.57	0.37, -0.34
42	56666.5030	293.12	+0.79, -1.19	33.02	0.45, -0.53
43	56691.7851	349.58	+2.64, -2.54	-13.55	1.14, -1.74
44	56799.9614	349.39	+2.89, -4.12	18.05	1.94, -1.80
45	56817.6364	106.26	+2.68, -2.15	1.31	1.04, -0.86
46	56819.2044	110.65	+0.53, -0.61	11.45	0.19, -0.19
47	56843.6687	25.88	+1.85, -2.98	2.54	1.79, -1.76
48	56923.7211	169.72	+0.70, -0.84	-1.60	0.52, -0.30
49	56927.1608	50.89	+3.91, -5.14	-0.63	1.49, -1.42
50	57049.4813	100.37	+1.36, -1.62	4.59	0.79, -0.67
51	57157.9416	91.49	+0.93, -0.74	12.14	0.53, -0.50
52	57217.9097	326.29	+1.50, -1.31	26.36	1.89, -2.19
53	57246.7591	328.27	+0.75, -0.88	6.17	0.48, -0.53
54	57265.2178	54.76	+0.92, -0.93	34.00	1.14, -1.20
55	57269.7597	133.77	+0.53, -0.88	28.08	0.51, -0.55

Continued on next page

Table A.1 – continued from previous page

Index	Time [MJD]	RA [deg]	RA err [deg]	Dec [deg]	Dec err [deg]
56	57284.2057	279.54	+1.75, -2.29	30.35	2.18, -1.51
57	57288.0268	103.23	+0.70, -1.15	3.96	0.60, -0.75
58	57291.9012	194.55	+0.79, -1.23	-4.56	0.94, -0.63
59	57312.6757	197.53	+2.47, -2.72	19.95	3.00, -2.29
60	57340.8735	76.16	+1.36, -1.37	12.71	0.65, -0.72
61	57348.5316	262.05	+0.87, -1.06	-2.24	0.64, -0.67
62	57391.4438	79.41	+0.83, -0.75	5.00	0.87, -0.97
63	57415.1835	263.76	+1.10, -1.80	-14.90	1.08, -1.20
64	57443.8804	311.87	+2.19, -1.77	60.06	1.65, -1.38
65	57478.5652	151.22	+0.66, -0.66	15.48	0.66, -0.73
66	57518.6640	352.88	+1.76, -1.45	1.90	0.75, -0.67
67	57600.0799	214.50	+0.75, -0.75	-0.33	0.75, -0.75
68	57606.5150	122.78	+0.88, -1.23	-0.71	0.56, -0.56
69	57614.9069	200.04	+3.12, -2.68	-32.13	1.74, -1.25
70	57655.7411	241.13	+4.92, -5.89	1.34	3.40, -2.79
71	57662.4392	192.57	+2.50, -2.07	37.12	1.51, -2.48
72	57672.0796	26.38	+0.66, -0.66	9.55	0.66, -0.66
73	57673.6126	190.06	+2.20, -4.04	-7.48	2.18, -2.99
74	57709.3320	78.66	+1.85, -1.93	1.60	1.91, -1.79
75	57732.8380	46.36	+2.38, -0.92	15.25	0.93, -1.08
76	57758.1419	309.95	+5.01, -7.56	8.16	2.00, -3.34
77	57833.3141	98.26	+1.32, -0.92	-15.06	1.04, -1.20
78	57887.3002	227.37	+1.23, -1.10	30.65	1.40, -0.99
79	57930.5193	280.99	+3.03, -1.63	8.80	1.13, -0.90
80	57938.2926	230.45	+1.67, -1.71	23.36	1.10, -0.89
81	57951.8177	208.39	+1.67, -1.19	25.16	1.41, -1.35
82	57968.0838	1.10	+4.48, -1.76	4.63	0.41, -0.41
83	57974.5971	21.27	+0.75, -1.06	-2.28	0.60, -0.67
84	57989.5538	41.92	+3.04, -3.56	12.37	1.45, -1.30
85	58018.8712	77.43	+1.14, -0.75	5.79	0.64, -0.41
86	58019.0213	173.45	+2.38, -2.55	-2.54	0.90, -1.30
87	58041.0656	162.91	+2.98, -1.72	-15.48	1.62, -1.99
88	58063.7775	340.14	+0.61, -0.62	7.44	0.31, -0.26

Continued on next page

Table A.1 – continued from previous page

Index	Time [MJD]	RA [deg]	RA err [deg]	Dec [deg]	Dec err [deg]
89	58141.6771	77.12	+2.51, -2.90	8.01	0.41, -0.49
90	58218.7768	218.50	+0.79, -1.28	0.56	0.75, -0.71
91	58225.2785	305.73	+3.60, -1.58	-4.41	0.68, -0.74
92	58369.8330	144.98	+1.49, -2.20	-2.39	1.16, -1.12
93	58414.6927	270.18	+1.89, -1.72	-8.42	1.13, -1.55
94	58442.7087	25.71	+5.54, -5.28	11.72	2.41, -4.50
95	58443.5800	132.19	+7.34, -6.99	32.93	4.19, -3.57
96	58507.1555	307.44	+0.53, -1.14	-32.22	0.96, -0.31
97	58528.6727	228.25	+0.79, -0.53	-4.14	0.37, -0.30
98	58535.3512	268.59	+1.41, -1.58	-17.00	1.25, -0.50
99	58606.7244	120.19	+0.66, -0.66	6.43	0.68, -0.75
100	58618.4506	127.88	+0.79, -0.83	12.60	0.49, -0.46
101	58647.8294	312.19	+0.66, -0.79	26.57	0.75, -0.71
102	58653.5516	343.52	+4.13, -3.16	10.28	2.01, -2.76
103	58694.8685	226.14	+1.28, -1.97	10.77	1.03, -1.18
104	58748.4047	167.30	+2.81, -2.72	-22.27	3.39, -3.30
105	58748.9611	5.71	+1.19, -1.27	-1.53	0.90, -0.78
106	58757.8398	313.99	+6.94, -2.46	12.79	1.65, -1.64
107	58806.0427	229.31	+5.49, -4.97	3.77	2.47, -2.24
108	58857.9873	165.45	+3.61, -4.39	11.80	1.18, -1.30
109	58999.3295	255.37	+2.46, -2.55	26.61	2.32, -3.25
110	59015.6176	142.95	+1.15, -1.40	3.66	1.16, -1.01
111	59118.3293	96.46	+0.70, -0.53	-4.33	0.60, -0.75
112	59121.7421	29.53	+0.53, -0.53	3.47	0.71, -0.34
113	59129.9179	265.17	+0.48, -0.49	5.34	0.30, -0.19
114	59167.6288	105.73	+0.93, -1.27	5.87	1.01, -1.05
115	59168.0885	195.12	+1.23, -1.45	1.38	1.27, -1.08
116	59183.8485	30.54	+1.10, -1.27	-12.10	1.14, -1.11
117	59192.4276	6.86	+1.01, -1.19	-9.25	0.94, -1.10
118	59204.5256	261.69	+2.28, -2.46	41.81	1.25, -1.14
119	59205.0391	206.37	+0.88, -0.75	13.44	0.54, -0.35
120	59255.4958	206.06	+1.40, -0.95	4.78	0.62, -0.56
121	59437.0852	270.79	+1.07, -1.08	25.28	0.79, -0.84

Continued on next page

Table A.1 – continued from previous page

Index	Time [MJD]	RA [deg]	RA err [deg]	Dec [deg]	Dec err [deg]
122	59479.7620	60.73	+0.88, -0.61	-4.18	0.37, -0.53

Table A.1: All alert events where I investigate the origin region in this work. The time is the detection time, RA and Dec list the best reconstruction coordinates, with RA err and Dec err as the 90% confidence level uncertainties.



## Appendix B

# Parameter recovery for time-dependent analysis

### B.1 Flare: $\sigma_T = 55.18$ days, no spectral index scan

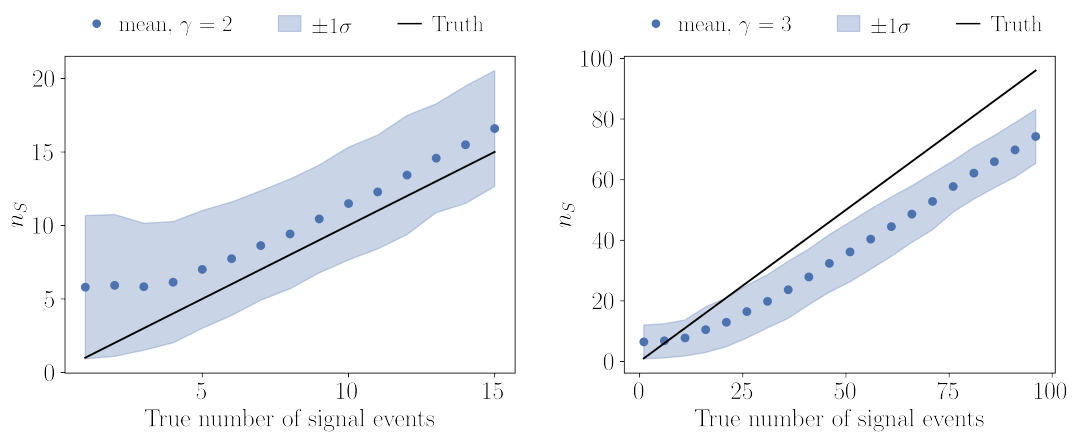


Figure B.1: Recovery of  $n_S$  with increasing flare strength (x-axis). The simulated flare had  $\sigma = 55.18$  d. The black line shows the truth. The blue dots depict the fitted mean value and the shaded blue region is  $\pm 1\sigma$ .

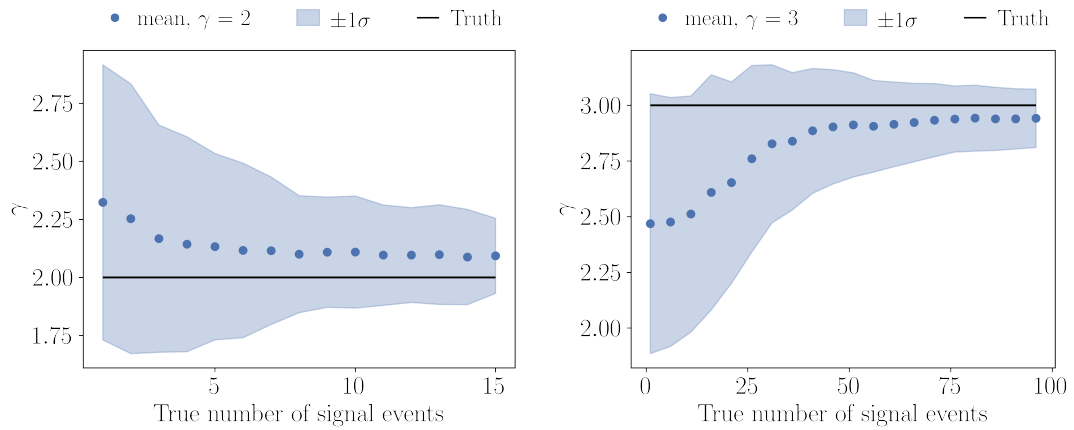


Figure B.2: Recovery of  $\gamma$  with increasing flare strength (x-axis). The simulated flare had  $\sigma_T = 55.18$  d. The black line shows the truth. The blue dots depict the fitted mean value and the shaded blue region is  $\pm 1\sigma$ .

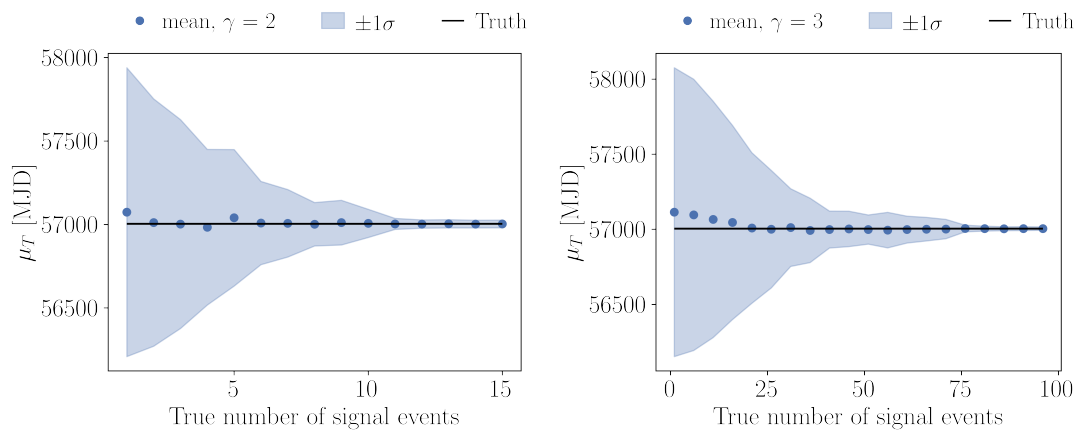


Figure B.3: Recovery of  $\mu_T$  with increasing flare strength (x-axis). The simulated flare had  $\sigma = 55.18$  d. The black line shows the truth. The blue dots depict the fitted mean value and the shaded blue region is  $\pm 1\sigma$ .

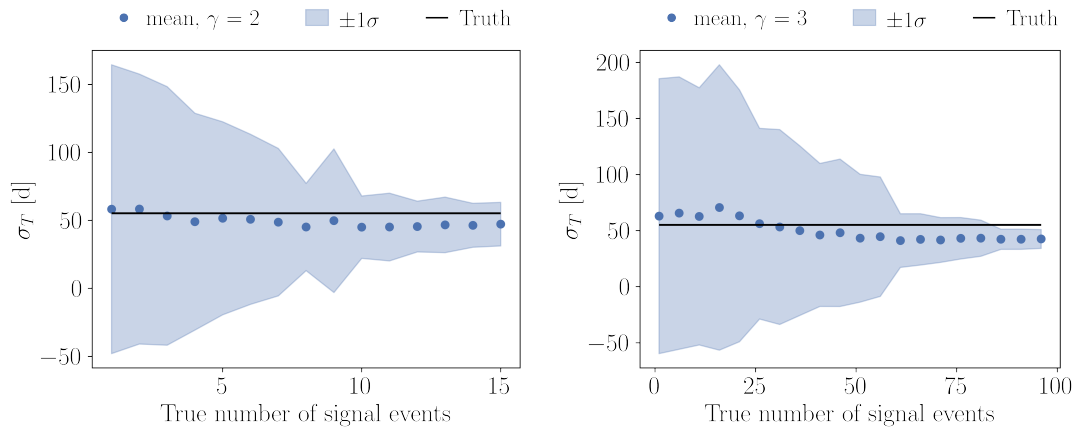


Figure B.4: Recovery of  $\sigma_T$  with increasing flare strength (x-axis). The simulated flare had  $\sigma_T = 55.18$  d. The black line shows the truth. The blue dots depict the fitted mean value and the shaded blue region is  $\pm 1\sigma$ .

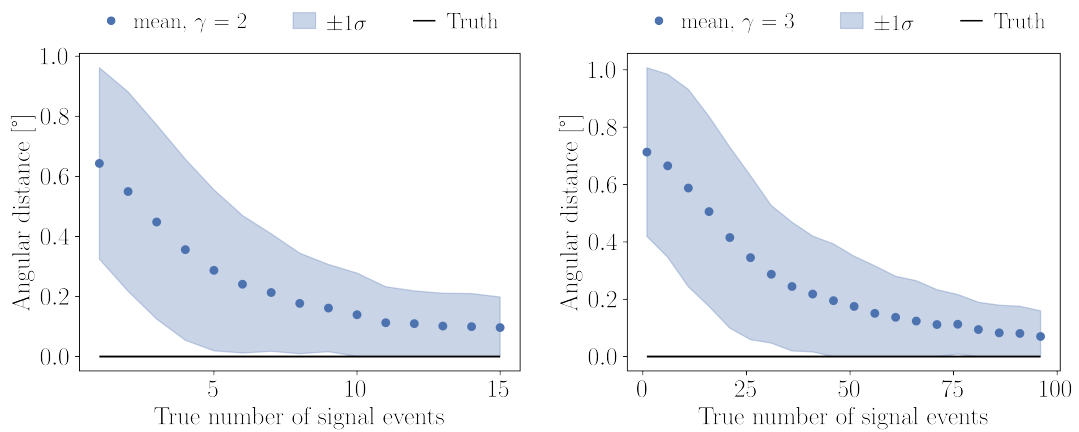


Figure B.5: Recovery of the simulated source position with increasing flare strength (x-axis). The simulated flare had  $\sigma_T = 55.18$  d. The black line shows the truth. The blue dots depict the fitted mean value and the shaded blue region is  $\pm 1\sigma$ .

## B.2 Flare: $\sigma_T = 55.18$ days, with spectral index scan

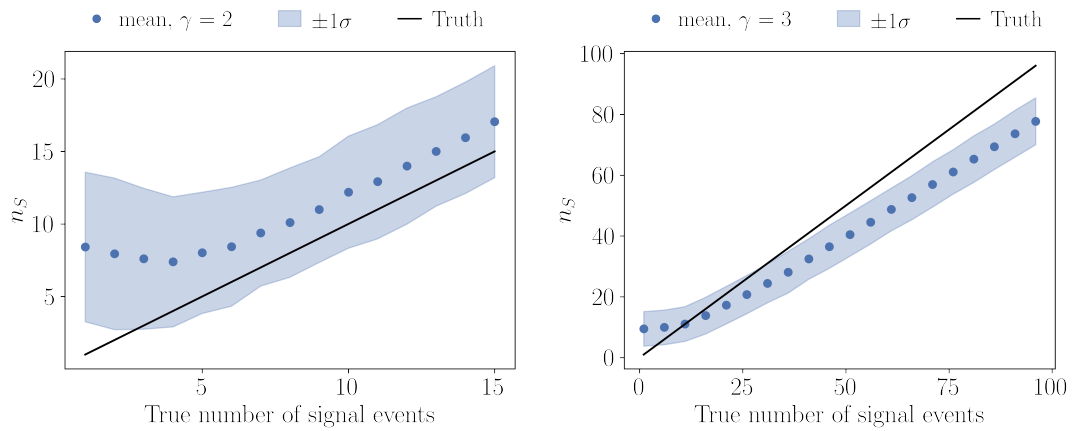


Figure B.6: Recovery of  $n_S$  with increasing flare strength (x-axis). The simulated flare had  $\sigma = 55.18$  d. The black line shows the truth. The blue dots depict the fitted mean value and the shaded blue region is  $\pm 1\sigma$ .

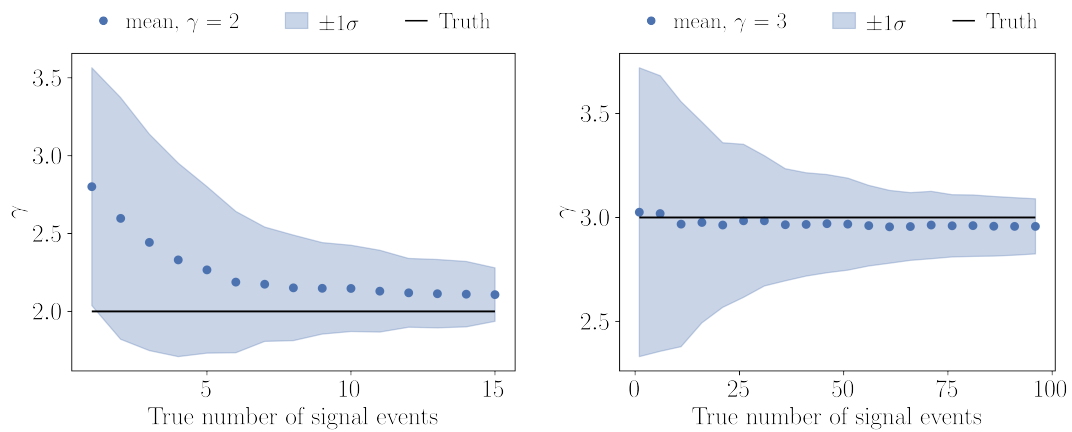


Figure B.7: Recovery of  $\gamma$  with increasing flare strength (x-axis). The simulated flare had  $\sigma_T = 55.18$  d. The black line shows the truth. The blue dots depict the fitted mean value and the shaded blue region is  $\pm 1\sigma$ .

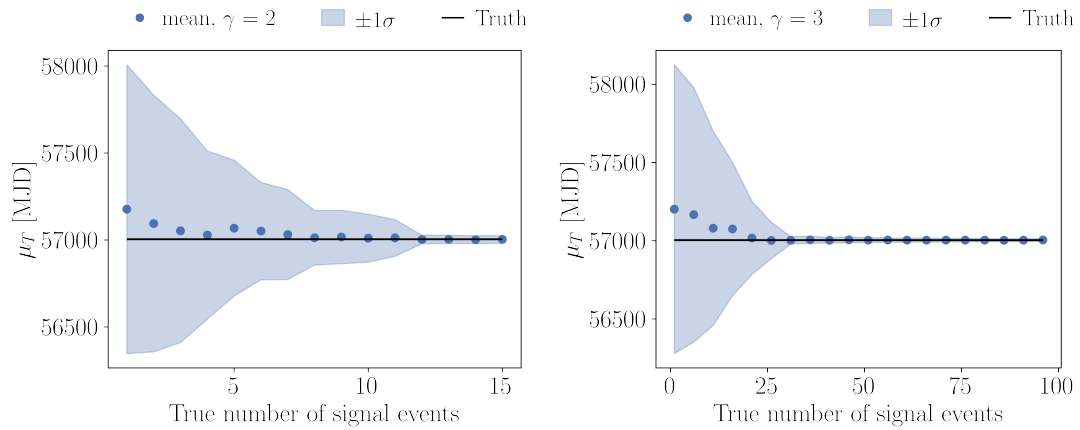


Figure B.8: Recovery of  $\mu_T$  with increasing flare strength (x-axis). The simulated flare had  $\sigma = 55.18$  d. The black line shows the truth. The blue dots depict the fitted mean value and the shaded blue region is  $\pm 1\sigma$ .

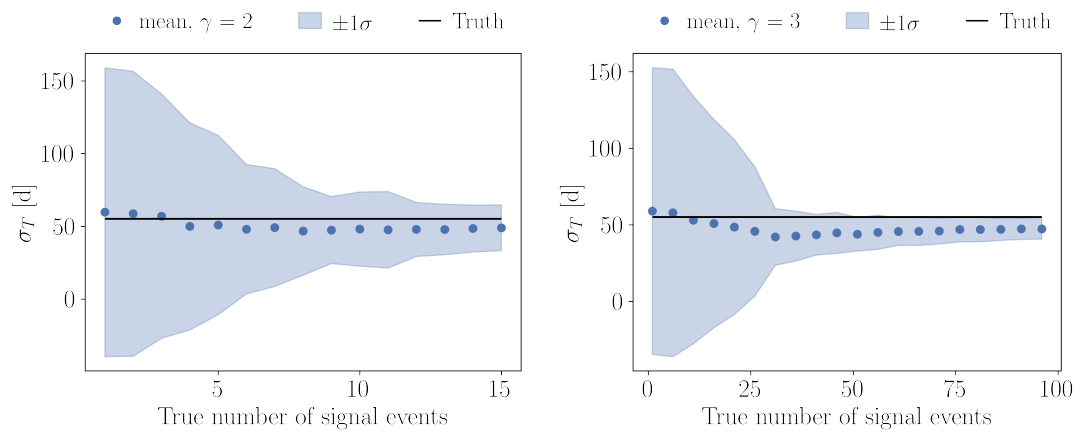


Figure B.9: Recovery of  $\sigma_T$  with increasing flare strength (x-axis). The simulated flare had  $\sigma_T = 55.18$  d. The black line shows the truth. The blue dots depict the fitted mean value and the shaded blue region is  $\pm 1\sigma$ .

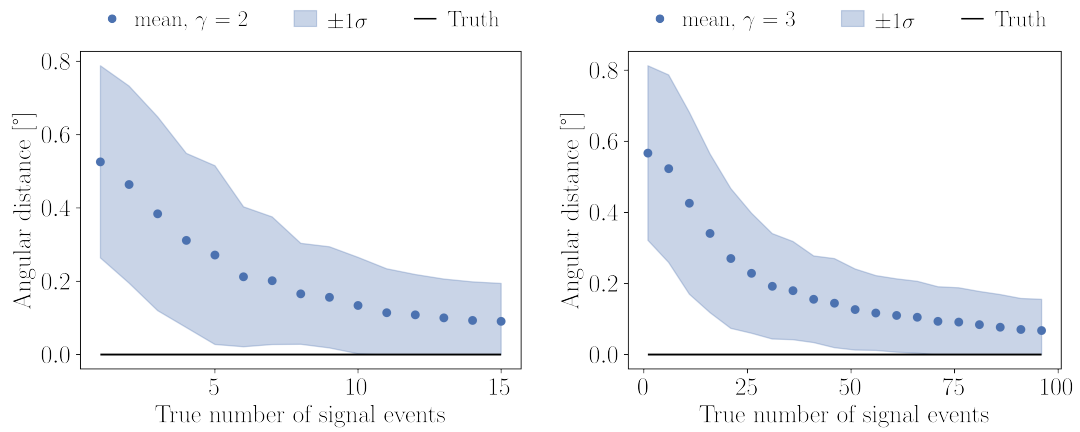


Figure B.10: Recovery of the simulated source position with increasing flare strength (x-axis). The simulated flare had  $\sigma_T = 55.18$  d. The black line shows the truth. The blue dots depict the fitted mean value and the shaded blue region is  $\pm 1\sigma$ .

### B.3 Flare: $\sigma_T = 10$ days, $\gamma = 2$

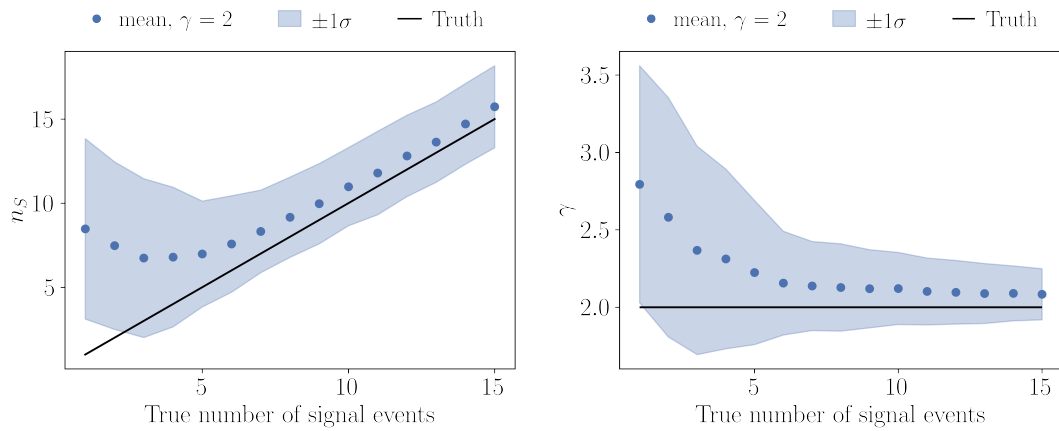


Figure B.11: Recovery of  $n_S$  and  $\gamma$  with increasing flare strength (x-axis). The simulated flare had  $\sigma_T = 10$  d. The black line shows the truth. The blue dots depict the fitted mean value and the shaded blue region is  $\pm 1\sigma$ .

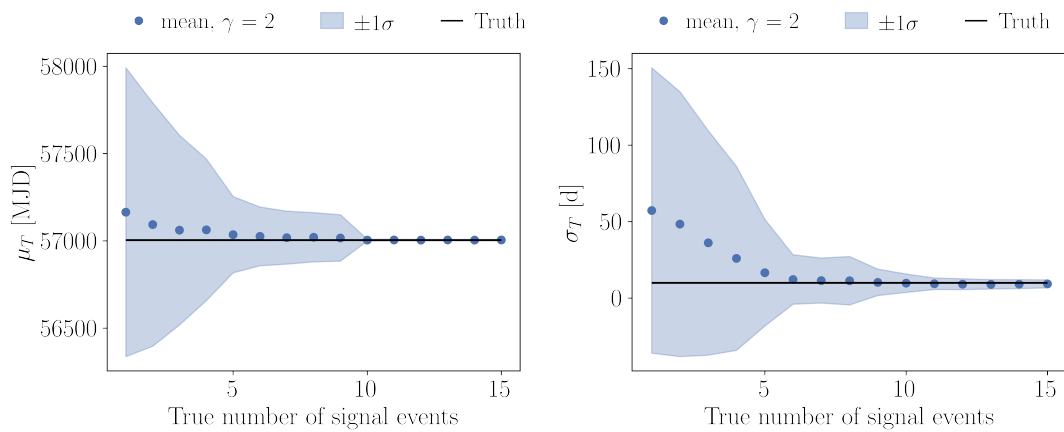


Figure B.12: Recovery of  $\mu_T$  and  $\sigma_T$  with increasing flare strength (x-axis). The simulated flare had  $\sigma_T = 10$  d. The black line shows the truth. The blue dots depict the fitted mean value and the shaded blue region is  $\pm 1\sigma$ .

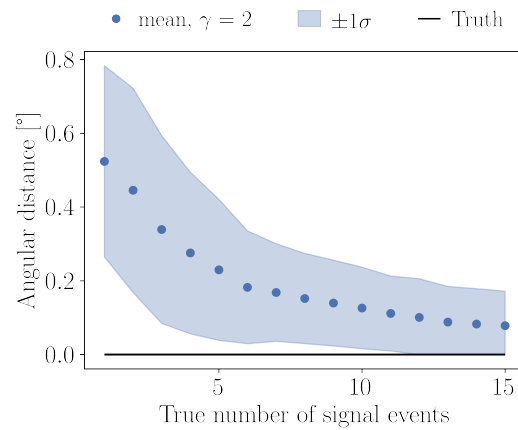


Figure B.13: Recovery of the source position with increasing flare strength (x-axis). The simulated flare had  $\sigma = 10$  d. The black line shows the truth. The blue dots depict the fitted mean value and the shaded blue region is  $\pm 1\sigma$ .

#### B.4 Flare: $\sigma_T = 100$ days, $\gamma = 2.0$

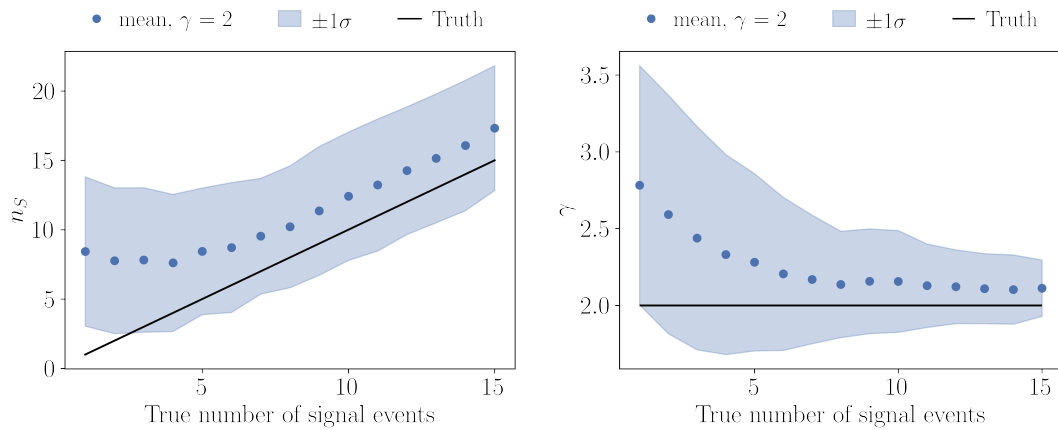


Figure B.14: Recovery of  $n_S$  and  $\gamma$  with increasing flare strength (x-axis). The simulated flare had  $\sigma_T = 100$  d. The black line shows the truth. The blue dots depict the fitted mean value and the shaded blue region is  $\pm 1\sigma$ .

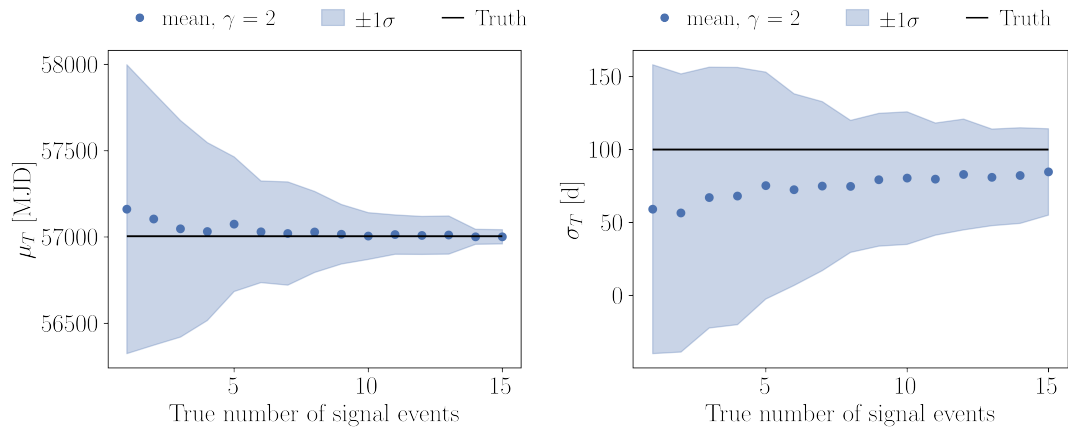


Figure B.15: Recovery of  $\mu_T$  and  $\sigma_T$  with increasing flare strength (x-axis). The simulated flare had  $\sigma_T = 100$  d. The black line shows the truth. The blue dots depict the fitted mean value and the shaded blue region is  $\pm 1\sigma$ .

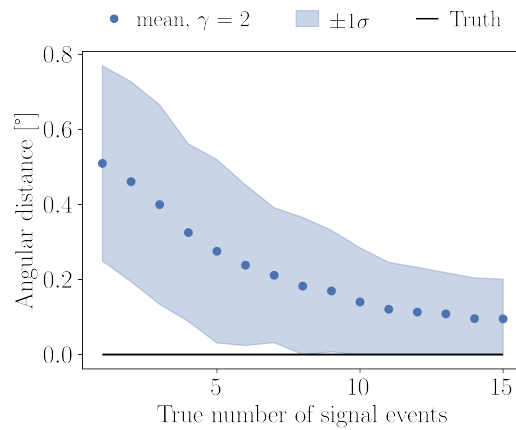


Figure B.16: Recovery of the source position with increasing flare strength (x-axis). The simulated flare had  $\sigma = 100$  d. The black line shows the truth. The blue dots depict the fitted mean value and the shaded blue region is  $\pm 1\sigma$ .



# Appendix C

## Time-integrated results

Index	RA [deg]	Dec [deg]	$n_S$	$\gamma$	$p_{local}$	$\Phi_{90\%100\text{TeV}}$ [TeV cm <sup>2</sup> s] <sup>-1</sup>	$p_{global}$
13	137.87	-2.69	37.50	3.20	0.0151	$6.88 \times 10^{-17}$	0.98
14	237.00	19.41	46.18	4.00	0.0287	$9.00 \times 10^{-17}$	
106	318.48	11.88	13.38	2.08	0.0280	$9.20 \times 10^{-17}$	
54	54.99	33.66	34.34	4.00	0.0443	$8.95 \times 10^{-17}$	
83	22.02	-2.13	28.76	2.93	0.0426	$5.00 \times 10^{-17}$	
2	298.74	11.74	38.86	4.00	0.0364	$5.58 \times 10^{-17}$	
16	68.36	40.82	4.48	1.71	0.0525	$7.31 \times 10^{-17}$	
23	237.76	19.08	37.66	4.00	0.0710	$5.77 \times 10^{-17}$	
25	171.74	26.44	11.18	2.31	0.0741	$6.35 \times 10^{-17}$	
60	75.38	12.87	13.39	2.17	0.0666	$7.66 \times 10^{-17}$	
10	284.83	3.32	16.71	2.38	0.0659	$4.77 \times 10^{-17}$	
74	79.40	2.75	20.01	2.49	0.0633	$6.31 \times 10^{-17}$	
50	50.69	-0.44	43.72	4.00	0.0618	$6.17 \times 10^{-17}$	
72	26.38	9.55	9.84	2.13	0.0784	$6.01 \times 10^{-17}$	
44	349.58	-13.17	12.27	2.64	0.0731	$2.15 \times 10^{-16}$	
45	350.01	19.02	40.34	3.91	0.1032	$7.68 \times 10^{-17}$	
90	218.32	-0.15	32.53	3.49	0.1129	$4.11 \times 10^{-17}$	
40	190.68	-2.35	26.39	4.00	0.1085	$4.22 \times 10^{-17}$	
11	307.86	1.36	11.50	2.42	0.1353	$3.24 \times 10^{-17}$	
93	269.42	-7.48	15.52	2.95	0.1462	$8.71 \times 10^{-17}$	
65	151.55	15.98	30.25	3.05	0.1565	$5.88 \times 10^{-17}$	

Continued on next page

Table C.1 – continued from previous page

Index	RA [deg]	Dec [deg]	$n_S$	$\gamma$	$p_{local}$	$\Phi_{90\%100\text{TeV}}$ [TeV cm <sup>2</sup> s] <sup>-1</sup>	$p_{global}$
77	99.20	-15.86	11.40	3.81	0.1576	$2.11 \times 10^{-16}$	
84	43.34	12.18	40.03	3.49	0.1641	$7.54 \times 10^{-17}$	
85	77.43	5.38	16.73	2.54	0.1652	$4.18 \times 10^{-17}$	
55	133.77	27.71	22.04	4.00	0.2027	$4.68 \times 10^{-17}$	
99	120.35	6.05	24.65	2.81	0.1984	$3.85 \times 10^{-17}$	
120	206.26	4.41	26.47	2.89	0.2029	$3.79 \times 10^{-17}$	
81	208.19	25.69	5.14	1.86	0.2172	$7.67 \times 10^{-17}$	
9	111.36	-0.37	25.89	4.00	0.2139	$2.89 \times 10^{-17}$	
4	141.25	47.32	17.24	2.61	0.2069	$5.56 \times 10^{-17}$	
28	70.62	19.43	8.08	2.09	0.2181	$4.92 \times 10^{-17}$	
15	273.27	36.20	22.40	2.72	0.2202	$6.14 \times 10^{-17}$	
30	171.12	27.73	32.96	3.94	0.2337	$5.37 \times 10^{-17}$	
31	353.91	-1.20	20.58	2.65	0.2373	$3.11 \times 10^{-17}$	
18	9.38	7.59	5.54	2.09	0.2403	$4.38 \times 10^{-17}$	
113	265.17	5.15	21.84	4.00	0.2845	$2.81 \times 10^{-17}$	
115	194.76	2.47	17.33	2.48	0.2575	$3.76 \times 10^{-17}$	
33	93.74	14.17	18.68	2.58	0.2633	$4.00 \times 10^{-17}$	
47	27.54	2.74	36.77	3.79	0.2849	$3.52 \times 10^{-17}$	
34	225.59	-4.09	14.38	2.78	0.2968	$3.24 \times 10^{-17}$	
7	330.73	11.10	21.11	2.90	0.3099	$3.12 \times 10^{-17}$	
119	206.90	13.27	20.54	3.16	0.2971	$3.70 \times 10^{-17}$	
112	29.35	3.30	22.47	3.12	0.2979	$2.82 \times 10^{-17}$	
94	26.90	7.81	47.41	4.00	0.3012	$7.00 \times 10^{-17}$	
114	104.46	6.38	28.34	3.01	0.2993	$3.57 \times 10^{-17}$	
122	60.27	-3.99	6.55	4.00	0.3391	$2.86 \times 10^{-17}$	
79	283.21	9.37	32.19	3.43	0.3270	$4.65 \times 10^{-17}$	
59	195.23	20.14	8.95	2.09	0.3258	$6.66 \times 10^{-17}$	
75	46.95	15.99	32.99	3.15	0.3241	$5.19 \times 10^{-17}$	
56	277.48	29.41	25.41	2.83	0.3200	$6.23 \times 10^{-17}$	
78	227.78	30.25	28.65	4.00	0.3330	$5.41 \times 10^{-17}$	
86	171.49	-2.36	8.32	2.19	0.3404	$3.58 \times 10^{-17}$	
52	91.86	12.32	23.31	3.25	0.3399	$3.72 \times 10^{-17}$	

Continued on next page

Table C.1 – continued from previous page

Index	RA [deg]	Dec [deg]	$n_S$	$\gamma$	$p_{local}$	$\Phi_{90\%100\text{TeV}}$ [TeV cm <sup>2</sup> s] <sup>-1</sup>	$p_{global}$
49	168.88	-1.43	20.41	4.00	0.3460	$2.03 \times 10^{-17}$	
88	340.75	7.44	19.33	4.00	0.3682	$2.66 \times 10^{-17}$	
109	255.82	26.80	26.23	2.85	0.3633	$8.03 \times 10^{-17}$	
70	237.60	1.14	41.83	4.00	0.3804	$4.43 \times 10^{-17}$	
102	343.52	9.69	42.18	3.38	0.3987	$5.17 \times 10^{-17}$	
87	164.10	-14.76	11.78	3.90	0.3940	$1.73 \times 10^{-16}$	
46	105.48	1.66	25.18	2.74	0.3952	$2.69 \times 10^{-17}$	
97	228.84	-3.96	6.79	4.00	0.4633	$2.40 \times 10^{-17}$	
66	354.25	1.40	27.02	4.00	0.4145	$2.90 \times 10^{-17}$	
92	144.38	-3.14	18.45	4.00	0.4210	$3.28 \times 10^{-17}$	
100	128.67	12.76	5.42	2.18	0.4334	$3.36 \times 10^{-17}$	
110	143.14	3.32	21.32	2.82	0.4553	$3.30 \times 10^{-17}$	
63	264.13	-15.07	8.15	3.88	0.4672	$1.34 \times 10^{-16}$	
91	304.94	-4.97	12.09	4.00	0.4650	$4.46 \times 10^{-17}$	
98	269.80	-16.11	9.81	3.67	0.4748	$1.57 \times 10^{-16}$	
5	306.96	19.44	15.41	2.38	0.4874	$4.83 \times 10^{-17}$	
108	167.45	12.39	31.98	3.15	0.4791	$5.15 \times 10^{-17}$	
101	312.19	25.86	7.93	2.24	0.4721	$4.10 \times 10^{-17}$	
26	329.57	1.82	19.70	4.00	0.4932	$1.85 \times 10^{-17}$	
41	344.50	1.94	4.08	2.21	0.5191	$2.00 \times 10^{-17}$	
37	301.20	10.50	5.10	2.17	0.5078	$3.23 \times 10^{-17}$	
68	122.25	-0.34	18.24	3.96	0.5056	$2.54 \times 10^{-17}$	
6	266.87	13.40	9.33	2.66	0.5741	$2.43 \times 10^{-17}$	
27	180.72	3.55	19.65	3.14	0.5541	$2.51 \times 10^{-17}$	
69	200.71	-31.94	9.69	3.55	0.5701	$4.89 \times 10^{-16}$	
117	5.67	-9.06	7.22	2.95	0.5708	$6.52 \times 10^{-17}$	
51	99.29	4.59	23.19	3.09	0.5732	$3.08 \times 10^{-17}$	
39	289.16	-14.21	6.66	3.15	0.5860	$9.48 \times 10^{-17}$	
64	312.60	59.86	9.68	2.06	0.5920	$8.38 \times 10^{-17}$	
25	199.80	32.58	16.22	2.75	0.6065	$4.64 \times 10^{-17}$	
73	187.17	-6.89	9.57	2.26	0.6065	$7.43 \times 10^{-17}$	
80	230.24	23.91	16.44	2.66	0.6192	$4.83 \times 10^{-17}$	

Continued on next page

Table C.1 – continued from previous page

Index	RA [deg]	Dec [deg]	$n_S$	$\gamma$	$p_{local}$	$\Phi_{90\%100\text{TeV}}$ [TeV cm <sup>2</sup> s] <sup>-1</sup>	$p_{global}$
105	4.80	-1.92	16.74	2.82	0.6227	$2.82 \times 10^{-17}$	
47	110.83	11.45	4.77	3.57	0.8196	$2.46 \times 10^{-17}$	
61	261.34	-2.58	9.54	2.82	0.6706	$2.72 \times 10^{-17}$	
104	166.88	-20.47	5.88	2.16	0.6770	$2.80 \times 10^{-16}$	
22	37.34	18.88	27.49	3.83	0.6964	$4.67 \times 10^{-17}$	
32	169.25	20.84	22.64	2.87	0.7080	$4.45 \times 10^{-17}$	
107	233.04	3.02	35.13	3.54	0.7336	$4.06 \times 10^{-17}$	
58	193.67	-3.81	6.84	4.00	0.7429	$3.21 \times 10^{-17}$	
118	263.47	42.52	6.25	1.99	0.7397	$6.92 \times 10^{-17}$	
20	266.48	-5.10	9.66	3.55	0.7439	$3.81 \times 10^{-17}$	
12	115.64	-10.72	1.53	2.35	0.7609	$4.62 \times 10^{-17}$	
116	30.72	-11.91	6.42	3.38	0.7580	$9.04 \times 10^{-17}$	
95	127.53	35.53	26.45	2.65	0.7676	$8.66 \times 10^{-17}$	
3	347.90	22.20	33.17	4.00	0.7855	$4.86 \times 10^{-17}$	
96	307.97	-32.03	2.48	2.49	0.8092	$3.57 \times 10^{-16}$	
121	270.36	25.11	13.05	4.00	0.7943	$4.65 \times 10^{-17}$	
38	284.97	19.11	19.88	4.00	0.7964	$4.12 \times 10^{-17}$	
42	293.71	33.32	7.76	2.89	0.8267	$3.93 \times 10^{-17}$	
52	326.72	27.30	7.78	2.44	0.8027	$6.09 \times 10^{-17}$	
89	79.63	8.01	19.75	4.00	0.8080	$3.55 \times 10^{-17}$	
57	103.41	3.96	2.01	2.14	0.8219	$2.81 \times 10^{-17}$	
62	79.41	5.00	12.34	3.04	0.8261	$2.83 \times 10^{-17}$	
82	4.61	4.36	16.46	4.00	0.8494	$3.26 \times 10^{-17}$	
19	194.36	9.59	25.50	4.00	0.8611	$4.15 \times 10^{-17}$	
36	33.79	10.09	2.16	2.01	0.9065	$2.55 \times 10^{-17}$	
103	225.75	10.77	12.59	2.88	0.8840	$4.01 \times 10^{-17}$	
111	96.46	-5.08	0.55	3.35	0.9965	$3.58 \times 10^{-17}$	
67	214.31	-0.89	8.92	3.32	0.9406	$2.55 \times 10^{-17}$	
76	310.75	9.07	9.19	2.17	0.9306	$5.71 \times 10^{-17}$	
21	222.47	0.89	17.33	3.34	0.9382	$3.45 \times 10^{-17}$	
71	193.07	37.50	14.94	3.19	0.9427	$7.36 \times 10^{-17}$	
53	327.74	5.82	1.69	3.75	0.9972	$2.74 \times 10^{-17}$	

Continued on next page

Table C.1 – continued from previous page

Index	RA [deg]	Dec [deg]	$n_s$	$\gamma$	$p_{local}$	$\Phi_{90\%100\text{TeV}}$ [TeV cm <sup>2</sup> s] <sup>-1</sup>	$p_{global}$
17	314.47	8.39	30.90	3.32	0.9937	$4.50 \times 10^{-17}$	
29	204.43	-2.47	0.00	2.56	0.9985	$1.87 \times 10^{-17}$	
1	29.32	1.12	0.00	2.83	1.0000	$1.83 \times 10^{-17}$	
8	88.31	0.33	0.00	3.20	1.0000	$2.04 \times 10^{-17}$	
35	130.01	-10.69	0.00	1.50	1.0000	$5.02 \times 10^{-17}$	

Table C.1: The results of the individual time-integrated analysis. The first column contains the index of the alert event as in Table A.1. The two following columns list the best-fit position. The fourth and fifth column contain the best-fit parameter of the likelihood optimization  $n_s$  and  $\gamma$ . The sixth column shows the local p-values, the seventh column the 90% confidence level upper flux limits, and the last column lists the corrected global p-value of the analysis.



# Appendix D

## Time-dependent results

Index	RA [deg]	Dec [deg]	$n_S$	$\gamma$	$\mu_T$	$\sigma_T$	$p_{local}$	$p_{global}$
85	77.43	5.38	11.98	2.31	57000.7031	64.0307	0.0014	0.156
17	318.42	1.75	10.41	2.45	57007.9336	19.8442	0.0173	
107	227.72	5.10	9.48	2.38	57774.1328	9.1265	0.0156	
60	75.77	13.20	5.19	2.07	58155.1719	9.6950	0.0189	
33	93.74	14.35	14.45	2.96	57078.4609	39.2202	0.0213	
30	169.60	28.76	8.52	3.04	56152.6133	5.3688	0.0252	
83	21.27	-2.95	18.44	2.90	57186.4688	236.1476	0.0335	
120	206.26	4.41	19.76	3.02	57426.9648	102.6704	0.0511	
99	120.19	5.87	12.71	2.68	56266.5312	51.2488	0.0552	
87	164.10	-17.07	8.10	3.80	58493.1641	94.1068	0.0733	
47	24.89	1.56	11.01	2.70	57763.5469	22.4285	0.0778	
90	217.59	0.03	9.40	2.55	57645.5469	28.5480	0.0842	
23	238.14	18.42	8.52	3.03	57173.0508	5.0000	0.0828	
104	165.83	-23.82	6.90	3.12	58903.9766	19.6423	0.0860	
11	307.86	1.36	3.16	2.04	57056.1836	7.2675	0.0953	
27	180.53	3.88	13.77	3.69	56469.8281	26.4728	0.0964	
101	312.19	26.04	4.81	2.65	58691.6328	5.0000	0.1036	
12	115.82	-10.53	4.32	2.61	58700.5625	19.4638	0.1136	
44	350.80	-14.90	5.34	3.08	57862.2852	13.4693	0.1100	
100	127.71	12.14	7.16	2.61	57213.6367	5.4103	0.1075	
115	194.94	1.74	5.59	2.61	58528.5781	5.6445	0.1152	
52	326.72	27.49	5.81	1.91	57677.4141	5.0000	0.1138	

Continued on next page

Table D.1 – continued from previous page

Index	RA [deg]	Dec [deg]	$n_S$	$\gamma$	$\mu_T$	$\sigma_T$	$p_{local}$	$p_{global}$
6	266.87	13.40	6.67	2.39	55551.3789	36.5352	0.1173	
25	171.74	26.44	11.23	2.67	58062.7500	119.8404	0.1215	
16	68.36	40.82	3.93	1.66	58433.6680	23.1572	0.1260	
73	188.33	-6.10	9.37	2.68	56698.1172	77.9146	0.1231	
36	33.62	9.90	4.87	1.98	55815.2734	9.7686	0.1207	
4	141.48	47.48	20.87	2.54	57931.1055	268.4064	0.1316	
50	48.32	0.49	17.16	3.53	55870.1094	52.2769	0.1923	
52	91.68	12.14	10.51	3.43	57694.1562	12.3198	0.2027	
108	168.46	11.80	7.88	2.61	57074.8672	7.1600	0.2264	
2	298.56	11.55	8.18	2.67	56998.0430	12.5098	0.2243	
103	226.14	10.77	5.93	2.55	55499.8086	9.1107	0.2467	
109	255.82	27.00	13.24	2.92	58939.9648	31.5749	0.2476	
28	70.81	19.08	8.34	2.85	58292.5898	11.7033	0.2545	
7	331.46	10.71	11.97	3.13	57753.2734	18.2160	0.2560	
105	4.80	-0.81	10.26	2.77	57853.8672	20.9690	0.2773	
74	77.50	2.55	12.44	2.49	57406.7148	143.9114	0.2895	
34	224.10	-4.09	5.26	4.00	56352.4023	16.9100	0.3230	
5	306.55	19.63	10.43	2.84	57728.1250	36.6549	0.3278	
121	271.00	25.11	18.65	4.00	56857.9570	125.0721	0.3334	
78	227.37	30.25	7.27	4.00	56554.0156	5.9930	0.3394	
110	142.35	2.82	9.97	3.29	57011.4141	9.8073	0.3438	
62	79.41	5.00	8.33	2.77	55880.8516	23.1637	0.3553	
54	54.06	34.00	5.54	2.38	55464.8359	8.2564	0.3389	
113	265.01	5.34	11.57	2.66	58747.4922	136.7696	0.3495	
51	100.95	4.98	13.56	2.74	57683.2500	42.5008	0.3632	
59	195.23	19.76	5.95	1.95	57777.2109	42.8650	0.3678	
72	26.38	9.71	2.64	1.83	55868.7539	19.5539	0.3795	
40	193.20	-3.22	4.72	3.27	56069.0664	5.0000	0.3907	
3	347.47	24.93	19.50	4.00	58816.7578	66.5288	0.3889	
61	261.34	-2.58	2.18	2.23	56311.4570	5.0000	0.3989	
86	173.25	-2.54	5.89	3.94	58914.2227	7.9130	0.4038	
47	110.83	11.64	3.10	2.01	56283.5664	5.0000	0.4027	
31	353.16	-1.40	4.50	2.61	57484.9023	5.0000	0.4116	

Continued on next page

Table D.1 – continued from previous page

Index	RA [deg]	Dec [deg]	$n_S$	$\gamma$	$\mu_T$	$\sigma_T$	$p_{local}$	$p_{global}$
106	317.26	12.24	10.38	2.17	55647.7852	193.7156	0.4244	
69	200.71	-31.94	9.17	2.68	57640.5703	148.9319	0.4612	
81	207.80	26.04	6.19	2.04	57909.0469	35.1746	0.4675	
35	130.17	-10.28	1.97	3.46	55727.0117	5.0000	0.4750	
37	301.37	10.50	4.16	2.06	56186.3203	58.7150	0.4786	
8	88.50	0.46	3.75	4.00	58729.3281	5.0000	0.4732	
32	166.79	21.76	17.27	3.06	58039.0859	104.7940	0.4850	
96	307.97	-32.03	5.75	2.71	58223.1016	129.9188	0.4902	
26	329.40	1.12	10.31	4.00	57346.4844	20.3527	0.4900	
65	151.05	14.93	10.71	2.69	56073.0430	74.2338	0.4964	
55	133.55	27.71	12.73	4.00	57202.0547	96.2399	0.4948	
102	341.35	11.01	23.55	3.50	55931.6094	224.7134	0.5026	
53	327.92	5.82	7.41	3.54	57306.9141	5.0000	0.5114	
10	284.83	3.32	2.92	1.95	58860.4023	51.3738	0.5190	
1	29.51	1.23	4.52	4.00	58151.7422	5.0000	0.5207	
97	228.25	-4.44	4.67	4.00	57925.0430	22.9265	0.5396	
18	9.38	7.59	2.45	1.76	56919.8164	132.5799	0.5462	
114	105.55	6.38	10.56	3.26	57437.8477	72.8099	0.5482	
98	268.20	-16.29	8.79	3.93	55171.0078	32.1326	0.5584	
75	47.55	15.44	6.99	2.85	56015.0703	6.4394	0.5645	
19	199.21	8.87	9.84	3.33	58511.6367	16.4783	0.5784	
21	223.65	1.67	6.06	2.04	57753.5703	57.9965	0.5861	
46	105.67	0.97	8.75	2.52	56044.2188	61.7499	0.5978	
49	168.88	-1.43	12.14	4.00	57033.5938	134.6016	0.6045	
88	340.60	7.59	6.69	4.00	56225.1094	10.1721	0.6303	
122	60.12	-3.99	4.24	4.00	57539.1133	33.0843	0.6427	
20	266.67	-5.10	9.44	3.81	57443.7852	122.4720	0.6486	
92	144.78	-2.95	12.23	4.00	58406.2930	94.6716	0.6668	
79	282.81	8.26	16.67	2.98	57870.5039	144.4034	0.6615	
80	230.45	23.54	8.44	2.91	56927.2930	12.7210	0.6840	
91	307.53	-4.97	6.03	2.39	57104.9609	25.8640	0.6758	
95	130.33	36.92	10.91	4.00	55468.5742	50.9458	0.6829	
93	270.56	-7.29	6.61	2.10	58532.3047	44.2205	0.6880	

Continued on next page

Table D.1 – continued from previous page

Index	RA [deg]	Dec [deg]	$n_S$	$\gamma$	$\mu_T$	$\sigma_T$	$p_{local}$	$p_{global}$
82	359.34	4.36	11.18	3.54	56649.6133	25.5849	0.6839	
112	29.00	3.47	3.64	4.00	57044.6719	5.0000	0.6866	
70	237.20	1.14	16.00	3.27	56123.1172	64.5211	0.6997	
22	37.14	18.69	16.67	2.89	57494.0156	112.0472	0.7260	
66	354.64	1.73	4.05	2.30	57815.2812	5.0000	0.7296	
25	199.80	32.58	6.94	2.41	55762.6211	38.3663	0.7447	
119	207.07	13.27	6.99	3.26	56078.1992	19.9749	0.7434	
39	289.35	-15.33	3.13	3.60	58115.5938	7.8179	0.7545	
63	263.76	-15.07	5.68	3.72	57963.9062	136.4733	0.7559	
15	272.55	36.20	5.39	1.97	55849.8711	39.8678	0.7604	
57	102.85	3.77	5.77	4.00	57411.5938	5.0000	0.7689	
77	97.34	-15.06	2.86	3.94	57966.3906	5.0000	0.7921	
111	96.46	-5.08	3.54	3.78	55790.2656	14.3759	0.8013	
117	6.66	-9.98	9.12	3.27	55227.0000	69.3446	0.8183	
94	25.91	7.61	24.88	3.40	56859.0508	99.0618	0.8241	
84	39.94	13.64	23.44	4.00	58516.4336	221.2949	0.8317	
14	235.34	19.76	10.65	2.42	58482.0586	75.8464	0.8405	
89	77.12	7.68	4.52	4.00	57328.8672	5.0000	0.8437	
58	194.20	-3.81	6.96	2.76	55442.5664	224.2951	0.8436	
76	310.55	6.39	9.45	2.80	55955.8125	23.3402	0.8526	
67	214.12	-0.71	6.49	3.58	57509.4023	21.6424	0.8684	
29	205.30	-2.65	6.59	3.19	56483.9531	6.8775	0.8706	
64	312.23	60.79	5.30	2.32	56902.9258	6.8139	0.8784	
9	111.16	-0.21	6.61	2.97	58058.7109	19.1716	0.9042	
13	137.87	-2.87	20.28	3.26	57963.1055	385.9940	0.9014	
68	122.43	-1.08	9.92	3.52	55389.4336	127.3298	0.9058	
56	280.64	30.35	12.20	2.57	57864.8789	153.2840	0.9104	
41	345.19	1.40	8.92	3.69	55980.0977	34.6768	0.9304	
116	30.54	-11.15	3.03	2.49	57403.2852	5.0000	0.9257	
42	293.51	33.32	4.21	4.00	56102.2188	5.0000	0.9398	
38	287.16	19.47	10.07	4.00	55636.9180	45.2478	0.9606	
45	346.71	18.24	12.32	2.61	55259.0781	143.0812	0.9670	
118	263.21	42.52	6.51	3.44	56063.5625	5.5481	0.9770	

Continued on next page

Table D.1 – continued from previous page

Index	RA [deg]	Dec [deg]	$n_S$	$\gamma$	$\mu_T$	$\sigma_T$	$p_{local}$	$p_{global}$
71	191.42	35.21	4.87	1.60	55301.3594	41.7014	0.9944	

Table D.1: The results of the time-dependent analysis. The first column contains the alert index as in Table A.1. The next two columns list the best-fit position. The fourth and fifth column contain the best-fit parameter of the likelihood optimization  $n_S$  and  $\gamma$ . The sixth and seventh column list the best-fit results for the Gaussian time window with mean  $\mu_T$  and width  $\sigma_t$ . The second to last column shows the local p-values, and the last column the corrected global p-value of the analysis.

## D.1 P-value distribution and parameter distribution

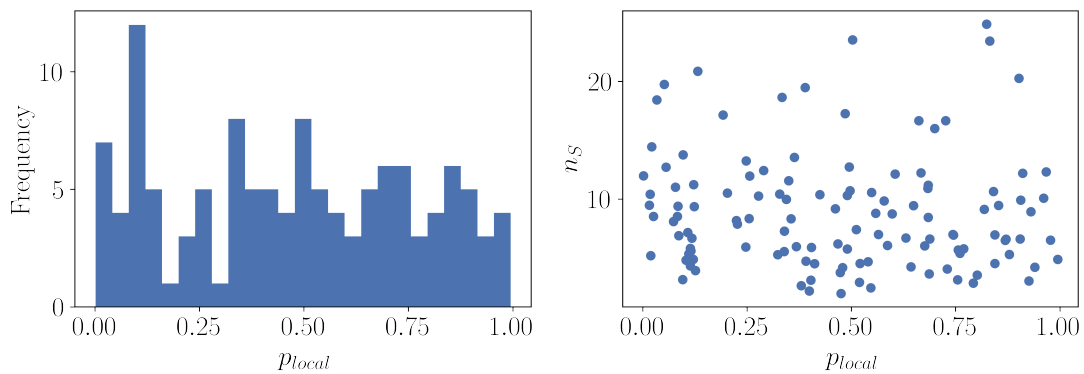


Figure D.1: **Left:** The distribution of local p-values from the time-dependent search. **Right:** P-values vs. the fitted  $n_S$  values.

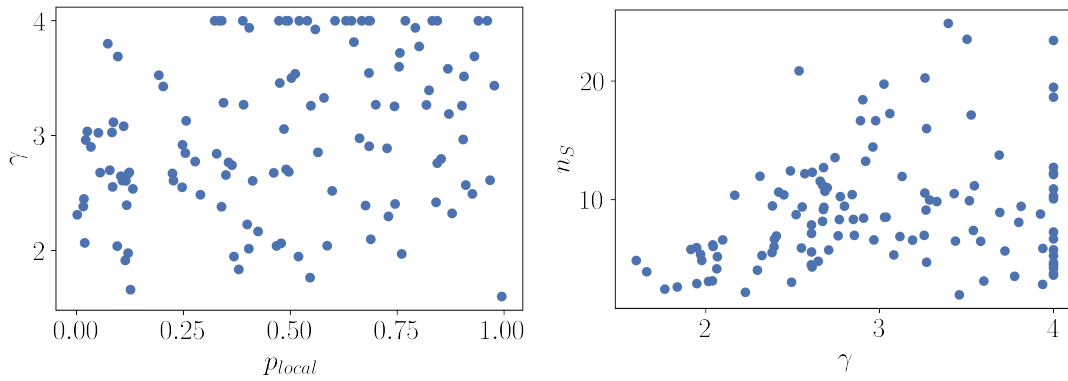


Figure D.2: **Left:** Local p-value vs. the fitted  $\gamma$  values. **Right:** The fitted spectral indices  $\gamma$  vs. the fitted  $n_S$ . Softer emission with a higher spectral index requires more signal neutrinos.

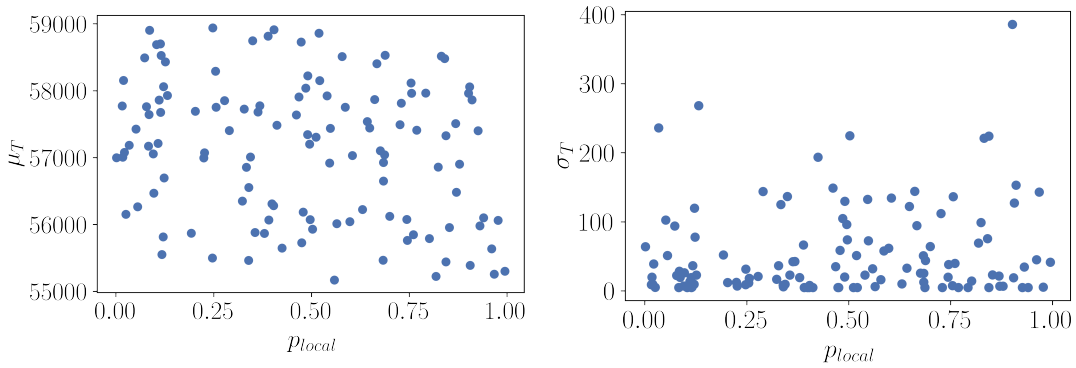


Figure D.3: **Left:** P-value vs. the fitted  $\mu_T$ . **Right:** P-value vs. the fitted  $\sigma_T$ .

## D.2 Event views of top 9 contributing events to TXS 0506+056 neutrino flare

This section shows event views of the top 9 contributing event to the neutrino flare of TXS 0506+056 as seen by the IceCube detector. The grey lines are the strings of the IceCube detector and each dot corresponds to a DOM. The bubbles show the DOMs where light has been detected. The size of the bubble scales with the amount of light (and hence energy) deposited in a DOM. The color indicates the photon arrival time, with red for early arrival times and blue for later arrival times. The red arrow displays the reconstructed track of the traversing muon.

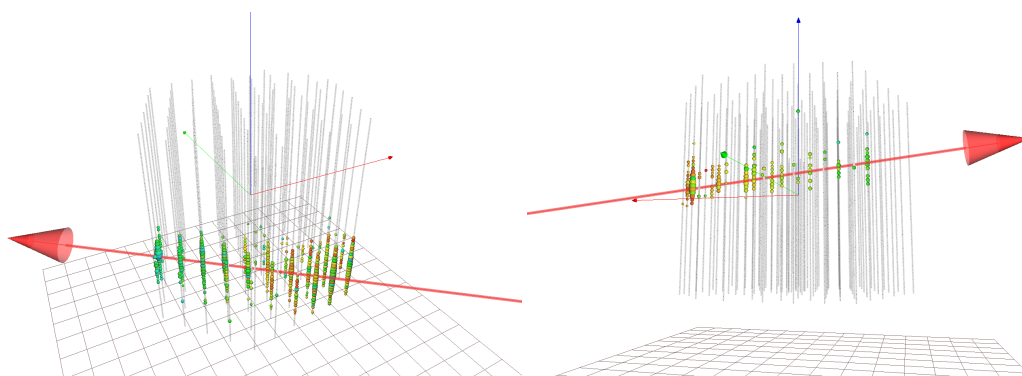


Figure D.4: Event view of the two most contributing events to the neutrino flare of TXS 0506+056

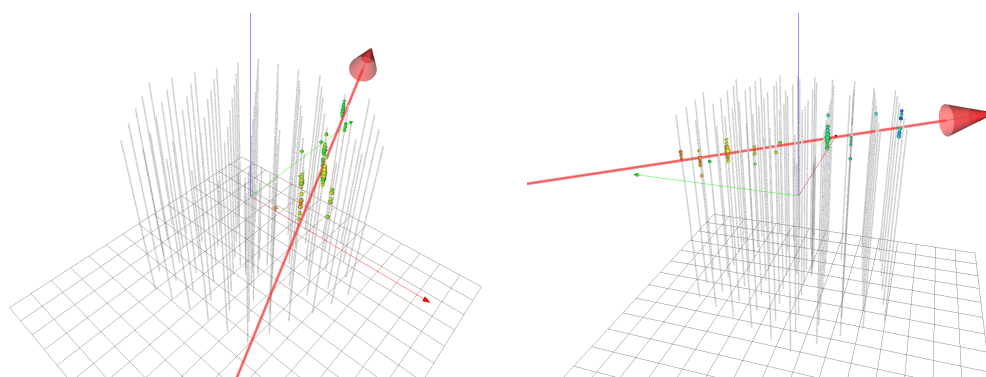


Figure D.5: Event view of the 3rd and 4th most contributing events to the neutrino flare of TXS 0506+056

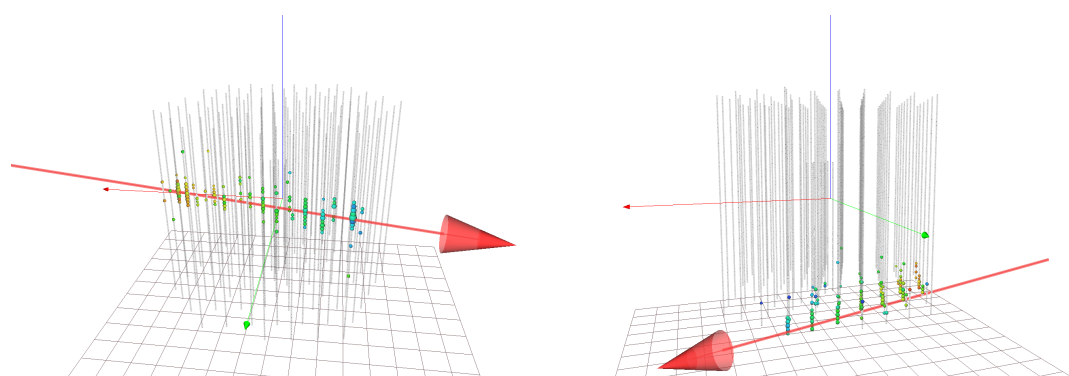


Figure D.6: Event view of the 5th and 6th most contributing events to the neutrino flare of TXS 0506+056

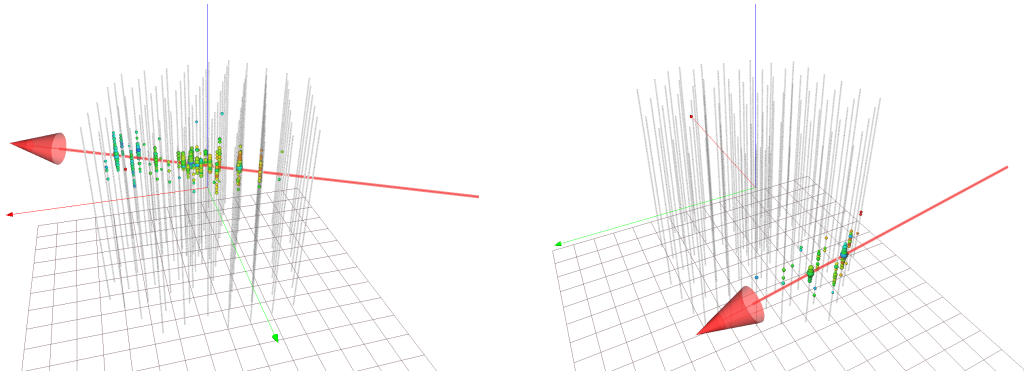


Figure D.7: Event view of the 7th and 8th most contributing events to the neutrino flare of TXS 0506+056

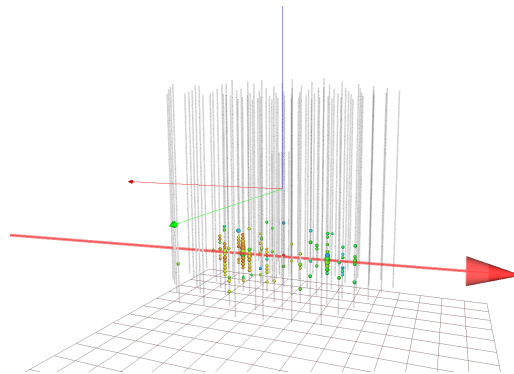


Figure D.8: Event view of the 9th most contributing events to the neutrino flare of TXS 0506+056

## Bibliography

- [1] K. Kotera and A. V. Olinto, “The Astrophysics of Ultrahigh-Energy Cosmic Rays”, *Annual Review of Astronomy and Astrophysics*, vol. 49, no. 1, pp. 119–153, 2011. DOI: 10.1146/annurev-astro-081710-102620. eprint: <https://doi.org/10.1146/annurev-astro-081710-102620>. [Online]. Available: <https://doi.org/10.1146/annurev-astro-081710-102620>.
- [2] V. F. Hess, “Über Beobachtungen der durchdringenden Strahlung bei sieben Freiballonfahrten”, *Phys. Z.*, vol. 13, pp. 1084–1091, 1912.
- [3] T. Bister, “Anisotropies in the arrival directions of ultra-high-energy cosmic rays measured at the Pierre Auger Observatory”, *Phys. Scripta*, vol. 96, no. 7, p. 074003, 2021. DOI: 10.1088/1402-4896/abf451.
- [4] M. G. Hauser and E. Dwek, “The Cosmic Infrared Background: Measurements and Implications”, *Annual Review of Astronomy and Astrophysics*, vol. 39, no. 1, pp. 249–307, 2001. DOI: 10.1146/annurev.astro.39.1.249. eprint: <https://doi.org/10.1146/annurev.astro.39.1.249>.
- [5] MAGIC Collaboration, J. Albert, E. Aliu, *et al.*, “Very-High-Energy gamma rays from a Distant Quasar: How Transparent Is the Universe?”, *Science*, vol. 320, no. 5884, p. 1752, Jun. 2008. DOI: 10.1126/science.1157087. arXiv: 0807.2822 [astro-ph].
- [6] M. Ackermann, M. Ajello, A. Allafort, *et al.*, “The Imprint of the Extragalactic Background Light in the Gamma-Ray Spectra of Blazars”, *Science*, vol. 338, no. 6111, p. 1190, Nov. 2012. DOI: 10.1126/science.1227160. arXiv: 1211.1671 [astro-ph.CO].
- [7] F. W. Stecker, M. A. Malkan, and S. T. Scully, “Intergalactic Photon Spectra from the Far-IR to the UV Lyman Limit for  $0 < z < 6$  and the Optical Depth of the Universe to High-Energy Gamma Rays”, *The Astrophysical Journal*, vol. 648, no. 2, pp. 774–783, Sep. 2006, ISSN: 1538-4357. DOI: 10.1086/506188. [Online]. Available: <http://dx.doi.org/10.1086/506188>.

- [8] F. Halzen and D. Hooper, “High-energy neutrino astronomy: the cosmic ray connection”, *Reports on Progress in Physics*, vol. 65, no. 7, pp. 1025–1078, Jun. 2002. DOI: 10.1088/0034-4885/65/7/201. [Online]. Available: <https://doi.org/10.1088/0034-4885/65/7/201>.
- [9] IceCube Collaboration, “Evidence for High-Energy Extraterrestrial Neutrinos at the IceCube Detector”, *Science*, vol. 342, no. 6161, 1242856, p. 1242856, Nov. 2013. DOI: 10.1126/science.1242856. arXiv: 1311.5238 [astro-ph.HE].
- [10] M. Aartsen, M. Ackermann, J. Adams, *et al.*, “The IceCube Neutrino Observatory: instrumentation and online systems”, *Journal of Instrumentation*, vol. 12, no. 03, P03012–P03012, Mar. 2017, ISSN: 1748-0221. DOI: 10.1088/1748-0221/12/03/p03012. [Online]. Available: <http://dx.doi.org/10.1088/1748-0221/12/03/P03012>.
- [11] C. M. Urry and P. Padovani, “Unified Schemes for Radio-Loud Active Galactic Nuclei”, *PASP*, vol. 107, p. 803, Sep. 1995. DOI: 10.1086/133630. arXiv: astro-ph/9506063 [astro-ph].
- [12] M. G. Aartsen *et al.*, “Multimessenger observations of a flaring blazar coincident with high-energy neutrino IceCube-170922A”, *Science*, vol. 361, eaat1378, 2018. DOI: 10.1126/science.aat1378. eprint: arXiv:1807.08816.
- [13] S. Ansoldi, L. A. Antonelli, C. Arcaro, *et al.*, “The Blazar TXS 0506+056 Associated with a High-energy Neutrino: Insights into Extragalactic Jets and Cosmic-Ray Acceleration”, *ApJ*, vol. 863, no. 1, L10, p. L10, Aug. 2018. DOI: 10.3847/2041-8213/aad083. arXiv: 1807.04300 [astro-ph.HE].
- [14] P. Padovani, P. Giommi, E. Resconi, *et al.*, “Dissecting the region around IceCube-170922A: the blazar TXS 0506+056 as the first cosmic neutrino source”, *MNRAS*, vol. 480, no. 1, pp. 192–203, Oct. 2018. DOI: 10.1093/mnras/sty1852. arXiv: 1807.04461 [astro-ph.HE].
- [15] A. U. Abeysekera, A. Archer, W. Benbow, *et al.*, “VERITAS Observations of the BL Lac Object TXS 0506+056”, *ApJ*, vol. 861, no. 2, L20, p. L20, Jul. 2018. DOI: 10.3847/2041-8213/aad053. arXiv: 1807.04607 [astro-ph.HE].
- [16] M. G. Aartsen *et al.*, “Neutrino emission from the direction of the blazar TXS 0506+056 prior to the IceCube-170922A alert”, *Science*, vol. 361, pp. 147–151, 2018. DOI: 10.1126/science.aat2890. arXiv: 1807.08794 [astro-ph.HE].
- [17] T. K. Gaisser, R. Engel, and E. Resconi, “Frontmatter”, in *Cosmic Rays and Particle Physics*, 2nd ed. Cambridge University Press, 2016, pp. i–iv.
- [18] T. Glauch, “The Origin of High-Energy Cosmic Particles: IceCube Neutrinos and the Blazar Case”, Dissertation, Technische Universität München, München, 2021.

- [19] B. Peters, “Primary cosmic radiation and extensive air showers”, *Il Nuovo Cimento*, vol. 22, no. 4, pp. 800–819, Nov. 1961. doi: 10.1007/BF02783106.
- [20] A. M. Hillas, “Cosmic Rays: Recent Progress and some Current Questions”, *arXiv e-prints*, astro-ph/0607109, astro-ph/0607109, Jul. 2006. arXiv: astro-ph/0607109 [astro-ph].
- [21] T. K. Gaisser, “Spectrum of cosmic-ray nucleons, kaon production, and the atmospheric muon charge ratio”, *Astroparticle Physics*, vol. 35, no. 12, pp. 801–806, Jul. 2012. doi: 10.1016/j.astropartphys.2012.02.010. arXiv: 1111.6675 [astro-ph.HE].
- [22] M. Aguilar, D. Aisa, B. Alpat, *et al.*, “Precision measurement of the proton flux in primary cosmic rays from rigidity 1 gv to 1.8 tv with the alpha magnetic spectrometer on the international space station”, *Phys. Rev. Lett.*, vol. 114, p. 171 103, 17 Apr. 2015. doi: 10.1103/PhysRevLett.114.171103. [Online]. Available: <https://link.aps.org/doi/10.1103/PhysRevLett.114.171103>.
- [23] Y. S. Yoon, T. Anderson, A. Barrau, *et al.*, “Proton and Helium Spectra from the CREAM-III Flight”, *The Astrophysical Journal*, vol. 839, no. 1, p. 5, Apr. 2017, ISSN: 1538-4357. doi: 10.3847/1538-4357/aa68e4. [Online]. Available: <http://dx.doi.org/10.3847/1538-4357/aa68e4>.
- [24] R. Alfaro, C. Alvarez, J. D. Álvarez, *et al.*, “All-particle cosmic ray energy spectrum measured by the HAWC experiment from 10 to 500 TeV”, *Physical Review D*, vol. 96, no. 12, Dec. 2017, ISSN: 2470-0029. doi: 10.1103/physrevd.96.122001. [Online]. Available: <http://dx.doi.org/10.1103/PhysRevD.96.122001>.
- [25] M. Amenomori, X. J. Bi, D. Chen, *et al.*, “The All-Particle Spectrum of Primary Cosmic Rays in the Wide Energy Range from 1014 to 1017 eV Observed with the Tibet-III Air-Shower Array”, *The Astrophysical Journal*, vol. 678, no. 2, pp. 1165–1179, May 2008, ISSN: 1538-4357. doi: 10.1086/529514. [Online]. Available: <http://dx.doi.org/10.1086/529514>.
- [26] M. G. Aartsen, R. Abbasi, Y. Abdou, *et al.*, “Measurement of the cosmic ray energy spectrum with IceTop-73”, *Physical Review D*, vol. 88, no. 4, Aug. 2013, ISSN: 1550-2368. doi: 10.1103/physrevd.88.042004. [Online]. Available: <http://dx.doi.org/10.1103/PhysRevD.88.042004>.
- [27] S. Ter-Antonyan, “Sharp knee phenomenon of primary cosmic ray energy spectrum”, *Physical Review D*, vol. 89, no. 12, Jun. 2014, ISSN: 1550-2368. doi: 10.1103/physrevd.89.123003. [Online]. Available: <http://dx.doi.org/10.1103/PhysRevD.89.123003>.

- [28] T. Antoni, W. Apel, A. Badea, *et al.*, “KASCADE measurements of energy spectra for elemental groups of cosmic rays: Results and open problems”, *Astroparticle Physics*, vol. 24, no. 1-2, pp. 1–25, Sep. 2005, ISSN: 0927-6505. DOI: 10.1016/j.astropartphys.2005.04.001. [Online]. Available: <http://dx.doi.org/10.1016/j.astropartphys.2005.04.001>.
- [29] W. Apel, J. Arteaga-Velázquez, K. Bekk, *et al.*, “The spectrum of high-energy cosmic rays measured with KASCADE-Grande”, *Astroparticle Physics*, vol. 36, no. 1, pp. 183–194, Aug. 2012, ISSN: 0927-6505. DOI: 10.1016/j.astropartphys.2012.05.023. [Online]. Available: <http://dx.doi.org/10.1016/j.astropartphys.2012.05.023>.
- [30] T. Abu-Zayyad, K. Belov, D. J. Bird, *et al.*, “Measurement of the Cosmic-Ray Energy Spectrum and Composition from 1017 to 1018.3eV Using a Hybrid Technique”, *The Astrophysical Journal*, vol. 557, no. 2, pp. 686–699, Aug. 2001, ISSN: 1538-4357. DOI: 10.1086/322240. [Online]. Available: <http://dx.doi.org/10.1086/322240>.
- [31] R. U. Abbasi, T. Abu-Zayyad, M. Allen, *et al.*, “First Observation of the Greisen-Zatsepin-Kuzmin Suppression”, *Physical Review Letters*, vol. 100, no. 10, Mar. 2008, ISSN: 1079-7114. DOI: 10.1103/PhysRevLett.100.101101. [Online]. Available: <http://dx.doi.org/10.1103/PhysRevLett.100.101101>.
- [32] Y. Tsunesada, T. AbuZayyad, D. Ivanov, *et al.*, “Energy Spectrum of Ultra-High-Energy Cosmic Rays Measured by The Telescope Array”, in *35th International Cosmic Ray Conference (ICRC2017)*, ser. International Cosmic Ray Conference, vol. 301, Jan. 2017, p. 535.
- [33] M. Huber, “Multi-Messenger correlation study of Fermi-LAT blazars and high-energy neutrinos observed in IceCube”, Dissertation, Technische Universität München, München, 2020.
- [34] A. M. Hillas, “The Origin of Ultra-High-Energy Cosmic Rays”, *ARA&A*, vol. 22, pp. 425–444, Jan. 1984. DOI: 10.1146/annurev.aa.22.090184.002233.
- [35] K. Greisen, “End to the Cosmic-Ray Spectrum?”, *Phys. Rev. Lett.*, vol. 16, pp. 748–750, 17 Apr. 1966. DOI: 10.1103/PhysRevLett.16.748. [Online]. Available: <https://link.aps.org/doi/10.1103/PhysRevLett.16.748>.
- [36] G. T. Zatsepin and V. A. Kuz'min, “Upper Limit of the Spectrum of Cosmic Rays”, *Soviet Journal of Experimental and Theoretical Physics Letters*, vol. 4, p. 78, Aug. 1966.
- [37] T. Stanev, *High Energy Cosmic Rays*, ser. Springer Praxis Books. Springer Berlin Heidelberg, 2021, ISBN: 9783030715670.

- [38] E. Fermi, “On the Origin of the Cosmic Radiation”, *Phys. Rev.*, vol. 75, pp. 1169–1174, 8 Apr. 1949. DOI: 10.1103/PhysRev.75.1169. [Online]. Available: <https://link.aps.org/doi/10.1103/PhysRev.75.1169>.
- [39] L. O. Drury, “REVIEW ARTICLE: An introduction to the theory of diffusive shock acceleration of energetic particles in tenuous plasmas”, *Reports on Progress in Physics*, vol. 46, no. 8, pp. 973–1027, Aug. 1983. DOI: 10.1088/0034-4885/46/8/002.
- [40] R. Blandford and D. Eichler, “Particle acceleration at astrophysical shocks: A theory of cosmic ray origin”, *Phys. Rep.*, vol. 154, no. 1, pp. 1–75, Oct. 1987. DOI: 10.1016/0370-1573(87)90134-7.
- [41] S. Woosley and T. Janka, “The physics of core-collapse supernovae”, *Nature Physics*, vol. 1, no. 3, pp. 147–154, Dec. 2005, ISSN: 1745-2481. DOI: 10.1038/nphys172. [Online]. Available: <http://dx.doi.org/10.1038/nphys172>.
- [42] S. P. Reynolds, “Supernova Remnants at High Energy”, *Annual Review of Astronomy and Astrophysics*, vol. 46, no. 1, pp. 89–126, 2008. DOI: 10.1146/annurev.astro.46.060407.145237. eprint: <https://doi.org/10.1146/annurev.astro.46.060407.145237>.
- [43] M. Spurio, *Probes of Multimessenger Astrophysics*. 2018. DOI: 10.1007/978-3-319-96854-4.
- [44] J. C. Mihos and L. Hernquist, “Gasdynamics and Starbursts in Major Mergers”, *The Astrophysical Journal*, vol. 464, p. 641, Jun. 1996, ISSN: 1538-4357. DOI: 10.1086/177353. [Online]. Available: <http://dx.doi.org/10.1086/177353>.
- [45] V. Springel, T. di Matteo, and L. Hernquist, “Modelling feedback from stars and black holes in galaxy mergers”, *Monthly Notices of the Royal Astronomical Society*, vol. 361, no. 3, pp. 776–794, Aug. 2005, ISSN: 0035-8711. DOI: 10.1111/j.1365-2966.2005.09238.x. eprint: <https://academic.oup.com/mnras/article-pdf/361/3/776/2939002/361-3-776.pdf>. [Online]. Available: <https://doi.org/10.1111/j.1365-2966.2005.09238.x>.
- [46] N. A. Reddy, D. K. Erb, C. C. Steidel, *et al.*, “A census of optical and near-infrared selected star-forming and passively evolving galaxies at redshift  $z \sim 2$ ”, *The Astrophysical Journal*, vol. 633, no. 2, p. 748, 2005.
- [47] S. Juneau, K. Glazebrook, D. Crampton, *et al.*, “Cosmic star formation history and its dependence on galaxy stellar mass”, *The Astrophysical Journal Letters*, vol. 619, no. 2, p. L135, 2005.
- [48] I. Tamborra, S. Ando, and K. Murase, “Star-forming galaxies as the origin of diffuse high-energy backgrounds: gamma-ray and neutrino connections, and implications for starburst history”, *Journal of Cosmology and Astroparticle*

- Physics*, vol. 2014, no. 09, pp. 043–043, Sep. 2014, ISSN: 1475-7516. DOI: 10.1088/1475-7516/2014/09/043. [Online]. Available: <http://dx.doi.org/10.1088/1475-7516/2014/09/043>.
- [49] H. Dannerbauer, D. Rigopoulou, D. Lutz, *et al.*, “Follow-up near-infrared spectroscopy of ultraluminous infrared galaxies observed by ISO”, *Astronomy & Astrophysics*, vol. 441, no. 3, pp. 999–1010, 2005.
- [50] S. R. Kulkarni, D. A. Frail, M. H. Wieringa, *et al.*, “Radio emission from the unusual supernova 1998bw and its association with the  $\gamma$ -ray burst of 25 April 1998”, *Nature*, vol. 395, no. 6703, pp. 663–669, Oct. 1998. DOI: 10.1038/27139.
- [51] D. Eichler, M. Livio, T. Piran, *et al.*, “Nucleosynthesis, neutrino bursts and  $\gamma$ -rays from coalescing neutron stars”, *Nature*, vol. 340, no. 6229, pp. 126–128, Jul. 1989. DOI: 10.1038/340126a0.
- [52] R. Narayan, B. Paczynski, and T. Piran, “Gamma-ray bursts as the death throes of massive binary stars”, *The Astrophysical Journal*, vol. 395, p. L83, Aug. 1992, ISSN: 1538-4357. DOI: 10.1086/186493. [Online]. Available: <http://dx.doi.org/10.1086/186493>.
- [53] P. Padovani, D. M. Alexander, R. J. Assef, *et al.*, “Active galactic nuclei: what’s in a name?”, *The Astronomy and Astrophysics Review*, vol. 25, no. 1, Aug. 2017, ISSN: 1432-0754. DOI: 10.1007/s00159-017-0102-9. [Online]. Available: <http://dx.doi.org/10.1007/s00159-017-0102-9>.
- [54] C. M. Urry and P. Padovani, “Unified Schemes for Radio-Loud Active Galactic Nuclei”, *Publications of the Astronomical Society of the Pacific*, vol. 107, p. 803, Sep. 1995, ISSN: 1538-3873. DOI: 10.1086/133630. [Online]. Available: <http://dx.doi.org/10.1086/133630>.
- [55] M. G. Aartsen, M. Ackermann, J. Adams, *et al.*, “Time-Integrated Neutrino Source Searches with 10 Years of IceCube Data”, *Physical Review Letters*, vol. 124, no. 5, Feb. 2020, ISSN: 1079-7114. DOI: 10.1103/physrevlett.124.051103. [Online]. Available: <http://dx.doi.org/10.1103/PhysRevLett.124.051103>.
- [56] R. Abbasi, M. Ackermann, J. Adams, *et al.*, “Search for Multi-flare Neutrino Emissions in 10 yr of IceCube Data from a Catalog of Sources”, *ApJ*, vol. 920, no. 2, L45, p. L45, Oct. 2021. DOI: 10.3847/2041-8213/ac2c7b. arXiv: 2109.05818 [astro-ph.HE].
- [57] P. Giommi, T. Glauch, P. Padovani, *et al.*, “Dissecting the regions around icecube high-energy neutrinos: Growing evidence for the blazar connection”, *Monthly Notices of the Royal Astronomical Society*, vol. 497, no. 1, pp. 865–878,

- Jul. 2020, ISSN: 1365-2966. DOI: 10.1093/mnras/staa2082. [Online]. Available: <http://dx.doi.org/10.1093/mnras/staa2082>.
- [58] P. Zyla *et al.*, “Review of Particle Physics”, *PTEP*, vol. 2020, no. 8, p. 083C01, 2020. DOI: 10.1093/ptep/ptaa104.
- [59] P. B. Dev, D. Kazanas, R. Mohapatra, *et al.*, “Heavy right-handed neutrino dark matter and PeV neutrinos at IceCube”, *Journal of Cosmology and Astroparticle Physics*, vol. 2016, no. 08, pp. 034–034, Aug. 2016, ISSN: 1475-7516. DOI: 10.1088/1475-7516/2016/08/034. [Online]. Available: <http://dx.doi.org/10.1088/1475-7516/2016/08/034>.
- [60] M. Spurio, *Particles and Astrophysics: A Multi-Messenger Approach*, ser. Astronomy and Astrophysics Library. Springer International Publishing, 2017, ISBN: 9783319345390. [Online]. Available: <https://books.google.de/books?id=u8rgAQAACAAJ>.
- [61] K. Murase and I. Bartos, “High-Energy Multimessenger Transient Astrophysics”, *Annual Review of Nuclear and Particle Science*, vol. 69, no. 1, pp. 477–506, 2019. DOI: 10.1146/annurev-nucl-101918-023510. eprint: <https://doi.org/10.1146/annurev-nucl-101918-023510>. [Online]. Available: <https://doi.org/10.1146/annurev-nucl-101918-023510>.
- [62] M. Aartsen *et al.*, “Evidence for High-Energy Extraterrestrial Neutrinos at the IceCube Detector”, *Science*, vol. 342, no. 6161, 2013, ISSN: 0036-8075. DOI: 10.1126/science.1242856. eprint: <https://science.sciencemag.org/content/342/6161/1242856.full.pdf>. [Online]. Available: <https://science.sciencemag.org/content/342/6161/1242856>.
- [63] M. G. Aartsen, M. Ackermann, J. Adams, *et al.*, “Characteristics of the Diffuse Astrophysical Electron and Tau Neutrino Flux with Six Years of IceCube High Energy Cascade Data”, *Phys. Rev. Lett.*, vol. 125, no. 12, 121104, p. 121 104, Sep. 2020. DOI: 10.1103/PhysRevLett.125.121104.
- [64] J. Stettner, *Measurement of the Diffuse Astrophysical Muon-Neutrino Spectrum with Ten Years of IceCube Data*, 2019. arXiv: 1908.09551 [astro-ph.HE].
- [65] H. Niederhausen and Y. Xu, “High Energy Astrophysical Neutrino Flux Measurement Using Neutrino-induced Cascades Observed in 4 Years of IceCube Data”, in *Proceedings of 35th International Cosmic Ray Conference — PoS(ICRC2017)*, vol. 301, 2017, p. 968. DOI: 10.22323/1.301.0968.
- [66] A. Schneider, *Characterization of the Astrophysical Diffuse Neutrino Flux with IceCube High-Energy Starting Events*, 2019. arXiv: 1907.11266 [astro-ph.HE].
- [67] D. Seckel, T. Stanev, and T. K. Gaisser, “Signatures of Cosmic-Ray Interactions on the Solar Surface”, *ApJ*, vol. 382, p. 652, Dec. 1991. DOI: 10.1086/170753.

- [68] G. Ingelman and M. Thunman, “High energy neutrino production by cosmic ray interactions in the Sun”, *Phys. Rev. D*, vol. 54, no. 7, pp. 4385–4392, Oct. 1996. DOI: 10.1103/PhysRevD.54.4385. arXiv: hep-ph/9604288 [hep-ph].
- [69] K. C. Y. Ng, J. F. Beacom, A. H. G. Peter, *et al.*, “Solar atmospheric neutrinos: A new neutrino floor for dark matter searches”, *Phys. Rev. D*, vol. 96, no. 10, 103006, p. 103 006, Nov. 2017. DOI: 10.1103/PhysRevD.96.103006. arXiv: 1703.10280 [astro-ph.HE].
- [70] S. Meighen-Berger, “Precision background modeling for neutrino telescopes”, Dissertation, Technische Universität München, München, 2021.
- [71] P. H. Barrett, L. M. Bollinger, G. Cocconi, *et al.*, “Interpretation of Cosmic-Ray Measurements Far Underground”, *Reviews of Modern Physics*, vol. 24, no. 3, pp. 133–178, Jul. 1952. DOI: 10.1103/RevModPhys.24.133.
- [72] R. P. Feynman, “Very High-Energy Collisions of Hadrons”, *Phys. Rev. Lett.*, vol. 23, pp. 1415–1417, 24 Dec. 1969. DOI: 10.1103/PhysRevLett.23.1415. [Online]. Available: <https://link.aps.org/doi/10.1103/PhysRevLett.23.1415>.
- [73] E. Vitagliano, I. Tamborra, and G. Raffelt, “Grand unified neutrino spectrum at Earth: Sources and spectral components”, *Reviews of Modern Physics*, vol. 92, no. 4, 045006, p. 045 006, Oct. 2020. DOI: 10.1103/RevModPhys.92.045006. arXiv: 1910.11878 [astro-ph.HE].
- [74] A. Fedynitch, R. Engel, T. K. Gaisser, *et al.*, “Calculation of conventional and prompt lepton fluxes at very high energy”, in *European Physical Journal Web of Conferences*, ser. European Physical Journal Web of Conferences, vol. 99, Aug. 2015, p. 08 001. DOI: 10.1051/epjconf/20159908001. arXiv: 1503.00544 [hep-ph].
- [75] B. Pontecorvo, “Mesonium and Antimesonium”, *Soviet Journal of Experimental and Theoretical Physics*, vol. 6, p. 429, Jan. 1958.
- [76] Z. Maki, M. Nakagawa, and S. Sakata, “Remarks on the Unified Model of Elementary Particles”, *Progress of Theoretical Physics*, vol. 28, no. 5, pp. 870–880, Nov. 1962. DOI: 10.1143/PTP.28.870.
- [77] I. Esteban, M. C. Gonzalez-Garcia, A. Hernandez-Cabezudo, *et al.*, “Global analysis of three-flavour neutrino oscillations: synergies and tensions in the determination of  $\theta_{23}$ ,  $\delta_{CP}$ , and the mass ordering”, *Journal of High Energy Physics*, vol. 2019, no. 1, 106, p. 106, Jan. 2019. DOI: 10.1007/JHEP01(2019)106. arXiv: 1811.05487 [hep-ph].
- [78] P. de Salas, D. Forero, C. Ternes, *et al.*, “Status of neutrino oscillations 2018:  $3\sigma$  hint for normal mass ordering and improved CP sensitivity”, *Physics Letters*

- B*, vol. 782, pp. 633–640, 2018, ISSN: 0370-2693. DOI: <https://doi.org/10.1016/j.physletb.2018.06.019>. [Online]. Available: <https://www.sciencedirect.com/science/article/pii/S0370269318304672>.
- [79] I. Ribas, C. Jordi, F. Vilardell, *et al.*, “First Determination of the Distance and Fundamental Properties of an Eclipsing Binary in the Andromeda Galaxy”, *The Astrophysical Journal*, vol. 635, no. 1, pp. L37–L40, Nov. 2005, ISSN: 1538-4357. DOI: 10.1086/499161. [Online]. Available: <http://dx.doi.org/10.1086/499161>.
- [80] M. Ahlers, K. Helbing, and C. Pérez de los Heros, “Probing particle physics with IceCube”, *European Physical Journal C*, vol. 78, no. 11, p. 924, Nov. 2018. DOI: 10.1140/epjc/s10052-018-6369-9. arXiv: 1806.05696 [astro-ph.HE].
- [81] S. L. Glashow, “Resonant Scattering of Antineutrinos”, *Phys. Rev.*, vol. 118, pp. 316–317, 1 Apr. 1960. DOI: 10.1103/PhysRev.118.316. [Online]. Available: <https://link.aps.org/doi/10.1103/PhysRev.118.316>.
- [82] M. G. Aartsen, R. Abbasi, M. Ackermann, *et al.*, “Detection of a particle shower at the Glashow resonance with IceCube”, *Nature*, vol. 591, no. 7849, pp. 220–224, Mar. 2021, ISSN: 1476-4687. DOI: 10.1038/s41586-021-03256-1. [Online]. Available: <http://dx.doi.org/10.1038/s41586-021-03256-1>.
- [83] A. Cooper-Sarkar, P. Mertsch, and S. Sarkar, “The high energy neutrino cross-section in the Standard Model and its uncertainty”, *Journal of High Energy Physics*, vol. 2011, no. 8, Aug. 2011, ISSN: 1029-8479. DOI: 10.1007/jhep08(2011)042. [Online]. Available: [http://dx.doi.org/10.1007/JHEP08\(2011\)042](http://dx.doi.org/10.1007/JHEP08(2011)042).
- [84] R. Gandhi, C. Quigg, M. Hall Reno, *et al.*, “Ultra-high-energy neutrino interactions”, *Astroparticle Physics*, vol. 5, no. 2, pp. 81–110, Aug. 1996. DOI: 10.1016/0927-6505(96)00008-4. arXiv: hep-ph/9512364 [hep-ph].
- [85] A. Palladino, M. Spurio, and F. Vissani, “Neutrino Telescopes and High-Energy Cosmic Neutrinos”, *Universe*, vol. 6, no. 2, p. 30, 2020. DOI: 10.3390/universe6020030. arXiv: 2009.01919 [astro-ph.HE].
- [86] M. G. Aartsen, G. C. Hill, A. Kyriacou, *et al.*, “Measurement of the multi-TeV neutrino interaction cross-section with IceCube using Earth absorption”, *Nature*, vol. 551, no. 7682, pp. 596–600, Nov. 2017. DOI: 10.1038/nature24459. arXiv: 1711.08119 [hep-ex].
- [87] A. M. Dziewonski and D. L. Anderson, “Preliminary reference Earth model”, *Physics of the Earth and Planetary Interiors*, vol. 25, no. 4, pp. 297–356, Jun. 1981. DOI: 10.1016/0031-9201(81)90046-7.

- [88] L. Landau and E. Lifshitz, “Chapter XIV - The Passage Of Fast Particles Through Matter”, in *Electrodynamics of Continuous Media (Second Edition)*, ser. Course of Theoretical Physics, L. Landau and E. Lifshitz, Eds., Second Edition, vol. 8, Amsterdam: Pergamon, 1984, pp. 394–412, ISBN: 978-0-08-030275-1. DOI: <https://doi.org/10.1016/B978-0-08-030275-1.50020-5>. [Online]. Available: <https://www.sciencedirect.com/science/article/pii/B9780080302751500205>.
- [89] I. Frank and I. Tamm, “Coherent Visible Radiation of Fast Electrons Passing Through Matter”, in *Selected Papers*, B. M. Bolotovskii, V. Y. Frenkel, and R. Peierls, Eds. Berlin, Heidelberg: Springer Berlin Heidelberg, 1991, pp. 29–35, ISBN: 978-3-642-74626-0. DOI: 10.1007/978-3-642-74626-0\_2. [Online]. Available: [https://doi.org/10.1007/978-3-642-74626-0\\_2](https://doi.org/10.1007/978-3-642-74626-0_2).
- [90] M. Ackermann, J. Ahrens, X. Bai, *et al.*, “Optical properties of deep glacial ice at the South Pole”, *Journal of Geophysical Research: Atmospheres*, vol. 111, no. D13, 2006. DOI: <https://doi.org/10.1029/2005JD006687>. eprint: <https://agupubs.onlinelibrary.wiley.com/doi/pdf/10.1029/2005JD006687>. [Online]. Available: <https://agupubs.onlinelibrary.wiley.com/doi/abs/10.1029/2005JD006687>.
- [91] M. G. Aartsen, M. Ackermann, J. Adams, *et al.*, “Search for Astrophysical Sources of Neutrinos Using Cascade Events in IceCube”, *The Astrophysical Journal*, vol. 846, no. 2, p. 136, Sep. 2017, ISSN: 1538-4357. DOI: 10.3847/1538-4357/aa8508. [Online]. Available: <http://dx.doi.org/10.3847/1538-4357/aa8508>.
- [92] J. G. Learned and S. Pakvasa, “Detecting tau-neutrino oscillations at PeV energies”, *Astroparticle Physics*, vol. 3, no. 3, pp. 267–274, May 1995, ISSN: 0927-6505. DOI: 10.1016/0927-6505(94)00043-3. [Online]. Available: [http://dx.doi.org/10.1016/0927-6505\(94\)00043-3](http://dx.doi.org/10.1016/0927-6505(94)00043-3).
- [93] L. Pasquali and M. H. Reno, “Tau neutrino fluxes from atmospheric charm”, *Physical Review D*, vol. 59, no. 9, Mar. 1999, ISSN: 1089-4918. DOI: 10.1103/physrevd.59.093003. [Online]. Available: <http://dx.doi.org/10.1103/PhysRevD.59.093003>.
- [94] E. Waxman and J. Bahcall, “High energy neutrinos from astrophysical sources: An upper bound”, *Physical Review D*, vol. 59, no. 2, Dec. 1998, ISSN: 1089-4918. DOI: 10.1103/physrevd.59.023002. [Online]. Available: <http://dx.doi.org/10.1103/PhysRevD.59.023002>.

- [95] T. K. Gaisser, “Neutrino Astronomy: Physics Goals, Detector Parameters”, *arXiv e-prints*, astro-ph/9707283, astro-ph/9707283, Jul. 1997. arXiv: astro-ph/9707283 [astro-ph].
- [96] R. Abbasi, Y. Abdou, M. Ackermann, *et al.*, “IceTop: The surface component of IceCube”, *Nuclear Instruments and Methods in Physics Research Section A: Accelerators, Spectrometers, Detectors and Associated Equipment*, vol. 700, pp. 188–220, Feb. 2013, ISSN: 0168-9002. DOI: 10.1016/j.nima.2012.10.067. [Online]. Available: <http://dx.doi.org/10.1016/j.nima.2012.10.067>.
- [97] T. I. Collaboration. (2013). IceCube Digital Optical Module, [Online]. Available: [https://gallery.icecube.wisc.edu/internal/v/GraphicRe/visuals/dom/DOMNoHarnessWhiteback\\_lg.jpg.html](https://gallery.icecube.wisc.edu/internal/v/GraphicRe/visuals/dom/DOMNoHarnessWhiteback_lg.jpg.html) (visited on 11/04/2021).
- [98] IceCube Collaboration, R. Abbasi, M. Ackermann, *et al.*, “IceCube Data for Neutrino Point-Source Searches Years 2008-2018”, *arXiv e-prints*, arXiv:2101.09836, arXiv:2101.09836, Jan. 2021. arXiv: 2101.09836 [astro-ph.HE].
- [99] M. G. Aartsen *et al.*, “The IceCube Realtime Alert System”, *Astropart. Phys.*, vol. 92, pp. 30–41, 2017. DOI: 10.1016/j.astropartphys.2017.05.002. arXiv: 1612.06028 [astro-ph.HE].
- [100] M. Aartsen, M. Ackermann, J. Adams, *et al.*, “The IceCube realtime alert system”, *Astroparticle Physics*, vol. 92, pp. 30–41, 2017, ISSN: 0927-6505. DOI: <https://doi.org/10.1016/j.astropartphys.2017.05.002>. [Online]. Available: <https://www.sciencedirect.com/science/article/pii/S0927650516302249>.
- [101] S. Coenders, “High-energy cosmic ray accelerators: searches with IceCube neutrinos”, Dissertation, Technische Universität München, München, 2016.
- [102] IceCube Collaboration, M. G. Aartsen, K. Abraham, *et al.*, “Very high-energy gamma-ray follow-up program using neutrino triggers from IceCube”, *Journal of Instrumentation*, vol. 11, no. 11, P11009, Nov. 2016. DOI: 10.1088/1748-0221/11/11/P11009. arXiv: 1610.01814 [hep-ex].
- [103] J. Ahrens, X. Bai, R. Bay, *et al.*, “Muon track reconstruction and data selection techniques in AMANDA”, *Nuclear Instruments and Methods in Physics Research Section A: Accelerators, Spectrometers, Detectors and Associated Equipment*, vol. 524, no. 1-3, pp. 169–194, May 2004, ISSN: 0168-9002. DOI: 10.1016/j.nima.2004.01.065. [Online]. Available: <http://dx.doi.org/10.1016/j.nima.2004.01.065>.
- [104] M. G. Aartsen, R. Abbasi, M. Ackermann, *et al.*, “Energy reconstruction methods in the IceCube neutrino telescope”, vol. 9, no. 03, P03009–P03009, Mar.

2014. DOI: 10.1088/1748-0221/9/03/p03009. [Online]. Available: <https://doi.org/10.1088/1748-0221/9/03/p03009>.
- [105] L. Rädcl, “Measurement of High-Energy Muon Neutrinos with the IceCube Neutrino Observatory”, Veröffentlicht auf dem Publikationsserver der RWTH Aachen University; Dissertation, RWTH Aachen University, 2017, Dissertation, RWTH Aachen University, Aachen, 2017, 1 Online-Ressource (xv, 191 Seiten) : Illustrationen, Diagramme. DOI: 10.18154/RWTH-2017-10054. [Online]. Available: <https://publications.rwth-aachen.de/record/709576>.
- [106] M. G. Aartsen, K. Abraham, M. Ackermann, *et al.*, “Observation and Characterization of a Cosmic Muon Neutrino Flux from the Northern Hemisphere using six years of IceCube data”, *The Astrophysical Journal*, vol. 833, no. 1, p. 3, Dec. 2016, ISSN: 1538-4357. DOI: 10.3847/0004-637x/833/1/3. [Online]. Available: <http://dx.doi.org/10.3847/0004-637X/833/1/3>.
- [107] M. C. R. Zoll, *Preparations for the next solar WIMP Analysis with IceCube : Advances in simulation, filtering, event topology identification and analysis approach*, 2014. [Online]. Available: <http://su.diva-portal.org/smash/record.jsf?pid=diva2%5C%3A699510&dsid=8572>.
- [108] L. Hyafil and R. L. Rivest, “Constructing optimal binary decision trees is NP-complete”, *Information Processing Letters*, vol. 5, no. 1, pp. 15–17, 1976, ISSN: 0020-0190. DOI: [https://doi.org/10.1016/0020-0190\(76\)90095-8](https://doi.org/10.1016/0020-0190(76)90095-8). [Online]. Available: <https://www.sciencedirect.com/science/article/pii/0020019076900958>.
- [109] M. G. Aartsen, K. Abraham, M. Ackermann, *et al.*, “All-sky Search for Time-integrated Neutrino Emission from Astrophysical Sources with 7 yr of IceCube Data”, *The Astrophysical Journal*, vol. 835, no. 2, p. 151, Jan. 2017, ISSN: 1538-4357. DOI: 10.3847/1538-4357/835/2/151. [Online]. Available: <http://dx.doi.org/10.3847/1538-4357/835/2/151>.
- [110] M. G. Aartsen, R. Abbasi, Y. Abdou, *et al.*, “Search for time-independent neutrino emission from astrophysical sources with 3 yr of IceCube data”, vol. 779, no. 2, p. 132, Dec. 2013. DOI: 10.1088/0004-637x/779/2/132. [Online]. Available: <https://doi.org/10.1088/0004-637x/779/2/132>.
- [111] E. Blaufuss, T. Kintscher, L. Lu, *et al.*, “The Next Generation of IceCube Real-time Neutrino Alerts”, in *Proceedings of 36th International Cosmic Ray Conference – PoS(ICRC2019)*, vol. 358, 2019, p. 1021. DOI: 10.22323/1.358.1021.
- [112] “Very high-energy gamma-ray follow-up program using neutrino triggers from icecube”, *Journal of Instrumentation*, vol. 11, no. 11, P11009, Nov. 2016,

- ISSN: 1748-0221. DOI: 10.1088/1748-0221/11/11/p11009. [Online]. Available: <http://dx.doi.org/10.1088/1748-0221/11/11/P11009>.
- [113] J. G. Learned and K. Mannheim, “High-Energy Neutrino Astrophysics”, *Annual Review of Nuclear and Particle Science*, vol. 50, no. 1, pp. 679–749, 2000. DOI: 10.1146/annurev.nucl.50.1.679. eprint: <https://doi.org/10.1146/annurev.nucl.50.1.679>. [Online]. Available: <https://doi.org/10.1146/annurev.nucl.50.1.679>.
- [114] C. Haack, “Observation of high-energy neutrinos from the galaxy and beyond”, Veröffentlicht auf dem Publikationsserver der RWTH Aachen University; Dissertation, RWTH Aachen University, 2020, Dissertation, RWTH Aachen University, Aachen, 2020, 1 Online-Ressource (xiii, 233 Seiten) : Illustrationen, Diagramme. DOI: 10.18154/RWTH-2020-07059. [Online]. Available: <https://publications.rwth-aachen.de/record/793612>.
- [115] G. Casella and R. L. Berger, *Statistical inference*. Cengage Learning, 2021.
- [116] N. van Eijndhoven, O. Fadiran, and G. Japaridze, “Implementation of a Gauss convoluted Pandel PDF for track reconstruction in neutrino telescopes”, *Astroparticle Physics*, vol. 28, no. 4-5, pp. 456–462, Dec. 2007, ISSN: 0927-6505. DOI: 10.1016/j.astropartphys.2007.09.001. [Online]. Available: <http://dx.doi.org/10.1016/j.astropartphys.2007.09.001>.
- [117] N. Whitehorn, J. van Santen, and S. Lafebre, “Penalized splines for smooth representation of high-dimensional Monte Carlo datasets”, *Computer Physics Communications*, vol. 184, no. 9, pp. 2214–2220, 2013, ISSN: 0010-4655. DOI: <https://doi.org/10.1016/j.cpc.2013.04.008>. [Online]. Available: <https://www.sciencedirect.com/science/article/pii/S0010465513001434>.
- [118] F. Bradascio and T. Glüsenkamp, “Improving the muon track reconstruction of IceCube and IceCube-Gen2”, *EPJ Web of Conferences*, vol. 207, C. Spiering, Ed., p. 05 002, 2019, ISSN: 2100-014X. DOI: 10.1051/epjconf/201920705002. [Online]. Available: <http://dx.doi.org/10.1051/epjconf/201920705002>.
- [119] M. G. Aartsen, R. Abbasi, Y. Abdou, *et al.*, “Observation of the cosmic-ray shadow of the Moon with IceCube”, *Physical Review D*, vol. 89, no. 10, May 2014, ISSN: 1550-2368. DOI: 10.1103/physrevd.89.102004. [Online]. Available: <http://dx.doi.org/10.1103/PhysRevD.89.102004>.
- [120] G. Cowan, *Statistical data analysis*. Oxford university press, 1998.
- [121] T. Neunhöffer, “Die Entwicklung eines neuen Verfahrens zur Suche nach kosmischen Neutrino-Punktquellen mit dem AMANDA-Neutrinoteleskop”, ger, PhD thesis, Mainz, 2004. DOI: <http://doi.org/10.25358/openscience-2482>.

- [122] —, “Estimating the angular resolution of tracks in neutrino telescopes based on a likelihood analysis”, *Astroparticle Physics*, vol. 25, no. 3, pp. 220–225, Apr. 2006, ISSN: 0927-6505. DOI: 10.1016/j.astropartphys.2006.01.002. [Online]. Available: <http://dx.doi.org/10.1016/j.astropartphys.2006.01.002>.
- [123] E. P. Vogel, “Noboloid - an improved likelihood estimation for angular uncertainties of muon tracks in icecube”, Master’s thesis, RWTH Aachen, 2017. [Online]. Available: [https://www.institut3b.physik.rwth-aachen.de/global/show\\_document.asp?id=aaaaaaaaaawhudl](https://www.institut3b.physik.rwth-aachen.de/global/show_document.asp?id=aaaaaaaaaawhudl).
- [124] R. Abbasi, Y. Abdou, M. Ackermann, *et al.*, “An improved method for measuring muon energy using the truncated mean of  $dE/dx$ ”, *Nuclear Instruments and Methods in Physics Research Section A: Accelerators, Spectrometers, Detectors and Associated Equipment*, vol. 703, pp. 190–198, Mar. 2013, ISSN: 0168-9002. DOI: 10.1016/j.nima.2012.11.081. [Online]. Available: <http://dx.doi.org/10.1016/j.nima.2012.11.081>.
- [125] J. Neyman and E. S. Pearson, “On the Problem of the Most Efficient Tests of Statistical Hypotheses”, *Philosophical Transactions of the Royal Society of London Series A*, vol. 231, pp. 289–337, Jan. 1933. DOI: 10.1098/rsta.1933.0009.
- [126] S. S. Wilks, “The Large-Sample Distribution of the Likelihood Ratio for Testing Composite Hypotheses”, *The Annals of Mathematical Statistics*, vol. 9, no. 1, pp. 60–62, 1938. DOI: 10.1214/aoms/1177732360. [Online]. Available: <https://doi.org/10.1214/aoms/1177732360>.
- [127] R. Barlow, “Extended maximum likelihood”, *Nuclear Instruments and Methods in Physics Research Section A: Accelerators, Spectrometers, Detectors and Associated Equipment*, vol. 297, no. 3, pp. 496–506, 1990.
- [128] R. H. Byrd, P. Lu, J. Nocedal, *et al.*, “A limited memory algorithm for bound constrained optimization”, *SIAM Journal on scientific computing*, vol. 16, no. 5, pp. 1190–1208, 1995.
- [129] C. Zhu, R. H. Byrd, P. Lu, *et al.*, “Algorithm 778: L-BFGS-B: Fortran subroutines for large-scale bound-constrained optimization”, *ACM Transactions on mathematical software (TOMS)*, vol. 23, no. 4, pp. 550–560, 1997.
- [130] J. L. Morales and J. Nocedal, “Remark on “Algorithm 778: L-BFGS-B: Fortran subroutines for large-scale bound constrained optimization”, *ACM Transactions on Mathematical Software (TOMS)*, vol. 38, no. 1, pp. 1–4, 2011.
- [131] J. Braun, J. Dumm, F. De Palma, *et al.*, “Methods for point source analysis in high energy neutrino telescopes”, *Astropart. Phys.*, vol. 29, pp. 299–305,

2008. DOI: 10.1016/j.astropartphys.2008.02.007. arXiv: 0801.1604 [astro-ph].
- [132] P. Charlot, D. A. Boboltz, A. L. Fey, *et al.*, “The Celestial Reference Frame at 24 and 43 GHz. II. Imaging”, *Astronomical Journal*, vol. 139, no. 5, pp. 1713–1770, 2010. DOI: 10.1088/0004-6256/139/5/1713. arXiv: 1003.1067 [astro-ph.GA].
- [133] J. Braun, M. Baker, J. Dumm, *et al.*, “Time-dependent point source search methods in high energy neutrino astronomy”, *Astroparticle Physics*, vol. 33, no. 3, pp. 175–181, Apr. 2010. DOI: 10.1016/j.astropartphys.2010.01.005. arXiv: 0912.1572 [astro-ph.IM].
- [134] M. Aartsen, M. Ackermann, J. Adams, *et al.*, “Searches for time-dependent neutrino sources with icecube data from 2008 to 2012”, *The Astrophysical Journal*, vol. 807, no. 1, p. 46, 2015.
- [135] R. Abbasi *et al.*, “A Search for Time-dependent Astrophysical Neutrino Emission with IceCube Data from 2012 to 2017”, *Astrophys. J.*, vol. 911, no. 1, p. 67, Apr. 2021. DOI: 10.3847/1538-4357/abe7e6.
- [136] M. Karl, P. Eller, and A. Schubert, “Search for high-energy neutrino sources from the direction of IceCube alert events”, in *Proceedings of 37th International Cosmic Ray Conference – PoS(ICRC2021)*, vol. 395, 2021, p. 940. DOI: 10.22323/1.395.0940.
- [137] P. Eller and L. Shtembari, *A goodness-of-fit test based on a recursive product of spacings*, 2021. arXiv: 2111.02252 [stat.ME].
- [138] G. Hinton and T. J. Sejnowski, *Unsupervised learning: foundations of neural computation*. MIT press, 1999.
- [139] A. P. Dempster, N. M. Laird, and D. B. Rubin, “Maximum Likelihood from Incomplete Data via the EM Algorithm”, *Journal of the Royal Statistical Society. Series B (Methodological)*, vol. 39, no. 1, pp. 1–38, 1977, ISSN: 00359246. [Online]. Available: <http://www.jstor.org/stable/2984875>.
- [140] W. Press, W. H. S. Teukolsky, *et al.*, *Numerical Recipes 3rd Edition: The Art of Scientific Computing*. Cambridge University Press, 2007, ISBN: 9780521880688. [Online]. Available: <https://books.google.de/books?id=1aA0dzK3FegC>.
- [141] M. Karl, “Search for Neutrino Emission in IceCube’s Archival Data from the Direction of IceCube Alert Events”, in *36th International Cosmic Ray Conference (ICRC2019)*, ser. International Cosmic Ray Conference, vol. 36, Jul. 2019, p. 929. arXiv: 1908.05162 [astro-ph.HE].
- [142] P. Padovani, P. Giommi, R. Falomo, *et al.*, “The spectra of IceCube neutrino (SIN) candidate sources - II. Source characterization”, *MNRAS*, vol. 510, no. 2,

- pp. 2671–2688, Feb. 2022. DOI: 10.1093/mnras/stab3630. arXiv: 2112.05394 [astro-ph.HE].
- [143] E. Waxman and J. N. Bahcall, “High-energy neutrinos from astrophysical sources: An Upper bound”, *Phys. Rev.*, vol. D59, p. 023002, 1999. DOI: 10.1103/PhysRevD.59.023002. arXiv: hep-ph/9807282 [hep-ph].
- [144] Y.-L. Chang, C. Brandt, and P. Giommi, “The Open Universe VOU-Blazars tool”, *Astronomy and Computing*, vol. 30, p. 100350, Jan. 2020, ISSN: 2213-1337. DOI: 10.1016/j.ascom.2019.100350. [Online]. Available: <http://dx.doi.org/10.1016/j.ascom.2019.100350>.
- [145] R. Abbasi, M. Ackermann, J. Adams, *et al.*, “Improved Characterization of the Astrophysical Muon-Neutrino Flux with 9.5 Years of IceCube Data”, *arXiv e-prints*, arXiv:2111.10299, arXiv:2111.10299, Nov. 2021. arXiv: 2111.10299 [astro-ph.HE].
- [146] W. B. Atwood, A. A. Abdo, M. Ackermann, *et al.*, “The Large Area Telescope on the Fermi Gamma-Ray Space Telescope Mission”, *ApJ*, vol. 697, no. 2, pp. 1071–1102, Jun. 2009. DOI: 10.1088/0004-637X/697/2/1071. arXiv: 0902.1089 [astro-ph.IM].
- [147] J. R. Mattox, D. L. Bertsch, J. Chiang, *et al.*, “The Likelihood Analysis of EGRET Data”, *ApJ*, vol. 461, p. 396, Apr. 1996. DOI: 10.1086/177068.
- [148] M. Petropoulou, S. Dimitrakoudis, P. Padovani, *et al.*, “Photohadronic origin of  $\gamma$ -ray BL Lac emission: implications for IceCube neutrinos”, *Monthly Notices of the Royal Astronomical Society*, vol. 448, no. 3, pp. 2412–2429, Mar. 2015, ISSN: 0035-8711. DOI: 10.1093/mnras/stv179. eprint: <https://academic.oup.com/mnras/article-pdf/448/3/2412/6008935/stv179.pdf>. [Online]. Available: <https://doi.org/10.1093/mnras/stv179>.
- [149] M. Petropoulou, K. Murase, M. Santander, *et al.*, “Multi-epoch Modeling of TXS 0506+056 and Implications for Long-term High-energy Neutrino Emission”, *ApJ*, vol. 891, no. 2, p. 115, Mar. 2020. DOI: 10.3847/1538-4357/ab76d0. arXiv: 1911.04010 [astro-ph.HE].
- [150] A. Reimer, M. Böttcher, and S. Buson, “Cascading Constraints from Neutrino-emitting Blazars: The Case of TXS 0506+056”, *ApJ*, vol. 881, no. 1, p. 46, Aug. 2019. DOI: 10.3847/1538-4357/ab2bff. arXiv: 1812.05654 [astro-ph.HE].
- [151] R. Xue, R.-Y. Liu, Z.-R. Wang, *et al.*, “A Two-zone Blazar Radiation Model for “Orphan” Neutrino Flares”, *ApJ*, vol. 906, no. 1, p. 51, Jan. 2021. DOI: 10.3847/1538-4357/abc886. arXiv: 2011.03681 [astro-ph.HE].

- [152] S. T. Myers, N. J. Jackson, I. W. A. Browne, *et al.*, “The Cosmic Lens All-Sky Survey - I. Source selection and observations”, *MNRAS*, vol. 341, pp. 1–12, May 2003. DOI: 10.1046/j.1365-8711.2003.06256.x. eprint: astro-ph/0211073.
- [153] S. E. Healey, R. W. Romani, G. B. Taylor, *et al.*, “CRATES: An All-Sky Survey of Flat-Spectrum Radio Sources”, *ApJS*, vol. 171, pp. 61–71, Jul. 2007. DOI: 10.1086/513742. eprint: astro-ph/0702346.
- [154] N. Jackson, R. A. Battye, I. W. A. Browne, *et al.*, “A survey of polarization in the JVAS/CLASS flat-spectrum radio source surveys - I. The data and catalogue production”, *MNRAS*, vol. 376, pp. 371–377, Mar. 2007. DOI: 10.1111/j.1365-2966.2007.11442.x. eprint: astro-ph/0703273.
- [155] E. Nieppola, M. Tornikoski, A. Lähteenmäki, *et al.*, “37 GHz Observations of a Large Sample of BL Lacertae Objects”, *AJ*, vol. 133, pp. 1947–1953, May 2007. DOI: 10.1086/512609. arXiv: 0705.0887.
- [156] J. J. Condon, W. D. Cotton, E. W. Greisen, *et al.*, “The NRAO VLA Sky Survey”, *AJ*, vol. 115, pp. 1693–1716, May 1998. DOI: 10.1086/300337.
- [157] A. E. Wright, M. R. Griffith, B. F. Burke, *et al.*, “The Parkes-MIT-NRAO (PMN) surveys. 2: Source catalog for the southern survey (delta greater than -87.5 deg and less than -37 deg)”, *ApJS*, vol. 91, pp. 111–308, Mar. 1994. DOI: 10.1086/191939.
- [158] Planck Collaboration, P. A. R. Ade, N. Aghanim, *et al.*, “Planck early results. VII. The Early Release Compact Source Catalogue”, *A&A*, vol. 536, A7, A7, Dec. 2011. DOI: 10.1051/0004-6361/201116474. arXiv: 1101.2041.
- [159] P. C. Gregory, W. K. Scott, K. Douglas, *et al.*, “The GB6 Catalog of Radio Sources”, *ApJS*, vol. 103, p. 427, Apr. 1996. DOI: 10.1086/192282.
- [160] R. L. White and R. H. Becker, “A new catalog of 30,239 1.4 GHz sources”, *ApJS*, vol. 79, pp. 331–467, Apr. 1992. DOI: 10.1086/191656.
- [161] Planck Collaboration, P. A. R. Ade, N. Aghanim, *et al.*, “Planck 2013 results. XXVIII. The Planck Catalogue of Compact Sources”, *A&A*, vol. 571, A28, A28, Nov. 2014. DOI: 10.1051/0004-6361/201321524. arXiv: 1303.5088.
- [162] Planck Collaboration, P. A. R. Ade, N. Aghanim, *et al.*, “Planck 2015 results. XXVI. The Second Planck Catalogue of Compact Sources”, *ArXiv e-prints*, Jul. 2015. arXiv: 1507.02058.
- [163] E. L. Wright, P. R. M. Eisenhardt, A. K. Mainzer, *et al.*, “The Wide-field Infrared Survey Explorer (WISE): Mission Description and Initial On-orbit Performance”, *AJ*, vol. 140, 1868, pp. 1868–1881, Dec. 2010. DOI: 10.1088/0004-6256/140/6/1868. arXiv: 1008.0031 [astro-ph.IM].

- [164] L. Bianchi, B. Efremova, J. Herald, *et al.*, “Catalogues of hot white dwarfs in the Milky Way from GALEX’s ultraviolet sky surveys: constraining stellar evolution”, *MNRAS*, vol. 411, pp. 2770–2791, Mar. 2011. DOI: 10.1111/j.1365-2966.2010.17890.x. arXiv: 1011.1733 [astro-ph.SR].
- [165] V. D’Elia, M. Perri, S. Puccetti, *et al.*, “The seven year Swift-XRT point source catalog (1SWXRT)”, *A&A*, vol. 551, A142, A142, Mar. 2013. DOI: 10.1051/0004-6361/201220863. arXiv: 1302.7113 [astro-ph.IM].
- [166] P. A. Evans, J. P. Osborne, A. P. Beardmore, *et al.*, “1SXPS: A Deep Swift X-Ray Telescope Point Source Catalog with Light Curves and Spectra”, *The Astrophysical Journal Supplement Series*, vol. 210, no. 1, p. 8, 2014. [Online]. Available: <http://stacks.iop.org/0067-0049/210/i=1/a=8>.
- [167] W. Voges, B. Aschenbach, T. Boller, *et al.*, “The ROSAT all-sky survey bright source catalogue”, *A&A*, vol. 349, pp. 389–405, Sep. 1999. eprint: astro-ph/9909315.
- [168] T. Boller, M. J. Freyberg, J. Trümper, *et al.*, “Second ROSAT all-sky survey (2RXS) source catalogue”, *aap*, vol. 588, A103, A103, Apr. 2016. DOI: 10.1051/0004-6361/201525648.
- [169] A. A. Abdo, M. Ackermann, M. Ajello, *et al.*, “Fermi Large Area Telescope First Source Catalog”, *ApJS*, vol. 188, pp. 405–436, Jun. 2010. DOI: 10.1088/0067-0049/188/2/405. arXiv: 1002.2280 [astro-ph.HE].
- [170] P. L. Nolan, A. A. Abdo, M. Ackermann, *et al.*, “Fermi Large Area Telescope Second Source Catalog”, *ApJS*, vol. 199, 31, p. 31, Apr. 2012. DOI: 10.1088/0067-0049/199/2/31. arXiv: 1108.1435 [astro-ph.HE].
- [171] F. Acero, M. Ackermann, M. Ajello, *et al.*, “Fermi Large Area Telescope Third Source Catalog”, *ApJS*, vol. 218, 23, p. 23, Jun. 2015. DOI: 10.1088/0067-0049/218/2/23. arXiv: 1501.02003 [astro-ph.HE].
- [172] B. Bartoli, P. Bernardini, X. J. Bi, *et al.*, “TeV Gamma-Ray Survey of the Northern Sky Using the ARGO-YBJ Detector”, *The Astrophysical Journal*, vol. 779, no. 1, p. 27, 2013. [Online]. Available: <http://stacks.iop.org/0004-637X/779/i=1/a=27>.
- [173] P. Giommi, G. Arrigo, U. Barres De Almeida, *et al.*, “The Open Universe Initiative”, *arXiv e-prints*, arXiv:1805.08505, arXiv:1805.08505, May 2018. arXiv: 1805.08505 [astro-ph.IM].